Ice-nucleating particles in the central Arctic

by

Grace Courtney Elouise Porter

Submitted in accordance with the requirements for the degree of
Doctor of Philosophy

The University of Leeds
School of Earth and Environment

&

School of Physics and Astronomy

June 2021

The candidate confirms that the work submitted is her own, except where work which has formed part of jointly-authored publications has been included. The contribution of the candidate and the other authors to this work has been explicitly indicated below. The candidate confirms that appropriate credit has been given within the thesis where reference has been made to the work of others.

Grace C. E. Porter., Sebastien N. F. Sikora., Michael P. Adams., Ulrike Proske., Alexander D. Harrison., Mark D. Tarn., Ian M. Brooks., and Benjamin J. Murray. 'Resolving the size of ice-nucleating particles with a balloon deployable aerosol sampler: the SHARK'. Published in *Atmospheric Measurement Techniques* (2020).

This publication forms Chapter 2 of this thesis. I designed and led the development of the SHARK with support from IMB, BJM and SNFS. SNFS built the electronic components of the shark with assistance from myself. I planned and carried out experiments with support from MPA, UP, IMB, ADH and MDT. I analysed the data and prepared the figures within the manuscript, and I wrote the manuscript which had input from all authors.

Grace C. E. Porter., Michael P. Adams., Ian M. Brooks., Luisa Ickes., Linn Karlsson., Caroline Leck., Matthew E. Salter., Julia Schmale., Karolina Siegel., Sebastien N. F. Sikora., Mark D. Tarn., Jutta Vüllers., Heini Wernli., Paul Zieger., Julika Zinke and Benjamin J. Murray. 'Origin and variability of ice-nucleating particles close to the summertime North Pole'. *In preparation.*

This body of work forms Chapter 3 of this thesis. I planned and organised the fieldwork part of this work with support from MPA, IMB, MDT, MES, PZ and BJM. I planned and carried out ice-nucleation experiments with the support of MPA. I planned and carried out SHARK flights and sampling with the support of IMB, and MPA. The equivalent black carbon data was provided by PZ, LK and JS. The dimethyl sulfide, transmission electron microscopy and ion chromatography data was provided by CL, LI and KS. The particle surface area data was provided by LK and PZ. I analysed the back trajectories for the air parcels, which were provided by JV and HW. I analysed the data and prepared the figures for the manuscript except for Figure 1 which was produced by BJM, and I wrote the manuscript which had input from all authors.

Grace C. E. Porter., Sebastien N. F. Sikora., Jung-uk Shim., Benjamin J. Murray and Mark D. Tarn. 'On-chip density-based sorting of supercooled droplets and frozen droplets in continuous flow'. Published in *Lab on a chip* (2020).

This publication forms Chapter 4 of this thesis. I designed and developed the microfluidic chip with support from MDT. I carried out the experiments and analysed the data. I prepared the manuscript with support from MDT, and produced all figures in the manuscript except Figure 4 which was produced by MDT. I wrote the manuscript with support from MDT and it had contributions from all authors.

Acknowledgements

Abstract

A small subset of aerosol particles can induce ice-nucleation in supercooled liquid droplets. These ice-nucleating particles (INP) are responsible for the primary, heterogeneous nucleation of ice in clouds, and knowledge of their concentrations, sources and characteristics is necessary to accurately represent these mixed-phased clouds in models. This is particularly important in regions such as the central Arctic Ocean, where there are persistent mixed-phased clouds that help shape the radiative budget of the Arctic but very few measurements of INP, none of which are at cloud altitude.

This thesis aimed to tackle the dearth of central Arctic INP data through the design and use of novel instrumentation, and a field campaign aboard an icebreaker which saw measurements of INP measurements made at both ship and cloud level close to the North Pole (88-90°N). Firstly, a high-volume, size-selective aerosol sampler capable of being deployed for hours at a time at altitudes and temperatures relevant for mixed phased clouds was designed and tested. This sampler was used on a 2-month campaign to the central Arctic ocean from August-September 2018, alongside ship-based INP measurements. The central Arctic INP concentrations at sea-level were highly variable, with concentrations as low as could be expected in the Southern Oceans, and as high as those measured in rural farmland. The INP were found to be heat-sensitive, and the most active samples originated from the Arctic coasts of Russia. The samples with the least INP activity were from the pack ice and Canadian Arctic. The concentrations measured at cloud-level were often decoupled from those at the surface, demonstrating the necessity for more airborne measurements of INP. Additionally, the INP at cloud-level were often smaller than expected, at <0.25 μm in aerodynamic diameter. Finally, in order to better probe the characteristics of sampled INP in the future, a microfluidic device capable of sorting ice crystals containing INP active at a specific temperature from the bulk sample was developed.

Table of Contents

List of Tables

List of Figures

1. Introduction

1.1. The importance of clouds in Earth's atmosphere

Clouds are a key regulator in the Earth's energy balance between incoming, and outgoing radiation. Their radiative effects are dependent on a number of factors, including their phase, altitude and optical thickness. The competition between incoming shortwave radiation from the sun and outgoing longwave radiation from the planet is therefore greatly influenced by the presence and types of clouds (Hartmann et al., 1992; Storelvmo et al., 2015). The radiative impact of clouds is called the cloud-radiative effect, and is of current interest due to the importance of this mechanism in the warming of the Earth. Modelling the behaviour of clouds in order to predict future trends is complicated, with competing processes which are not fully understood.

Clouds can exist in the ice phase, the liquid phase or a mix of the two, called mixed-phase clouds. On a large scale, the phase is predominantly driven by location in the troposphere, with clouds much higher up more likely to contain more ice, such as cirrus clouds, which are thin, wispy, and entirely composed of ice. These clouds are optically thin, and so, in general, transmit more solar radiation than the optically thick, liquid or mixed-phase Stratus clouds within the mid to low troposphere (Hartmann et al., 1992).

Mixed-phase clouds are of particular interest owing to the variation in radiative and precipitative effects with the changing ratio of ice and water in the cloud. However, the phase sensitivity of mixed phase clouds is complex, and additional factors besides temperature, such as secondary ice production and seeding from higher altitude clouds, dictate the amount of ice and water content in these clouds (Storelvmo, 2017).

The ice content of a cloud strongly influences the lifetime, optical thickness, and radiative forcing of the cloud, as seen in Figure 1.1. A cloud consisting of mostly ice crystals has a lower albedo (reflectivity) than a cloud which is mostly liquid water. Therefore a cloud with large ice crystals allows more shortwave solar radiation to be transmitted to the Earth. This usually results in a net warming effect. The opposite is true of mostly liquid clouds, which usually exhibit a net cooling effect. However, the processes dictating cloud ice content are, as yet, not well characterised, and mixed-phase clouds are often only crudely represented in global models (Prenni et al., 2007; Storelvmo, 2017).
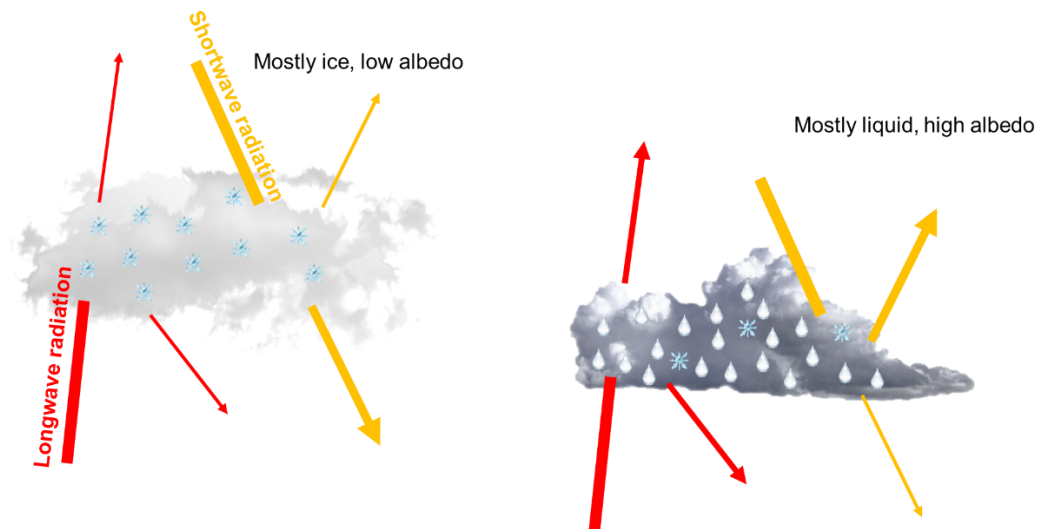
Figure 1.1- Radiative effect of clouds influenced by ice and liquid water content.

1.2. Ice nucleation

Liquid water is metastable at temperatures below 0 °C, where ice then becomes the most stable phase. Water which exists below 0 °C is therefore referred to as supercooled, due to its instability. In small volumes of water where nucleation sites are less likely to be present, a sample can supercool to well below 0 °C. Cloud-sized droplets may reach below -33 °C (Herbert et al., 2015) in the absence of particles, and below this temperature, spontaneous nucleation will become increasingly probable.

1.2.1. Primary and secondary ice formation

The transition from supercooled liquid water droplet to ice crystal occurs when the energy barrier for nucleation is overcome. The transition can be via primary or secondary processes. Primary nucleation in droplets involves the nucleation of ice, either spontaneously (homogeneous nucleation) or via the presence of a particle (heterogeneous nucleation). Secondary production, however, is induced in supercooled water droplets by other ice crystals. There are multiple ways in which ice crystals may induce freezing in a liquid droplet, such as collision fragmentation, rime splintering and droplet shattering (Field et al., 2016). Primary ice nucleation is responsible for the initial formation of ice crystals in a liquid cloud, and where nucleation requires a particle it is highly dependent on the type of particle.

1.2.2. Classical nucleation theory

One of the classic ways used to describe the nucleation of ice is classical nucleation theory (CNT) (Gibbs, 1948; Mullin, 2001). This theory is based on the assumption that nucleation is a time dependant, stochastic process, with uniform nucleation probability throughout the liquid in homogeneous solutions, or on the particle in heterogeneous suspensions.

1.2.2.1. Homogeneous ice nucleation

The homogeneous nucleation of water can be described by the energy changes as the constituent molecules coagulate to form clusters. The excess, or Gibbs free energy ΔG of the system between the cluster and the bulk liquid can be described by the sum of the free energies of the surface ΔG_s and volume ΔG_v between the cluster and the liquid (Mullin, 2001):

$$\Delta G = \Delta G_s + \Delta G_V \qquad \qquad \textbf{Equ 1.1}$$

The growth in cluster size is thermodynamically favourable in supercooled water above a critical cluster size, r_c, but there is a cost associated with forming a liquid-ice interface. Assuming the cluster is a sphere of radius r with a surface interfacial tension γ, the surface term, ΔG_s, a positive quantity representing the cost of forming the surface, can be described by:

$$\Delta G_s = 4\pi r^2 \gamma \qquad \qquad \textbf{Equ 1.2}$$

The volume term, ΔG_V, can be described by:

$$\Delta G_V = \frac{4}{3}\pi r^3 \Delta G_{vu} \qquad \qquad \textbf{Equ 1.3}$$

Where ΔG_{vu} is the free energy per unit volume of the transformation, and is a negative quantity representing the energy gain of forming clusters in a supercooled environment. Therefore, because of the free energies competing as cluster size increases, the total Gibbs free energy ΔG of the cluster is at a maximum at r_c, which is the minimum size of a stable cluster. This can be found by setting the derivative of ΔG with respect to r to zero:

$$\Delta G = 4\pi r^2 \gamma + \frac{4}{3}\pi r^3 \Delta G_{vu} \qquad \qquad \textbf{Equ 1.4}$$

$$\frac{d\Delta G}{dr} = 8\pi r \gamma + 4\pi r^2 \Delta G_{vu} = 0 \qquad \qquad \textbf{Equ 1.5}$$

Rearranging for the critical radius, r_c:

$$r_c = \frac{-2\gamma}{\Delta G_{vu}} \qquad \qquad \textbf{Equ 1.6}$$

Combining with **Equ 1.1** to find the maximum Gibbs free energy, ΔG_{crit}:

$$\Delta G_{crit} = \frac{16\pi\gamma^3}{\Delta G_{vu}{}^2} + \frac{-32\pi\gamma^3}{3\Delta G_{vu}{}^2} = \frac{16\pi\gamma^3}{3\Delta G_{vu}{}^2} \qquad \textbf{Equ 1.7}$$

Particle size and solubility can be related using the Gibbs-Thomson relationship:

$$\ln S = \frac{2\gamma v}{kTr} \qquad \textbf{Equ 1.8}$$

Where S is the supersaturation ratio with respect to the nucleating phase of ice, v is the molecular volume of water in ice, γ is the concentration of the solution over the equilibrium saturation at temperature T, and k is the Boltzmann constant. This can be used to express ΔG_{vu}:

$$\Delta G_{vu} = \frac{-2\gamma}{r_c} = \frac{-kT \ln S}{v} \qquad \textbf{Equ 1.9}$$

Therefore, ΔG_{crit} can be defined as:

$$\Delta G_{crit} = \frac{16\pi\gamma^3 v^2}{3(kT \ln S)^2} \qquad \textbf{Equ 1.10}$$

The rate of nucleation, J_{Hom}, defines the number of nucleation events per unit time and volume, and is an important outcome of classical nucleation theory. J_{Hom} can be expressed in the form of the Arrhenius equation:

$$J_{Hom} = A_{Hom} e^{\frac{-\Delta G}{kT}} = A_{Hom} \, e^{\frac{-16\pi\gamma^3 v^2}{3k^3 T^3 (\ln S)^2}} \qquad \textbf{Equ 1.11}$$

Where A_{Hom} is a reaction constant, also known as the pre-exponential factor. This nucleation rate per volume, J_{Hom} can then be compared to experimental values, where the rate of nucleation per unit volume is explicitly measured.

1.2.2.2.   Heterogeneous ice nucleation

It is incredibly difficult to remove any impurities in a sample of water that may alter the freezing process. Therefore, in larger (> mL) volumes of water it is rare to achieve true spontaneous, or homogeneous, nucleation. Heterogeneous nucleation is much more common and relies on the presence of at least one particle, or coagulation of particles, to overcome the free energy barrier. Such a particle is usually referred to as an ice-nucleating particle (INP). For heterogeneous nucleation to occur at higher temperatures than for homogeneous nucleation, the free energy of producing a cluster of critical size must be smaller than the free energy for homogeneous nucleation ΔG_{crit}. Heterogeneous nucleation is additionally dependant on the surface interactions with the particle. The alteration in the free energy of heterogeneous nucleation caused by interactions with the surface can be described using a wetting angle, where here this angle is that which exists between the crystalline nucleus forming and the particle surface, θ,:

$$\phi = \frac{(2+\cos(\theta))(1-\cos(\theta))^2}{4} \qquad \textbf{Equ 1.12}$$

Where ϕ denotes the factor of alteration in the free energy of critical cluster formation under heterogeneous compared to homogeneous conditions. When θ is equal to 180°, ϕ is equal to 1, meaning the particle has absolutely no effect on the nucleation. Conversely, if θ is equal to 0°, then ϕ is 0, and the particle is the most efficient possible ice nucleator, reducing the energy barrier to zero. Therefore:

$$\Delta G_{het\ crit} = \phi \Delta G_{hom\ crit} \qquad \textbf{Equ 1.13}$$

Which can then be substituted into the Arrhenius equation:

$$J_{het} = A_{Het} e^{\frac{-\phi \Delta G}{kT}} = A_{Het}\ e^{\frac{-16\pi\gamma^3 v^2}{3k^3 T^3 (\ln S)^2}} \frac{(2+\cos(\theta))(1-\cos(\theta))^2}{4} \qquad \textbf{Equ 1.14}$$

There are numerous assumptions in place when applying CNT, including that the clusters are spherical, that the nucleating ability throughout the liquid is uniform, and that the surface of the particle is uniform in heterogeneous ice nucleation. Despite this, the experimental values for homogeneous nucleation align with the theoretical surprisingly well (Koop and Murray, 2016; Tarn et al., 2021), but there are other descriptions , such as the singular description, which may be more appropriate for comparison to heterogeneous nucleation experiments on real world samples.

1.2.3. Singular description for heterogeneous nucleation

The singular description assumes the effects of time dependence are negligible compared to particle-to-particle variability, and so describes nucleation probability as a function of temperature only (Vali, 1971). A site at which nucleation occurs is referred to as an active site, and is the area of the particle surface on which nucleation is thought to be induced at a specific, characteristic temperature for that site. The activity of the sites can be influenced by the surface topography and/or the surface chemistry (Connolly et al., 2009; Vali, 2014; Whale et al., 2017; Kiselev et al., 2017; Holden et al., 2019), and so the determination of factors which influence these active sites is difficult.

In a sample of mixed particle types, this description makes the determination of the INP concentration significantly simpler by removing time dependence, and assuming that the INPs are Poisson distributed, where those with the highest characteristic temperature will dominate nucleation in a droplet as the temperature is reduced. A cumulative nucleation spectra in terms of active sites per unit volume can be obtained from experimental fraction

frozen data (the fraction of droplets frozen at each measured temperature) over a range of temperatures, using a form of the time-independent singular model (Vali, 1971):

$$K(T) = -\frac{\ln(1-f(T))}{V}$$

Equ 1.15

Where the cumulative quantity, *K(T)*, is the density of active sites per unit volume of sample, *V*, and *f(T)* is the fraction of droplets frozen as a function of temperature, which increases as the temperature decreases.

The cumulative spectra is useful for determining the characteristics of INPs in a sample, as the quantity can be scaled to different experimental volumes. It is possible to calculate a concentration of INPs per volume of air sampled onto a filter, or a concentration of INPs per unit volume of a liquid sample for instance.

The differential spectra, *k(T)*, describes the density of active sites per unit volume per temperature interval, *ΔT*:

$$k(T) = \frac{-\ln(1-f(T))}{V \cdot \Delta T}$$

Equ 1.16

The differential spectra gives a number of sites active within a temperature interval of a sample, and so may be used to account for the effects of background contaminants in a sample where water was added, as well as to produce error predictions (Vali, 2019).

The singular description is well used in current ice nucleation studies and can describe most of the experimentally produced results (Vali, 2014). Additionally, the relatively simple representation of INP activity with a characteristic temperature allows for easier integration into climate models. Hence, for the following chapters, this singular description is used to calculate and describe INP concentrations.

1.2.4. Other descriptions for heterogeneous nucleation

It is worth noting the existence of the modified singular description, which attempts to correct for the difference observed when conducting experiments at different cooling rates (Vali and Stansbury, 1966; Vali, 2008). The modified singular approach introduces the reliance on the cooling rate, *R*, to describe the differential spectra as (Vali, 1994):

$$k(T) = -\frac{\bar{a}}{RV} e^{-\bar{b}T}$$

Equ 1.17

Where $\bar{a}$ and $\bar{b}$ are constants which depend on the ice nucleating material present. More recent models for heterogeneous ice nucleation which have

been developed include the framework for reconciling observable stochastic time-dependence (FROST) framework (Herbert et al., 2014), which is based on CNT, and the soccer ball model (Niedermeier et al., 2011; Niedermeier et al., 2014) which uses CNT to reconcile the differences between stochastic and singular models.

1.2.5. Modes of heterogeneous ice nucleation

There are up to four modes of heterogeneous ice nucleation (shown in a simplified form in Figure 1.2): i) deposition, ii) contact, iii) condensation and iv) immersion (Vali et al., 2015).

i) In deposition mode, nucleation occurs on the surface of the INP when water vapour in the surrounding environment is supersaturated with respect to ice. Therefore no bulk liquid water needs to be present for this to occur, as opposed to during contact, condensation and immersion freezing.

ii) Contact freezing occurs as an INP comes into physical contact with the surface of a supercooled liquid water droplet. Contact nucleation is efficient, but the precise mechanism behind the nucleation is still unclear (Maeda, 2021).

iii) Condensation mode freezing requires particles onto which water can condense. As the liquid forms around the particle, it immediately freezes (Hoose and Möhler, 2012).

iv) Immersion mode freezing requires a particle to be immersed in supercooled water, but these particles are not necessarily a cloud condensation nuclei (CCN), which activate as a cloud droplet first (although it is more common for the particle to serve as a CCN and then cause ice nucleation). The particle is suspended in water and nucleation occurs when the characteristic freezing temperature of that INP is reached.

There has been debate about whether condensation freezing should be separated from the immersion and deposition modes when describing the microphysics of nucleation, and this is still ongoing (Vali et al., 2015). Additionally, it has been suggested that deposition mode nucleation may actually occur due to the presence of small amounts of supercooled liquid water in nanoscale pores and cracks on the particle surface which have formed through capillary condensation, a process known as pore condensation freezing (PCF) (Marcolli, 2014; Wagner et al., 2016; David et

al., 2019). The size of the pore and concavity of the surface due to the pore shape result in an inverse kelvin effect, which means water may form in an environment subsaturated with respect to water.

In mixed-phase clouds, it is thought that immersion mode dominates the primary ice production, with secondary influences from contact freezing (Murray et al., 2012; Hande and Hoose, 2017). It has also very recently been determined that different ice nucleation modes are preferential for different active sites (Holden et al., 2021). Holden et al., demonstrated immersion and deposition nucleation had very little correlation between their active sites. The modes of heterogeneous nucleation are still not completely understood, and therefore it is helpful to classify the conditions under which ice nucleation experiments have been performed.

For field and laboratory experiments relevant to mixed-phased clouds, one of the most common ways to determine the ice-nucleating activity of an aerosol or liquid sample is via immersion freezing experiments (detailed in Section 1.4. It is an accessible and useful method to study atmospheric and lab samples of potential INPs (Hoose and Möhler, 2012; Murray et al., 2012; Wex et al., 2015; Hiranuma et al., 2015; Kanji et al., 2017; DeMott et al., 2017). The experiments described in the results chapters were conducted in immersion mode.
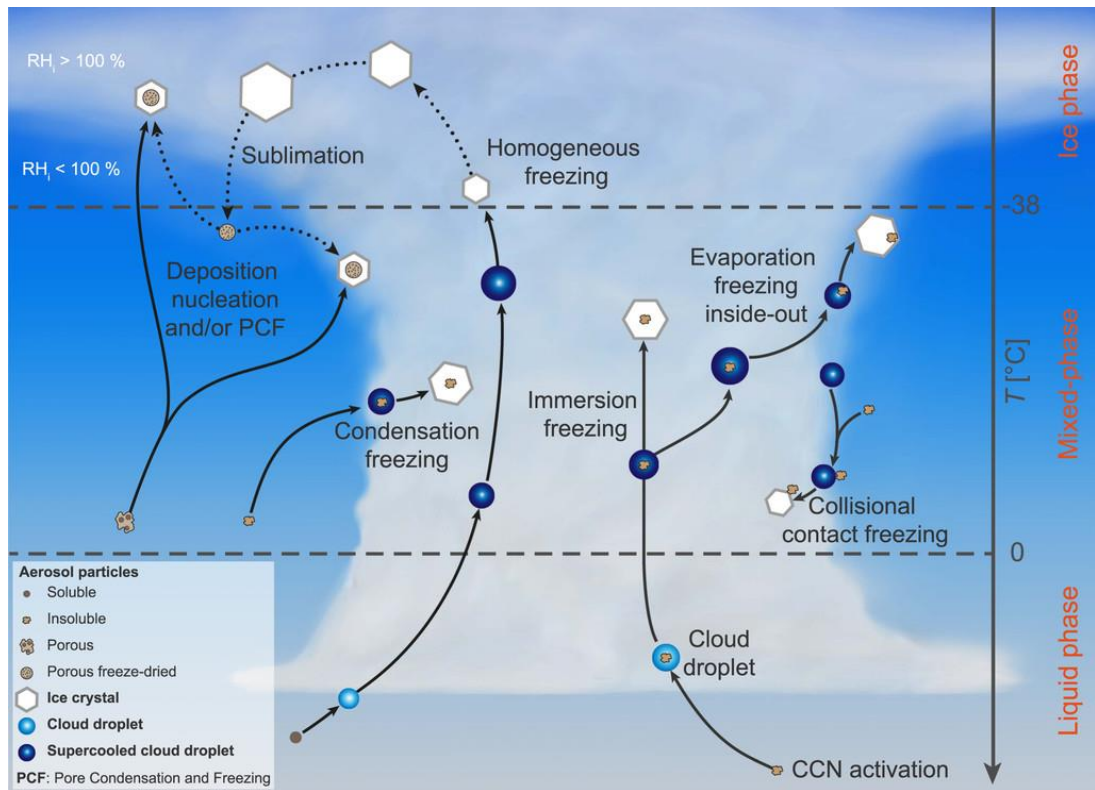
Figure 1.2 - The modes of ice nucleation in the atmosphere. Figure extracted from Kanji et al. (2017).

1.3.   Aerosol sampling and characterisation

In order to better understand and predict the behaviour of mixed-phased clouds, a deeper understanding of the factors affecting their ice content is required (Schmale et al., 2021). In order to achieve this, more measurements need to be undertaken of INP concentrations in differing environments in order to elucidate INP characteristics and sources. Only through more measurements can an understanding of how INP will affect local clouds in the future be achieved.

The sampling of atmospheric aerosol for use in ice-nucleation studies can be accomplished in a number of ways, which usually involve the pulling of air into a chamber (Möhler et al., 2001; Möhler et al., 2021), volume of water (e.g via an impinger) (Carvalho et al., 2008; Mirzaee et al., 2016; Šantl-Temkiv et al., 2017), or through a filter via the use of a pump (Lindsley, 2016; Sanchez-Marroquin et al., 2019). Depending on the amount of flow required, pumps of different sizes and powers can be used, where smaller, lighter and less power-hungry pumps can be used if volumes on the order of around 1 L·min^{-1} of air are acceptable, for instance in high-aerosol environments. However, in low aerosol environments, it can be more efficient to sample on the order of 100 L·min^{-1} of air instead of increasing the

sampling time. There is a balance to this, however, as some techniques may be overloaded by too much aerosol, for instance, when sampling aerosol onto a filter the filter may eventually become blocked.

1.3.1. Filter-based sampling

Filter sampling is the method of pulling sample air through a filter of specific pore size or fibre density in order to capture aerosol particles onto the filter, which can then be recovered for later analysis (Lindsley, 2016). In the case of porous filters (or fibrous filters with pore size equivalents), the pores can be of a size which is much larger than the smallest particles which can be captured (Soo et al., 2016).

There are at least five mechanisms for the capture of particles on-filter: interception, impaction, diffusion, electrostatic attraction and sedimentation (Lindsley, 2016). Interception occurs when particles close to or larger than the pore size come into contact with the filter material as they follow the air stream, whereas impaction occurs when the inertia of a particle is great enough that it continues moving forwards onto the filter when the air stream changes direction (see Section 1.3.2). Diffusion is important for very small particles ($\leq$ 0.1 μm) which are affected by random Brownian motion. The Brownian motion causes motion in the airstream and allows the deposition of particles onto the filter. Electrostatic attraction is used to attract charged aerosol particles onto charged filters. Sedimentation occurs due to gravitational forces acting on larger particles, and is particularly important for filters facing upwards interacting with particles flowing downwards with respect to gravity.

High-flow rate airstreams are less affected by sedimentation as flow forces overcome gravitational forces. Each of these mechanisms affect a different size of particle and the interaction between them means the total collection efficiency is similar to that shown in Figure 1.3 (where electrostatic attraction isn't shown as it is difficult to model). Across all of the mechanisms by which particles can be captured by a filter, there is a high collection efficiency for both larger and smaller particles, with a dip of lower efficiency at particle sizes around a few hundred nanometres in diameter. The location and size of the dip in efficiency is related to the filter material, pore size, flow rate and a number of other factors including the size and shape of the aerosol.
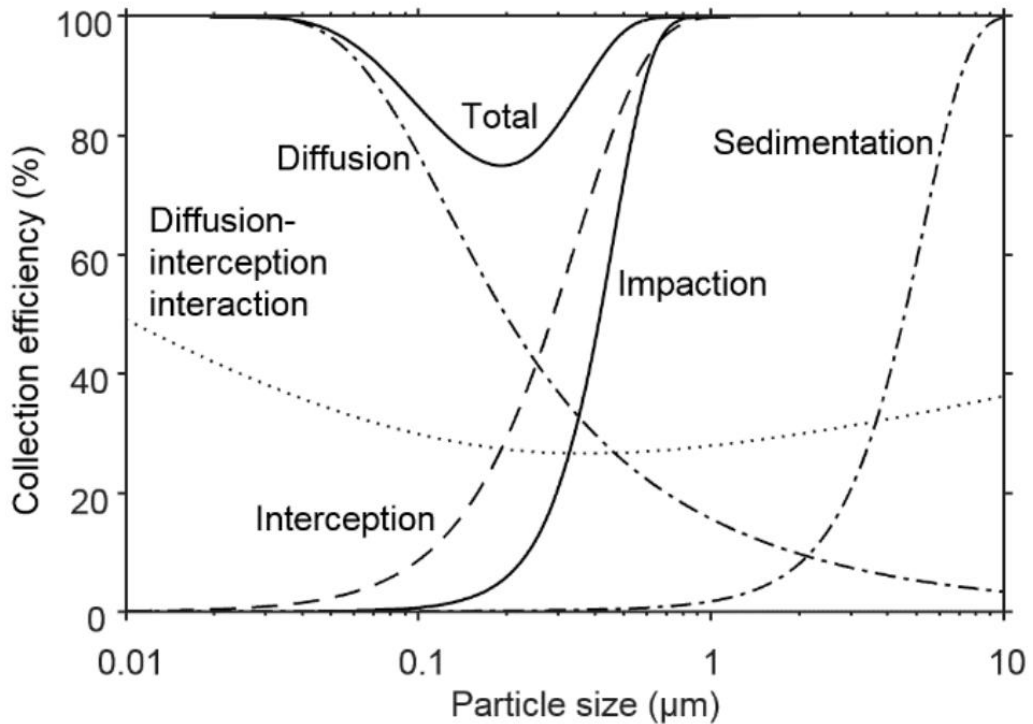
Figure 1.3 – Simulated collection efficiencies for a filter. The filter is fibrous, 1 mm thick with 2 μm fibers using an air velocity of 0.1 m s^{-1}, with air flowing downwards, and electrostatic interaction not included due to difficulty in modelling. Figure extracted from Lindsley (2016).

1.3.2. Impaction-based sampling

In addition to sampling through a filter via pores or fibres, some samplers use the impaction mechanism to capture particles onto thin films. For example, cascade impactors have a series of stages around or through which particles of below a certain size can pass. Particles with a larger aerodynamic diameter cannot follow the streamlines and are impacted upon the impaction plates of that stage. Through this mechanism (shown in Figure 1.4), aerosol can be size-separated and collected onto films for analysis. An after filter collects the particles which are small enough to flow around all of the stages at the set flow rate, either for analysis, or to prevent the pump from becoming clogged.
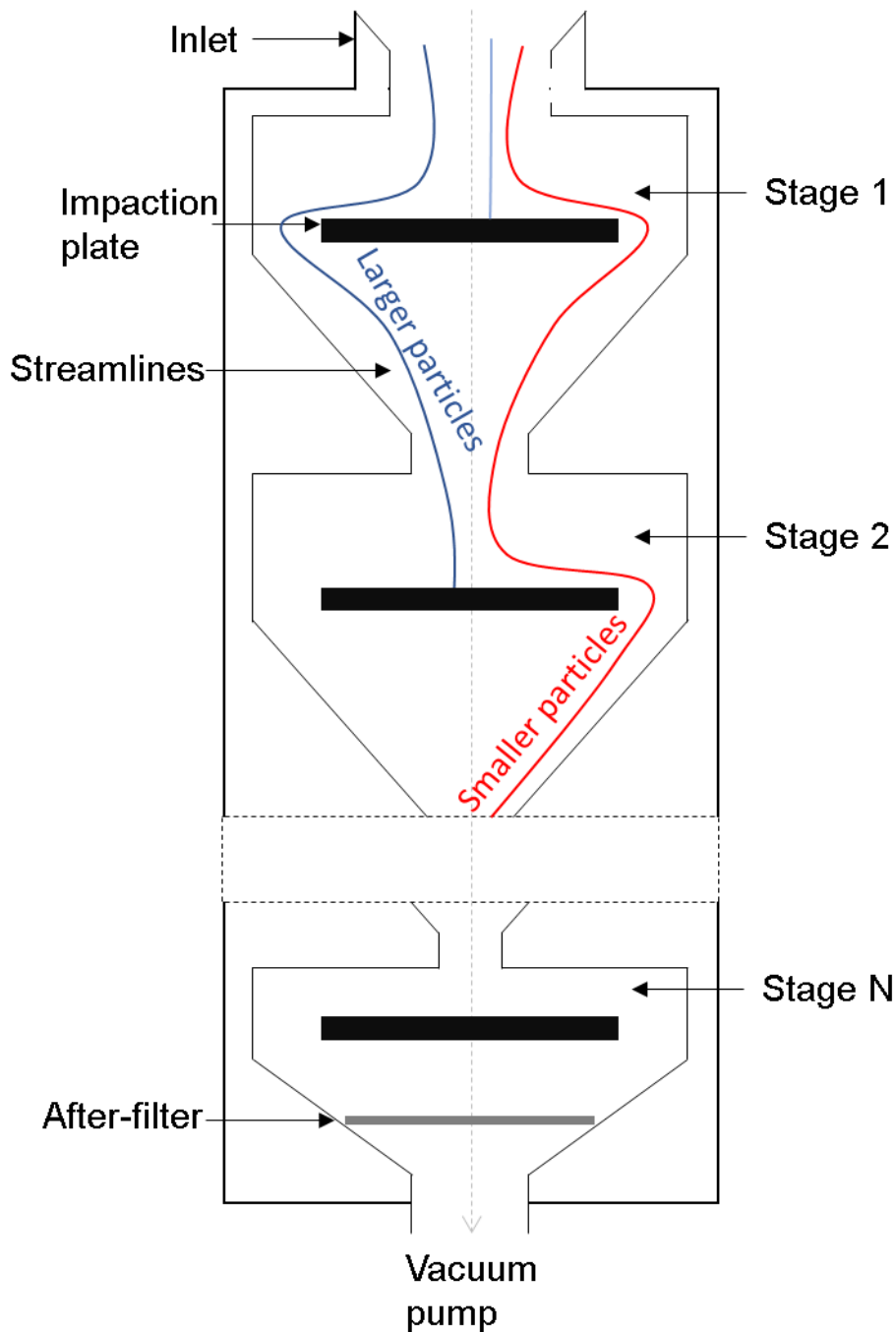
Figure 1.4 - Schematic of a cascade impactor and the streamlines interacting with the stages. The smaller particles with less inertia are more likely to reach the higher N stages, as larger particles are impacted first.

Aerosol can also be passed through a single impactor of specific size cut off, only allowing particles below a specific size to pass through before interaction with filters, films or other collection media. The most common size cut-offs are 10 μm (PM$_{10}$) or 2.5 μm (PM$_{2.5}$), because of the relevance of these sizes in medical fields to determine aerosol effects on lungs. The

smaller PM2.5 aerosol is more likely to settle deeper in the lungs, whereas the larger PM10 aerosol would interact more with upper airways (Darquenne, 2012). Particle size also significantly affects residence time in the atmosphere, with particles a few hundred nanometres in size having a residence time, or lifetime, in the atmosphere on the order of weeks, whereas larger, 10 µm particles may have a residence time of only hours (Jaenicke, 2007).

1.4.   INP measurement techniques

INPs are rare aerosol particles, making up a very small subset, only 10^{-5} – 10^{-3}, of the bulk atmospheric particle population (Rogers et al., 1998). However, in a cloud droplet, only one INP is required to induce nucleation. This makes determining the particles responsible for the nucleation very difficult when the sample population is mixed, such as for atmospheric aerosol or field samples where techniques like manual subdivision of samples is employed to isolate INPs (Hill et al., 2016), or other techniques such as mass spectroscopy (Pratt et al., 2009) and SEM (Sanchez-Marroquin et al., 2019) are used to characterise the aerosol. Even once an INP has been identified, there may exist individual active sites on the surface which may have different characteristic critical temperatures (Holden et al., 2019). Additionally, the length of storage of INPs once collected has a noticeable effect on their ice-nucleating activity (Beall et al., 2020), making the analysis of atmospheric samples even more difficult. Despite this, there are a number of methods for collecting atmospheric aerosol in a way which allows the ice-nucleating activity to be probed, from filter sampling, to impactors, impingers and on-line INP instrumentation (described below) (Kanji et al., 2017; Cziczo et al., 2017; DeMott et al., 2018).

The characteristics of sampled bulk aerosol can then be correlated to INP activity and estimations of the sources of the INPs can be made. Probing the concentrations, origins and types of INPs in a lab or field environment usually requires the use of equipment which induces and monitors the freezing of INPs in a controlled environment. This section focuses on the immersion freezing mode, which is arguably the most atmospherically relevant for mixed-phase clouds due to the importance of the presence liquid droplets for ice formation in clouds and the relative rarity of contact nucleation (Murray et al., 2012; Hande and Hoose, 2017). Some experimental methods begin with particles of aerosol onto which a liquid

droplet can be formed and frozen by inducing supersaturation with respect to water and ice, such as cloud chambers and some Continuous Flow Diffusion Chambers (CFDCs). Other methods may immerse collected aerosol particles in liquid, or use liquid sample to form droplets. After particles are immersed in liquid droplets the temperature is reduced and freezing induced, before the detection of freezing events, which can be carried out in a variety of ways.

There are instruments which measure INP concentrations at or close to real-time, and these instruments are usually referred to as on-line instruments. Conversely, there are instruments which gather aerosol over a sampling period (usually hours to days), and then the INP analysis is performed on the entire sample.

1.4.1. On-line techniques

On-line instruments for the measurement of atmospheric INPs allow concentrations to be gathered close to real-time, and allow easier access to long-term monitoring. This is extremely attractive in environments with high INP and aerosol concentrations which change quickly, or for low-aerosol environments where long-term measurements may elucidate seasonal cycles or changes. However, higher time resolution often means a lower detection limit. Two of the most used on-line instruments for ice nucleation research are continuous flow diffusion chambers (CFDCs) and cloud chambers.

1.4.1.1. Continuous flow diffusion chambers (CFDCs)

A CFDC is an instrument which induces specific temperature and humidity conditions, where a sheath flow constrains an aerosol flow to a region of well-defined temperature and humidity. The control of saturation conditions with respect to ice (for probing deposition and immersion modes), and sometimes water (for probing immersion mode), is achieved by a temperature gradient between the walls (shown in a simplified schematic in Figure 1.5), which are either parallel plates or concentric cylinders. In the upper section of a CFDC the aerosol particles are allowed to nucleate and grow. The ice crystals which form are significantly larger than the aerosol particles, and grow faster than any water droplets which form due to the relative supersaturation with respect to ice. Some CFDCs expose the aerosol to conditions which force evaporation of remaining liquid droplets, enhancing the differences between the ice crystals and particles. A particle detector/counter will then determine the number of ice crystals and this can

be compared to the total aerosol concentration in order to determine the INP concentration at the set conditions.

There are a few drawbacks to this technique, mainly the effects of icing on the walls allowing frost to form and ice crystals from the walls to enter the flow which are counted as ice crystals. The need to regularly replace the ice on the walls requires downtime. Additionally, because the INP concentrations can only be achieved for one temperature at a time, it can be difficult to determine an appropriate temperature for the sampled aerosol. There is a trade-off between having a low enough temperature to give a signal, but a high enough temperature to detect rarer INP types. However, the advantages of being able to measure INP concentrations in real-time mean that CFDCs are still one of the most common on-line ice-nucleation instruments, especially on-board aircraft (Rogers et al., 2001; DeMott et al., 2015). Additionally, autonomous instrumentation is being developed, decreasing the user burden and opening the door for long-term CFDC based INP measurements (Brunner and Kanji, 2021).
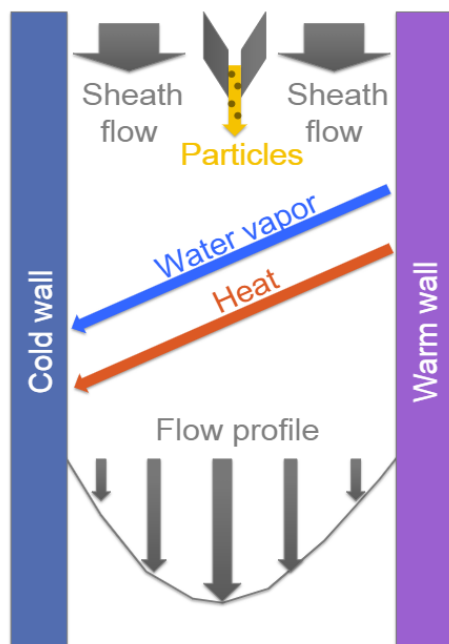
Figure 1.5 - Idealised schematic showing the principle of operation of a CFDC. A temperature gradient between an ice-coated wall and a warmer wall allows control of the supersaturation of the environment with respect to ice. The particle-laden flow is centred between the walls and particle-free sheath flows ensure the particles stay within the laminar region of the flow where the conditions are controlled. Figure extracted from Garimella et al. (2017).

1.4.1.2. Expansion chambers

Cloud chambers work on the principle of adiabatic expansion to cool gas inside the chamber via the reduction of pressure. The schematic in Figure 1.6 shows the flow of aerosol through the system during an expansion where ice crystals are formed in the chamber and counted with an optical particle counter (OPC) (Garimella et al., 2017). The cloud chamber is named so because it simulates the conditions experienced when particle filled gas rises through the atmosphere. Similarly to CFDCs, immersion and deposition modes can in principle both be probed depending on the saturation conditions with respect to water and ice set within the chamber before the expansion. Cloud chambers such as the Aerosol Interactions and Dynamics in the Atmosphere (AIDA) chamber are used in laboratory studies of collected aerosol and specific known INP types. Cloud chambers suffer from similar drawbacks to CFDCs in that they have reduced sensitivity compared to off-line techniques when sampling in low INP environments. Large-volume chambers have been built, such as the AIDA chamber, but the cleaning cycle in between expansions is a long process, and it is not portable. Based on the same principles as the AIDA chamber, a new portable instrument called the Portable Ice nucleation Experiment (PINE) chamber was developed in order to allow cloud chambers to be deployed on campaigns with limited space availability, such as those based on aircraft and ships (Möhler et al., 2021). There are several positives of long term measurements close to real-time, such as reduced user burden, increased time and temperature resolution for measurements, the ability to gain seasonal data and information about the effects of sporadic events on the INP populations.
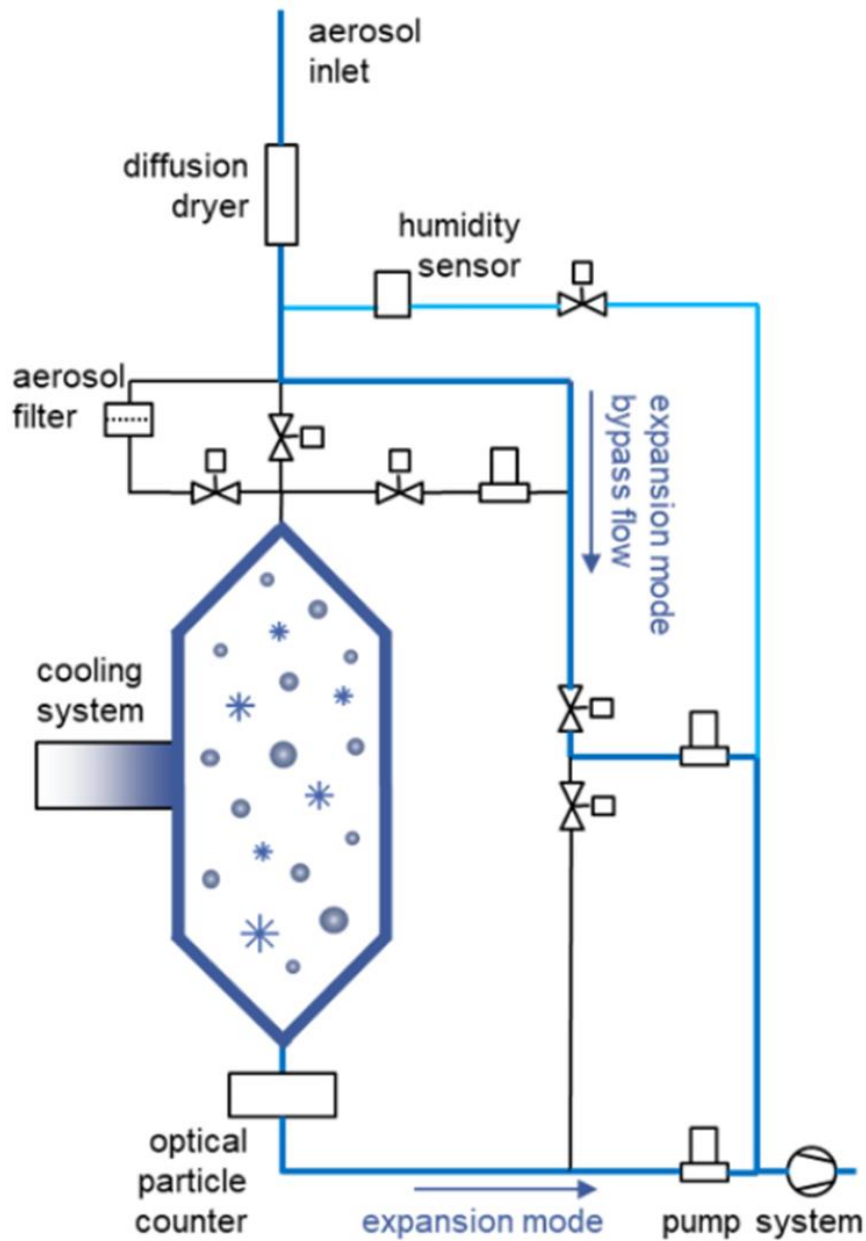
Figure 1.6 – A schematic demonstrating the working principle of a cloud chamber during an expansion. The chamber is shown filled with liquid droplets and ice crystals, and air is pulled out of the chamber to enter an optical particle counter. Figure adapted from Möhler et al. (2021).

1.4.2. Off-line techniques

Off-line methods of atmospheric ice nucleation studies involve the collection of aerosol over a time period, before analysis of the sample as a whole. This gives much lower time resolution than on-line instrumentation (samples on the order of hours to days as opposed to minutes for on-line instrumentation), but has the advantages of generally being much more

portable and therefore easier to take into the field, being cheaper to buy and more accessible, and allowing rarer INPs to be more easily detected due to the ability to increase the sample size. An accessible technique for the off-line study of immersion mode ice nucleation uses a cold stage and is referred to as a drop freeze assay. One of the main drawbacks in conventional drop freeze assays is the difficulty in accessing the lowest temperature INPs due to the introduction of impurities to the sample. Ideally a mixture of off-line and on-line techniques would be deployed whenever possible, especially since this would increase both the time and the temperature resolution of measurements. However, for field studies of atmospheric aerosol, off-line techniques remain some of the most accessible, especially for low INP environments.

1.4.2.1. Conventional cold stage techniques

The term drop freezing assay comes from the method of generating (manually or via a machine) sample droplets onto a cold stage, before reducing the temperature of the stage and thus the droplets, and observing the droplet freezing events. The freezing process can be seen in Figure 1.7a-d, where droplets which have been pipetted onto a substrate on a cold stage are frozen as the stage temperature is reduced, and detected via an optical camera. The sample can consist of unaltered collected liquid samples, such as river-water (Knackstedt et al., 2018), sea surface microlayer (Wilson et al., 2015; Irish et al., 2017; Ickes et al., 2020) or cloud water and precipitation (Pratt et al., 2009; Joly et al., 2013; Petters and Wright, 2015). However, the sample can also be made up of suspensions of particles such as mineral dusts in ultra-pure water (Atkinson et al., 2013; Hiranuma et al., 2015), or aerosol which has been collected on a filter and then washed into ultra-pure water (O'Sullivan et al., 2018; Tarn et al., 2018; Schneider et al., 2020; Adams et al., 2020) . The sample-filled droplets can be pipetted directly onto the stage, or onto a substrate such as coated glass, oil, or a filter (Whale et al., 2015; Tobo, 2016; Price et al., 2018; Polen et al., 2018; Harrison et al., 2018a). Each substrate type is associated with slightly different levels of contamination, but the general principle remains the same. Usually dry air or dry Nitrogen gas is passed over the cold stage during the reduction in temperature in order to stop the formation of condensation on the plate or substrate, and therefore prevent contact freezing from interfering with immersion mode studies.
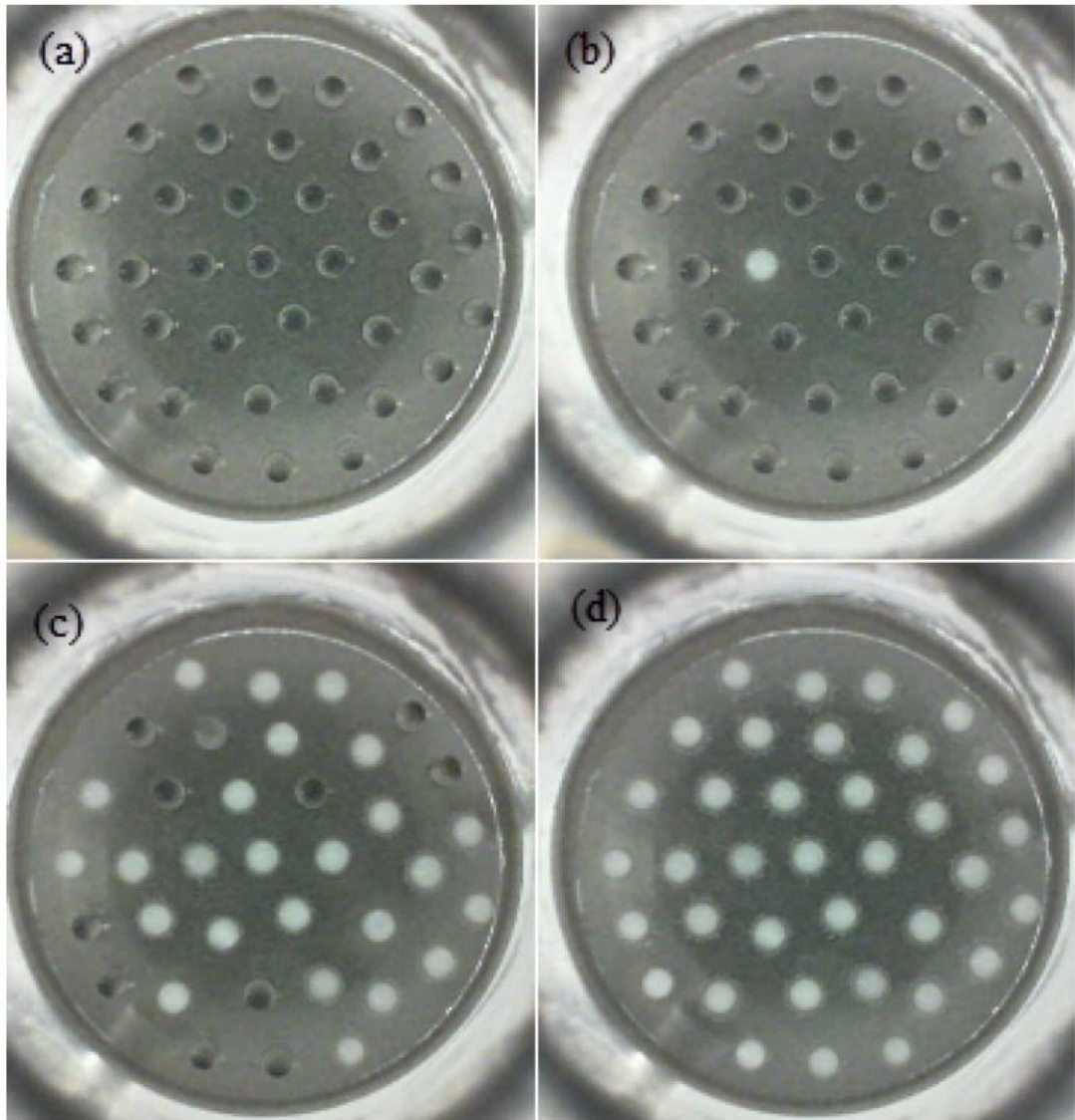
Figure 1.7 – Droplets (1 µL) pipetted onto a glass substrate being cooled on a cold stage. The droplets are shown as the temperature of the cold stage is reduced, where a) none of the droplets have frozen, b) one droplet has frozen, c) many droplets have frozen and d) all of the droplets have frozen. Figure extracted from Whale et al. (2015).

Detection of freezing events can be achieved in a number of ways, owing to the changes in droplet temperature, optical scattering properties and heat release of the phase change. Infrared sensors can be used to measure the temperature of the droplets (which are usually in small wells for this type of experiment) as the stage temperature is reduced. As the phase of each droplet/well changes, the temperature is momentarily increased to the water-ice equilibrium temperature of 0 °C due to the release of latent heat (Harrison et al., 2018b) and so infrared sensors can be used to detect this latent heat release upon freezing. This latent heat released can also be

detected by calorimetry (Westh et al., 1991; Han et al., 2008). The optical light scattering properties change as the droplet nucleates to form an ice crystal, and this alteration in properties is most obvious during the initial, dendritic stage of crystal growth owing to the number of new liquid-ice interfaces being formed. This can be easily detected using optical cameras in real-time. The ease and accessibility of observing nucleation in this way means there are a number of studies which use optical detection in drop-freeze assays (Stopelli et al., 2014; Whale et al., 2015; Budke and Koop, 2015; Tobo, 2016; Tarn et al., 2019; Miller et al., 2021). The results chapters also all used a form of optical detection in analysis of INPs.

An advantage of drop freeze assays is the INP spectra with respect to a wide range of temperatures which can be produced in a single experiment. Using droplets of smaller sizes, such as pL droplets created using microfluidics (discussed in detail in Section 1.4.2.2) or a nebuliser are less likely to contain impurities or warmer INPs (Whale et al., 2015; Tobo, 2016; Tarn et al., 2018), and so smaller droplets can probe the colder end of the INP spectra (Vali, 1971). Conversely, µL- mL droplets deposited via pipetting have much higher backgrounds, but can more easily measure the rarer, warmer temperature INPs. In drop-freeze assays, usually only a small amount of collected sample is needed to perform one freezing experiment. This means that repeat runs can be performed, and also that subsets of the sample can be diluted or exposed to different conditions in order to determine the effect on ice-nucleating ability. The most common example of this is a heat test (described in later chapters), which involves taking a subset of a sample and exposing it to temperatures which would denature any proteins that may be present (Christner, Morris, et al., 2008; Christner, Cai, et al., 2008; Wilson et al., 2015; Hill et al., 2016; O'Sullivan et al., 2018). Therefore, the effectiveness of INPs which relied on proteins would be reduced or removed, and so biogenic, proteinaceous INPs could be identified. The ability to analyse a subset of the collected sample is extremely useful when there are fewer instruments available to collect aerosol for analysis.

A drawback of the drop freeze assays is the high backgrounds due to contamination of substrates and water. It has been suggested that a silanised coverslip substrate is the most appropriate for drop freezing assays, due to their availability, cost efficiency and consistency in freezing behaviour (Polen et al., 2018). The ultra-pure water used to suspend particles for ice-nucleation studies can have a large influence on the

contamination of the sample. It is common to use Milli-Q systems to produce ultra-pure or bottled HPLC-grade water when Milli-Q systems are unavailable or unreliable. It is important that the ice-nucleating activity of the water used is determined before experimental runs, so that the backgrounds can be either represented or removed from the calculated INP concentrations. Additionally, drop freeze assays suffer from evaporation of the droplets, which can be mitigated by controlling the dry air flow and beginning cooling as soon as possible after the droplets have been deposited onto the stage. It would be advantageous to adapt the technique to reduce these drawbacks (high backgrounds and evaporation), whilst keeping the aspects of the technique that make is so accessible and usable with other analysis techniques. Microfluidic platforms provide many methods to achieve this, and are discussed in Section 1.4.2.2.

Because of the large variation in methods for drop freezing assays, it is important to ensure that methods used are well explained and the raw data in the form of a fraction of droplets frozen at specific temperatures (from here on referred to as a fraction frozen curve) given wherever possible, to allow comparison with other studies (Polen et al., 2018).

1.4.2.2. Microfluidic technology

The control of fluid flow in miniaturised devices via microstructures is broadly referred to as microfluidics (Whitesides, 2006; Tarn and Pamme, 2013; Sackmann et al., 2014). In recent years microfluidics has been applied in a number of off-line ice-nucleation studies, owing to the reduced contamination pathways, smaller droplet sizes, and increased ability to automate and integrate processes (Reicher et al., 2018; Tarn et al., 2018; Reicher et al., 2019b; Tarn et al., 2020; Roy et al., 2021). Microfluidic devices are often referred to as lab-on-a-chip devices because of the breadth of analytical techniques that can be downscaled and integrated on a single chip. The "chip" in lab-on-a-chip referring to the small, microchanneled device, and is usually centimetres in size with structures on the µm scale. Once designed and fabricated, a microfluidic chip can be placed atop a cold stage and used in droplet freezing experiments.

Fabrication

In terms of fabricating a microfluidic device, a number of materials can be used to create the microstructures which will influence the fluid flow. The material chosen will affect chemical stability, thermal and optical properties,

or ease of fabrication (Ren et al., 2013). A soft, optically clear material like polydimethylsiloxane (PDMS) elastomer, is very commonly used in soft lithography for microfluidics (Effenhauser et al., 1997; Duffy et al., 1998; McDonald et al., 2000). Many devices are produced using photolithography, which creates microchannels by first exposing the desired channel design onto a layer of photoresist, usually via laser-writing or UV-light through a mask (Duffy et al., 1998; McCreedy, 2001). The unexposed photoresist is then removed, leaving a raised design onto which PDMS can be poured and cured. The PDMS is then peeled away, revealing the channel design. Inlet and outlet holes for one or more fluids are punched into the soft PDMS. The PDMS is then bonded to a substrate. This forms the chip, into which tubing can be placed to allow liquids to flow into and out of the chip's channels, with flow rates controlled by syringe pumps. A simplified version of this process is shown in Figure 1.8. Hard materials, such as glass, can also be etched to create the channel design. In the case of glass, hydrofluoric acid, or a glass-etching cream is used to etch the channels, before inlet and outlet holes are drilled and the etched glass is bonded to a glass substrate (Yuen and Goral, 2012).
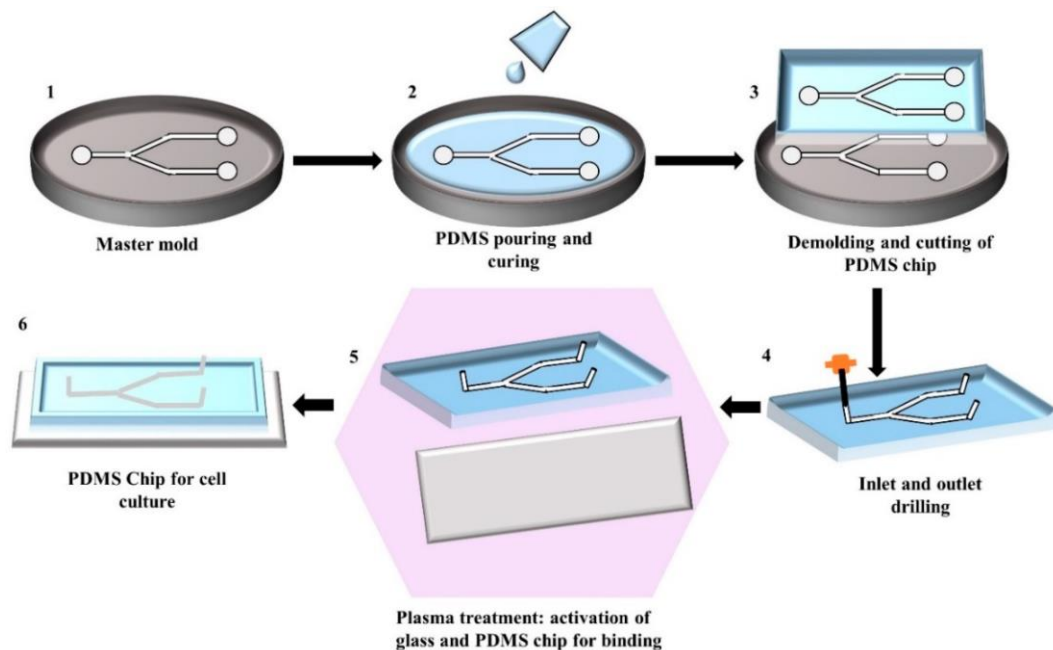
Figure 1.8 - The method of producing PDMS microfluidic chips via soft lithography. There is first a master mold produced, often via photolithographic processes, where the design is raised from the surface at a height equal to the desired channel height for the chip. The PDMS is poured, cured and cut from the master before inlet and outlet holes are made and the chip is bonded to a glass substrate, ready for tubing to be fitted. Figure extracted from Akther et al. (2020).

Droplet microfluidics

Numerous analytical techniques can be miniaturised and used on-chip. This is one of the reasons why microfluidics is already used in a wide range of fields, from environmental science (Tarn et al., 2019; Reicher et al., 2019a), food science (Kiani and Sun, 2011), to organic synthesis (Watts and Wiles, 2012). One of the methods for storing and manipulating sample in a flow is by producing sample droplets. Microfluidics can be used to produce monodisperse sample droplets at rates of thousands per second, and allows the manipulation and analysis of those droplets on-chip (Teh et al., 2008; Casadevall i Solvas and deMello, 2011; Chou et al., 2015; Zhu and Wang, 2017). Droplet microfluidics involves the creation of droplets, also referred to as the dispersed phase, in an immiscible medium which acts as a continuous phase. The dispersed phase is injected into the continuous phase and a mixture of flow rate control and channel design produces droplets in flow. Examples of channel designs which would be used to produce droplets include the T-junction (Figure 1.9a) or a flow focusing junction (Figure 1.9b). The T-junction only has one channel carrying the continuous phase, and produced droplets via shearing the dispersed medium. The flow-focusing junction contains two continuous phase channels which meet to pinch off the dispersed phase into droplets. Both methods can be easily fabricated in PDMS, but the T-junction droplets are likely to be a little more monodisperse, and the flow-focusing junction has higher flexibility in droplet size (Abate et al., 2009). These methods allow monodisperse droplets to be produced with high-throughputs and are simple to fabricate in common chip materials. An example of a droplet system is the generation of water-in-oil droplets, where water is the dispersed phase in the continuous oil medium, and using this technique, 100s to 1000s of monodisperse droplets can be produced per second.
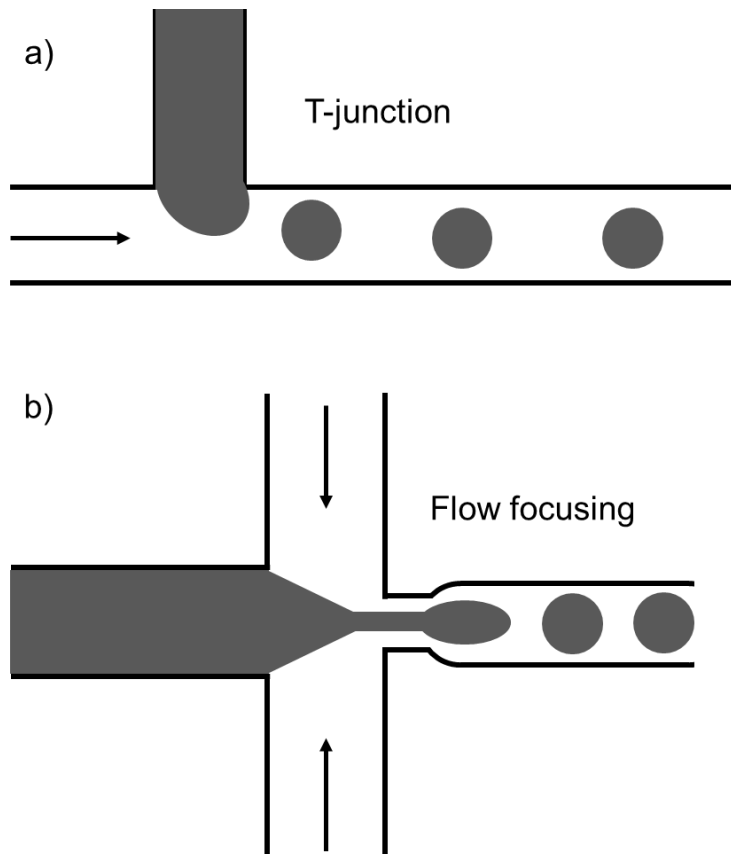
Figure 1.9 – Examples of high-throughput droplet production techniques in microfluidics. a) The T-junction and b) the flow focusing junctions are the most common techniques used to produce monodisperse droplets at high rates.

Some microfluidic systems have been developed for ice nucleation studies using water-in-oil droplets. Most use a method of production and storage of the droplets, wherein a population of droplets is produced on-chip, then held on/off the chip atop a cold stage and the droplet freezing events observed (Reicher et al., 2017; Tarn et al., 2018; Reicher et al., 2019a; Brubaker et al., 2020; Tarn et al., 2020), similar to the cold stage techniques discussed in Section 1.4.2.1. Surfactant can be added to the continuous phase to prevent droplets from coagulating (Reicher et al., 2018; Tarn et al., 2020), but create and store techniques have also demonstrated that contact freezing does not significantly influence nucleation despite close packing of droplets (Tarn et al., 2018). Some techniques freeze droplets in continuous flow (Stan et al., 2009; Stan et al., 2010; Tarn et al., 2020; Roy et al., 2021). Freezing in-flow provides a potential benefit over store and create, in that it is possible to perform single-droplet analysis after the droplet has frozen, though such analysis has not been seen in the literature at the time of writing. For this, a

sorting technique would need to be determined and applied, to separate the frozen ice crystals out from the droplets.

Sorting

The passive separation and sorting of populations of cells or particles based on a number of physical differences such as size, density, charge is possible using microfluidics (Sajeesh and Sen, 2014; Wyatt Shields IV et al., 2015; Bayareh, 2020). Sorting of these populations allows cells or particles with specific properties to be isolated or concentrated for further analysis or storage. It is also possible to use active sorting techniques such as magnetophoresis (Pamme and Wilhelm, 2006; Al-Hetlani et al., 2010), acoustophoresis (Petersson et al., 2007; Lenshof et al., 2012) or electrophoresis (Raymond et al., 1994; Johnson and Bowser, 2018) to sort populations of droplets/cells/particles. However, in the case of ice nucleation, it would be preferential to apply as few treatments to the sample as possible in order to avoid altering the properties of the INP. Therefore passive sorting is a more likely technique for use in ice-nucleation. Passive sorting, where no external instrumentation is needed to exert a force on the population to be sorted, can be achieved via a number of means. From split flow thin-cell fractionation (SPLITT) (Springston et al., 1987), to the use of centrifugal platforms (Haeberle et al., 2006; Strohmeier et al., 2015; Ukita et al., 2017), and filtering (Burger and Ducrée, 2012). An example of a passive sorting method for particles of differing sizes which could be used to sort ice crystals from liquid droplets in a microfluidic device, called pinched flow fractionation is shown in Figure 1.10 (Yamada et al., 2004). This method introduces particle filled liquid via one inlet and particle-free liquid via another inlet. The control of the flow in the two inlets presses the particles along one wall in a pinched section of the chip, and then as the chip expands, the particles differences in position are amplified as they enter different areas of the flow profile. The ability to passively isolate INPs via microfluidics in such a manner would allow downstream or off-chip analysis of INPs active at specific temperatures, using techniques such as DNA analysis (Garcia et al., 2012; Huffman et al., 2013; Hill et al., 2014; Šantl-Temkiv et al., 2019) and Raman spectroscopy (Iwata and Matsuki, 2018). With the recent developments in continuous flow ice nucleation studies, a method of separating the droplets from the ice crystals formed at specific temperatures is a step towards a system which could produce, freeze and analyse droplets for ice nucleation on-chip. A method for this separation is presented and discussed in Chapter 4.
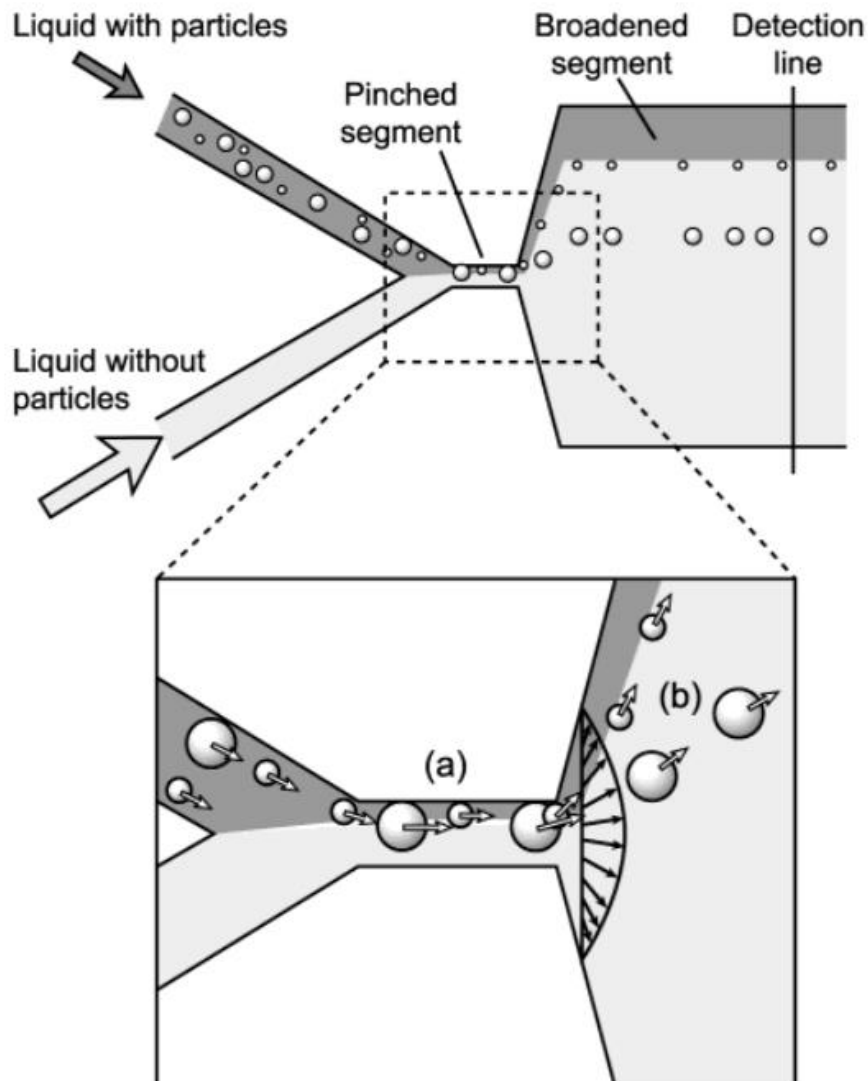
Figure 1.10 - An example of a passive sorting mechanism for differently sized particles via pinched-flow fractionation. a) Particle filled liquid enters the pinched section via one inlet, and particle-free liquid enters via another inlet, forcing the particles against one wall. b) The difference in the position of the particles is enhanced once they enter an expanding chamber. Figure extracted from Yamada et al. (2004).

Microfluidics in ice nucleation

In future studies, a total analysis system for ice nucleation studies is possible, and for field work is extremely desirable. A system like this could allow automated monitoring of INP concentrations on-chip. Sampling of aerosol can already be performed on-chip (Jing and Sui, 2017; Metcalf et al., 2018), and such systems could be integrated with particle sorting processes, such as the one described in Chapter 4, to enable analysis of single particles

in-flow, or the capture of INP active at specific temperatures for off-chip analysis. Recent advances in the automated detection of freezing events would allow automated analysis of large amounts of freezing data via, for example, machine learning (Roy et al., 2021). Finally, the addition of automated sample analysis for isolated populations of INPs and inactive aerosol for specific temperatures could be used.

1.5. Known types of ice-nucleating particles

Although INPs make up a small subset of bulk aerosol, they are found in some of the most pristine, to the most polluted environments. There is not a definite picture of what makes a good INP, but in general surface chemistry and/or topography is known to be important in the nucleation and growth of ice on the particle surface (Pruppacher and Klett, 1997; Hoose and Möhler, 2012; Murray et al., 2012; Kanji et al., 2017). For insoluble particles such as mineral dusts, the surface topography is known to play a factor in the ice-nucleating activity, with specific active sites nucleating ice at a characteristic temperature (Vali, 2014; Kiselev et al., 2017; Holden et al., 2019). This may be due to the exposed crystalline surface providing an energetically favourable template for ice to arrange upon (Kiselev et al., 2017).

For the biological particles or, bioaerosol made up of proteinaceous material, ice-nucleating macromolecules have been identified which have their own characteristic temperature of nucleation (Hartmann et al., 2013; Pummer et al., 2015). For both mineral dusts and bioaerosols, surface hydroxyl -OH groups may provide a surface for the templating of ice in a similar way to a lattice structure in mineral dusts. However, in this case the structure is brought about via the arrangement of water molecules as they create hydrogen bonds on the surface -OH groups, and by the efficient removal of latent heat (Pandey et al., 2016). This surface dependence means that, in some cases, the larger the INP, the more efficient it is at nucleating ice (Pruppacher and Klett, 1997), but this is not always the case (Mason et al., 2016; Porter et al., 2020a).

As discussed previously, larger aerosol particles have a significantly shorter residence time in the atmosphere, and so there is less propensity for larger, usually more efficient, ice nucleators to be transported long distances from their sources. Both mineral dusts and biological INP (whether from terrestrial or marine sources) make up the majority of observed active INP types in the regime relevant for mixed-phase clouds (Hoose et al., 2010; Vergara-Temprado et al., 2017; O'Sullivan et al., 2018; Ladino et al., 2019), but there

are other INP types which may become important on shorter timescales, at specific locations, or at colder temperatures.

1.5.1. Mineral dusts

Mineral dust can refer to dust particles from deserts, volcanos and soils. Mineral dust INPs are one of the most atmospherically important INP types, due to the high emission rates and presence of sources around the globe (Hoose and Möhler, 2012; Murray et al., 2012). Larger dust particles are thought to have higher activity, presumably because of the greater surface area and so increased availability of active sites (Welti et al., 2009; Hartmann et al., 2016). The ice-nucleating activity of dusts has been observed to mostly occupy the INP temperature spectrum at temperatures <−15 °C (Murray et al., 2012), and is produced by a number of mineral types. One of the most ice-active minerals is potassium-rich feldspar (K-feldspar), and most of the activity observed in dust samples can be attributed solely to K-feldspar if it is present (Atkinson et al., 2013; Augustin-Bauditz et al., 2014; Niedermeier et al., 2015; Boose et al., 2016; Harrison et al., 2016; Harrison et al., 2019). Due to the abundance and importance of K-feldspar in mineral dust samples, some parameterisations for the activity of mineral dusts only use the contribution from K-feldspar (Atkinson et al., 2013; Harrison et al., 2016; Vergara-Temprado et al., 2017).

When discussing mineral dusts, it is usually assumed that low latitude dust (LLD) is the subject. This LLD comes from regions around the equator, vast deserts and arid environments. However, as this dust can be long-range transported, it is not only important for the regions where it is produced (DeMott et al., 2003; Huang et al., 2015; O'Sullivan et al., 2018). Although it is less likely to reach higher latitudes, it is very prominent in more local regions (McFarquhar et al., 2011; Price et al., 2018; Reicher et al., 2019b). High latitude dust (HLD) has more recently been identified as a potentially important source of ice-active dust in the higher latitudes (Tobo et al., 2019; Sanchez-Marroquin et al., 2020). The sources of HLD are very different than for LLD, as HLD is more associated with, for instance, glacial outwash plains and volcanic activity in Iceland than deserts near the equator. This is especially interesting looking to the future, when glaciers are expected to retreat further, exposing more areas for this dust to become aerosolised and affect the local atmosphere (Tobo et al., 2019).

1.5.2. Bioaerosol

Bioaerosols refers to a wide range of airborne biological material, such as whole cells, viruses, fungal spores, biological fragments, and phytoplankton. The ice-nucleating ability of particles produced in terrestrial vegetation and marine waters has been known for a long time (Schnell and Vali, 1972; Schnell and Vali, 1975), but there was often debate about the importance of bioaerosols compared to the highly active and widespread mineral dusts (Hoose et al., 2010).

Some of the most active INPs, the most efficient ice nucleators, are of biological origin. Bioaerosols can occupy the higher temperatures of the INP temperature spectrum, with some active at temperatures as high as -2°C (Christner, Morris, et al., 2008; Murray et al., 2012). This is not only important atmospherically, but also commercially. For instance, the bacterium *Pseudomonas syringae* is such an efficient ice nucleator that it is used in the commercial production of artificial snow under the brand name Snomax®. Therefore, even in cases where bioaerosols are not the overall dominant INP type, they may dominate ice-nucleating activity for lower altitude clouds at temperatures above -15 °C, where mineral dusts are less active (Spracklen and Heald, 2014).

Sea spray aerosol (SSA) is one of the most abundant types of aerosol by mass on Earth, and vast ocean cover allows marine biogenic particles to be aerosolised via wave-breaking and bubble bursting (Wilson et al., 2015). Additionally, at higher latitudes such as the high Arctic and southern oceans where mineral dust influences are reduced, marine biogenic aerosol has been shown to become atmospherically important (Vergara-Temprado et al., 2017; McCluskey et al., 2019). Phytoplankton and their exudates have long been considered an important source of marine organic aerosol, due to their ice-nucleating ability and their ubiquity in the sea surface microlayer that allows them to be aerosolised (Schnell, 1975; Schnell and Vali, 1976; Wang et al., 2015; Wilson et al., 2015; McCluskey et al., 2016; DeMott et al., 2016; Creamean et al., 2019; Ickes et al., 2020). Additionally, marine bacteria associated with phytoplankton blooms could also be an important INP, especially at higher temperatures (McCluskey et al., 2016). Phytoplankton exudates have been shown to enter Arctic clouds (Orellana et al., 2011), and so this rich source of SSA which can enter the atmosphere is likely important in modulating cloud processes in these remote regions. The size of SSA is usually small, on the order of 0.2-1 µm (Wang et al., 2015; DeMott et al.,

2016), but they are also very hygroscopic, which reduces their residence time in the atmosphere.

Terrestrial sources of bioaerosol range from forests (Schneider et al., 2020), decaying vegetation (Schnell and Vali, 1976; Conen et al., 2016), soils (O'Sullivan et al., 2014; Hill et al., 2016), melting permafrost (Creamean et al., 2020), and rivers (Knackstedt et al., 2018), to agricultural processes (O'Sullivan et al., 2018; Suski et al., 2018) and more. Biogenic INPs can also be lofted into the atmosphere during forest fires and biomass burning (McCluskey et al., 2014). In terrestrial bioaerosols, nanoscale fragments of biological material such as bacteria, fungal spores and pollen grains, are important INPs (O'Sullivan et al., 2015; O'Sullivan et al., 2016; Knackstedt et al., 2018). Where the intact host grain or spore can be on the micron scale, bound fragments on the nanometre scale may contain most of the activity, and there can be orders of magnitudes more nanoscale fragments present for each spore or grain (O'Sullivan et al., 2015).

Detecting the presence of ice-nucleating biological material can be achieved using techniques such as modified Polymerase chain reaction (PCR) (Hill et al., 2014; Du et al., 2017), hydrogen peroxide treatment (O'Sullivan et al., 2014), or lysosome treatment (Christner, Cai, et al., 2008). One of the most simple tests for the presence of proteinaceous material is the heat test, where a sample is exposed to temperatures close to 100 °C for a period of minutes to tens of minutes in order to denature proteins that may be responsible for the ice-nucleating activity of the sample (Christner, Morris, et al., 2008; Conen et al., 2012; Wilson et al., 2015; Hill et al., 2016; Conen et al., 2017; O'Sullivan et al., 2018). If the heat test does not remove the activity of the sample, it is then likely that non-heat labile material such as mineral dusts are responsible for the activity.

The importance of bioaerosols for ice nucleation in the atmosphere is more accepted now, but measurements of biological INPs in the atmosphere are still lacking (Hill et al., 2017; Huang et al., 2021). This is partly due to the difficulty of sampling and storing biological material without altering its properties, and the difficulty in detecting whether the observed ice nucleation activity is due to biological material. However, more field measurements of INPs in general are necessary to better inform global and regional aerosol and climate models.

1.5.3. Other potentially important INP types

Pollution aerosol, specifically small particles of black carbon (or soot) caused by incomplete combustion, is usually of interest due to its negative effects on health, and contribution to the warming of the planet (Darquenne, 2012; Bond et al., 2013). Black carbon can be produced naturally in events like forest fires, volcanic eruptions and Savannah fires. Not all black carbon is created equal, and some sources may produce combustion products which possess different ice-nucleating efficiencies.

Fossil fuel burning and other anthropogenic combustion processes which produce black carbon have been shown to have little effect on ambient ice-nucleating particle concentrations, especially in urban environments (Levin et al., 2016; Schill et al., 2016; Chen et al., 2017; Adams et al., 2020; Kanji et al., 2020; Schill et al., 2020). Although there is not a negligible impact, black carbon tends to be active at temperatures lower than mineral dusts and biogenic INPs, so may only become important at higher altitudes in conditions close to -38 °C (Kanji et al., 2020). Volcanic ash is an interesting source of INPs due to the violent method of aerosolisation and dispersion in the atmosphere, and is challenging to directly sample due to the extreme heat of materials close to an eruption and difficulty navigating airspace filled with volcanic ash. However, recent ice nucleation studies focusing on volcanic ash demonstrate there is ice-nucleating activity present, possibly correlated with the presence of ice-active minerals such as feldspar (Mangan et al., 2017; Jahn et al., 2019; Maters et al., 2019). Forest fires may also loft ice-active biological material into the atmosphere, and so in events such as forest fires, it is difficult to distinguish the contribution of black carbon and biogenic material without instruments which could identify these materials in the sample (Jahn et al., 2020; Schill et al., 2020).

1.6.   Ice-nucleating particles in the central Arctic

The central Arctic refers to the central Arctic Ocean and the pack ice that covers it for most of the year; it is an exceptional environment, unlike any other on the planet. Because of the relative homogeneity of the sea ice, cloud cover plays an essential part in regulating Arctic climate and mixed-phased clouds are prominent and persistent in the central Arctic. However, the concentrations and effects of INPs on mixed-phase clouds is not well defined (Murray et al., 2021), and they are not well represented in large-scale models (Morrison et al., 2012; Pithan et al., 2016; Schmale et al.,

2021) which has consequences for the prediction of the surface energy budget in the Arctic (Xie et al., 2013).

There is a need for more measurements of INP in the central Arctic, but the distance from land, and the necessity to use specialised ships called *icebreakers* when traversing the environment makes measurements in this area difficult. Therefore the sources of aerosol, especially INPs in this part of the world are not well known. There are some land-based research stations located around the Arctic circle which although still remote, are a little easier to access. There have been some ice nucleation studies done using samples from these high Arctic stations, or land within the high Arctic circle (Flyger and Heidam, 1978; Mason et al., 2016; Conen et al., 2016; Si et al., 2018; Creamean et al., 2018; Wex et al., 2019; Si et al., 2019; Šantl-Temkiv et al., 2019; Porter et al., 2020a; Creamean et al., 2020). There have also been a few aircraft campaigns looking to determine INP concentrations in the atmosphere (Prenni et al., 2007; Sanchez-Marroquin et al., 2020; Hartmann et al., 2020). Unfortunately, aircraft campaigns are difficult to conduct closer to the north pole on the remote pack ice, as land (and therefore fuel) is distant. There have been very few ship-based campaigns which could spend significant amounts of time on the central Arctic pack ice (Bigg, 1996; Bigg and Leck, 2001; Hartmann et al., 2021), and as yet no airborne INP measurements around the North Pole. However, because of the regularly stratified nature of the Arctic atmosphere (Brooks et al., 2017), it is important that the relationship and differences between INP characteristics at sea-level and at those at cloud-level are known.

Many of the campaigns conducted around the high Arctic and more specifically the central Arctic ocean have hinted at marine biogenic sources of ice-nucleating particles (Bigg, 1996; Bigg and Leck, 2001; Hartmann et al., 2021). Results from a ship campaign to the central Arctic, close to the North Pole, are presented in Section 3, in which there is a more detailed discussion of previous campaigns and potential sources which affect central Arctic mixed-phase clouds.

1.7.   Project objectives

This work has a main overarching goal, split into three objectives. The main aim of the project is to further the understanding and characterisation of ice-nucleating particles in remote, low-aerosol environments such as the Central Arctic. To achieve this, atmospheric ice-nucleating particle concentrations were measured in the field with both currently available and novel

instrumentation. To support future studies, novel instrumentation that will improve the quality and quantity of information collected was designed, built and tested. Therefore three objectives of this work are described below, and where published work is presented, the contributions of each author will be detailed at the start of the relevant chapter.

The project objectives were:

1) **The building of a high-flow rate, size-selective aerosol sampling system which could be remotely operated, and deployed above the surface mixed boundary layer.** In preparation for a 2 month long field campaign to the central Arctic Ocean and North Pole, the Microbiology-Ocean-Cloud-Coupling in the High Arctic (MOCCHA 2018) campaign, a sampler capable of being deployed at altitude in order to determine INP concentrations above the surface mixed boundary layer was desired. However, a high-flow rate sampler was deemed necessary, due to the low aerosol concentration, and low expected INP concentrations. Additionally, size-selection of aerosol would help to identify possible types of INP present. There is no available commercial instrumentation that fits this description, and so an instrument called the Selective Height Aerosol Research Kit (SHARK) was conceptualised, designed and built by both myself and Sebastien Sikora, with technical advice and guidance provided by Benjamin Murray and Ian Brooks. This instrument would, for the first time, allow comparison between ice-nucleating particle concentrations within and above the surface mixed layer of the central Arctic Ocean, towards the determination of the particles' origin. The publication describing the design and operation of the SHARK and its capability when deployed across various environments was published in *Atmospheric Measurement Techniques* (Porter et al., 2020a). This paper makes up Chapter 2 of this thesis.

2) **To gather ice-nucleating particle concentration data in the high Arctic, specifically the central Arctic ocean, towards elucidating the characteristics and effects of the ice-nucleating particles present.** The characterisation of Arctic ice-nucleating particles includes the determination of their sources and concentrations, in order to provide information which could be used to predict their potential effects on local clouds. The MOCCHA expedition to the central Arctic Ocean was conceptualised before I began my PhD

studies in 2016, but the planning, tasks and decisions for our project including determining which instruments we would deploy and in what situations, were left to me with the technical support and supervision of Benjamin Murray. I led the INP project on-ship with the help of a fellow PhD student, Michael Adams, and throughout the campaign we were supported by Ian Brooks (who was leading his own project on-board), as there was extremely limited contact with Benjamin Murray who was ashore. Throughout the 2-month research cruise, a wealth of data was gathered including INP concentrations throughout the entire cruise at ship level, some size-resolved INP measurements at altitude, INP concentrations from testing fresh ocean samples sources at different depths, aerosol produced in a chamber designed to simulate oceanic turbulence, a floating chamber collecting bubble bursting aerosol and much more. Chapter 3 consists of a draft publication presenting INP concentration data at ship level and altitude (from the SHARK instrument), towards elucidating an origin of these particles. This paper will make up one of many exciting publications to come out of this interdisciplinary, international, and ongoing research effort.

3) **To design and create a method by which droplets containing low concentrations of sampled atmospheric aerosol could be separated, depending on the presence of an INP.** The specific analysis of ice-nucleating particles, isolated from a collected aerosol sample is difficult, due to the rarity of INPs in bulk aerosol. Additionally, contamination in ice nucleation studies is difficult to avoid in conventional pipetted droplet cold stage techniques. Microfluidics provides a relatively new method of producing monodisperse droplets on a chip for freezing studies in INP analysis. Due to the small size, high-throughput and potential for modular additions with on-chip analysis, there is still much potential in microfluidics as a technique for studying ice nucleation. Chapter 4 presents a method for the production, freezing and eventual separation of supercooled liquid droplets from frozen ice crystals in continuous flow on a single chip. The method of droplet production and the size of the droplets mean contamination is less likely than in conventional cold stage techniques, and the freezing of these droplets occurs in flow, meaning this process can be run continuously to determine INP concentrations for a relatively large sample volume. Finally, the separation technique

is the novel aspect of this design, allowing ice crystals containing INP to be separated in flow from the rest of the un-frozen sample and collected from a different outlet. This would allow for further analysis of the respective populations, in order to determine differences between the ice-active and ice-inactive particles. I had suggested developing a separation technique at the beginning of my PhD, and began designing and testing separation chips with helpful insights from Mark Tarn. A microfluidic chip and Peltier element-based cold stage for the production and freezing of droplets in continuous flow was developed and described in another publication (Tarn et al., 2020). The separation chip built on this design and used the differences in buoyancy between the liquid droplets and frozen ice crystals to passively separate the droplets. The article describing the technique was published in *Lab on a Chip* (Porter et al., 2020b).

1.8. Other work completed during PhD studies

Ickes et al., (2020) This paper involved a campaign of work comparing the ice-nucleating activity of lab-grown algae cultures and collected marine microlayer samples at the aerosol interaction and dynamics in the atmosphere (AIDA) facility in the Karlsruhe Institute of Technology (KIT). I brought Arctic microlayer samples which were collected by our group in 2015 to KIT, along with ice-nucleation instrumentation. I planned and carried out the warm-temperature INP experiments with support from MPA. I analysed all the warm-temperature INP data from the manuscript and contributed to discussions and the writing of the manuscript.

Adams et al., (2020) This paper investigated the effects of black carbon produced in a yearly cultural bonfire event on INP concentrations, and assessed that black carbon produced during the festival had no real impact on the INPs. I carried out experiments over the nights, and contributed to the discussions and writing of the paper.

O'Sullivan et al., (2018) This paper describes a field campaign based in UK farmland. It was concluded that biogenic INP are important in this region using a mixture of experiments and modelling. I carried out experiments and contributed to the analysis, discussions and writing of the paper.

Microfluidics papers: **Tarn et al., (2018)**; **Tarn et al., (2020)**; **Tarn et al., (2021)**. These three papers involve the analysis of INP using microfluidic devices. The 2018 paper used a create-and-store method to analyse data collected during the work in Adams et al., (2020) and O'Sullivan et al., (2018). The 2020 paper describes the Lab-on-a-chip-NIPI (LOC-NIPI) device which allows the production and freezing of droplets in-flow. The device was validated on Pollen and Snowmax®, and used to probe homogeneous nucleation. The 2021 paper utilised results from the 2020 paper to determine a parameterisation for the volume nucleation rate coefficient, $J_V(T)$. I carried out experiments and contributed to discussions and the writing of the papers.

Harrison et al., (2018a) This publication describes the development and validation of a large-volume freezing assay which detects ice-nucleation events via infrared (IR). The latent heat release upon freezing is detected in IR. The device was validated on K-feldspar and NX-illite. I collected and analysed a sample and contributed to the discussions and writing of the paper.

Zinke et al., (2021) This paper describes the development and testing of a novel cloud-water sampler which was deployed in the central Arctic. The cloud water sampler was deployed on a tethered balloon and collected water for chemical composition and INP analysis. I analysed samples for INP activity and contributed to discussions and the writing of the paper.

Adams et al., (In prep) This paper describes the first field deployment of the PINE chamber and validates it against other field instruments. It presents novel INP results in a boreal forest environment. I helped run experiments and contributed to the analysis and discussions.

Adams et al., (In prep) This paper compares measured INP concentrations against simulated concentrations in a boreal forest environment. It characterises the speciation of the INP types present over a two-month period. I ran experiments and contributed to the analysis. During this campaign I supervised a student who was completing a project abroad.

Harrison et al., (In prep) This manuscript describes a field campaign carried out in Barbados, investigating the effects of transport over the Atlantic on Saharan dust. I attended the field campaign, collecting and analysing samples, and I have contributed to discussions.

References

Abate, A.R., Poitzsch, A., Hwang, Y., Lee, J., Czerwinska, J. and Weitz, D.A. 2009. Impact of inlet channel geometry on microfluidic drop formation. *Physical Review E - Statistical, Nonlinear, and Soft Matter Physics.* **80**(2), p.026310.

Adams, M.P., Tarn, M.D., Sanchez-Marroquin, A., Porter, G.C.E., O'Sullivan, D., Harrison, A.D., Cui, Z., Vergara-Temprado, J., Carotenuto, F., Holden, M.A., Daily, M.I., Whale, T.F., Sikora, S.N.F., Burke, I.T., Shim, J.U., McQuaid, J.B. and Murray, B.J. 2020. A Major Combustion Aerosol Event Had a Negligible Impact on the Atmospheric Ice-Nucleating Particle Population. *Journal of Geophysical Research: Atmospheres.* **125**(22).

Akther, F., Yakob, S.B., Nguyen, N.-T. and Ta, H.T. 2020. Surface Modification Techniques for Endothelial Cell Seeding in PDMS Microfluidic Devices. *Biosensors.* **10**(11), p.182.

Al-Hetlani, E., Hatt, O.J., Vojtisek, M., Tarn, M.D., Iles, A. and Pamme, N. 2010. Sorting and Manipulation of Magnetic Droplets in Continuous Flow U. Hafeli, W. Schutt, & M. Zborowski, eds. *AIP Conf. Proc.* **1311**, pp.167–175.

Atkinson, J.D., Murray, B.J., Woodhouse, M.T., Whale, T.F., Baustian, K.J., Carslaw, K.S., Dobbie, S., O'Sullivan, D., Malkin, T.L., O 'sullivan, D. and Malkin, T.L. 2013. The importance of feldspar for ice nucleation by mineral dust in mixed-phase clouds. *Nature.* **498**(7454), pp.355–8.

Augustin-Bauditz, S., Wex, H., Kanter, S., Ebert, M., Niedermeier, D., Stolz, F., Prager, A. and Stratmann, F. 2014. The immersion mode ice nucleation behavior of mineral dusts: A comparison of different pure and surface modified dusts. *Geophys. Res. Lett.* **41**, pp.7375–7382.

Bayareh, M. 2020. An updated review on particle separation in passive microfluidic devices. *Chemical Engineering and Processing - Process Intensification.* **153**.

Beall, C.M., Lucero, D., Hill, T.C., Demott, P.J., Dale Stokes, M. and Prather, K.A. 2020. Best practices for precipitation sample storage for offline studies of ice nucleation in marine and coastal environments. *Atmospheric Measurement Techniques.* **13**(12), pp.6473–6486.

Bigg, E.K. 1996. Ice forming nuclei in the high Arctic. *Tellus, Series B: Chemical and Physical Meteorology.* **48**(2), pp.223–233.

Bigg, E.K. and Leck, C. 2001. Cloud-active particles over the central Arctic Ocean. *Journal of Geophysical Research Atmospheres.* **106**(D23), pp.32155–32166.

Bond, T.C., Doherty, S.J., Fahey, D.W., Forster, P.M., Berntsen, T., Deangelo, B.J., Flanner, M.G., Ghan, S., Kärcher, B., Koch, D., Kinne, S., Kondo, Y., Quinn, P.K., Sarofim, M.C., Schultz, M.G., Schulz, M., Venkataraman, C., Zhang, H., Zhang, S., Bellouin, N., Guttikunda, S.K., Hopke, P.K., Jacobson, M.Z., Kaiser, J.W., Klimont, Z., Lohmann, U., Schwarz, J.P., Shindell, D., Storelvmo, T., Warren, S.G. and Zender, C.S. 2013. Bounding the role of black carbon in the climate system: A

scientific assessment. *Journal of Geophysical Research Atmospheres*. **118**(11), pp.5380–5552.

Boose, Y., Sierau, B., García, M.I., Rodríguez, S., Alastuey, A., Linke, C., Schnaiter, M., Kupiszewski, P., Kanji, Z.A. and Lohmann, U. 2016. Ice nucleating particles in the Saharan Air Layer. *Atmos. Chem. Phys.* **16**(14), pp.9067–9087.

Brooks, I.M., Tjernström, M., Persson, P.O.G., Shupe, M.D., Atkinson, R.A., Canut, G., Birch, C.E., Mauritsen, T., Sedlar, J. and Brooks, B.J. 2017. The Turbulent Structure of the Arctic Summer Boundary Layer During The Arctic Summer Cloud-Ocean Study. *Journal of Geophysical Research: Atmospheres*. **122**(18), pp.9685–9704.

Brubaker, T., Polen, M., Cheng, P., Ekambaram, V., Somers, J., Anna, S.L. and Sullivan, R.C. 2020. Development and characterization of a "store and create" microfluidic device to determine the heterogeneous freezing properties of ice nucleating particles. *Aerosol Science and Technology*. **54**(1), pp.79–93.

Brunner, C. and Kanji, Z.A. 2021. Continuous online monitoring of ice-nucleating particles: development of the automated Horizontal Ice Nucleation Chamber (HINC-Auto). *Atmospheric Measurement Techniques*. **14**(1), pp.269–293.

Budke, C. and Koop, T. 2015. BINARY: An optical freezing array for assessing temperature and time dependence of heterogeneous ice nucleation. *Atmospheric Measurement Techniques*. **8**(2), pp.689–703.

Burger, R. and Ducrée, J. 2012. Handling and analysis of cells and bioparticles on centrifugal microfluidic platforms. *Expert Review of Molecular Diagnostics*. **12**(4), pp.407–421.

Carvalho, E., Sindt, C., Verdier, A., Galan, C., O'Donoghue, L., Parks, S. and Thibaudon, M. 2008. Performance of the Coriolis air sampler, a high-volume aerosol-collection system for quantification of airborne spores and pollen grains. *Aerobiologia*. **24**, pp.191–201.

Casadevall i Solvas, X. and deMello, A. 2011. Droplet microfluidics: recent developments and future applications. *Chem. Commun.* **47**, pp.1936–1942.

Chen, J., Wu, Z., Augustin-Bauditz, S., Grawe, S., Hartmann, M., Pei, X., Liu, Z., Ji, D. and Wex, H. 2017. Ice nucleating particle concentrations unaffected by urban air pollution in Beijing, China 2. *Atmos. Chem. Phys. Discuss.*

Chou, W.-L., Lee, P.-Y., Yang, C.-L., Huang, W.-Y. and Lin, Y.-S. 2015. Recent Advances in Applications of Droplet Microfluidics. *Micromachines*. **6**, p.1249.

Christner, B.C., Cai, R., Morris, C.E., McCarter, K.S., Foreman, C.M., Skidmore, M.L., Montross, S.N. and Sands, D.C. 2008. Geographic, seasonal, and precipitation chemistry influence on the abundance and activity of biological ice nucleators in rain and snow. *Proc. Natl. Acad. Sci. U.S.A.* **105**(48), pp.18854–18859.

Christner, B.C., Morris, C.E., Foreman, C.M., Cai, R. and Sands, D.C. 2008.

Ubiquity of Biological Ice Nucleators in Snowfall. *Science.* **319**(5867), p.1214.

Conen, F., Eckhardt, S., Gundersen, H., Stohl, A. and Yttri, K.E. 2017. Rainfall drives atmospheric ice-nucleating particles in the coastal climate of southern Norway. *Atmos. Chem. Phys.* **17**, pp.11065–11073.

Conen, F., Henne, S., Morris, C.E. and Alewell, C. 2012. Atmospheric ice nucleators active ≥ −12 °C can be quantified on PM10 filters. *Atmos. Meas. Tech.* **5**, pp.321–327.

Conen, F., Stopelli, E. and Zimmermann, L. 2016. Clues that decaying leaves enrich Arctic air with ice nucleating particles. *Atmospheric Environment.* **129**, pp.91–94.

Connolly, P.J., Möhler, O., Field, P.R., Saathoff, H., Burgess, R., Choularton, T. and Gallagher, M. 2009. Studies of heterogeneous freezing by three different desert dust samples. *Atmospheric Chemistry and Physics.* **9**(8), pp.2805–2824.

Creamean, J.M., Cross, J.N., Pickart, R., McRaven, L., Lin, P., Pacini, A., Hanlon, R., Schmale, D.G., Ceniceros, J., Aydell, T., Colombi, N., Bolger, E. and DeMott, P.J. 2019. Ice Nucleating Particles Carried From Below a Phytoplankton Bloom to the Arctic Atmosphere. *Geophysical Research Letters.* **46**(14), pp.8572–8581.

Creamean, J.M., Hill, T.C.J., Demott, P.J., Uetake, J., Kreidenweis, S. and Douglas, T.A. 2020. Thawing permafrost: An overlooked source of seeds for Arctic cloud formation. *Environmental Research Letters.* **15**(8), p.084022.

Creamean, J.M., Kirpes, R.M., Pratt, K.A., Spada, N.J., Maahn, M., De Boer, G., Schnell, R.C. and China, S. 2018. Marine and terrestrial influences on ice nucleating particles during continuous springtime measurements in an Arctic oilfield location. *Atmospheric Chemistry and Physics.* **18**(24), pp.18023–18042.

Cziczo, D.J., Ladino, L., Boose, Y., Kanji, Z.A., Kupiszewski, P., Lance, S., Mertes, S. and Wex, H. 2017. Measurements of Ice Nucleating Particles and Ice Residuals. *Meteorological Monographs.* **58**(1), 8.1-8.13.

Darquenne, C. 2012. Aerosol deposition in health and disease. *Journal of Aerosol Medicine and Pulmonary Drug Delivery.* **25**(3), pp.140–147.

David, R.O., Marcolli, C., Fahrni, J., Qiu, Y., Perez Sirkin, Y.A., Molinero, V., Mahrt, F., Brühwiler, D., Lohmann, U. and Kanji, Z.A. 2019. Pore condensation and freezing is responsible for ice formation below water saturation for porous particles. *Proceedings of the National Academy of Sciences of the United States of America.* **116**(17), pp.8184–8189.

DeMott, P.J., Hill, T.C.J., McCluskey, C.S., Prather, K.A., Collins, D.B., Sullivan, R.C., Ruppel, M.J., Mason, R.H., Irish, V.E., Lee, T., Hwang, C.Y., Rhee, T.S., Snider, J.R., McMeeking, G.R., Dhaniyala, S., Lewis, E.R., Wentzell, J.J.B., Abbatt, J., Lee, C., Sultana, C.M., Ault, A.P., Axson, J.L., Diaz Martinez, M., Venero, I., Santos-Figueroa, G., Stokes, M.D., Deane, G.B., Mayol-Bracero, O.L., Grassian, V.H., Bertram, T.H., Bertram, A.K., Moffett, B.F. and Franc, G.D. 2016. Sea spray aerosol as

a unique source of ice nucleating particles. *Proceedings of the National Academy of Sciences*. **113**(21), pp.5797–5803.

DeMott, P.J., Hill, T.C.J.J., Petters, M.D., Bertram, A.K., Tobo, Y., Mason, R.H., Suski, K.J., McCluskey, C.S., Levin, E.J.T.T., Schill, G.P., Boose, Y., Rauker, A.M., Miller, A.J., Zaragoza, J., Rocci, K., Rothfuss, N.E., Taylor, H.P., Hader, J.D., Chou, C., Huffman, J.A., Pöschl, U., Prenni, A.J. and Kreidenweis, S.M. 2017. Comparative measurements of ambient atmospheric concentrations of ice nucleating particles using multiple immersion freezing methods and a continuous flow diffusion chamber. *Atmospheric Chemistry and Physics*. **17**(18), pp.11227–11245.

DeMott, P.J., Möhler, O., Cziczo, D.J., Hiranuma, N., Petters, M.D., Petters, S.S., Belosi, F., Bingemer, H.G., Brooks, S.D., Budke, C., Burkert-Kohn, M., Collier, K.N., Danielczok, A., Eppers, O., Felgitsch, L., Garimella, S., Grothe, H., Herenz, P., Hill, T.C.J., Höhler, K., Kanji, Z.A., Kiselev, A., Koop, T., Kristensen, T.B., Krüger, K., Kulkarni, G., Levin, E.J.T., Murray, B.J., Nicosia, A., O'Sullivan, D., Peckhaus, A., Polen, M.J., Price, H.C., Reicher, N., Rothenberg, D.A., Rudich, Y., Santachiara, G., Schiebel, T., Schrod, J., Seifried, T.M., Stratmann, F., Sullivan, R.C., Suski, K.J., Szakáll, M., Taylor, H.P., Ullrich, R., Vergara-Temprado, J., Wagner, R., Whale, T.F., Weber, D., Welti, A., Wilson, T.W., Wolf, M.J. and Zenker, J. 2018. The Fifth International Workshop on Ice Nucleation phase 2 (FIN-02): laboratory intercomparison of ice nucleation measurements. *Atmos. Meas. Tech.* **11**, pp.6231–6257.

DeMott, P.J., Prenni, A.J., McMeeking, G.R., Sullivan, R.C., Petters, M.D., Tobo, Y., Niemand, M., Möhler, O., Snider, J.R., Wang, Z. and Kreidenweis, S.M. 2015. Integrating laboratory and field data to quantify the immersion freezing ice nucleation activity of mineral dust particles. *Atmospheric Chemistry and Physics*. **15**(1), pp.393–409.

DeMott, P.J., Sassen, K., Poellot, M.R., Baumgardner, D., Rogers, D.C., Brooks, S.D., Prenni, A.J. and Kreidenweis, S.M. 2003. African dust aerosols as atmospheric ice nuclei. *Geophys. Res. Lett.* **30**, p.1732.

Du, R., Du, P., Lu, Z., Ren, W., Liang, Z., Qin, S., Li, Z., Wang, Y. and Fu, P. 2017. Evidence for a missing source of efficient ice nuclei. *Scientific Reports*. **7**(1), p.39673.

Duffy, D.C., McDonald, J.C., Schueller, O.J.A. and Whitesides, G.M. 1998. Rapid prototyping of microfluidic systems in poly(dimethylsiloxane). *Analytical Chemistry*. **70**(23), pp.4974–4984.

Effenhauser, C.S., Bruin, G.J.M., Paulus, A. and Ehrat, M. 1997. Integrated Capillary Electrophoresis on Flexible Silicone Microdevices: Analysis of DNA Restriction Fragments and Detection of Single DNA Molecules on Microchips. *Analytical Chemistry*. **69**(17), pp.3451–3457.

Field, P.R., Lawson, R.P., Brown, P.R.A., Lloyd, G., Westbrook, C., Moisseev, D., Miltenberger, A., Nenes, A., Blyth, A., Choularton, T., Connolly, P., Buehl, J., Crosier, J., Cui, Z., Dearden, C., DeMott, P., Flossmann, A., Heymsfield, A., Huang, Y., Kalesse, H., Kanji, Z.A., Korolev, A., Kirchgaessner, A., Lasher-Trapp, S., Leisner, T., McFarquhar, G., Phillips, V., Stith, J. and Sullivan, S. 2016. Chapter 7.

Secondary Ice Production - current state of the science and recommendations for the future. *Meteorological Monographs.* **58**, 7.1-7.20.

Flyger, H. and Heidam, N.Z. 1978. Ground level measurements of the summer tropospheric aerosol in Northern Greenland. *Journal of Aerosol Science.* **9**(2), pp.157–168.

Garcia, E., Hill, T.C.J., Prenni, A.J., DeMott, P.J., Franc, G.D. and Kreidenweis, S.M. 2012. Biogenic ice nuclei in boundary layer air over two U.S. high plains agricultural regions. *Journal of Geophysical Research Atmospheres.* **117**(17), p.D18.

Garimella, S., Rothenberg, D.A., Wolf, M.J., David, R.O., Kanji, Z.A., Wang, C., Rösch, M. and Cziczo, D.J. 2017. Uncertainty in counting ice nucleating particles with continuous flow diffusion chambers. *Atmospheric Chemistry and Physics.* **17**(17), pp.10855–10864.

Gibbs, J. 1948. *The collected works of J. Willard Gibbs.* New Haven: Yale Univ. Press.

Haeberle, S., Brenner, T., Zengerle, R. and Ducrée, J. 2006. Centrifugal extraction of plasma from whole blood on a rotating disk. *Lab Chip.* **6**, pp.776–781.

Han, X., Ma, H.B., Wilson, C. and Critser, J.K. 2008. Effects of nanoparticles on the nucleation and devitrification temperatures of polyol cryoprotectant solutions. *Microfluidics and Nanofluidics.* **4**(4), pp.357–361.

Hande, L.B. and Hoose, C. 2017. Partitioning the primary ice formation modes in large eddy simulations of mixed-phase clouds. *Atmos. Chem. Phys.* **17**, pp.14105–14118.

Harrison, A.D., Lever, K., Sanchez-Marroquin, A., Holden, M.A., Whale, T.F., Tarn, M.D., McQuaid, J.B. and Murray, B.J. 2019. The ice-nucleating ability of quartz immersed in water and its atmospheric importance compared to K-feldspar. *Atmos. Chem. Phys.* **19**, pp.11343–11361.

Harrison, A.D., Whale, T.F., Carpenter, M.A., Holden, M.A., Neve, L., O'Sullivan, D., Vergara Temprado, J. and Murray, B.J. 2016. Not all feldspars are equal: a survey of ice nucleating properties across the feldspar group of minerals. *Atmospheric Chemistry and Physics.* **16**(17), pp.10927–10940.

Harrison, A.D., Whale, T.F., Rutledge, R., Lamb, S., Tarn, M.D., Porter, G.C.E., Adams, M.P., McQuaid, J.B., Morris, G.J. and Murray, B.J. 2018a. An instrument for quantifying heterogeneous ice nucleation in multiwell plates using infrared emissions to detect freezing. *Atmospheric Measurement Techniques.* **11**(10), pp.5629–5641.

Harrison, A.D., Whale, T.F., Rutledge, R., Lamb, S., Tarn, M.D., Porter, G.C.E., Adams, M.P., McQuaid, J.B., Morris, G.J. and Murray, B.J. 2018b. An instrument for quantifying heterogeneous ice nucleation in multiwell plates using infrared emissions to detect freezing. *Atmospheric Measurement Techniques.* **11**(10), pp.5629–5641.

Hartmann, D.L., Ockert-Bell, M.E. and Michelsen, M.L. 1992. The Effect of

Cloud Type on Earth's Energy Balance: Global Analysis. *Journal of Climate.* **5**(11), pp.1281–1304.

Hartmann, M., Adachi, K., Eppers, O., Haas, C., Herber, A., Holzinger, R., Hünerbein, A., Jäkel, E., Jentzsch, C., van Pinxteren, M., Wex, H., Willmes, S. and Stratmann, F. 2020. Wintertime Airborne Measurements of Ice Nucleating Particles in the High Arctic: A Hint to a Marine, Biogenic Source for Ice Nucleating Particles. *Geophysical Research Letters.* **47**(13).

Hartmann, M., Gong, X., Kecorius, S., Van Pinxteren, M., Vogl, T., Welti, A., Wex, H., Zeppenfeld, S., Herrmann, H., Wiedensohler, A. and Stratmann, F. 2021. Terrestrial or marine - indications towards the origin of ice-nucleating particles during melt season in the European Arctic up to 83.7gN. *Atmospheric Chemistry and Physics.* **21**(15), pp.11613–11636.

Hartmann, S., Augustin, S., Clauss, T., Wex, H., Šantl-Temkiv, T., Voigtländer, J., Niedermeier, D. and Stratmann, F. 2013. Immersion freezing of ice nucleation active protein complexes. *Atmos. Chem. Phys.* **13**, pp.5751–5766.

Hartmann, S., Wex, H., Clauss, T., Augustin-Bauditz, S., Niedermeier, D., Rösch, M. and Stratmann, F. 2016. Immersion Freezing of Kaolinite: Scaling with Particle Surface Area. *J. Atmos. Sci.* **73**, pp.263–278.

Herbert, R.J., Murray, B.J., Dobbie, S.J. and Koop, T. 2015. Sensitivity of liquid clouds to homogenous freezing parameterizations. *Geophys. Res. Lett.* **42**(5), pp.1599–1605.

Herbert, R.J., Murray, B.J., Whale, T.F., Dobbie, S.J. and Atkinson, J.D. 2014. Representing time-dependent freezing behaviour in immersion mode ice nucleation. *Atmospheric Chemistry and Physics.* **14**(16), pp.8501–8520.

Hill, T.C.J., DeMott, P.J., Conen, F. and Möhler, O. 2017. Impacts of Bioaerosols on Atmospheric Ice Nucleation Processes *In*: *Microbiology of Aerosols* [Online]. Hoboken, NJ, USA: John Wiley & Sons, Inc., pp.195–219. [Accessed 18 March 2021]. Available from: http://doi.wiley.com/10.1002/9781119132318.ch3a.

Hill, T.C.J., Demott, P.J., Tobo, Y., Fröhlich-Nowoisky, J., Moffett, B.F., Franc, G.D. and Kreidenweis, S.M. 2016. Sources of organic ice nucleating particles in soils. *Atmospheric Chemistry and Physics.* **16**(11), pp.7195–7211.

Hill, T.C.J., Moffett, B.F., DeMott, P.J., Georgakopoulos, D.G., Stump, W.L. and Franc, G.D. 2014. Measurement of Ice Nucleation-Active Bacteria on Plants and in Precipitation by Quantitative PCR. *Appl. Environ. Microbiol.* **80**, pp.1256–1267.

Hiranuma, N., Augustin-Bauditz, S., Bingemer, H., Budke, C., Curtius, J., Danielczok, A., Diehl, K., Dreischmeier, K., Ebert, M., Frank, F., Hoffmann, N., Kandler, K., Kiselev, A., Koop, T., Leisner, T., Möhler, O., Nillius, B., Peckhaus, A., Rose, D., Weinbruch, S., Wex, H., Boose, Y., Demott, P.J., Hader, J.D., Hill, T.C.J., Kanji, Z.A., Kulkarni, G., Levin, E.J.T., McCluskey, C.S., Murakami, M., Murray, B.J., Niedermeier, D.,

Petters, M.D., O'Sullivan, D., Saito, A., Schill, G.P., Tajiri, T., Tolbert, M.A., Welti, A., Whale, T.F., Wright, T.P. and Yamashita, K. 2015. A comprehensive laboratory study on the immersion freezing behavior of illite NX particles: A comparison of 17 ice nucleation measurement techniques. *Atmospheric Chemistry and Physics*. **15**(5), pp.2489–2518.

Holden, M.A., Campbell, J.M., Meldrum, F.C., Murray, B.J. and Christenson, H.K. 2021. Active sites for ice nucleation differ depending on nucleation mode. *Proceedings of the National Academy of Sciences of the United States of America*. **118**(18).

Holden, M.A., Whale, T.F., Tarn, M.D., O'Sullivan, D., Walshaw, R.D., Murray, B.J., Meldrum, F.C. and Christenson, H.K. 2019. High-speed imaging of ice nucleation in water proves the existence of active sites. *Science Advances*. **5**, p.eaav4316.

Hoose, C., Kristjánsson, J.E. and Burrows, S.M. 2010. How important is biological ice nucleation in clouds on a global scale? *Environmental Research Letters*. **5**(2), p.24009.

Hoose, C. and Möhler, O. 2012. Heterogeneous ice nucleation on atmospheric aerosols: a review of results from laboratory experiments. *Atmos. Chem. Phys. Atmospheric Chemistry and Physics*. **12**(20), pp.9817–9854.

Huang, S., Hu, W., Chen, J., Wu, Z., Zhang, D. and Fu, P. 2021. Overview of biological ice nucleating particles in the atmosphere. *Environment International*. **146**, p.106197.

Huang, Z., Huang, J., Hayasaka, T., Wang, S., Zhou, T. and Jin, H. 2015. Short-cut transport path for Asian dust directly to the Arctic: A case study. *Environmental Research Letters*. **10**(11), p.114018.

Huffman, J.A., Prenni, A.J., Demott, P.J., Pöhlker, C., Mason, R.H., Robinson, N.H., Fröhlich-Nowoisky, J., Tobo, Y., Després, V.R., Garcia, E., Gochis, D.J., Harris, E., Müller-Germann, I., Ruzene, C., Schmer, B., Sinha, B., Day, D.A., Andreae, M.O., Jimenez, J.L., Gallagher, M., Kreidenweis, S.M., Bertram, A.K. and Pöschl, U. 2013. High concentrations of biological aerosol particles and ice nuclei during and after rain. *Atmospheric Chemistry and Physics*. **13**(13), pp.6151–6164.

Ickes, L., Porter, G.C.E., Wagner, R., Adams, M.P., Bierbauer, S., Bertram, A.K., Bilde, M., Christiansen, S., Ekman, A.M.L., Gorokhova, E., Höhler, K., Kiselev, A.A., Leck, C., Möhler, O., Murray, B.J., Schiebel, T., Ullrich, R. and Salter, M.E. 2020. The ice-nucleating activity of Arctic sea surface microlayer samples and marine algal cultures. *Atmospheric Chemistry and Physics*. **20**(18), pp.11089–11117.

Irish, V.E., Elizondo, P., Chen, J., Choul, C., Charette, J., Lizotte, M., Ladino, L.A., Wilson, T.W., Gosselin, M., Murray, B.J., Polishchuk, E., Abbatt, J.P.D., Miller, L.A. and Bertram, A.K. 2017. Ice-nucleating particles in Canadian Arctic sea-surface microlayer and bulk seawater. *Atmospheric Chemistry and Physics*. **17**(17), pp.10583–10595.

Iwata, A. and Matsuki, A. 2018. Characterization of individual ice residual particles by the single droplet freezing method: a case study in the Asian dust outflow region. *Atmos. Chem. Phys.* **18**, pp.1785–1804.

Jaenicke, R. 2007. *Aerosol Physics and Chemistry. In: Landolt-Börnstein Numerical Data and Functional Relationships in Science and Technology New Series Group V: Geophysics and Space Research Volume 4 Meteorology Subvolume b, Physical and Chemical Properties of the Air* (G. Fischer, ed.).

Jahn, L.G., Fahy, W.D., Williams, D.B. and Sullivan, R.C. 2019. Role of Feldspar and Pyroxene Minerals in the Ice Nucleating Ability of Three Volcanic Ashes. *ACS Earth and Space Chemistry*. **3**(4), pp.626–636.

Jahn, L.G., Polen, M.J., Jahl, L.G., Brubaker, T.A., Somers, J. and Sullivan, R.C. 2020. Biomass combustion produces ice-active minerals in biomass-burning aerosol and bottom ash. *Proceedings of the National Academy of Sciences of the United States of America*. **117**(36), pp.21928–21937.

Jing, W. and Sui, G. 2017. Bioanalysis within Microfluidics: A Review *In*: *Recent Progress in Colloid and Surface Chemistry with Biological Applications* [Online]. ACS Symposium Series. American Chemical Society, pp.245–268. Available from: http://dx.doi.org/10.1021/bk-2015-1215.ch013.

Johnson, A.C. and Bowser, M.T. 2018. Micro free flow electrophoresis. *Lab Chip*. **18**, pp.27–40.

Joly, M., Attard, E., Sancelme, M., Deguillaume, L., Guilbaud, C., Morris, C.E., Amato, P. and Delort, A.-M. 2013. Ice nucleation activity of bacteria isolated from cloud water. *Atmos. Environ.* **70**, pp.392–400.

Kanji, Z.A., Ladino, L.A., Wex, H., Boose, Y., Burkert-Kohn, M., Cziczo, D.J. and Krämer, M. 2017. Overview of Ice Nucleating Particles. *Meteorological Monographs*. **58**, 1.1-1.33.

Kanji, Z.A., Welti, A., Corbin, J.C. and Mensah, A.A. 2020. Black Carbon Particles Do Not Matter for Immersion Mode Ice Nucleation. *Geophysical Research Letters*. **47**(11).

Kiani, H. and Sun, D.W. 2011. Water crystallization and its importance to freezing of foods: A review. *Trends in Food Science and Technology*. **22**(8), pp.407–426.

Kiselev, A., Bachmann, F., Pedevilla, P., Cox, S.J., Michaelides, A., Gerthsen, D. and Leisner, T. 2017. Active sites in heterogeneous ice nucleation-the example of K-rich feldspars. *Science*. **355**(6323), pp.367–371.

Knackstedt, K.A., Moffett, B.F., Hartmann, S., Wex, H., Hill, T.C.J., Glasgo, E.D., Reitz, L.A., Augustin-Bauditz, S., Beall, B.F.N., Bullerjahn, G.S., Fröhlich-Nowoisky, J., Grawe, S., Lubitz, J., Stratmann, F. and McKay, R.M.L. 2018. Terrestrial Origin for Abundant Riverine Nanoscale Ice-Nucleating Particles. *Environmental Science and Technology*. **52**(21), pp.12358–12367.

Koop, T. and Murray, B.J. 2016. A physically constrained classical description of the homogeneous nucleation of ice in water. *The Journal of Chemical Physics*. **145**(21), p.211915.

Ladino, L., Raga, G., Alvarez-Ospina, H., Andino-Enríquez, M., Rosas, I.,

Martínez, L., Salinas, E., Miranda, J., Ramírez-Díaz, Z., Figueroa, B., Chou, C., Bertram, A., Quintana, E., Maldonado, L., Si, M. and Irish, V. 2019. Ice-nucleating particles in a coastal tropical site. *Atmospheric Chemistry and Physics*. **19**(9), pp.6147–6165.

Lenshof, A., Magnusson, C. and Laurell, T. 2012. Acoustofluidics 8: Applications of acoustophoresis in continuous flow microsystems. *Lab Chip*. **12**, pp.1210–1223.

Levin, E.J.T., McMeeking, G.R., DeMott, P.J., McCluskey, C.S., Carrico, C.M., Nakao, S., Jayarathne, T., Stone, E.A., Stockwell, C.E., Yokelson, R.J. and Kreidenweis, S.M. 2016. Ice-nucleating particle emissions from biomass combustion and the potential importance of soot aerosol. *J. Geophys. Res. Atmos.* **121**, pp.5888–5903.

Lindsley, W.G. 2016. Filter Pore Size and Aerosol Sample Collection *In*: P. F. O'Connor, ed. *NIOSH Manual of Analytical Methods (NMAM), 5th Edition* [Online]. Department of Health and Human Services, Centers for Disease Control and Prevention, National Institute for Occupational Safety and Health, pp.1–14. [Accessed 30 July 2018]. Available from: https://www.cdc.gov/niosh/docs/2014-151/pdfs/chapters/chapter-fp.pdf.

Maeda, N. 2021. Brief Overview of Ice Nucleation. *Molecules (Basel, Switzerland)*. **26**(2), p.392.

Mangan, T.P., Atkinson, J.D., Neuberg, J.W., O'Sullivan, D., Wilson, T.W., Whale, T.F., Neve, L., Umo, N.S., Malkin, T.L. and Murray, B.J. 2017. Heterogeneous Ice nucleation by soufriere hills volcanic ash immersed in water droplets. *PLoS ONE*. **12**(1).

Marcolli, C. 2014. Deposition nucleation viewed as homogeneous or immersion freezing in pores and cavities. *Atmospheric Chemistry and Physics*. **14**(4), pp.2071–2104.

Mason, R.H., Si, M., Chou, C., Irish, V.E., Dickie, R., Elizondo, P., Wong, R., Brintnell, M., Elsasser, M., Lassar, W.M., Pierce, K.M., Leaitch, W.R., MacDonald, A.M., Platt, A., Toom-Sauntry, D., Sarda-Estève, R., Schiller, C.L., Suski, K.J., Hill, T.C.J., Abbatt, J.P.D., Huffman, J.A., DeMott, P.J. and Bertram, A.K. 2016. Size-resolved measurements of ice-nucleating particles at six locations in North America and one in Europe. *Atmospheric Chemistry and Physics*. **16**(3), pp.1637–1651.

Maters, E.C., Dingwell, D.B., Cimarelli, C., Müller, D., Whale, T.F. and Murray, B.J. 2019. The importance of crystalline phases in ice nucleation by volcanic ash. *Atmospheric Chemistry and Physics*. **19**(8), pp.5451–5465.

McCluskey, C.S., DeMott, P.J., Ma, P. -L. and Burrows, S.M. 2019. Numerical Representations of Marine Ice-Nucleating Particles in Remote Marine Environments Evaluated Against Observations. *Geophysical Research Letters*. **46**(13), pp.7838–7847.

McCluskey, C.S., DeMott, P.J., Prenni, A.J., Levin, E.J.T., McMeeking, G.R., Sullivan, A.P., Hill, T.C.J., Nakao, S., Carrico, C.M. and Kreidenweis, S.M. 2014. Characteristics of atmospheric ice nucleating particles associated with biomass burning in the US: Prescribed burns and wildfires. *J. Geophys. Res. Atmos.* **119**, pp.10458–10470.

McCluskey, C.S., Hill, T.C.J., Malfatti, F., Sultana, C.M., Lee, C., Santander, M. V, Beall, C.M., Moore, K.A., Cornwell, G.C., Collins, D.B., Prather, K.A., Jayarathne, T., Stone, E.A., Azam, F., Kreidenweis, S.M. and DeMott, P.J. 2016. A dynamic link between ice nucleating particles released in nascent sea spray aerosol and oceanic biological activity during two mesocosm experiments. *Journal of the Atmospheric Sciences.*, JAS-D-16-0087.1.

McCreedy, T. 2001. Rapid prototyping of glass and PDMS microstructures for micro total analytical systems and micro chemical reactors by microfabrication in the general laboratory. *Analytica Chimica Acta.* **427**, pp.39–43.

McDonald, J.C., Duffy, D.C., Anderson, J.R., Chiu, D.T., Wu, H., Schueller, O.J.A. and Whitesides, G.M. 2000. Fabrication of microfluidic systems in poly(dimethylsiloxane). *Electrophoresis.* **21**(1), pp.27–40.

McFarquhar, G.M., Ghan, S., Verlinde, J., Korolev, A., Strapp, J.W., Schmid, B., Tomlinson, J.M., Wolde, M., Brooks, S.D., Cziczo, D., Dubey, M.K., Fan, J., Flynn, C., Gultepe, I., Hubbe, J., Gilles, M.K., Laskin, A., Lawson, P., Leaitch, W.R., Liu, P., Liu, X., Lubin, D., Mazzoleni, C., MacDonald, A.M., Moffet, R.C., Morrison, H., Ovchinnikov, M., Shupe, M.D., Turner, D.D., Xie, S., Zelenyuk, A., Bae, K., Freer, M. and Glen, A. 2011. Indirect and semi-direct aerosol campaign: The impact of arctic aerosols on clouds. *Bulletin of the American Meteorological Society.* **92**(2), pp.183–201.

Metcalf, A.R., Narayan, S. and Dutcher, C.S. 2018. A review of microfluidic concepts and applications for atmospheric aerosol science. *Aerosol Science and Technology.* **52**(3), pp.310–329.

Miller, A.J., Brennan, K.P., Mignani, C., Wieder, J., David, R.O. and Borduas-Dedekind, N. 2021. Development of the drop Freezing Ice Nuclei Counter (FINC), intercomparison of droplet freezing techniques, and use of soluble lignin as an atmospheric ice nucleation standard. *Atmospheric Measurement Techniques.* **14**(4), pp.3131–3151.

Mirzaee, I., Song, M., Charmchi, M. and Sun, H. 2016. A microfluidics-based on-chip impinger for airborne particle collection. *Lab on a Chip.* **16**(12), pp.2254–2264.

Möhler, O., Adams, M., Lacher, L., Vogel, F., Nadolny, J., Ullrich, R., Boffo, C., Pfeuffer, T., Hobl, A., Weiß, M., Vepuri, H.S.K., Hiranuma, N. and Murray, B.J. 2021. The Portable Ice Nucleation Experiment (PINE): a new online instrument for laboratory studies and automated long-term field observations of ice-nucleating particles. *Atmospheric Measurement Techniques.* **14**(2), pp.1143–1166.

Möhler, O., Nink, A., Saathoff, H., Schaefers, S., Schnaiter, M., Schöck, W. and Schurath, U. 2001. The Karlsruhe Aerosol Chamber Facility Aida : Technical Description and First Results of Homogeneous and Heterogeneous Ice Nucleation Experiments. *Proc.of the Workshop on Ion-Aerosol-Cloud Interactions, CERN, Geneve, CH, April 18-20, 2001 CERN-No. 2001-007.*, pp.1–6.

Morrison, H., De Boer, G., Feingold, G., Harrington, J., Shupe, M.D. and

Sulia, K. 2012. Resilience of persistent Arctic mixed-phase clouds. *Nature Geoscience.* **5**(1), pp.11–17.

Mullin, J.W.W. 2001. *Crystallization (4th Ed.).*

Murray, B.J., Carslaw, K.S. and Field, P.R. 2021. Opinion: Cloud-phase climate feedback and the importance of ice-nucleating particles. *Atmospheric Chemistry and Physics.* **21**(2), pp.665–679.

Murray, B.J., O'sullivan, D., Atkinson, J.D. and Webb, M.E. 2012. Ice nucleation by particles immersed in supercooled cloud droplets. *Chemical Society Reviews.* **41**(19), pp.6519–6554.

Niedermeier, D., Augustin-Bauditz, S., Hartmann, S., Wex, H., Ignatius, K. and Stratmann, F. 2015. Can we define an asymptotic value for the ice active surface site density for heterogeneous ice nucleation? *Journal of Geophysical Research: Atmospheres.* **120**, pp.5036–5046.

Niedermeier, D., Ervens, B., Clauss, T., Voigtländer, J., Wex, H., Hartmann, S. and Stratmann, F. 2014. A computationally efficient description of heterogeneous freezing: A simplified version of the Soccer ball model. *Geophysical Research Letters.* **41**(2), pp.736–741.

Niedermeier, D., Shaw, R.A., Hartmann, S., Wex, H., Clauss, T., Voigtländer, J. and Stratmann, F. 2011. Heterogeneous ice nucleation: Exploring the transition from stochastic to singular freezing behavior. *Atmospheric Chemistry and Physics.* **11**(16), pp.8767–8775.

O'Sullivan, D., Adams, M.P.P., Tarn, M.D.D., Harrison, A.D.D., Vergara-Temprado, J., Porter, G.C.E.C.E., Holden, M.A.A., Sanchez-Marroquin, A., Carotenuto, F., Whale, T.F.F., McQuaid, J.B.B., Walshaw, R., Hedges, D.H.P.H.P., Burke, I.T.T., Cui, Z. and Murray, B.J.J. 2018. Contributions of biogenic material to the atmospheric ice-nucleating particle population in North Western Europe. *Scientific Reports.* **8**(1), p.13821.

O'Sullivan, D., Murray, B.J., Malkin, T.L., Whale, T.F., Umo, N.S., Atkinson, J.D., Price, H.C., Baustian, K.J., Browse, J. and Webb, M.E. 2014. Ice nucleation by fertile soil dusts: Relative importance of mineral and biogenic components. *Atmospheric Chemistry and Physics.* **14**(4), pp.1853–1867.

O'Sullivan, D., Murray, B.J., Ross, J.F. and Webb, M.E. 2016. The adsorption of fungal ice-nucleating proteins on mineral dusts: A terrestrial reservoir of atmospheric ice-nucleating particles. *Atmospheric Chemistry and Physics.* **16**(12), pp.7879–7887.

O'Sullivan, D., Murray, B.J., Ross, J.F., Whale, T.F., Price, H.C., Atkinson, J.D., Umo, N.S. and Webb, M.E. 2015. The relevance of nanoscale biological fragments for ice nucleation in clouds. *Scientific Reports.* **5**(1), p.8082.

Orellana, M. V, Matrai, P.A., Leck, C., Rauschenberg, C.D., Lee, A.M. and Coz, E. 2011. Marine microgels as a source of cloud condensation nuclei in the high Arctic. *Proceedings of the National Academy of Sciences.* **108**(33), pp.13612–13617.

Pamme, N. and Wilhelm, C. 2006. Continuous sorting of magnetic cells via

on-chip free-flow magnetophoresis. *Lab Chip*. **6**, pp.974–980.

Pandey, R., Usui, K., Livingstone, R.A., Fischer, S.A., Pfaendtner, J., Backus, E.H.G., Nagata, Y., Fröhlich-Nowoisky, J., Schmüser, L., Mauri, S., Scheel, J.F., Knopf, D.A., Pöschl, U., Bonn, M. and Weidner, T. 2016. Ice-nucleating bacteria control the order and dynamics of interfacial water. *Science Advances*. **2**.

Petersson, F., Åberg, L., Swärd-Nilsson, A.-M. and Laurell, T. 2007. Free Flow Acoustophoresis: Microfluidic-Based Mode of Particle and Cell Separation. *Anal. Chem.* **79**, pp.5117–5123.

Petters, M.D. and Wright, T.P. 2015. Revisiting ice nucleation from precipitation samples. *Geophysical Research Letters*. **42**(20), pp.8758–8766.

Pithan, F., Ackerman, A., Angevine, W.M., Hartung, K., Ickes, L., Kelley, M., Medeiros, B., Sandu, I., Steeneveld, G.J., Sterk, H.A.M., Svensson, G., Vaillancourt, P.A. and Zadra, A. 2016. Select strengths and biases of models in representing the Arctic winter boundary layer over sea ice: the Larcform 1 single column model intercomparison. *Journal of Advances in Modeling Earth Systems*. **8**(3), pp.1345–1357.

Polen, M., Brubaker, T., Somers, J. and Sullivan, R.C. 2018. Cleaning up our water: Reducing interferences from nonhomogeneous freezing of 'pure' water in droplet freezing assays of ice-nucleating particles. *Atmospheric Measurement Techniques*. **11**(9), pp.5315–5334.

Porter, G.C.E., Sikora, S.N.F., Adams, M.P., Proske, U., Harrison, A.D., Tarn, M.D., Brooks, I.M. and Murray, B.J. 2020. Resolving the size of ice-nucleating particles with a balloon deployable aerosol sampler: The SHARK. *Atmospheric Measurement Techniques*. **13**(6), pp.2905–2921.

Porter, G.C.E., Sikora, S.N.F., Shim, J.U., Murray, B.J. and Tarn, M.D. 2020. On-chip density-based sorting of supercooled droplets and frozen droplets in continuous flow. *Lab on a Chip*. **20**(21), pp.3876–3887.

Pratt, K.A., DeMott, P.J., French, J.R., Wang, Z., Westphal, D.L., Heymsfield, A.J., Twohy, C.H., Prenni, A.J. and Prather, K.A. 2009. In situ detection of biological particles in cloud ice-crystals. *Nature Publishing Group*. **2**(6), pp.398–401.

Prenni, A.J., Harrington, J.Y., Tjernstöm, M., DeMott, P.J., Avramov, A., Long, C.N., Kreidenweis, S.M., Olsson, P.Q. and Verlinde, J. 2007. Can ice-nucleating aerosols affect arctic seasonal climate? *Bulletin of the American Meteorological Society*. **88**(4), pp.541–550.

Price, H.C., Baustian, K.J., McQuaid, J.B., Blyth, A., Bower, K.N., Choularton, T., Cotton, R.J., Cui, Z., Field, P.R., Gallagher, M., Hawker, R., Merrington, A., Miltenberger, A., Neely, R.R., Parker, S.T., Rosenberg, P.D., Taylor, J.W., Trembath, J., Vergara-Temprado, J., Whale, T.F., Wilson, T.W., Young, G. and Murray, B.J. 2018. Atmospheric Ice-Nucleating Particles in the Dusty Tropical Atlantic. *Journal of Geophysical Research: Atmospheres*. **123**(4), pp.2175–2193.

Pruppacher, H.R. and Klett, J.D. 1997. *Microphysics of Clouds and Precipitation* 2nd ed. Kluwer Academic Publishers.

Pummer, B.G., Budke, C., Augustin-Bauditz, S., Niedermeier, D., Felgitsch, L., Kampf, C.J., Huber, R.G., Liedl, K.R., Loerting, T., Moschen, T., Schauperl, M., Tollinger, M., Morris, C.E., Wex, H., Grothe, H., Pöschl, U., Koop, T. and Fröhlich-Nowoisky, J. 2015. Ice nucleation by water-soluble macromolecules. *Atmospheric Chemistry and Physics*. **15**(8), pp.4077–4091.

Raymond, D.E., Manz, A. and Widmer, H.M. 1994. Continuous Sample Pretreatment Using a Free-Flow Electrophoresis Device Integrated onto a Silicon Chip. *Anal. Chem.* **66**, pp.2858–2865.

Reicher, N., Budke, C., Eickhoff, L., Raveh-Rubin, S., Kaplan-Ashiri, I., Koop, T. and Rudich, Y. 2019a. Size-dependent ice nucleation by airborne particles during dust events in the eastern Mediterranean. *Atmospheric Chemistry and Physics*. **19**(17), pp.11143–11158.

Reicher, N., Budke, C., Eickhoff, L., Raveh-Rubin, S., Kaplan-Ashiri, I., Koop, T. and Rudich, Y. 2019b. Size-dependent ice nucleation by airborne particles during dust events in the Eastern Mediterranean. *Atmospheric Chemistry and Physics Discussions.*, pp.1–26.

Reicher, N., Segev, L. and Rudich, Y. 2018. The Weizmann Supercooled Droplets Observation on a Microarray (WISDOM) and application for ambient dust. *Atmospheric Measurement Techniques*. **11**(1), pp.233–248.

Reicher, N., Segev, L. and Rudich, Y. 2017. The Weizmann Supercooled Droplets Observation on Microarray (WISDOM). *Atmospheric Ice Nucleation Conference (AINC 2017)*. **Book of ab**, p.48.

Ren, K., Zhou, J. and Wu, H. 2013. Materials for microfluidic chip fabrication. *Accounts of Chemical Research*. **46**(11), pp.2396–2406.

Rogers, D.C., Demott, P.J. and Kreidenweis, S.M. 2001. Airborne measurements of tropospheric ice-nucleating aerosol particles in the Arctic spring. *Journal of Geophysical Research*. **106**(D14), pp.15053–15063.

Rogers, D.C., DeMott, P.J., Kreidenweis, S.M. and Chen, Y. 1998. Measurements of ice nucleating aerosols during SUCCESS. *Geophysical Research Letters*. **25**, pp.1383–1386.

Roy, P., House, M.L. and Dutcher, C.S. 2021. A microfluidic device for automated high throughput detection of ice nucleation of snomax®. *Micromachines*. **12**(3), pp.1–18.

Sackmann, E.K., Fulton, A.L. and Beebe, D.J. 2014. The present and future role of microfluidics in biomedical research. *Nature*. **507**(7491), pp.181–9.

Sajeesh, P. and Sen, A.K. 2014. Particle separation and sorting in microfluidic devices: A review. *Microfluid. Nanofluid.* **17**(1), pp.1–52.

Sanchez-Marroquin, A., Arnalds, O., Baustian-Dorsi, K.J., Browse, J., Dagsson-Waldhauserova, P., Harrison, A.D., Maters, E.C., Pringle, K.J., Vergara-Temprado, J., Burke, I.T., McQuaid, J.B., Carslaw, K.S. and Murray, B.J. 2020. Iceland is an episodic source of atmospheric ice-nucleating particles relevant for mixed-phase clouds. *Science*

Advances. **6**(26), pp.8137–8161.

Sanchez-Marroquin, A., Hedges, D.H.P., Hiscock, M., Parker, S.T., Rosenberg, P.D., Trembath, J., Walshaw, R., Burke, I.T., McQuaid, J.B. and Murray, B.J. 2019. Characterisation of the filter inlet system on the FAAM BAe-146 research aircraft and its use for size-resolved aerosol composition measurements. *Atmospheric Measurement Techniques*. **12**(11), pp.5741–5763.

Šantl-Temkiv, T., Amato, P., Gosewinkel, U., Thyrhaug, R., Charton, A., Chicot, B., Finster, K., Bratbak, G. and Löndahl, J. 2017. High-Flow-Rate Impinger for the Study of Concentration, Viability, Metabolic Activity, and Ice-Nucleation Activity of Airborne Bacteria. *Environmental Science & Technology*. **51**, pp.11224–11234.

Šantl-Temkiv, T., Lange, R., Beddows, D., Rauter, U., Pilgaard, S., Dall'osto, M., Gunde-Cimerman, N., Massling, A. and Wex, H. 2019. Biogenic Sources of Ice Nucleating Particles at the High Arctic Site Villum Research Station. *Environmental Science and Technology*. **53**(18), pp.10580–10590.

Schill, G.P., DeMott, P.J., Emerson, E.W., Rauker, A.M.C., Kodros, J.K., Suski, K.J., Hill, T.C.J., Levin, E.J.T., Pierce, J.R., Farmer, D.K. and Kreidenweis, S.M. 2020. The contribution of black carbon to global ice nucleating particle concentrations relevant to mixed-phase clouds. *Proceedings of the National Academy of Sciences of the United States of America*. **117**(37), pp.22705–22711.

Schill, G.P., Jathar, S.H., Kodros, J.K., Levin, E.J.T., Galang, A.M., Friedman, B., Link, M.F., Farmer, D.K., Pierce, J.R., Kreidenweis, S.M. and DeMott, P.J. 2016. Ice-nucleating particle emissions from photochemically aged diesel and biodiesel exhaust. *Geophys. Res. Lett.* **43**, pp.5524–5531.

Schmale, J., Zieger, P. and Ekman, A.M.L.L. 2021. Aerosols in current and future Arctic climate. *Nature Climate Change*. **11**(2), pp.95–105.

Schneider, J., Höhler, K., Heikkilä, P., Keskinen, J., Bertozzi, B., Bogert, P., Schorr, T., Umo, N.S., Vogel, F., Brasseur, Z., Wu, Y., Hakala, S., Duplissy, J., Moisseev, D., Kulmala, M., Adams, M., Murray, B., Korhonen, K., Hao, L., Thomson, E., Castarède, D., Leisner, T., Petäjä, T. and Möhler, O. 2020. The seasonal cycle of ice-nucleating particles linked to the abundance of biogenic aerosol in boreal forests. *Atmospheric Chemistry and Physics Discussions*., pp.1–18.

Schnell, R.C. 1975. Ice nuclei produced by laboratory cultured marine phytoplankton. *Geophysical Research Letters*. **2**(11), pp.500–502.

Schnell, R.C. and Vali, G. 1972. Atmospheric Ice Nuclei from Decomposing Vegetation. *Nature*. **236**, pp.163–165.

Schnell, R.C. and Vali, G. 1976. Biogenic Ice Nuclei: Part I. Terrestrial and Marine Sources. *Journal of the Atmospheric Sciences*. **33**(8), pp.1554–1564.

Schnell, R.C. and Vali, G. 1975. Freezing nuclei in marine waters. *Tellus*. **27**, pp.321–323.

Si, M., Evoy, E., Yun, J., Xi, Y., Hanna, S.J., Chivulescu, A., Rawlings, K., Veber, D., Platt, A., Kunkel, D., Hoor, P., Sharma, S., Richard Leaitch, W. and Bertram, A.K. 2019. Concentrations, composition, and sources of ice-nucleating particles in the Canadian High Arctic during spring 2016. *Atmospheric Chemistry and Physics*. **19**(5), pp.3007–3024.

Si, M., Irish, V.E., Mason, R.H., Vergara-Temprado, J., Hanna, S.J., Ladino, L.A., Yakobi-Hancock, J.D., Schiller, C.L., Wentzell, J.J.B., Abbatt, J.P.D., Carslaw, K.S., Murray, B.J. and Bertram, A.K. 2018. Ice-nucleating ability of aerosol particles and possible sources at three coastal marine sites. *Atmospheric Chemistry and Physics*. **18**(21), pp.15669–15685.

Soo, J.-C.C., Monaghan, K., Lee, T., Kashon, M. and Harper, M. 2016. Air sampling filtration media: Collection efficiency for respirable size-selective sampling. *Aerosol Science and Technology*. **50**(1), pp.76–87.

Spracklen, D. V. and Heald, C.L. 2014. The contribution of fungal spores and bacteria to regional and global aerosol number and ice nucleation immersion freezing rates. *Atmospheric Chemistry and Physics*. **14**(17), pp.9051–9059.

Springston, S.R., Myers, M.N. and Giddings, J.C. 1987. Continuous Particle Fractionation Based on Gravitational Sedimentation in Split-Flow Thin Cells. *Analytical Chemistry*. **59**(2), pp.344–350.

Stan, C.A., Schneider, G.F., Shevkoplyas, S.S., Hashimoto, M., Ibanescu, M., Wiley, B.J. and Whitesides, G.M. 2009. A microfluidic apparatus for the study of ice nucleation in supercooled water drops. *Lab on a Chip*. **9**(16), pp.2293–2305.

Stan, C.A., Wiley, B.J., Schneider, G.F., Ibanescu, M. and Whitesides, G.M. 2010. Measurement of heterogeneous ice nucleation rates in supercooled water using a high-throughput microfluidic apparatus. *Abstracts of Papers of the American Chemical Society*. **240**.

Stopelli, E., Conen, F., Zimmermann, L., Alewell, C. and Morris, C.E. 2014. Freezing nucleation apparatus puts new slant on study of biological ice nucleators in precipitation. *Atmos. Meas. Tech.* **7**, pp.129–134.

Storelvmo, T. 2017. Aerosol Effects on Climate via Mixed-Phase and Ice Clouds. *Annual Review of Earth and Planetary Sciences*. **45**(1), pp.199–222.

Storelvmo, T., Tan, I. and Korolev, A. V. 2015. Cloud Phase Changes Induced by CO2 Warming--a Powerful yet Poorly Constrained Cloud-Climate Feedback. *Current Climate Change Reports*. **1**(4), pp.288–296.

Strohmeier, O., Keller, M., Schwemmer, F., Zehnle, S., Mark, D., Von Stetten, F., Zengerle, R. and Paust, N. 2015. Centrifugal microfluidic platforms: advanced unit operations and applications. *Chemical Society Reviews*. **44**(17), pp.6187–6229.

Suski, K.J., Hill, T.C.J., Levin, E.J.T., Miller, A., DeMott, P.J. and Kreidenweis, S.M. 2018. Agricultural harvesting emissions of ice-nucleating particles. *Atmos. Chem. Phys.* **18**(18), pp.13755–13771.

Tarn, M., Sikora, S., Porter, G., Wyld, B., Alayof, M., Reicher, N., Harrison,

A., Rudich, Y., Shim, J. and Murray, B. 2020. On-chip analysis of atmospheric ice-nucleating particles in continuous flow. *Lab on a Chip*. **20**(16), pp.2889–2910.

Tarn, M.D. and Pamme, N. 2013. Microfluidics *In*: J. Reedijk, ed. *Elsevier Reference Module in Chemistry, Molecular Sciences and Chemical Engineering*. Waltham, MA: Elsevier.

Tarn, M.D., Sikora, S.N.F., Porter, G.C.E., O'Sullivan, D., Adams, M., Whale, T.F., Harrison, A.D., Vergara-Temprado, J., Wilson, T.W., Shim, J. uk and Murray, B.J. 2018. The study of atmospheric ice-nucleating particles via microfluidically generated droplets. *Microfluid. Nanofluid.* **22**(5), p.52.

Tarn, M.D., Sikora, S.N.F., Porter, G.C.E., Shim, J.U. and Murray, B.J. 2021. Homogeneous freezing of water using microfluidics. *Micromachines*. **12**(2), pp.1–23.

Tarn, M.D., Sikora, S.N.F., Porter, G.C.E., Wyld, B.V., Reicher, N., Alayof, M., Harrison, A.D., Rudich, Y., Shim, J.-U. and Murray, B.J. 2019. Continuous flow analysis of atmospheric ice-nucleating particles in the eastern mediterranean *In*: *23rd International Conference on Miniaturized Systems for Chemistry and Life Sciences, MicroTAS 2019*.

Teh, S.-Y., Lin, R., Hung, L.-H. and Lee, A.P. 2008. Droplet microfluidics. *Lab Chip*. **8**, pp.198–220.

Tobo, Y. 2016. An improved approach for measuring immersion freezing in large droplets over a wide temperature range. *Sci Rep*. **6**(August), p.32930.

Tobo, Y., Adachi, K., DeMott, P.J., Hill, T.C.J., Hamilton, D.S., Mahowald, N.M., Nagatsuka, N., Ohata, S., Uetake, J., Kondo, Y. and Koike, M. 2019. Glacially sourced dust as a potentially significant source of ice nucleating particles. *Nature Geoscience*. **12**(4), pp.253–258.

Ukita, Y., Oguro, T. and Takamura, Y. 2017. Density-gradient-assisted centrifugal microfluidics: an approach to continuous-mode particle separation. *Biomed. Microdevices*. **19**, p.24.

Vali, G. 1994. Freezing Rate Due to Heterogeneous Nucleation. *Journal of the Atmospheric Sciences*. **51**(13), pp.1843–1856.

Vali, G. 2014. Interpretation of freezing nucleation experiments: Singular and stochastic; Sites and surfaces. *Atmospheric Chemistry and Physics*. **14**(11), pp.5271–5294.

Vali, G. 1971. Quantitative Evaluation of Experimental Results an the Heterogeneous Freezing Nucleation of Supercooled Liquids. *Journal of the Atmospheric Sciences*. **28**(3), pp.402–409.

Vali, G. 2008. Repeatability and randomness in heterogeneous freezing nucleation. *Atmospheric Chemistry and Physics*. **8**(16), pp.5017–5031.

Vali, G. 2019. Revisiting the differential freezing nucleus spectra derived from drop-freezing experiments: methods of calculation, applications, and confidence limits. *Atmos. Meas. Tech*. **12**, pp.1219–1231.

Vali, G., DeMott, P.J., Möhler, O. and Whale, T.F. 2015. Technical Note: A

proposal for ice nucleation terminology. *Atmospheric Chemistry and Physics*. **15**(18), pp.10263–10270.

Vali, G. and Stansbury, E.J. 1966. TIME-DEPENDENT CHARACTERISTICS OF THE HETEROGENEOUS NUCLEATION OF ICE. *Can. J. Phys.* **44**, pp.477–502.

Vergara-Temprado, J., Murray, B.J., Wilson, T.W., O'Sullivan, D., Browse, J., Pringle, K.J., Ardon-Dryer, K., Bertram, A.K., Burrows, S.M., Ceburnis, D., Demott, P.J., Mason, R.H., O'Dowd, C.D., Rinaldi, M. and Carslaw, K.S. 2017. Contribution of feldspar and marine organic aerosols to global ice nucleating particle concentrations. *Atmospheric Chemistry and Physics*. **17**(5), pp.3637–3658.

Wagner, R., Kiselev, A., Möhler, O., Saathoff, H. and Steinke, I. 2016. Pre-activation of ice-nucleating particles by the pore condensation and freezing mechanism. *Atmospheric Chemistry and Physics*. **16**(4), pp.2025–2042.

Wang, X., Sultana, C.M., Trueblood, J., Hill, T.C.J., Malfatti, F., Lee, C., Laskina, O., Moore, K.A., Beall, C.M., McCluskey, C.S., Cornwell, G.C., Zhou, Y., Cox, J.L., Pendergraft, M.A., Santander, M. V, Bertram, T.H., Cappa, C.D., Azam, F., DeMott, P.J., Grassian, V.H. and Prather, K.A. 2015. Microbial Control of Sea Spray Aerosol Composition: A Tale of Two Blooms. *ACS Central Science*. **1**(3), pp.124–131.

Watts, P. and Wiles, C. 2012. Micro reactors, flow reactors and continuous flow synthesis. *Journal of Chemical Research*., pp.181–193.

Welti, A., Lüönd, F., Stetzer, O. and Lohmann, U. 2009. Influence of particle size on the ice nucleating ability of mineral dusts. *Atmospheric Chemistry and Physics*. **9**(18), pp.6705–6715.

Westh, P., Kristiansen, J. and Hvidt, A. 1991. ICE-nucleating activity in the freeze-tolerant tardigrade Adorybiotus coronifer. *Comparative Biochemistry and Physiology -- Part A: Physiology*. **99**(3), pp.401–404.

Wex, H., Augustin-Bauditz, S., Boose, Y., Budke, C., Curtius, J., Diehl, K., Dreyer, A., Frank, F., Hartmann, S., Hiranuma, N., Jantsch, E., Kanji, Z.A., Kiselev, A., Koop, T., Möhler, O., Niedermeier, D., Nillius, B., Rösch, M., Rose, D., Schmidt, C., Steinke, I. and Stratmann, F. 2015. Intercomparing different devices for the investigation of ice nucleating particles using Snomax® as test substance. *Atmospheric Chemistry and Physics*. **15**(3), pp.1463–1485.

Wex, H., Huang, L., Zhang, W., Hung, H., Traversi, R., Becagli, S., Sheesley, R.J., Moffett, C.E., Barrett, T.E., Bossi, R., Skov, H., Hünerbein, A., Lubitz, J., Löffler, M., Linke, O., Hartmann, M., Herenz, P. and Stratmann, F. 2019. Annual variability of ice-nucleating particle concentrations at different Arctic locations. *Atmospheric Chemistry and Physics*. **19**(7), pp.5293–5311.

Whale, T.F., Holden, M.A., Kulak, A.N., Kim, Y.-Y., Meldrum, F.C., Christenson, H.K. and Murray, B.J. 2017. The role of phase separation and related topography in the exceptional ice-nucleating ability of alkali feldspars. *Physical Chemistry Chemical Physics*. **19**, pp.31186–31193.

Whale, T.F., Murray, B.J., O'Sullivan, D., Wilson, T.W., Umo, N.S., Baustian, K.J., Atkinson, J.D., Workneh, D.A. and Morris, G.J. 2015. A technique for quantifying heterogeneous ice nucleation in microlitre supercooled water droplets. *Atmospheric Measurement Techniques.* **8**(6), pp.2437–2447.

Whitesides, G.M. 2006. The origins and the future of microfluidics. *Nature.* **442**, pp.368–373.

Wilson, T.W., Ladino, L.A., Alpert, P.A., Breckels, M.N., Brooks, I.M., Browse, J., Burrows, S.M., Carslaw, K.S., Huffman, J.A., Judd, C., Kilthau, W.P., Mason, R.H., McFiggans, G., Miller, L.A., Nájera, J.J., Polishchuk, E., Rae, S., Schiller, C.L., Si, M., Temprado, J.V., Whale, T.F., Wong, J.P.S., Wurl, O., Yakobi-Hancock, J.D., Abbatt, J.P.D., Aller, J.Y., Bertram, A.K., Knopf, D.A. and Murray, B.J. 2015. A marine biogenic source of atmospheric ice-nucleating particles. *Nature.* **525**(7568), pp.234–238.

Wyatt Shields IV, C., Reyes, C.D. and Lopez, G.P. 2015. Microfluidic cell sorting: a review of the advances in the separation of cells from debulking to rare cell isolation. *Lab Chip.* **15**, pp.1230–1249.

Xie, S., Liu, X., Zhao, C. and Zhang, Y. 2013. Sensitivity of CAM5-simulated arctic clouds and radiation to ice nucleation parameterization. *Journal of Climate.* **26**(16), pp.5981–5999.

Yamada, M., Nakashima, M. and Seki, M. 2004. Pinched Flow Fractionation: Continuous Size Separation of Particles Utilizing a Laminar Flow Profile in a Pinched Microchannel.

Yuen, P.K. and Goral, V.N. 2012. Low-Cost Rapid Prototyping of Whole-Glass Microfluidic Devices. *J. Chem. Educ.* **89**, pp.1288–1292.

Zhu, P. and Wang, L. 2017. Passive and active droplet generation with microfluidics: a review. *Lab Chip.* **17**, pp.34–75.

Zinke, J., Salter, M.E., Leck, C., Lawler, M.J., Porter, G.C.E., Adams, M.P., Brooks, I.M., Murray, B.J. and Zieger, P. 2021. The development of a miniaturised balloon-borne cloud water sampler and its first deployment in the high Arctic. *Tellus, Series B: Chemical and Physical Meteorology.* **73**(1), pp.1–12.

2. Resolving the size of ice-nucleating particles with a balloon deployable aerosol sampler: the SHARK

Grace C. E. Porter[1,2], Sebastien N. F. Sikora[1], Michael P. Adams[1], Ulrike Proske[1,3], Alexander D. Harrison[1], Mark D. Tarn[1,2], Ian M. Brooks[1] & Benjamin J. Murray[1]

[1]School of Earth and Environment, University of Leeds, Leeds LS2 9JT, UK
[2]School of Physics and Astronomy, University of Leeds, Leeds LS2 9JT, UK
[3]Institute for Atmospheric and Environmental Sciences, Goethe University Frankfurt, Frankfurt am Main, Germany

Abstract. Ice-nucleating particles (INPs) affect cloud development, lifetime and radiative properties, hence it is important to know the abundance of INPs throughout the atmosphere. A critical factor in determining the lifetime and transport of INPs is their size, however very little size-resolved atmospheric INP concentration information exists. Here we present the development and application of a radio-controlled payload capable of collecting size-resolved aerosol from a tethered balloon for the primary purpose of off-line INP analysis. This payload, known as the SHARK (Selective Height Aerosol Research Kit), consists of two complementary cascade impactors for aerosol size-segregation from 0.25 to 10 µm, with an after-filter and top stage to collect particles below and above this range at flow rates up to 100 L min^{-1}. The SHARK also contains an optical particle counter to quantify aerosol size distribution between 0.38 and 10 µm, and a radiosonde for the measurement of temperature, pressure, GPS altitude, and relative humidity. This is all housed within a weatherproof box, can be run from batteries for up to 11 h and has a total weight of 9 kg. The radio control and live data link with the radiosonde allow the user to start and stop sampling depending on meteorological conditions and height, which can, for example, allow the user to avoid sampling in very humid or cloudy air, even when the SHARK is out of sight. While the collected aerosol could, in principle, be studied with an array of analytical techniques, this study demonstrates that the collected aerosol can be analysed with an off-line droplet freezing instrument to determine size-resolved INP concentrations, activated fractions and active site densities, producing similar results to those obtained using a standard PM_{10} aerosol sampler when summed over the appropriate size range. Test data, where the SHARK was sampling near ground level or suspended from a tethered balloon at 20 m altitude, is presented from four contrasting locations having very different size resolved

INP spectra: Hyytiälä (Southern Finland), Leeds (Northern England), Longyearbyen (Svalbard), and Cardington (Southern England).

2.1. Introduction

Atmospheric ice-nucleating particles (INPs) are not well understood, with knowledge of their concentration, sources, temporal variability, transport and size in its infancy (Murray et al., 2012; Kanji et al., 2017). This is of importance because clouds between 0 °C and around −35 °C can exist in a supercooled liquid, mixed-phase (ice and water) or glaciated (ice only) state depending in part on the presence or absence of INPs (Kanitz et al., 2011; Vergara-Temprado et al., 2018). In the absence of INP, cloud droplets can supercool to below ~−35°C (Herbert et al., 2015), but INP can trigger freezing at much higher temperatures (Kanji et al., 2017). These particles usually have concentrations that are orders of magnitude smaller than cloud condensation nuclei (CCN), and have a disproportionate impact on clouds because the nucleated ice crystals grow rapidly and precipitate out (Murray, 2017; Lohmann, 2017). In a shallow cloud, heterogeneous ice nucleation can result in dramatic reductions in cloud albedo by removal of supercooled liquid water (Storelvmo, 2017; Vergara-Temprado et al., 2018), whereas in deep convective clouds it can influence a web of microphysical processes in a complex way (Rosenfeld et al., 2011; Kanji et al., 2017; Deng et al., 2018). Hence, a greater understanding of INP lifetime, transport and distribution in the vertical profile is needed in order to better understand and model cloud processes and their response to a changing climate.

The size of an aerosol particle significantly affects its lifetime and therefore transport in the atmosphere, with particles of a few hundred nanometres potentially having a lifetime of weeks, whereas particles of 10 µm have a lifetime of only hours (Jaenicke, 2007). While composition is recognised to be an important controller of ice nucleation ability (Kanji et al., 2017), it has also been generally thought that the larger an aerosol particle, the more likely it is to serve as an INP (Pruppacher and Klett, 1997). However, the lifetime of coarse mode aerosol particles decreases rapidly with increasing size. Consistent with larger particles being better ice nucleators, parameterisations of INPs in the atmosphere have been proposed wherein the INP concentration is related to the concentration of aerosol particles

larger than 0.5 µm (DeMott et al., 2010; Tobo et al., 2013; DeMott et al., 2015). However, most atmospheric measurements of INPs report the sum of INPs below some threshold size set by an inlet or size cut, specified by the aerosol sampler used. For instance, DeMott et al. (2017) provides a comparison between a selection of instruments for the collection and subsequent INP analysis of aerosol, where the aerosol samplers have either a defined size cut-off or have collection efficiencies that decrease in magnitude above a defined size. Nevertheless, there are examples of field studies in which INPs have been size-resolved (Berezinski et al., 1988; Welti et al., 2009; Santachiara et al., 2010; Huffman et al., 2013; Mason et al., 2016; Si et al., 2018; Reicher et al., 2018; Creamean, Kirpes, et al., 2018). These studies generally show that while the fine mode aerosol particles are more abundant, coarse mode aerosol particles often contribute more to the INP population. In addition, the activated fraction (n_n) of coarse mode aerosol is usually greater than fine mode aerosol. However, in some field studies (Mason et al., 2016; Si et al., 2018), fine aerosol sometimes contributes more to the INP population than the coarse mode. Therefore, there is a need to determine INP sizes when quantifying atmospheric INP concentrations, as size is important for transport and lifetime and is therefore required to accurately model global INP populations.

Measurements of INPs in and above the boundary layer are crucial to understanding the contribution of local sources to the ice-nucleating activity in clouds, compared to transported aerosol. Aircraft measurements (e.g. Price et al., 2018; Rogers et al., 2001) and mountaintop observatories (e.g. Conen et al., 2015) have been used to quantify INP populations above the boundary layer. For example, it has been shown that there are differences in the INP concentrations measured when in and out of the boundary layer at the High Altitude Research Station Jungfraujoch (Switzerland) (Conen et al., 2015; Lacher et al., 2018). While these measurements are undoubtedly useful, mountaintop measurements are only possible in locations with sufficiently tall yet accessible mountains, and aircraft sampling is expensive and not necessarily possible in remote regions. It is therefore essential that instrumentation is available that can be used to sample aerosol at selected altitudes (including ground level) in order to determine INP concentrations throughout the vertical profile. Unmanned aerial vehicles (UAVs) are becoming more widely used in atmospheric science; these allow the

collection of aerosol at altitude at significantly lower cost than with manned aircraft, but are limited by relatively short battery lives, usually under 1 h, and potential propeller interference (Villa et al., 2016; Jacob et al., 2018).

Tethered kite and balloon systems have historically been used to make atmospheric measurements and collect aerosol samples with much longer sampling times (many hours are readily achievable) at altitudes up to 2 km and 5 km for tethered balloons and kites respectively (Armstrong et al., 1981; Balsley et al., 1998). An advantage of a balloon or kite system is that an instrument can be held at a chosen altitude for many hours without the balloon interfering with measurements, as the instrument can be suspended on a line many meters below the balloon. They can also stay inflated and in use for periods of many weeks, making them ideal for longer campaigns in remote environments. A new instrument called the Honing On VERtical Cloud and Aerosol properTies (HOVERCAT) (Creamean et al., 2018) provides the capability to sample aerosol for subsequent INP analysis on a tethered balloon or UAV, allowing both variable altitudes and static collection of non-size resolved aerosol smaller than 10 µm at 1.2 L min^{-1}. In the past, aerosols have been size-segregated using cascade impactors on a tethered balloon system (Reagan et al., 1984; Hara et al., 2013), but balloon-borne cascade impactor systems have not yet been adapted for the purpose of size-resolved INP analysis. The downsides of balloon-based platforms include the need for wind speeds below around 64.4 km h^{-1} to avoid damage to the balloon, and the possibility of 'icing' of the balloon and lines when deployed in a cold and humid environment, which could add to the weight of the payload and cause the system to sink, or fall slowly. Nevertheless, balloon and kite-borne measurements remain a valuable way to obtain continuous, high resolution measurements over a period of many hours in a single location at a range of altitudes.

In this paper, the design, testing and operation of a payload named the Selective Height Aerosol Research Kit (SHARK) is presented. It consists of two separate cascade impactor systems, operating at 9 and 100 L min^{-1}, for the size-sorting of ambient aerosol particles from 0.25 to 10 µm, with an after-filter and top stage to collect particles below and above this range for off-line INP (or other) analysis. The SHARK also features an optical particle

counter (OPC) and a radiosonde, which provides real-time measurements of relative humidity (RH), temperature, Global Positioning System (GPS) altitude and pressure. Weighing 9 kg, the payload is suitable for use with a 21 m^3 or larger tethered balloon such as in Figure 1.1 a where the SHARK is shown in-flight. The use of a tethered balloon and a high-capacity battery allow aerosol to be collected for up to 11 h at a user-selected altitude.
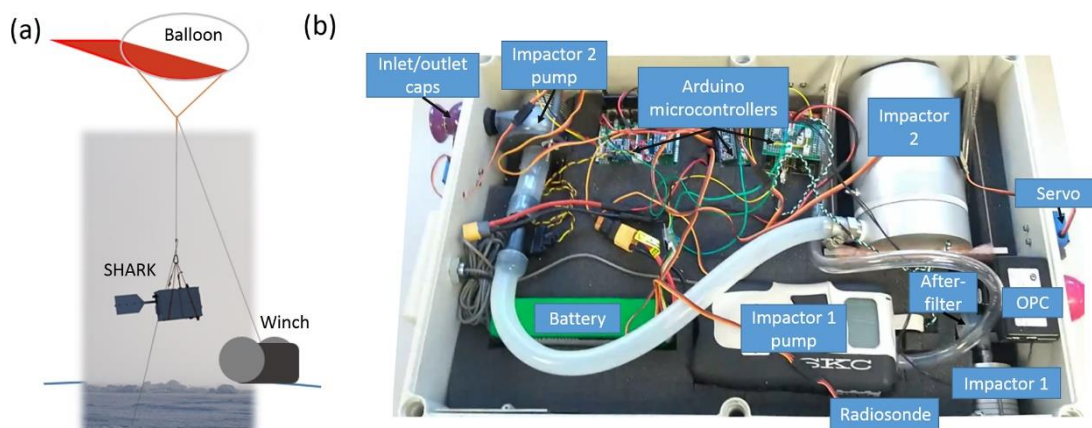
Figure 2.1- The SHARK. (a) The SHARK payload on a tethered balloon connected to ground by a winch. The photograph was taken during deployment in the High Arctic. (b) The components inside the SHARK payload labelled on a photograph. The payload featured a large impactor inlet at the top of the platform for Impactor 2, with the OPC inlet facing the front, and a small impactor inlet at the bottom for Impactor 1. The radiosond was at the bottom of the box, and the outlet valve for the pump system is shown at the back of the SHARK, where the 100 L min^{-1} pump for Impactor 2 vents.

2.2.   The design and development of the SHARK

2.2.1. Instrument description

The SHARK, shown in Figure 1.1, comprises two cascade impactors and corresponding pumps, alongside an OPC (OPC-N2, Alphasense, UK) and radiosonde (S1H2-R, Windsond, Sweden), all mounted within a weatherproof enclosure with a tail fin to orient it into the wind. A photograph of the internal components of the SHARK are shown in Figure 1.1b. The two cascade impactors were employed to collect particles across different size bins: Impactor 1 from 0.25-2.5 μm and Impactor 2 from 1-10 μm. Impactor 1 is a cascade impactor (U.S. Patent No. 6,786,105, Sioutas, SKC, UK), which requires a flow rate of 9 L min^{-1} and operates with a portable pump (Leland Legacy, SKC, UK). Impactor 2 is also a cascade impactor (MSP Model 128, TSI, USA), which requires a flow rate of 100 L min^{-1} at a pressure drop of

0.6 kPa (Marple et al., 1991; Misra et al., 2002), and for which a radial flow impeller (Radial Blower U51, Micronel, UK) was used in reverse as a lightweight pump (~120 g). These pumps maintain the volumetric flow rate through the impactors as temperature and atmospheric pressure change with altitude. The pump for Impactor 1 was calibrated to apply this adjustment to at least 2.3 km (Leland Legacy Sample Pump: Operating Instructions, SKC), although the presence of the after-filter may reduce the battery life at this altitude. The pump for Impactor 2 is supplied by a larger battery and should be able to maintain flow to at least the same altitude as the Impactor 1 pump, and over a longer period of time. The SHARK records the volume of air sampled through Impactor 1 during the flight, and so if the pump battery was depleted, or the pressure drop became too great before Impactor 2 had finished sampling, the Impactor 1 pump would shut down and store the recorded value for later analysis. Further testing of the SHARK would be required to define a maximum altitude limit that each SHARK component could operate at. In order to provide RH, temperature, GPS altitude and pressure data in real-time, the sensors and transmitter from a radiosonde were integrated into the system. The OPC measured aerosol size distributions, which were saved in the on-board memory. Servo-controlled caps covered the sample inlets and outlets to reduce contamination during ascent and descent, as well as to protect the components from cloud water. The operation of the SHARK components was controlled remotely via a radio link using an Arduino microcontroller board (16 km range); once the SHARK was at the desired altitude according to the constantly transmitting radiosonde, the inlet caps opened 10 s prior to the pumps and OPC starting in order to initiate aerosol sampling and monitoring. The payload components, including the servo inlet covers and Arduino control boards, were powered by a 5000 mAh battery (4S 14.8 V LiPo, Overlander, UK). The components were assembled into the SHARK payload with the static (i.e. no wind) weight budget of 10 kg for a 21 m^3 balloon (Skyhook Helikite, Allsopp Helikites Ltd., UK) in mind, hence the SHARK weighs 9 kg when fully instrumented.

The cascade impactors allow for the collection of size-segregated aerosol (further details are provided in Section 2.2) onto thin films (0.25 mm thickness) for subsequent off-line analysis, which can be used alongside information about the aerosol size distributions obtained via the OPC and

atmospheric conditions from the radiosonde. Our initial focus concerns the analysis of the ice-nucleating properties of the collected aerosol, but an array of analytical techniques could be applied to characterise the size-selected aerosol, including mass spectrometry, DNA analysis, scanning electron microscopy (SEM) and transmission electron microscopy (TEM) (Garcia et al., 2012; Huffman et al., 2013; Ault and Axson, 2017; Laskin et al., 2018).
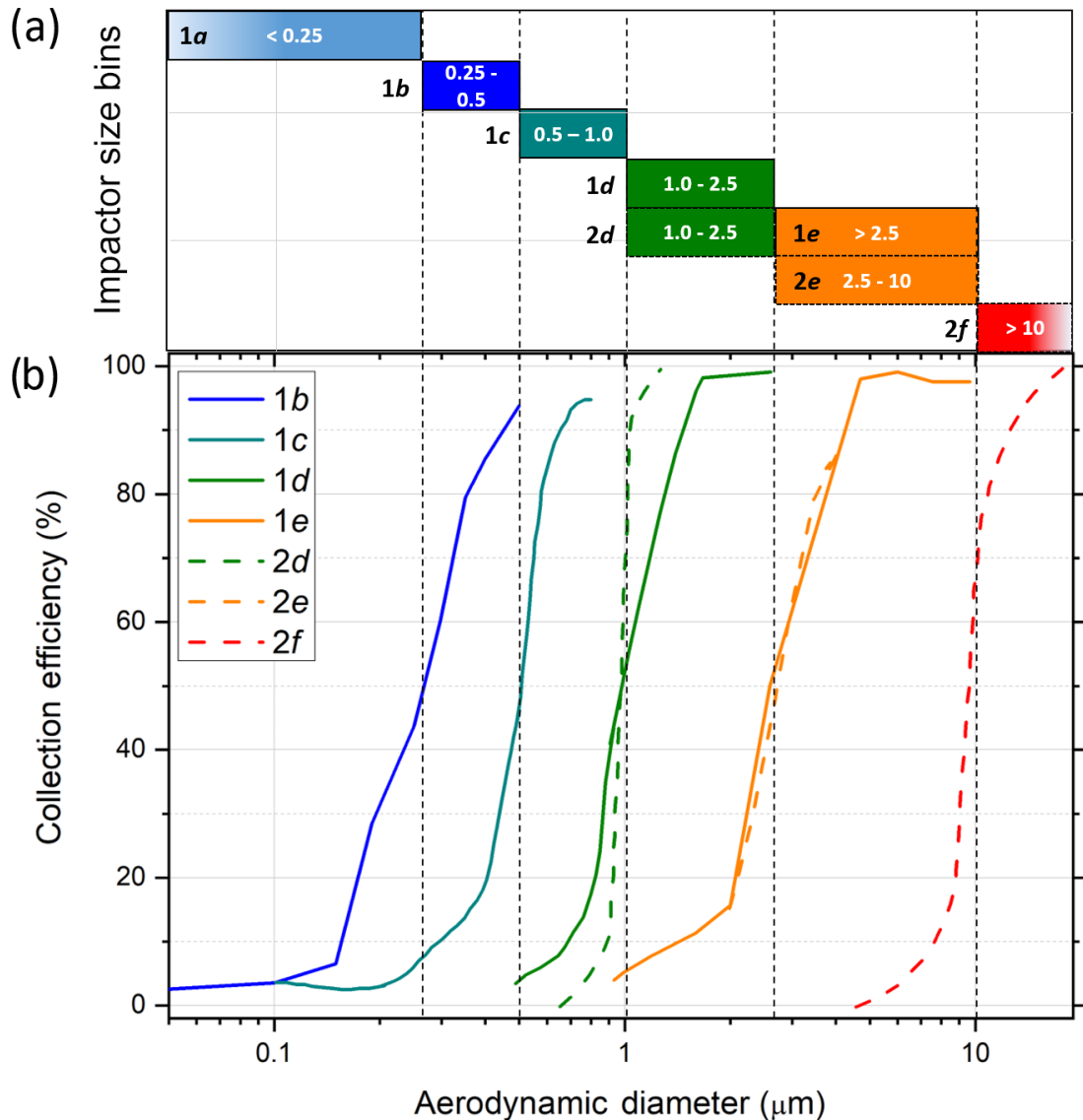
Figure 2.2- Collection efficiencies of each size bin of the two cascade impactors in the SHARK. (a) The size bins for each stage of Impactor 1 and 2 at flow rates of 9 and 100 L min−1, respectively. (b) Impactor efficiency curves for each stage. Impactor 1 has four stages (1b-e) and one after-filter (1a), while Impactor 2 has three stages (2d-f). Stages 1d and 2d as well as 1e and 2e should be approximately equivalent in terms of the aerosol size ranges collected.

2.2.2. Size-segregated collection of aerosol

Two separate cascade impactors were installed, each operating over different size ranges. This enabled size-resolved aerosol sampling onto substrates across both the fine and coarse modes at high flow rates, while keeping power consumption low enough to be run from batteries. Single impactor systems designed to operate across the accumulation and coarse modes simultaneously require a relatively large pressure drop that would typically require a prohibitively large (and heavy) pump and battery for this application.

Impactor 1 sorts aerosol into five size categories: <0.25 μm (this size bin is defined by the impactor after-filter and is hereafter referred to as 1*a*), 0.25-0.5 μm (from stage 1*b*), 0.5-1.0 μm (from stage 1*c*), 1.0-2.5 μm (from stage 1*d*), and >2.5 μm (from stage 1*e*). The size categories *b* to *e* correspond to the impactor stages where the 50 % collection cut-off diameter (d50) is the lower bound of each bin. The size bins and collection efficiencies for each impactor were digitised from data provided by the manufacturers, (Misra et al., 2002; Product Information Sheet - MSP) and are shown in Figure 2.2. Several collection substrates were tested by Misra et al. (2002), and the dataset from the Teflon substrates was chosen to represent Impactor 1 here as that substrate most closely resembled those used in this study. For Impactor 1, the particles were collected on 25 mm diameter filters of pore size 0.05 μm (Nuclepore Track-Etched Membrane polycarbonate filters, Whatman, UK). Filters were used as impactor substrates rather than films since they have very low background contamination and are easier to obtain. Size category 1*a* corresponds to an after-filter situated after Impactor 1, which comprised a 47 mm diameter polycarbonate filter with a pore size of 5 μm (Nuclepore Track-Etched Membrane) to maintain the flow rate. The collection efficiency of the after-filter was estimated to be 50-100 % at 0.25 μm and below (Soo et al., 2016). Impactor 2 collected aerosol particles into three size categories: 1.0-2.5 μm (2*d*), 2.5-10 μm (2*e*), and >10 μm (2*f*), also illustrated in Figure 2.2. 75 mm diameter filters of pore size 0.05 μm (Nuclepore Track-Etched Membrane polycarbonate filters) were used in Impactor 2. An after-filter could not be used with this impactor since its

inclusion increased the required pressure drop to beyond what the pump could supply at 100 L min^{-1}.

A further benefit of using these two impactors in tandem is that, in the size ranges where they overlap of 1.0-2.5 µm (stage *d*) and 2.5-10 µm (stage *e*), the impaction efficiencies are very similar, allowing a direct comparison between the two impactors in this size range. The stages are labelled *a* through *f* for the smallest to largest impactor stage sizes (including the after-filter), such that 1*d* and 2*d* refer to stage *d* (1.0-2.5 µm) on Impactors 1 and 2, respectively (see Figure 2.2). Background runs were produced by placing the substrates in the SHARK as if setting up to sample, before removing and analysing them as normal to determine the contamination introduced through the installation and recovery of the substrates.

Particle bounce, the bouncing of particles off the impaction substrate and the collection of these particles on the lower stages, has previously been identified as a factor that can cause biases when aerosol is collected by cascade impactors (Dzubay et al., 1976; Cheng and Yeh, 1979). The collection efficiency curves shown in Figure 2.2 for Impactor 1 already account for some degree of particle bounce, having been determined experimentally by Misra et al., (2002) using monodispersed polymer particles on a variety of substrates. However, the efficiency curves for Impactor 2 are based on theoretical predictions (Rader and Marple, 1985) and so do not account for any bounce effects. Since two of the stages of Impactors 1 and 2 overlap (stages *d* and *e*), it is possible to comment on the possible effects, or lack thereof, of particle bounce, based on the results obtained using each of the comparable stages. This is briefly addressed in section 2.3.4 where we show good agreement between these two impactors.

2.2.3. Size distribution measurements

The OPC produced binned particle size distributions from 0.38-17 µm every 1.38 s at a typical flow rate of 1.2 L min^{-1}. The OPC was remotely operated through the use of its serial link via an Arduino microcontroller board. Particle size, surface area and mass concentration data were produced from the raw OPC data, and these then used to calculate the fraction of the aerosol that act as an INP (activated fraction, $n_n(T)$), and to weight the INP data to particle surface area , generating the ice-active site density per

surface area ($n_s(T)$) of aerosol. The particle density used was 1.65 g cm^{-3}, as assumed by the OPC software, and they were assumed to be spherical. No correction was made for the hygroscopic growth of aerosol particles as this required assumptions about the chemical nature of the particles, and hygroscopic growth effects were minimised by avoiding sampling when the RH was above about 80 % (see next section).

2.2.4. Radiosonde data

Utilising the radio control built into the payload, real-time data informed decisions of when to turn the pumps on and off to sample. Continuous monitoring of the radiosonde data allows the user to avoid sampling under conditions where RH approached 100 %, at which point aerosol particles become excessively swollen with water or activated to cloud droplets. Hence, the influence of hygroscopic growth or cloud droplets on the collected aerosol could be minimised. The temperature and pressure measurements allowed the volume of air sampled by the impactors and OPC to be corrected to standard conditions (1 atm at 0 °C).

2.2.5. Housing and instrument orientation

The weatherproof housing consisted of an acrylonitrile butadiene styrene (ABS) polymer box with dimensions of 560 mm x 380 mm x 180 mm (IP67, Fibox). Holes to mount the impactors and OPCs were drilled so that Impactor 2 sat vertically upright and Impactor 1 was oriented 180° to Impactor 2 so that it faced downwards, ensuring that both impactors were always oriented 90° to the wind. The OPC was at 90° to both impactors and facing towards the front of the box, into the wind (see Figure 2.3a-c) See section 2.6 for the rationale of the positioning of the OPC and impactor inlets. The tail fin, which is mounted to the lid of the box, was designed to keep the SHARK orientated into the wind, and was fabricated from rigid polyvinyl chloride (PVC) sheet. Impactor 1 had its own mounting screws by which it was attached to the box, whilst for Impactor 2 a custom mount was built. Securing ropes were threaded through reinforced holes in the box and connected via a carabiner for quick and easy attachment to the balloon instrument line, as seen in Figure 1.1a. Modular foam was used to keep all components in place during flight.
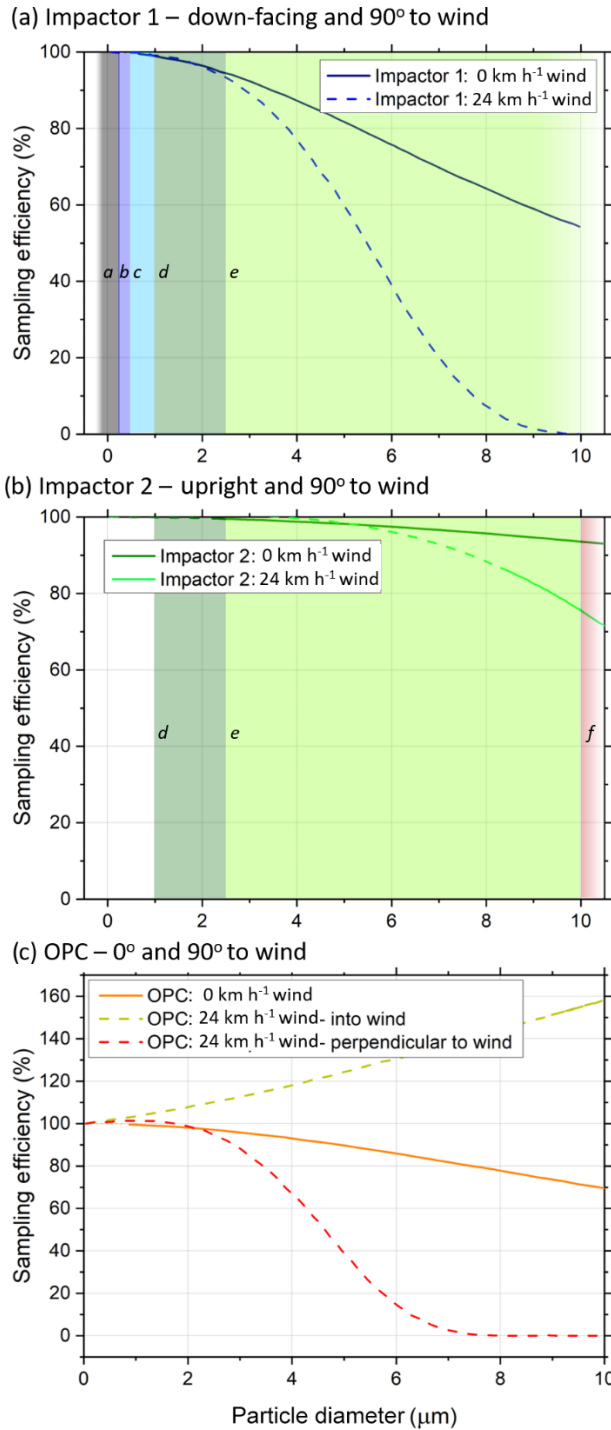
Figure 2.3- SHARK sampling efficiencies (a) The sampling efficiencies of Impactor 1, with and without wind, when sampling at 90° to the wind direction. (b) The sampling efficiencies of Impactor 2, with and without wind, when sampling at 90° to the wind direction. (c) The sampling efficiency of the OPC, with and without wind, when sampling at 0° and 90° to the wind direction (the OPC was deployed at 0° to the wind, based on this calculation). Solid lines denote model predictions within the formulas' validity range, and dotted lines represent approximations (Von Der Weiden et al., 2009).

2.2.6. Inlet sampling efficiencies via particle loss modelling

Calculation of the particle losses associated with the instrument inlets due to excessive wind speeds in various configurations were used to inform the design of the SHARK and to minimise sampling biases in higher wind conditions. The calculations were done using an open source particle loss calculator program in Igor Pro, the details and assumptions for which are presented in Von Der Weiden et al., (2009). The particle loss characteristics of the impactor and OPC inlets at their required flow rates were calculated for a wind speed of 0 and 24 km h^{-1}, the latter used as a maximum representative wind speed for operation. The wind speeds required for optimum performance are <8 km h^{-1} for the impactors and OPC, but the system may experience higher wind speeds. Hence, we use this modelling to guide our choice of positioning of the instrument relative to wind direction in order to minimise sampling biases at the inlets. The modelling also allows us to better understand which impactor stages (and OPC size bins) will be most affected by such biases. We make no attempt to correct the measurements for sampling biases, since this correction itself would carry substantial uncertainty, but used the calculations to inform us of the best configuration for the various inlets.

The inlet sampling efficiencies in the orientations chosen for the final design of the SHARK are shown in Figure 2.3. It is important to note that, due to their dissimilar inlet dimensions and operational flow rates, Impactors 1 and 2 are affected differently by the wind. The particle losses for the largest stages of each impactor are the most affected. Stages *a* to *d* on both impactors are only minimally affected by losses. The losses are more significant in stage e on both impactors, but the losses on 1e are greater than on 2*e* with a 50% cut off at around 5.5 μm and a negligible sampling efficiency above about 8 μm on 1*e*. These calculations also demonstrate that the losses are wind-speed dependent, but that in situations where there is significant wind, the results from Impactor 2 will be less influenced by losses than Impactor 1 at sizes above 2.5 μm

The OPC suffers up to 1.6 times oversampling for 10 μm particles when sampling into 24 km h^{-1} wind, but when oriented at 90° to the wind the

collection efficiency of >6 μm particles approaches 0 % (see Figure 2.3c). Therefore, the OPC has been positioned in the SHARK to be oriented into the wind to ensure data is collected for the whole size range, with the caveat of a sub-isokinetic oversampling of larger particles.

2.3.   Results and Discussion

The SHARK has been deployed at ground level and on a tethered balloon during development and testing at four locations for the collection and monitoring of aerosol: Cardington (UK), Hyytiälä (Finland), Leeds (UK), and Longyearbyen (Svalbard). Details of the sampling locations, periods, and instrumentation can be found in Table A1 of the Supplementary Information (SI). In this section, we present the results for this set of four SHARK deployments to illustrate the capabilities of the SHARK for quantifying ice-nucleating particle spectra as well as demonstrating that the technique is consistent with more established methods.
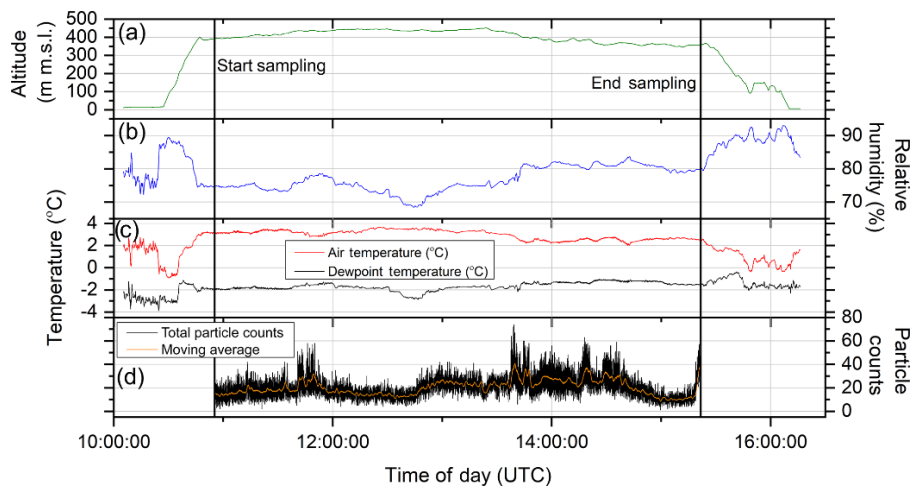
Figure 2.4-Windsond and optical particle counter (OPC) data for a flight during a campaign to the High Arctic. (a) The altitude of the SHARK payload throughout the 4.5 hour flight. The sampling start and end times are indicated as solid lines. The SHARK reached 450 m above Mean Sea Level (MSL) and in the last hour of flight was lowered to 350 m due to ice formation on the balloon, instrument and tether. (b) The humidity during the flight was monitored to ensure the SHARK was not sampling during unfavourable conditions. The SHARK was brought back down to ground level once the sampling had been stopped. (c) The ambient temperature was monitored alongside the dewpoint temperature. (d) Total particle counts throughout the sampling period, as monitored by the OPC.
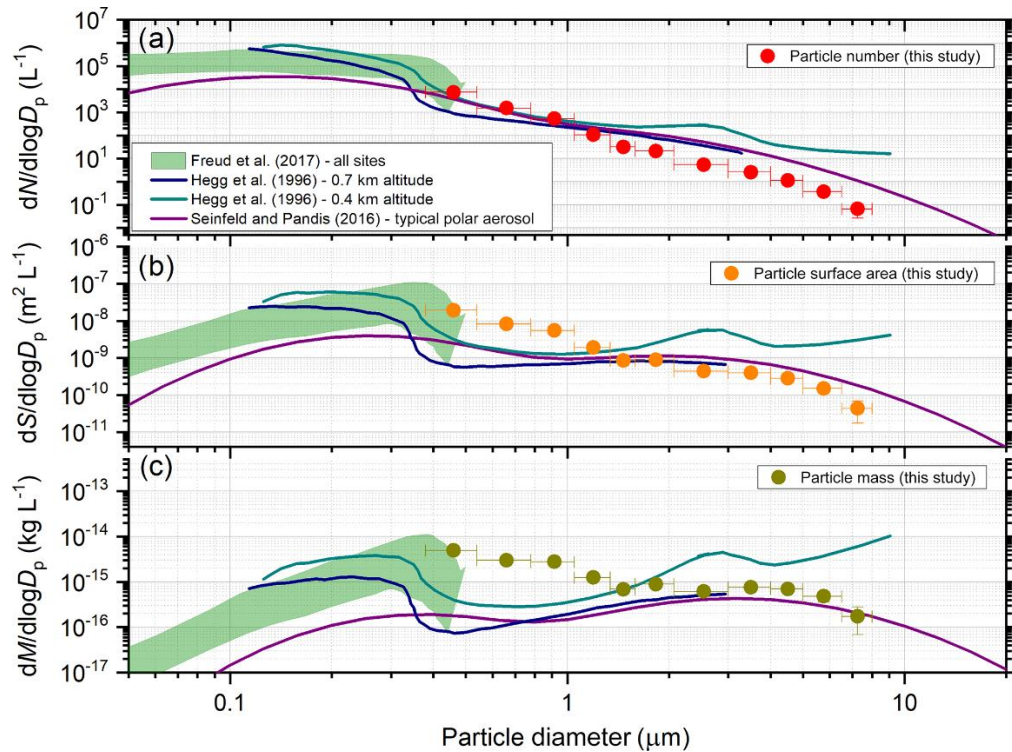
Figure 2.5-Size distribution data produced from OPC measurements.
(a) Particle number, (b) particle surface area and (c) particle mass size
distribution data above the surface temperature inversion during a test
run of the SHARK suite whilst deployed on a tethered balloon in the
High Arctic. Comparisons to previous studies at Arctic sites are shown
(Hegg et al., 1996; Seinfeld and Pandis, 2016; Freud et al., 2017). The
August aerosol number size distributions for all listed sites in Freud et
al., including Zeppelin, Nord, Alert, Barrow and Tiksi are shown. The
data from Hegg et al., at altitudes of 0.7 km and 0.4 km in Prudhoe
Bay, Alaska, are presented. The size distributions from Seinfeld and
Pandis are calculated given the parameters for multimode distributions
given in Table 8.3.

2.3.1. Meteorological and aerosol size distribution data from a SHARK flight

An example of the radiosonde and OPC data that was collected during a
SHARK flight is shown in Figure 2.4. The data was from a sampling event in
the High Arctic in the summer of 2018, during which the meteorological data
from the radiosonde and aerosol particle data from the OPC were collected
alongside impactor films for INP analysis (the INP results will be published
elsewhere). Throughout the 4.5 h flight the altitude, humidity and
temperature were closely monitored to inform decisions on sampling. The
sampling start and end times are indicated as solid lines in Figure 2.4. The

SHARK reached 450 m above Mean Sea Level (MSL) and in the last hour of flight lowered to 350 m due to ice formation on the balloon, instrument and tether. The RH during the flight was monitored to ensure the SHARK did not sample in humidity approaching saturation; the impactor and OPC manufacturers' specified thresholds for the components is 95 % RH, but we aim to only sample with the RH below this value (~80 %) in order to reduce the influence of hygroscopic growth on aerosol size. After sampling was stopped, the SHARK was brought down to ground level, resulting in the humidity rising. The ability to stop the sampling during the flight meant the impactors were covered and the pumps turned off during the descent and so did not sample the more humid environment. The ambient temperature was monitored alongside the dewpoint temperature to follow the surface inversions. The temperature inversion was used to determine where to stabilise the SHARK and begin sampling, as sampling was desired above the surface inversion for this run.

The total particle counts per 1.38 s interval from the OPC are shown in Figure 2.4d. Processing of the OPC data yielded the results shown in Figure 2.5 for the particle number ($dN/d\log D_p$), particle surface area ($dS/d\log D_p$) and particle mass ($dM/d\log D_p$) size distribution data for the sampling period, where D_p is the particle diameter. We present this data to demonstrate that the OPC produces reasonable data when used facing into wind while suspended from a balloon at altitude. Unfortunately, there is no direct comparison with other aerosol size distribution measurements at the sampling location. While the particle number concentration decreases roughly linearly with size, the surface and mass concentration curves have a mode at around 4 µm in Figure 2.5b and Figure 2.5c. This is consistent with previous studies conducted within the boundary layer in the Arctic (Hegg et al., 1996; Seinfeld and Pandis, 2016; Freud et al., 2017).

2.3.2. Deriving size-resolved INP concentrations from the SHARK samples

The ability to measure INP concentrations and properties using samples collected via the SHARK was tested by performing immersion mode droplet freezing assays on the sampled aerosols. Following a flight, impactor films were removed from both cascade impactors of the SHARK, then each

immersed in 5 mL of water and mixed on a vortex mixer for 5 min to wash the collected particles into suspension (O'Sullivan et al., 2018). This suspension was then analysed via a droplet freezing assay using the microlitre Nucleation by Immersed Particle Instrument (μL-NIPI) (Whale et al., 2015), in which 40-50 droplets of 1 μL volume were pipetted onto a hydrophobic glass slide atop a cold plate. A Perspex shield was placed over the cold stage and N$_2$ gas introduced to purge the chamber of moisture as the cold plate was cooled to −40 °C at 1 °C min^{-1}. The temperatures at which droplets froze were recorded using video analysis until the entire population had frozen. This allowed the fraction of droplets frozen as a function of temperature, $f_{ice}(T)$, to be calculated (Whale et al., 2015; O'Sullivan et al., 2018) using the equation $f_{ice}(T) = N_f / N_t$, where N_f is the number of frozen droplets at temperature T, and N_t is the total number of droplets. The INP concentration per volume of sampled air as a function of temperature, $[INP]_T$, was then calculated for each film using $f_{ice}(T)$, according to Equation 1 adapted from (Vali, 1971) to include weighting to the volume of air sampled:

$$[INP]_T = -\frac{\ln(1-f_{ice}(T))}{V_{droplet}} \cdot \frac{V_{wash}}{V_{air}}, \tag{1}$$

where $V_{droplet}$ is the droplet volume (i.e. 1 μL), V_{wash} is the amount of water into which the filter is immersed to produce the suspension for analysis (i.e. 5 mL), and V_{air} is the volume of air sampled.

2.3.3. Testing the SHARK INP concentrations against a standard aerosol sampler

In order to test whether the SHARK impactors were sampling in a representative manner, the SHARK was run concurrently with a filter-based particle sampler (BGI PQ100, Mesa Labs) and which is used as an EPA Federal Reference Method for PM$_{10}$ (designation no. RFPS-1298-124). This sampler was equipped with a PM10 head and an optional cyclone impactor which provided a size cut at 2.5 μm. Aerosol was collected onto 0.4 μm pore size Nuclepore Track-Etched Membrane polycarbonate filters at a flow rate of 16.7 L min^{-1} (i.e. 1 m^3 h^{-1}). This type of filter collects particles across the full range of available aerosol sizes, even at sizes smaller than the pore diameter, with high collection efficiencies (Soo et al., 2016; Lindsley, 2016). These polycarbonate filters have also been successfully employed in other ice nucleation field measurements (Huffman et al., 2013; McCluskey et al.,

2016; DeMott et al., 2016; Tarn et al., 2018; Harrison et al., 2018; Reicher et al., 2019). These substrates are known to have a low ice-nucleating ability and allow the collected particles to be released into suspension for subsequent INP analysis (O'Sullivan et al., 2018). The filters were analysed using the μL-NIPI in the same manner as for the impactor films collected using the SHARK. The PQ100 filter sampler was deployed alongside the SHARK in Cardington (UK) and in Hyytiälä (Finland).
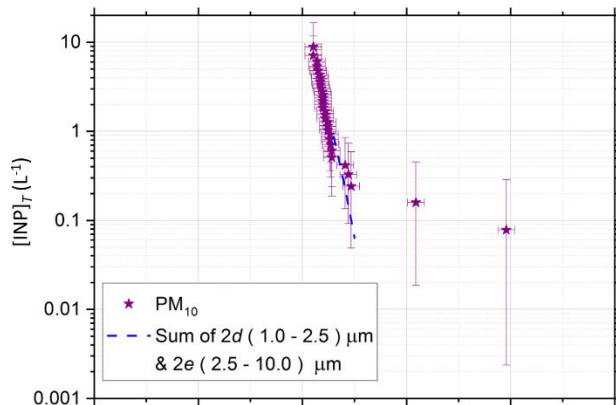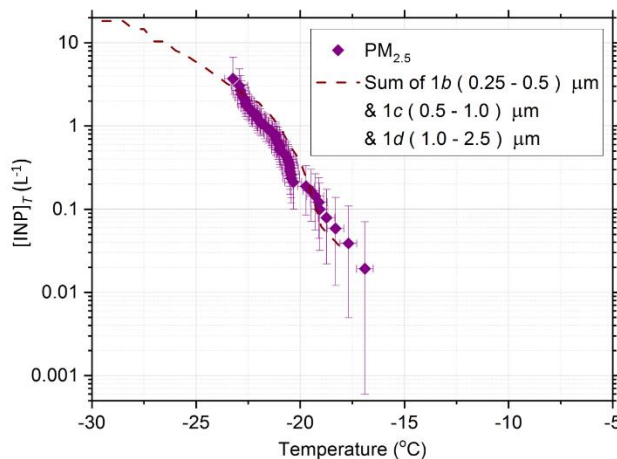
Figure 2.6-The sum of INP concentrations, [INP]T, for labelled stages measured at: (a) Cardington (UK) and (b) Hyytiälä (Finland) alongside data from a standard sampler. Cardington data was taken from Impactor 2 whilst on a tethered balloon at 20 m above ground level, and is shown against a PM10 sampler at ground level. Hyytiälä data was collected using Impactor 1 at ground level, alongside a PM2.5 sampler. The dotted lines indicate the sum of the INP concentrations for the SHARK impactor stages, calculated by weighting fice(T) to the volume of sampled air, and summing the concentrations in each temperature bin.

In order to compare the SHARK-derived, size-resolved INP data with the results of the PM$_{10}$ or PM$_{2.5}$ PQ100 filter sampler, the INP concentrations determined across the appropriate SHARK size categories were summed. In Figure 2.6a, data is presented from Cardington, where the sum of 2*d* and 2*e* from SHARK is compared with the filter sampler fitted with a PM$_{10}$ head (Impactor 1 was not available during this test). The SHARK was suspended from a tethered balloon roughly 20 m from the ground, whereas the filter sampler was on the ground (inlet ~150 cm above the surface), where both samplers were within the well-mixed boundary layer. The agreement is very good apart from two highest temperature points from the filter sampler, but note that the Poisson uncertainties on these points are substantial and also that the two samplers were separated vertically by 20 m.

We then show data from Hyytiälä in Figure 2.6b where we compare the INP spectrum from the filter sampler, with a PM$_{2.5}$ cut-off installed, with the sum of stages 1*b*, 1*c* and 1*d* (the after-filter, stage 1*a* was not used on Impactor 1 in this case). Here, both samplers were positioned within a few metres above the ground. Again, the agreement between the SHARK and the filter sampler was very good. For both Cardington and Hyytiälä, the smallest particles (<0.25 μm) were not sampled using the SHARK, but the agreement between the filter sampler and the SHARK implies that, in these cases, the smallest particles made a minor contribution to the overall INP population, which is what we would generally anticipate from the literature (Berezinski et al., 1988; Welti et al., 2009; Santachiara et al., 2010; Huffman et al., 2013; Mason et al., 2016; Si et al., 2018). The consistency between the SHARK and the filter sampler indicates that there are no major losses of aerosol in the SHARK sampler, at least relative to the PQ100 filter sampler.
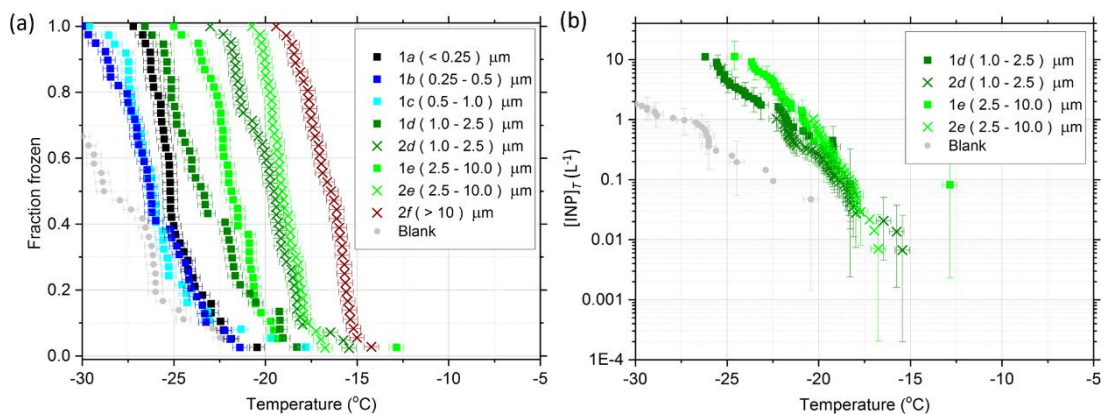
Figure 2.7- Ice-nucleating particle (INP) analysis of samples collected in Leeds (UK) using the SHARK. (a) The fraction of droplets frozen as a function of temperature, fice(T), for each stage of Impactors 1 and 2. The handling blank is shown in grey. (b) The INP concentrations for stage 'e' of both impactors (2.5-10 µm), highlighting their excellent agreement.

2.3.4. Consistency of INP concentrations between SHARK impactors

An example of data from the size-resolved collection and analysis of INPs is shown in Figure 2.7, from a sampling run performed in Leeds (UK). The f_{ice} (T) curves for each impactor stage are illustrated in Figure 2.7a. As discussed in section 2.2.2, there are two stages, d and e, which have similar size cuts on both stages. Using stage e as an example, it can be seen that while the fraction frozen curves for the two samplers are shifted by about 3 °C (Figure 2.7a), normalising to the volume of air sampled to yield $[INP]_T$ in Figure 2.7b shows that the INP spectra derived from stages 1e and 2e are consistent with one another. Stage 2e covers a lower range of INP concentrations than stage 1e by about 1 order of magnitude, because the flow rate through this impactor was more than a factor of 11.1 (100 L min^{-1}/ 9 L min^{-1}) higher and the probability of collecting rarer INP was increased by this factor. The agreement between the two impactors indicates that aerosol was collected with no significant losses/enhancements due to factors like particle bounce or wind observed. Based on the inlet particle loss calculations in Figure 2.3, higher losses may have been expected in impactor stage 1e, but these are not apparent here.
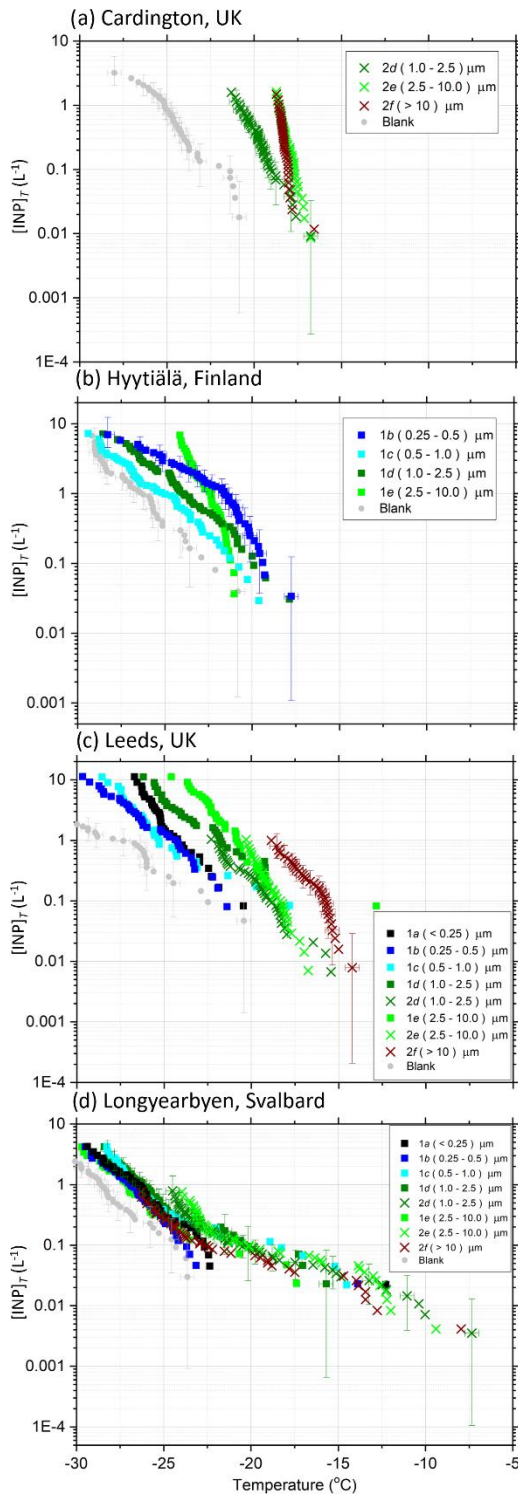
Figure 2.8-INP concentrations determined from each impactor stage of the SHARK at the four testing sites: (a) Cardington (UK), (b) Hyytiälä (Finland), (c) Leeds (UK) and (d) Longyearbyen (Svalbard). Handling blank data, which determine the baseline of the results, are shown in grey. Samples of the error bars are shown.
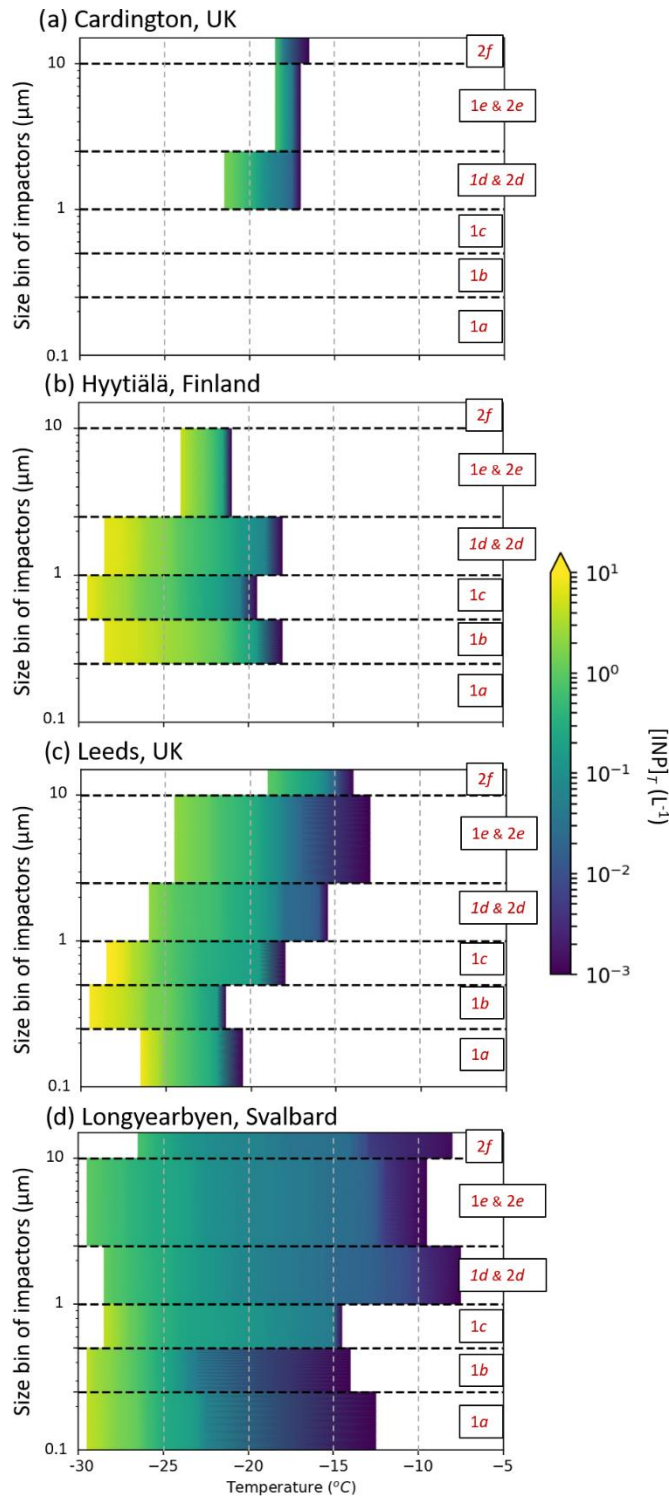
Figure 2.9-Size-resolved ice-nucleating particle concentrations (sr[INP]T) for the four test sites: (a) Cardington (UK), (b) Hyytiälä (Finland), (c) Leeds (UK) and (d) Longyearbyen (Svalbard). The colour bars indicate the INP concentration. The dotted lines on the y-axis indicate the size cuts of the impactors. The data from Figure 2.8 is presented here in an alternative format, which has the advantage of more clearly and concisely displaying the features of the INP spectrum in each size bin than the plots in Fig 2.8.

2.3.5. Size-resolved ice-nucleating particle (srINP) spectra at four locations

The derived size-resolved INP (srINP) concentrations for all four test sites are shown in Figure 2.8 and Figure 2.9. The $f_{ice}(T)$ curves for these test sites can be found in Figures A1 to A4 of the SI. Figure 2.8 shows the INP concentration spectra in the classic form, wherein INP concentrations are plotted against temperature for each size bin, whereas Figure 2.9 shows the same data in novel srINP plots to allow more intuitive comparison of the INP concentration contribution from each stage with respect to temperature. In Figure 2.9, where there were measurements from two impactors for the same stage (e.g. *d* and *e*), the INP concentrations were merged by taking an average at temperature intervals of 0.5 °C (also for Figure 2.6). The colour gradient in Figure 2.9 represents the temperature dependant concentration for each size bin and the overall steepness of the $d[INP]_T/dT$ curve. The steepness of the INP spectra can be useful in discriminating between different INP species. On inspection of Figure 2.8 and Figure 2.9, it can be seen that the spectra in the four locations have very different characteristics. Not only does the general shape of the spectra vary, but the size-dependence is also very different in the four locations. Due to the sample size, these variations could be attributed to the different aerosol population in each location, the time of year and meteorology, which could affect the INP concentrations and spectra (Kanji et al., 2017; Wex et al., 2019; Tobo et al., 2019; Šantl-Temkiv et al., 2019). We now discuss the size-resolved INP concentration spectra from these tests, bearing in mind that these four tests were one-offs and should not be regarded as characteristic of those sampling sites, but rather illustrative of the importance of making size-resolved measurements.

The first site testing of a prototype of the SHARK in which all of the components were installed was conducted in Cardington (UK) on the 15th of May 2018, but only Impactor 2 was used (see Figure 2.6a and Figure 2.8a). The Cardington site is an airfield, with large areas of grassy land near a main road, and the sampling was conducted during spring. In order to demonstrate the utility of the SHARK to make balloon-borne INP measurements whilst providing a comparison with a commercial ground-based sampler, the SHARK was sampling whilst suspended from a tethered balloon, flying roughly 20 m above the ground. The INP spectra (Figure 2.8a

and 9a) in this location are steep, increasing two orders of magnitude within 2.5 °C, and are centred around −18 to −20 °C; the $[INP]_T$ for 2*f* and 2*e* increases by an order of magnitude in just ~1 °C. The INPs in this location were dominated by particles greater than 2.5 µm, whereas particles between 1-2.5 µm made a smaller contribution and show a shallower d$[INP]_T$/d*T*, seen in Figure 2.9a as a larger spread of data. We speculate that the coarse mode INPs at this site were of biological origin, such as fungal material, pollen or bacteria with a steep INP spectrum (Kanji et al., 2017). Some fertile and agricultural soil samples have also been shown to be very active (Tobo et al., 2014; O'Sullivan et al., 2015; Hill et al., 2016; Steinke et al., 2016), and a mechanism for emissions of soil material into the atmosphere has been proposed (Wang et al., 2016). However, the steep portion of the INP spectrum for fertile soils tends to be at temperatures above ~-10°C, warmer than observed in the Cardington sample. The steepness of the curve and the temperature are consistent with ice nucleation by pollen (Pummer et al., 2012; O'Sullivan et al., 2015; Tarn et al., 2018). Although the size of whole pollen grains are often larger than 10 µm, pollen is known to release nanoscale materials that nucleate ice, which might be internally mixed with aerosol in this size bin.

In Hyytiälä (Finland), a field site in the boreal forest, the INP spectra contrast quite strongly with those in Cardington (see Figure 2.6b and Figure 2.8b). Sampling took place on the 11th of March 2018, when the Hyytiälä site was snow-covered and sampling was performed at the surface (inlet ~150 cm above surface). In this case only Impactor 1 was used without the after-filter installed. The complex nature of the size-dependence of INP is clear here. Intriguingly, in this location, the INP concentration was greatest for the smallest stage used (1*b*; 0.25-0.5 µm), and accounted for the majority of the INPs between −17 and −22 °C. The fewest INP came from the next smallest stage 1*c* (0.5-1 µm), while at temperatures below −23 °C, stage 1*e* contained the majority of the INPs. These results indicate that the INP spectra are complex, and that concentrations of INPs do not always increase with increasing size as might be expected. Huffman et al. (2013) reported INP concentration measurements in a forest ecosystem, where the particles between 1.8 and 5.6 µm enhanced during rain. Hence, as in the present study, Huffman et al. (2013) showed that INP activity does not always increase with size. The highest INP concentrations in Hyytiälä were

measured for aerosol sizes of 0.25-0.5 µm, and we note that these accumulation mode INPs would have lifetimes of many days to weeks in the atmosphere and could therefore be transported to locations and altitudes where they may influence clouds. Clearly, this would be an interesting location for more measurements with the full SHARK payload to gain further information on the long term INP concentration variations and the aerosol sizes responsible for them.

The testing in Leeds (UK) used both impactors at ground level with the SHARK suspended from a frame to allow orientation into wind. The Leeds sampling was conducted within the University of Leeds campus on a patch of grass on the 7th of June 2018 in close proximity to the School of Earth and Environment. In this test the full suite was deployed, including the impactors, after-filter and OPC. The particle number, surface and mass size distribution data for this test can be found in Figures A5 to A7 of the SI. It can be seen in Figure 2.8c that generally, the larger bins contained more active INP. The only exception to this occurred with the after-filter (< 0.25 µm), which had slightly higher INP concentrations below about −25 °C than the next two size bins (0.25-1.0 µm). As with the measurements in Hyytiälä, clearly more measurements illuminating the contribution of the smaller particles in similar environments would be beneficial since the atmospheric lifetime of these fine particles is relatively long. We note that a substantial proportion of INPs quantified just outside of Leeds in a previous study were heat-sensitive and therefore most likely of biological origin (O'Sullivan et al. 2018). In the future, conducting heat tests, as well as using Mass Spectrometry, SEM and DNA analysis with the size-resolved INP samples may help to identify the INP types in the various size fractions and highlight any differences between size ranges.

The final test was in Longyearbyen (Svalbard) from the 7th deck of the icebreaker Oden, 25 m above the surface, when moored ~200 m from the shore, overnight from the 23rd to the 24th of September 2018. The full SHARK payload was used in this case, with the OPC, both impactors and the after-filter on Impactor 1. The particle number, surface and mass size distribution data for this test can be found in Figures A8 to A10 of the SI. The INP spectra in this location, shown in Figure 2.8d was quite distinct from the

other three locations in that all size fractions contributed similarly to the INP population and there is a very shallow slope of $d\ln[\text{INP}]_T/dT$ (Figure 2.9d). We detected INPs at temperatures of up to -10 °C with concentrations of around 0.01 INP L^{-1}. These high-temperature INP concentrations are consistent with the summertime measurements reported at other Arctic locations, including Ny-Ålesund (Svalbard) (Wex et al., 2019). The INP in this region potentially originate from a range of sources. Tobo et al. (2019) recently reported that dust and biological material from glacial valleys in Svalbard may be an important source of INPs in the region. We also note that we sampled while the Oden was moored in the port of Longyearbyen where local pollution sources may have been significant (Zhao et al., 2019).

2.3.6. Ice-active surface site density, $n_s(T)$, and the activated fraction, $n_n(T)$

The addition of size distribution information to the INP concentration spectra allowed the calculation of the number of active sites per unit surface area, $n_s(T)$, and the activated fraction, $n_n(T)$, of the size-resolved samples. These quantities are determined by weighting the srINP concentrations to the total surface area and the aerosol number in each size bin, respectively, as shown in Equations 2 and 3.

$$n_s(T) = -\frac{\ln\left(1 - f_{\text{ice}}(T)\right)}{A_s}, \tag{2}$$

where A_s is the total surface area of the particles per droplet in a μL-NIPI droplet freezing assay. This was calculated for each impactor size range, using data from the relevant size bins of the OPC data.

$$n_n(T) = -\frac{\ln\left(1 - f_{\text{ice}}(T)\right)}{N}, \tag{3}$$

where N is the total number of particles sampled by the impactor in each size bin, calculated using the number concentration in each size category as measured by the OPC, and the volume of air sampled by the impactor. The size bins from the OPC which have been included in the calculations were matched to those in the impactors. The bin boundaries for the OPC calculations were within tens of nanometres of the impactor bin boundaries.

Calculating the $n_s(T)$ and $n_n(T)$ values from the INP data was only possible for some of the size ranges due to the sampling ranges of the

instrumentation employed. The smallest particle diameter measured by the OPC is 0.38 μm, i.e. above the lower limit of impactor stage 1*b*, while the largest impactor stage, 2*f* (>10 μm) has no defined upper bound. Therefore, the three bins (i.e. impactor stages) that were used to produce $n_s(T)$ and $n_n(T)$ were *c* (0.5-1.0 μm), *d* (1.0-2.5 μm) and *e* (2.5-10 μm). The $n_s(T)$ and $n_n(T)$ data were calculated for the field tests in Leeds and Longyearbyen; data from Cardington and Hyytiälä is not provided as the OPC was not in use at these sites.
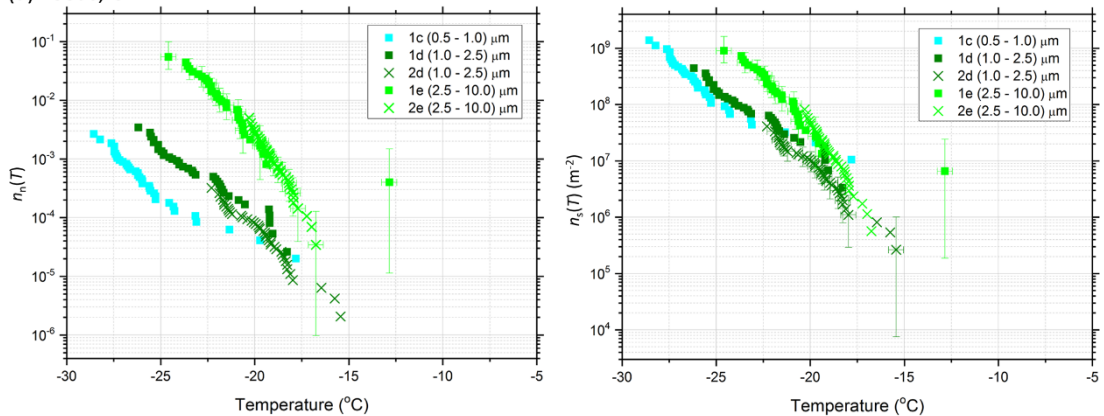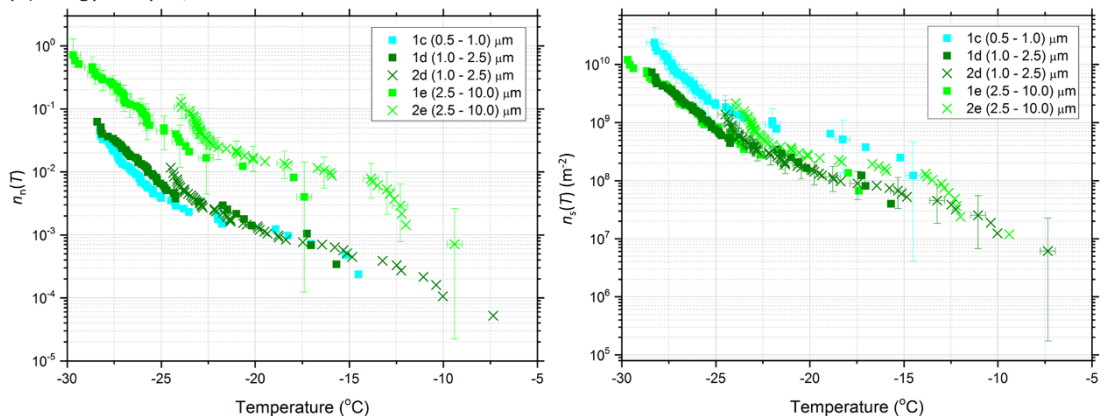
Figure 2.10-Plots showing (left) the activated fraction of aerosol (nn(T)) and (right) the number of active sites per surface area (ns(T)) for samples tested from two measurement sites: (a) Leeds (UK) and (b) Longyearbyen (Svalbard). The colours of the data points indicate the size bins of each impactor, and the different symbols represent the two impactors. Samples of the error bars are shown.

The plots of activated fraction shown in Figure 2.10 are addressed first. For the Leeds sample, there is a difference in the $n_n(T)$ values between bins *c* to *e* (Figure 2.10a), where the smallest bin is 1-3 orders of magnitude lower than the largest bin, with the middle bin in the centre of the two. In

Longyearbyen (Figure 2.10b), the $n_n(T)$ for bin e is about a factor of 10 larger than bin c, but bins c and d produce very similar values of $n_n(T)$. Overall, these $n_n(T)$ plots show that the coarse mode aerosol generally have a higher fraction of aerosol that serve as INPs than the fine mode, but there is variability in the dependence on size between the two samples. In contrast to the $n_n(T)$ values, the size resolved $n_s(T)$ data for both Leeds and Longyearbyen show that the data from the three size categories are all within a factor of 2-10 (close to our uncertainty estimates). Given the activity of aerosol across these bins scales with surface area, this data might indicate the same INP species is active across each bin at these sites.

2.4.   Conclusions

This paper describes a lightweight and portable payload, the SHARK, that is capable of collecting size-resolved aerosol particles alongside measurements of ambient temperature, relative humidity, pressure, GPS coordinates, aerosol number distribution and aerosol size distribution. The 9 kg payload was designed for use on a tethered balloon for measurements at user-selected altitudes for up to 11 h via radio controlled instrumentation, but can be used wherever it can be suspended. During a SHARK flight, the atmospheric conditions the SHARK experiences can be monitored in real-time via a radiosonde and sampling is controlled remotely, allowing the SHARK to be held at a user-defined height and to only sample under specific conditions (for instance above the surface boundary layer).

The SHARK samples aerosol onto filter/film substrates using two cascade impactors to allow aerosol size-segregation from 0.25 to 10 µm, with an after-filter and top stage to collect particles below and above this range. One impactor samples at 9 L min^{-1}, while the other samples at 100 L min^{-1}. The filters were collected here for the off-line analysis of INP concentrations and properties, but they could equally be used for other analyses such as mass spectrometry, DNA analysis, SEM, TEM and ion chromatography. A comparison of ambient INP concentrations measured using the SHARK to those measured using PM$_{10}$ and PM$_{2.5}$ aerosol samplers at ground level demonstrated excellent agreement between the instruments. Field testing was conducted in four locations close to ground level, and suspended on a tethered balloon at 20 m to demonstrate the capabilities of the SHARK.

The size resolved INP concentration spectra reveal complex behaviour. For example, in Hyytiälä the 0.25-0.5 μm aerosol size fraction had the most active INP, whereas in Leeds the INP concentration generally decreased with decreasing particle size. Ambient aerosol size distribution measured using the on-board OPC allowed the calculation of the activated fraction ($n_n(T)$) and ice-active surface site density ($n_s(T)$) data for the sampled INPs in the tests at Leeds and Longyearbyen. It was shown that $n_s(T)$ was consistent between 0.5 and 10 μm in these two locations at the times of sampling. It is the intention to make similar measurements in other locations, and at higher altitudes in the future.

Generally, it is expected that larger aerosol are more likely to nucleate ice (Pruppacher, H.R. and Klett, 1997) and our results are consistent with other size resolved INP measurements which indicate that the size distribution of INP varies spatially and temporarily e.g. (Mason et al., 2016; Si et al., 2018). Quantifying the size of INP, possibly in conjunction with other analytical techniques, is a useful means of identifying different INP types and their sources (Huffman et al., 2013). In addition, knowledge of their size will allow the improved representation of INP in global aerosol models where size is key determinant of lifetime and transport (Atkinson et al., 2013; Perlwitz et al., 2015; Vergara-Temprado et al., 2017). Clearly, more systematic and widespread measurements of INP size is needed in the future in a range of target locations.

The high sample flow rate, choice of low contamination aerosol collection substrates and long sampling durations mean that the payload is well suited for INP measurements, including those in low aerosol environments and locations with relatively low INP concentrations (down to below ~0.01 INP L^{-1} and at temperatures down to about −25 °C and below). The SHARK is an accessible tool for quantifying size-resolved atmospheric INP concentrations from a tethered balloon. This will allow improved determination of INP sizes, properties, and sources, towards ultimately improving model representations of atmospheric INP distributions.

Data availability

The data sets for this paper are available at https://doi.org/10.5518/744.

References

Armstrong, J.A., Russell, P.A., Sparks, L.E. and Drehmel, D.C. 1981. Tethered Balloon Sampling Systems for Monitoring Air Pollution. *Journal of the Air Pollution Control Association*. **31**(7), pp.735–743.

Atkinson, J.D., Murray, B.J., Woodhouse, M.T., Whale, T.F., Baustian, K.J., Carslaw, K.S., Dobbie, S., O'Sullivan, D., Malkin, T.L., O 'sullivan, D. and Malkin, T.L. 2013. The importance of feldspar for ice nucleation by mineral dust in mixed-phase clouds. *Nature*. **498**(7454), pp.355–8.

Ault, A.P. and Axson, J.L. 2017. Atmospheric Aerosol Chemistry: Spectroscopic and Microscopic Advances. *Analytical Chemistry*. **89**(1), pp.430–452.

Balsley, B.B., Jensen, M.L. and Frehlich, R.G. 1998. The use of state-of-the-art kites for profiling the lower atmosphere. *Boundary-Layer Meteorology*. **87**(1), pp.1–25.

Berezinski, N.A., Stepanov, G. V. and Khorguani, V.G. 1988. Ice-forming activity of atmospheric aerosol particles of different sizes. *Atmospheric Aerosols and Nucleation*. **309**, pp.709–712.

Cheng, Y.-S. and Yeh, H.-C. 1979. Particle bounce in cascade impactors. *Environmental Science & Technology*. **13**(11), pp.1392–1396.

Conen, F., Rodríguez, S., Hülin, C., Henne, S., Herrmann, E., Bukowiecki, N., Alewell, C., Rodri´guez, S., Rodri´guez, R., Hu¨glin, C. and Hu¨glin, H. 2015. Atmospheric ice nuclei at the high-altitude observatory Jungfraujoch. *Chemical and Physical Meteorology*. **67**(1).

Creamean, J.M., Kirpes, R.M., Pratt, K.A., Spada, N.J., Maahn, M., De Boer, G., Schnell, R.C. and China, S. 2018. Marine and terrestrial influences on ice nucleating particles during continuous springtime measurements in an Arctic oilfield location. *Atmospheric Chemistry and Physics*. **18**(24), pp.18023–18042.

Creamean, J.M., Primm, K., Tolbert, M.A., Hall, E.G., Wendell, J., Jordan, A., Sheridan, P.J., Smith, J. and Schnell, R.C. 2018. HOVERCAT: A novel aerial system for evaluation of aerosol-cloud interactions. *Atmospheric Measurement Techniques*. **11**(7), pp.3969–3985.

DeMott, P.J., Hill, T.C.J., McCluskey, C.S., Prather, K.A., Collins, D.B., Sullivan, R.C., Ruppel, M.J., Mason, R.H., Irish, V.E., Lee, T., Hwang, C.Y., Rhee, T.S., Snider, J.R., McMeeking, G.R., Dhaniyala, S., Lewis, E.R., Wentzell, J.J.B., Abbatt, J., Lee, C., Sultana, C.M., Ault, A.P., Axson, J.L., Diaz Martinez, M., Venero, I., Santos-Figueroa, G., Stokes, M.D., Deane, G.B., Mayol-Bracero, O.L., Grassian, V.H., Bertram, T.H.,

Bertram, A.K., Moffett, B.F. and Franc, G.D. 2016. Sea spray aerosol as a unique source of ice nucleating particles. *Proceedings of the National Academy of Sciences.* **113**(21), pp.5797–5803.

DeMott, P.J., Hill, T.C.J.J., Petters, M.D., Bertram, A.K., Tobo, Y., Mason, R.H., Suski, K.J., McCluskey, C.S., Levin, E.J.T.T., Schill, G.P., Boose, Y., Rauker, A.M., Miller, A.J., Zaragoza, J., Rocci, K., Rothfuss, N.E., Taylor, H.P., Hader, J.D., Chou, C., Huffman, J.A., Pöschl, U., Prenni, A.J. and Kreidenweis, S.M. 2017. Comparative measurements of ambient atmospheric concentrations of ice nucleating particles using multiple immersion freezing methods and a continuous flow diffusion chamber. *Atmos. Chem. Phys.* **17**(18), pp.11227–11245.

DeMott, P.J., Prenni, A.J., Liu, X., Kreidenweis, S.M., Petters, M.D., Twohy, C.H., Richardson, M.S., Eidhammer, T. and Rogers, D.C. 2010. Predicting global atmospheric ice nuclei distributions and their impacts on climate. *Proceedings of the National Academy of Sciences.* **107**(25), pp.11217–11222.

DeMott, P.J., Prenni, A.J., McMeeking, G.R., Sullivan, R.C., Petters, M.D., Tobo, Y., Niemand, M., Möhler, O., Snider, J.R., Wang, Z. and Kreidenweis, S.M. 2015. Integrating laboratory and field data to quantify the immersion freezing ice nucleation activity of mineral dust particles. *Atmospheric Chemistry and Physics.* **15**(1), pp.393–409.

Deng, X., Xue, H. and Meng, Z. 2018. The effect of ice nuclei on a deep convective cloud in South China. *Atmospheric Research.* **206**, pp.1–12.

Dzubay, T.G., Hines, L.E. and Stevens, R.K. 1976. Particle bounce errors in cascade impactors. *Atmospheric Environment (1967).* **10**(3), pp.229–234.

Freud, E., Krejci, R., Tunved, P., Leaitch, R., Nguyen, Q.T., Massling, A., Skov, H. and Barrie, L. 2017. Pan-Arctic aerosol number size distributions: Seasonality and transport patterns. *Atmospheric Chemistry and Physics.* **17**(13), pp.8101–8128.

Garcia, E., Hill, T.C.J., Prenni, A.J., DeMott, P.J., Franc, G.D. and Kreidenweis, S.M. 2012. Biogenic ice nuclei in boundary layer air over two U.S. high plains agricultural regions. *Journal of Geophysical Research Atmospheres.* **117**(17), p.D18.

Hara, K., Osada, K. and Yamanouchi, T. 2013. Tethered balloon-borne aerosol measurements: Seasonal and vertical variations of aerosol constituents over Syowa Station, Antarctica. *Atmospheric Chemistry and Physics.* **13**(17), pp.9119–9139.

Harrison, A.D., Whale, T.F., Rutledge, R., Lamb, S., Tarn, M.D., Porter, G.C.E., Adams, M.P., McQuaid, J.B., Morris, G.J. and Murray, B.J. 2018. An instrument for quantifying heterogeneous ice nucleation in multiwell plates using infrared emissions to detect freezing. *Atmospheric Measurement Techniques.* **11**(10), pp.5629–5641.

Hegg, D.A., Hobbs, P. V, Gassó, S., Nance, J.D. and Rangno, A.L. 1996. Aerosol measurements in the Arctic relevant to direct and indirect

radiative forcing. *Journal of Geophysical Research: Atmospheres.* **101**(D18), pp.23349–23363.

Herbert, R.J., Murray, B.J., Dobbie, S.J. and Koop, T. 2015. Sensitivity of liquid clouds to homogenous freezing parameterizations. *Geophys. Res. Lett.* **42**(5), pp.1599–1605.

Hill, T.C.J., Demott, P.J., Tobo, Y., Fröhlich-Nowoisky, J., Moffett, B.F., Franc, G.D. and Kreidenweis, S.M. 2016. Sources of organic ice nucleating particles in soils. *Atmospheric Chemistry and Physics.* **16**(11), pp.7195–7211.

Huffman, J.A., Prenni, A.J., Demott, P.J., Pöhlker, C., Mason, R.H., Robinson, N.H., Fröhlich-Nowoisky, J., Tobo, Y., Després, V.R., Garcia, E., Gochis, D.J., Harris, E., Müller-Germann, I., Ruzene, C., Schmer, B., Sinha, B., Day, D.A., Andreae, M.O., Jimenez, J.L., Gallagher, M., Kreidenweis, S.M., Bertram, A.K. and Pöschl, U. 2013. High concentrations of biological aerosol particles and ice nuclei during and after rain. *Atmospheric Chemistry and Physics.* **13**(13), pp.6151–6164.

Jacob, J.D., Chilson, P.B., Houston, A.L. and Smith, S.W. 2018. Considerations for atmospheric measurements with small unmanned aircraft systems. *Atmosphere.* **9**(7), p.252.

Jaenicke, R. 2007. *Aerosol Physics and Chemistry. In: Landolt-Börnstein Numerical Data and Functional Relationships in Science and Technology New Series Group V: Geophysics and Space Research Volume 4 Meteorology Subvolume b, Physical and Chemical Properties of the Air* (G. Fischer, ed.).

Kanitz, T., Seifert, P., Ansmann, A., Engelmann, R., Althausen, D., Casiccia, C. and Rohwer, E.G. 2011. Contrasting the impact of aerosols at northern and southern midlatitudes on heterogeneous ice formation. *Geophysical Research Letters.* **38**(17), n/a-n/a.

Kanji, Z.A., Ladino, L.A., Wex, H., Boose, Y., Burkert-Kohn, M., Cziczo, D.J. and Krämer, M. 2017. Overview of Ice Nucleating Particles. *Meteorological Monographs.* **58**, 1.1-1.33.

Lacher, L., Steinbacher, M., Bukowiecki, N., Herrmann, E., Zipori, A. and Kanji, Z.A. 2018. Impact of air mass conditions and aerosol properties on ice nucleating particle concentrations at the High Altitude Research Station Jungfraujoch. *Atmosphere.* **9**(9), p.363.

Laskin, J., Laskin, A. and Nizkorodov, S.A. 2018. Mass Spectrometry Analysis in Atmospheric Chemistry. *Analytical Chemistry.* **90**(1), pp.166–189.

Lindsley, W.G. 2016. Filter Pore Size and Aerosol Sample Collection *In*: P. F. O'Connor, ed. *NIOSH Manual of Analytical Methods (NMAM), 5th Edition* [Online]. Department of Health and Human Services, Centers for Disease Control and Prevention, National Institute for Occupational Safety and Health, pp.1–14. [Accessed 30 July 2018]. Available from: https://www.cdc.gov/niosh/docs/2014-151/pdfs/chapters/chapter-fp.pdf.

Lohmann, U. 2017. Anthropogenic Aerosol Influences on Mixed-Phase Clouds. *Current Climate Change Reports*. **3**(1), pp.32–44.

Marple, V.A., Rubow, K.L. and Behm, S.M. 1991. A microorifice uniform deposit impactor (moudi): Description, calibration, and use. *Aerosol Science and Technology*. **14**(4), pp.434–436.

Mason, R.H., Si, M., Chou, C., Irish, V.E., Dickie, R., Elizondo, P., Wong, R., Brintnell, M., Elsasser, M., Lassar, W.M., Pierce, K.M., Leaitch, W.R., MacDonald, A.M., Platt, A., Toom-Sauntry, D., Sarda-Estève, R., Schiller, C.L., Suski, K.J., Hill, T.C.J., Abbatt, J.P.D., Huffman, J.A., DeMott, P.J. and Bertram, A.K. 2016. Size-resolved measurements of ice-nucleating particles at six locations in North America and one in Europe. *Atmospheric Chemistry and Physics*. **16**(3), pp.1637–1651.

McCluskey, C.S., Hill, T.C.J., Malfatti, F., Sultana, C.M., Lee, C., Santander, M. V, Beall, C.M., Moore, K.A., Cornwell, G.C., Collins, D.B., Prather, K.A., Jayarathne, T., Stone, E.A., Azam, F., Kreidenweis, S.M. and DeMott, P.J. 2016. A dynamic link between ice nucleating particles released in nascent sea spray aerosol and oceanic biological activity during two mesocosm experiments. *Journal of the Atmospheric Sciences*., JAS-D-16-0087.1.

Misra, C., Singh, M., Shen, S., Sioutas, C. and Hall, P.M. 2002. Development and evaluation of a personal cascade impactor sampler (PCIS). *Aerosol Science*. **33**(7), pp.1027–1047.

Murray, B.J. 2017. Cracking the problem of ice nucleation. *Science*. **355**(6323), pp.346–347.

Murray, B.J., O'sullivan, D., Atkinson, J.D. and Webb, M.E. 2012. Ice nucleation by particles immersed in supercooled cloud droplets. *Chemical Society Reviews*. **41**(19), pp.6519–6554.

O'Sullivan, D., Adams, M.P.P., Tarn, M.D.D., Harrison, A.D.D., Vergara-Temprado, J., Porter, G.C.E.C.E., Holden, M.A.A., Sanchez-Marroquin, A., Carotenuto, F., Whale, T.F.F., McQuaid, J.B.B., Walshaw, R., Hedges, D.H.P.H.P., Burke, I.T.T., Cui, Z. and Murray, B.J.J. 2018. Contributions of biogenic material to the atmospheric ice-nucleating particle population in North Western Europe. *Scientific Reports*. **8**(1), p.13821.

O'Sullivan, D., Murray, B.J., Ross, J.F., Whale, T.F., Price, H.C., Atkinson, J.D., Umo, N.S. and Webb, M.E. 2015. The relevance of nanoscale biological fragments for ice nucleation in clouds. *Scientific Reports*. **5**(1), p.8082.

Perlwitz, J.P., Pérez García-Pando, C. and Miller, R.L. 2015. Predicting the mineral composition of dust aerosols - Part 1: Representing key processes. *Atmospheric Chemistry and Physics*. **15**(20), pp.11593–11627.

Price, H.C., Baustian, K.J., McQuaid, J.B., Blyth, A., Bower, K.N., Choularton, T., Cotton, R.J., Cui, Z., Field, P.R., Gallagher, M., Hawker, R., Merrington, A., Miltenberger, A., Neely, R.R., Parker, S.T.,

Rosenberg, P.D., Taylor, J.W., Trembath, J., Vergara-Temprado, J., Whale, T.F., Wilson, T.W., Young, G. and Murray, B.J. 2018. Atmospheric Ice-Nucleating Particles in the Dusty Tropical Atlantic. *Journal of Geophysical Research: Atmospheres*. **123**(4), pp.2175–2193.

Product Information Sheet - MSP n.d. Models 128,129,130 and 131—High Flow Impactors (HFI). [Accessed 3 October 2019]. Available from: http://www.mspcorp.com/resources/msp-pi-130-revb-us-high-flow-impactors-hfi-128-129-130-131.pdf.

Pruppacher, H.R. and Klett, J.D. 1997. *Microphysics of Clouds and Precipitation* 2nd Editio. Dordrecht: Kluwer Academic Publishers.

Pummer, B.G., Bauer, H., Bernardi, J., Bleicher, S. and Grothe, H. 2012. Suspendable macromolecules are responsible for ice nucleation activity of birch and conifer pollen. *Atmos. Chem. Phys.* **12**(5), pp.2541–2550.

Rader, D.J. and Marple, V.A. 1985. Effect of Ultra-Stokesian Drag and Particle Interception on Impaction Characteristics. *Aerosol Science and Technology*. **4**(2), pp.141–156.

Reagan, J.A., Apte, M. V., Bruhns, T. V. and Youngbluth, O. 1984. Lidar and Balloon-Borne Cascade Impactor Measurements of Aerosols: A Case Study. *Aerosol Science and Technology*. **3**(3), pp.259–275.

Reicher, N., Budke, C., Eickhoff, L., Raveh-Rubin, S., Kaplan-Ashiri, I., Koop, T. and Rudich, Y. 2019. Size-dependent ice nucleation by airborne particles during dust events in the Eastern Mediterranean. *Atmospheric Chemistry and Physics Discussions*., pp.1–26.

Reicher, N., Segev, L. and Rudich, Y. 2018. The Welzmann Supercooled Droplets Observation on a Microarray (WISDOM) and application for ambient dust. *Atmospheric Measurement Techniques*. **11**(1), pp.233–248.

Rogers, D.C., Demott, P.J. and Kreidenweis, S.M. 2001. Airborne measurements of tropospheric ice-nucleating aerosol particles in the Arctic spring. *Journal of Geophysical Research*. **106**(D14), pp.15053–15063.

Rosenfeld, D., Yu, X., Liu, G., Xu, X., Zhu, Y., Yue, Z., Dai, J., Dong, Z., Dong, Y. and Peng, Y. 2011. Glaciation temperatures of convective clouds ingesting desert dust, air pollution and smoke from forest fires. *Geophysical Research Letters*. **38**(21), n/a-n/a.

Santachiara, G., Di Matteo, L., Prodi, F. and Belosi, F. 2010. Atmospheric particles acting as Ice Forming Nuclei in different size ranges. *Atmospheric Research*. **96**(2–3), pp.266–272.

Šantl-Temkiv, T., Lange, R., Beddows, D., Rauter, U., Pilgaard, S., Dall'osto, M., Gunde-Cimerman, N., Massling, A. and Wex, H. 2019. Biogenic Sources of Ice Nucleating Particles at the High Arctic Site Villum Research Station. *Environmental Science and Technology*. **53**(18), pp.10580–10590.

Seinfeld, J.H. and Pandis, S.N. 2016. Atmospheric chemistry and physics :

from air pollution to climate change.

Si, M., Irish, V.E., Mason, R.H., Vergara-Temprado, J., Hanna, S.J., Ladino, L.A., Yakobi-Hancock, J.D., Schiller, C.L., Wentzell, J.J.B., Abbatt, J.P.D., Carslaw, K.S., Murray, B.J. and Bertram, A.K. 2018. Ice-nucleating ability of aerosol particles and possible sources at three coastal marine sites. *Atmospheric Chemistry and Physics.* **18**(21), pp.15669–15685.

SKC n.d. Leland Legacy Sample Pump: Operating Instructions. . (Form 40075 Rev 1910). [Accessed 25 February 2020]. Available from: https://www.skcinc.com/catalog/pdf/instructions/40075.pdf.

Soo, J.-C.C., Monaghan, K., Lee, T., Kashon, M. and Harper, M. 2016. Air sampling filtration media: Collection efficiency for respirable size-selective sampling. *Aerosol Science and Technology.* **50**(1), pp.76–87.

Steinke, I., Funk, R., Busse, J., Iturri, A., Kirchen, S., Leue, M., Möhler, O., Schwartz, T., Schnaiter, M., Sierau, B., Toprak, E., Ullrich, R., Ulrich, A., Hoose, C. and Leisner, T. 2016. Ice nucleation activity of agricultural soil dust aerosols from Mongolia, Argentina, and Germany. *Journal of Geophysical Research: Atmospheres.* **121**(22), pp.559–576.

Storelvmo, T. 2017. Aerosol Effects on Climate via Mixed-Phase and Ice Clouds. *Annual Review of Earth and Planetary Sciences.* **45**(1), pp.199–222.

Tarn, M.D., Sikora, S.N.F., Porter, G.C.E., O'Sullivan, D., Adams, M., Whale, T.F., Harrison, A.D., Vergara-Temprado, J., Wilson, T.W., Shim, J. uk and Murray, B.J. 2018. The study of atmospheric ice-nucleating particles via microfluidically generated droplets. *Microfluid. Nanofluid.* **22**(5), p.52.

Tobo, Y., Adachi, K., DeMott, P.J., Hill, T.C.J., Hamilton, D.S., Mahowald, N.M., Nagatsuka, N., Ohata, S., Uetake, J., Kondo, Y. and Koike, M. 2019. Glacially sourced dust as a potentially significant source of ice nucleating particles. *Nature Geoscience.* **12**(4), pp.253–258.

Tobo, Y., DeMott, P.J., Hill, T.C.J., Prenni, A.J., Swoboda-Colberg, N.G., Franc, G.D. and Kreidenweis, S.M. 2014. Organic matter matters for ice nuclei of agricultural soil origin. *Atmospheric Chemistry and Physics.* **14**(16), pp.8521–8531.

Tobo, Y., Prenni, A.J., Demott, P.J., Huffman, J.A., McCluskey, C.S., Tian, G., Pöhlker, C., Pöschl, U. and Kreidenweis, S.M. 2013. Biological aerosol particles as a key determinant of ice nuclei populations in a forest ecosystem. *Journal of Geophysical Research Atmospheres.* **118**(17), pp.10100–10110.

Vali, G. 1971. Quantitative Evaluation of Experimental Results an the Heterogeneous Freezing Nucleation of Supercooled Liquids. *Journal of the Atmospheric Sciences.* **28**(3), pp.402–409.

Vergara-Temprado, J., Miltenberger, A.K., Furtado, K., Grosvenor, D.P., Shipway, B.J., Hill, A.A., Wilkinson, J.M., Field, P.R., Murray, B.J. and

Carslaw, K.S. 2018. Strong control of Southern Ocean cloud reflectivity by ice-nucleating particles. *Proc. Natl. Acad. Sci. U. S. A.* **115**(11), pp.2687–2692.

Vergara-Temprado, J., Murray, B.J., Wilson, T.W., O'Sullivan, D., Browse, J., Pringle, K.J., Ardon-Dryer, K., Bertram, A.K., Burrows, S.M., Ceburnis, D., Demott, P.J., Mason, R.H., O'Dowd, C.D., Rinaldi, M. and Carslaw, K.S. 2017. Contribution of feldspar and marine organic aerosols to global ice nucleating particle concentrations. *Atmospheric Chemistry and Physics.* **17**(5), pp.3637–3658.

Villa, T., Salimi, F., Morton, K., Morawska, L. and Gonzalez, F. 2016. Development and Validation of a UAV Based System for Air Pollution Measurements. *Sensors.* **16**(12), p.2202.

Wang, B., Harder, T.H., Kelly, S.T., Piens, D.S., China, S., Kovarik, L., Keiluweit, M., Arey, B.W., Gilles, M.K. and Laskin, A. 2016. Airborne soil organic particles generated by precipitation. *Nature Geoscience.* **9**(6), pp.433–437.

Von Der Weiden, S.-L., Drewnick, F. and Borrmann, S. 2009. Particle Loss Calculator – a new software tool for the assessment of the performance of aerosol inlet systems. *Atmos. Meas. Tech.* **2**, pp.479–494.

Welti, A., Lüönd, F., Stetzer, O. and Lohmann, U. 2009. Influence of particle size on the ice nucleating ability of mineral dusts. *Atmospheric Chemistry and Physics.* **9**(18), pp.6705–6715.

Wex, H., Huang, L., Zhang, W., Hung, H., Traversi, R., Becagli, S., Sheesley, R.J., Moffett, C.E., Barrett, T.E., Bossi, R., Skov, H., Hünerbein, A., Lubitz, J., Löffler, M., Linke, O., Hartmann, M., Herenz, P. and Stratmann, F. 2019. Annual variability of ice-nucleating particle concentrations at different Arctic locations. *Atmospheric Chemistry and Physics.* **19**(7), pp.5293–5311.

Whale, T.F., Murray, B.J., O'Sullivan, D., Wilson, T.W., Umo, N.S., Baustian, K.J., Atkinson, J.D., Workneh, D.A. and Morris, G.J. 2015. A technique for quantifying heterogeneous ice nucleation in microlitre supercooled water droplets. *Atmospheric Measurement Techniques.* **8**(6), pp.2437–2447.

Zhao, B., Wang, Y., Gu, Y., Liou, K.-N., Jiang, J.H., Fan, J., Liu, X., Huang, L. and Yung, Y.L. 2019. Ice nucleation by aerosols from anthropogenic pollution. *Nature Geoscience.* **12**(8), pp.602–607.

3. Origin and variability of ice-nucleating particles close to the summertime North Pole

Grace C. E. Porter[1,2], Michael P. Adams[1], Ian M. Brooks[1], Luisa Ickes[3], Linn Karlsson[4,6], Caroline Leck[4,5], Matthew E. Salter[4,6], Julia Schmale[7,8], Karolina Siegel[5,6,4], Sebastien N. F. Sikora[1], Mark D. Tarn[1,2], Jutta Vüllers[1], Heini Wernl[i9], Paul Zieger[4,6], Julika Zinke[4,6], Benjamin J. Murray[1]

[1]School of Earth and Environment, University of Leeds, Leeds, UK
[2]School of Physics and Astronomy, University of Leeds, Leeds, UK
[3]Department of Space, Earth and Environment, Chalmers, Gothenburg, Sweden
[4]Bolin Centre for Climate Research, Stockholm University, Stockholm, Sweden
[5]Department of Meteorology, Stockholm University, Stockholm, Sweden
[6]Department of Environmental Science, Stockholm University, Stockholm, Sweden
[7]School of Architecture, Civil and Environmental Engineering, École Polytechnique fédérale de Lausanne, Switzerland
[8]Laboratory of Atmospheric Chemistry, Paul Scherrer Institute, Villigen, Switzerland
[9]Institute for Atmospheric and Climate Science, ETH Zürich, Zürich, Switzerland

Abstract. Mixed-phase clouds over the central Arctic Ocean are intricately linked to the Arctic climate and sea ice extent. The lifetime and radiative properties of these clouds are critically dependent on the partitioning between ice and supercooled water, but the sources and concentration of aerosol particles that nucleate ice are poorly defined (Morrison et al., 2011; Murray et al., 2021). Here, we show that ice-nucleating particle (INP) concentrations close to the North Pole (88 – 90°N) throughout August and September 2018 were extremely variable, with the temperature in which 0.1 INP L^{-1} were active ranging from –9 to -31°C. Back trajectory analysis (7 days) shows that air with the most active INPs originated in the seas north of Russia, whereas air with the least active INPs circulated over the pack ice for most of the duration of the back trajectory. This suggests that there were strong coastal marine sources of INPs, possibly associated with wind-driven sea spray production or dust from various islands and the coast of Russia, whereas the pack ice, open leads, and the marginal ice zone were much weaker sources. Heat testing of samples revealed that the INPs originating from the coast of Northern Russia were most likely of proteinaceous, biological origin. Our measurements, in combination with boundary layer inversion temperatures, imply that INP concentrations active at cloud temperatures were usually less than 0.02 INP L^{-1} throughout the campaign, which is consistent with the persistence of Arctic mixed-phase clouds (Stevens et al., 2018). However, if the high concentrations we observed early in the campaign happened to coincide with a lower temperature period, we would anticipate in excess of 1 INP L^{-1}, which would result in a substantial reduction in liquid water path with implications for Arctic surface

energy budget (Tan and Storelvmo, 2019). These findings suggest that Arctic cloud ice production, and therefore Arctic climate, might be sensitive to transport from latitudes that are experiencing marked climate change.

The Arctic is warming twice as fast as the global average (Mcbean et al., 2005; Cohen et al., 2014) and low-level Arctic clouds strongly influence the surface energy budget (Kay and L'Ecuyer, 2013). Low level mixed-phase clouds in the Arctic are frequent and persistent, exerting a significant long wave warming effect at the surface; the amount of ice and supercooled water in these clouds, and therefore their radiative effect, depends on an intricate balance of dynamical and microphysical processes (Morrison et al., 2012). However, the representation of Arctic clouds and their climate feedbacks pose a large source of uncertainty in projections of Arctic climate and sea ice loss (Boucher et al., 2013; Tan and Storelvmo, 2019).

A rare subset of the total aerosol particle population, ice-nucleating particles (INPs), can induce primary ice production in Arctic mixed-phased clouds when immersed in supercooled cloud droplets (Murray et al., 2012). In the summertime Arctic marine boundary layer, temperatures are usually much warmer than those required for homogeneous freezing of below about –33 °C (Herbert et al., 2015), hence heterogeneous nucleation on INPs determines the production of ice in clouds (at least in the absence of ice precipitating from overlying clouds). There are numerous identified INP types that can induce nucleation over a large range of temperatures (Hoose and Möhler, 2012; Murray et al., 2012; Kanji et al., 2017; Murray et al., 2021). However, the sources and ice-nucleating properties of INPs in the Arctic, especially the high Arctic, are poorly defined.

INP measurements have been made around the periphery of the Arctic circle from locations close to, or on, land (see compilations in refs (Welti et al., 2020; Murray et al., 2021)), but relatively few measurements have been made in the summertime central Arctic Ocean. Recent research suggests that there are significant terrestrial sources of Arctic INPs including glacial dust from Svalbard and Iceland (Tobo et al., 2019; Sanchez-Marroquin et al., 2020) terrestrial biological aerosol from boreal forests (Schneider et al., 2021), and even particles released from thawing permafrost (Jessie M Creamean et al., 2020).There is also a plethora of other high latitude dust sources that have not been investigated in terms of their ice-nucleating

ability (Bullard et al., 2016). Marine biogenic INPs emitted from the sea surface through bubble bursting are also thought to contribute to the INP population of the oceanic high-latitudes (Bigg, 1996; Bigg and Leck, 2001; Wilson et al., 2015; Vergara-Temprado et al., 2017; Irish et al., 2017; Wex et al., 2019; Ickes et al., 2020; Hartmann et al., 2020). Sea spray is thought to produce relatively low INP concentrations, but in the absence of other INP types it can dominate (DeMott et al., 2016; Vergara-Temprado et al., 2017; McCluskey et al., 2019).

Ground level observations at several land-based sites around the Arctic throughout the seasonal cycle showed the highest (but variable) INP concentrations during spring, summer and autumn and the lowest concentrations in winter, when local sources are likely covered in snow and ice (Wex et al., 2019). The literature suggests that there are marine and terrestrial INP sources which are sensitive to ice and snow cover around the Arctic, but it is unclear how important these sources are for clouds in the summertime central Arctic. Based on back trajectory analysis of INP measurements made in the central Arctic, Bigg (1996) suggested that there was an open ocean source of INPs active at –15 °C. Bigg and Leck (2001) suggested the pack ice edge and bubble bursting in local leads throughout the pack ice can serve as a source of INPs. Indeed, it has been shown that there is a reservoir of INPs in the seas around the Arctic (Wilson et al., 2015; Irish et al., 2017) and INP concentrations in the central Arctic decrease during the transition from Arctic summer to autumn, possibly due to the reduced availability of ice-free marine sources (Bigg and Leck, 2001).

While it is clear that there are strong sources of INPs in the low Arctic environment it is not clear if these INP are transported to the central Arctic. The current prevailing view is that aerosol within the summertime high Arctic boundary layer (often a shallow, well-mixed surface layer capped by a temperature inversion (Tjernström et al., 2012)) is thought to experience little effect from long-range transport (Kupiszewski et al., 2013), and with few sources of pollution in the central Arctic ocean (north of 80° in latitude), it has been suggested that local marine sources such as open leads may provide an important source of INPs (Bigg and Leck, 2001). However, it has also been suggested that aerosol particles can be entrained into the boundary layer by turbulence or via interaction with clouds (Morrison et al., 2012; Igel et al., 2017). While the boundary layer in the central Arctic is typically several 100m to over 1km deep, it is often decoupled from the

surface, with a turbulent surface mixed layer and cloud mixed layer separated by a weakly stable non-turbulent layer at ~100-300m (Brooks et al., 2017), as shown in Figure 3.1. Hence, measurements at the surface are not necessarily representative of those in the cloud mixed layer. Aerosol particles can also be advected into the central Arctic boundary layer through horizontal transport, but cloud formation and subsequent precipitation efficiently removes aerosol particles, especially during the Arctic summer (Matsui et al., 2011).
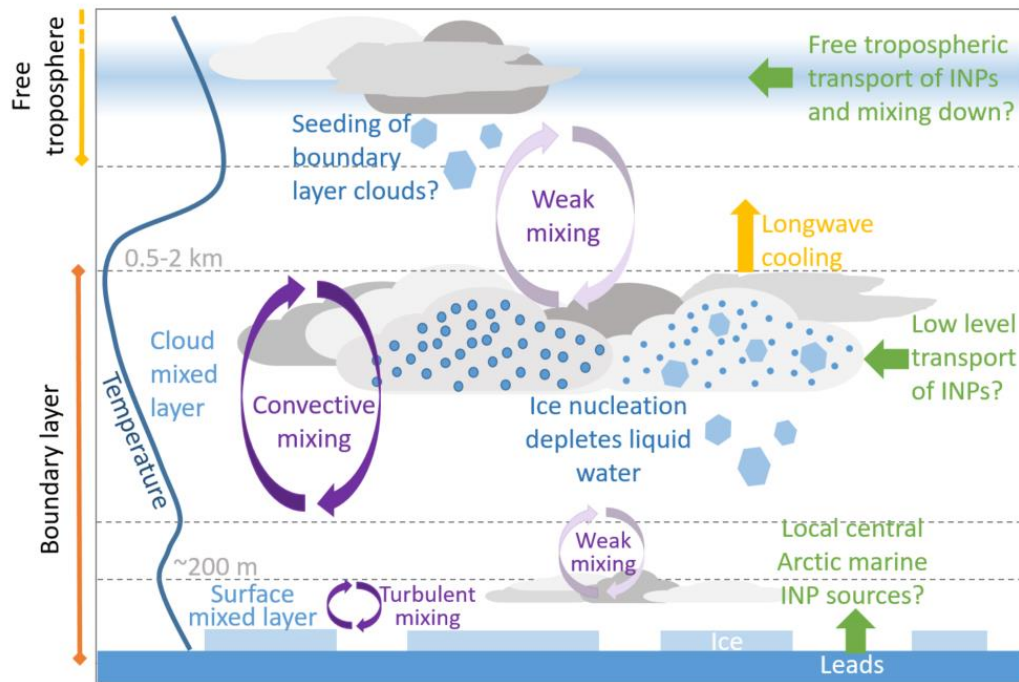
Figure 3.1 Central Arctic boundary layer structure and potential sources of INPs.

Here, we present temperature-resolved measurements of INP concentrations in the central Arctic during the Microbiology-Ocean-Cloud-Coupling in the High Arctic (MOCCHA) campaign which took place throughout August and September 2018. The campaign was part of the US-Swedish Arctic Ocean 2018 expedition on board the Swedish icebreaker *Oden*. The bulk of the measurements took place while *Oden* was moored to an ice floe in the inner pack ice area and drifted passively near the North Pole (88-90°N). We use backward trajectories alongside other measurements to suggest that the largest source of the most active INPs reaching the North Pole is outside of the pack ice, and near the coast of Russia.

3.1. Ice-nucleating particle concentrations in the surface mixed layer

Aerosol was sampled via a heated whole air inlet, 20 m above sea level, onto filters which were then analysed a matter of hours (or at most 1 day) later to derive INP concentration spectra (INP concentration as a function of temperature) using the Nucleation by Immersed Particle Instrument (see Methodology for details) (Whale et al., 2015). The concentration of INPs measured on-board the *Oden* was highly variable (Figure 3.2a), with INP activation temperatures ranging from -9 to -30 °C for a concentration of 0.1 INP L^{-1}, and concentrations varying from 6×10^{-3} INP L^{-1} to 2 INP L^{-1} at -15 °C. Placing the results from this cruise in context with other Arctic INP measurements, which are mostly from the periphery of the Arctic (Figure 3.2b), shows that the measured temperature range of active INPs is almost as large as from the combined literature. In particular, the variability in our INP spectra from August and September 2018 are comparable to those reported in the year-round measurements at coastal stations reported by Wex et al.(2019). In particular, it is striking that the lowest ice-nucleation activity we report is consistent with the wintertime measurements reported by Wex et al., but their summertime and autumn INP concentrations were typically high unlike our measurements in the central Arctic. This is consistent with the sources of INP in the central Arctic being weak, relative to sources in the lower latitude terrestrial or coastal Arctic regions. It is also consistent with the suggestion of Wex et al. that INP sources are weakened with ice and snow cover. Our results for the North Pole contrast strongly with measurements of INP over the Southern Ocean, where INP concentrations are typically at the low end of the range we observed here (McCluskey et al., 2018; Welti et al., 2020; Murray et al., 2021). Overall, our INP measurements indicate that the INP concentration spectra within the high Arctic surface mixed boundary layer can be extremely variable, perhaps far more variable than anywhere else on Earth. We revisit this issue later in the paper when we discuss our back trajectory analysis.

The nature of the INPs in the samples which exhibited the highest activity was examined by heating them. We tested for the presence of heat-sensitive material, which is an indication of proteinaceous biological ice-nucleating material (Christner, Morris, et al., 2008; Christner, Cai, et al., 2008; Wilson et al., 2015; Hill et al., 2016; O'Sullivan et al., 2018). The activity of samples that underwent the heat treatment was always reduced, with all of the

activity above -20 °C being removed (Figure 3.2a and Figure B1). Hence, it appears that the most active INP sampled close to the North Pole were most likely of biological origin.
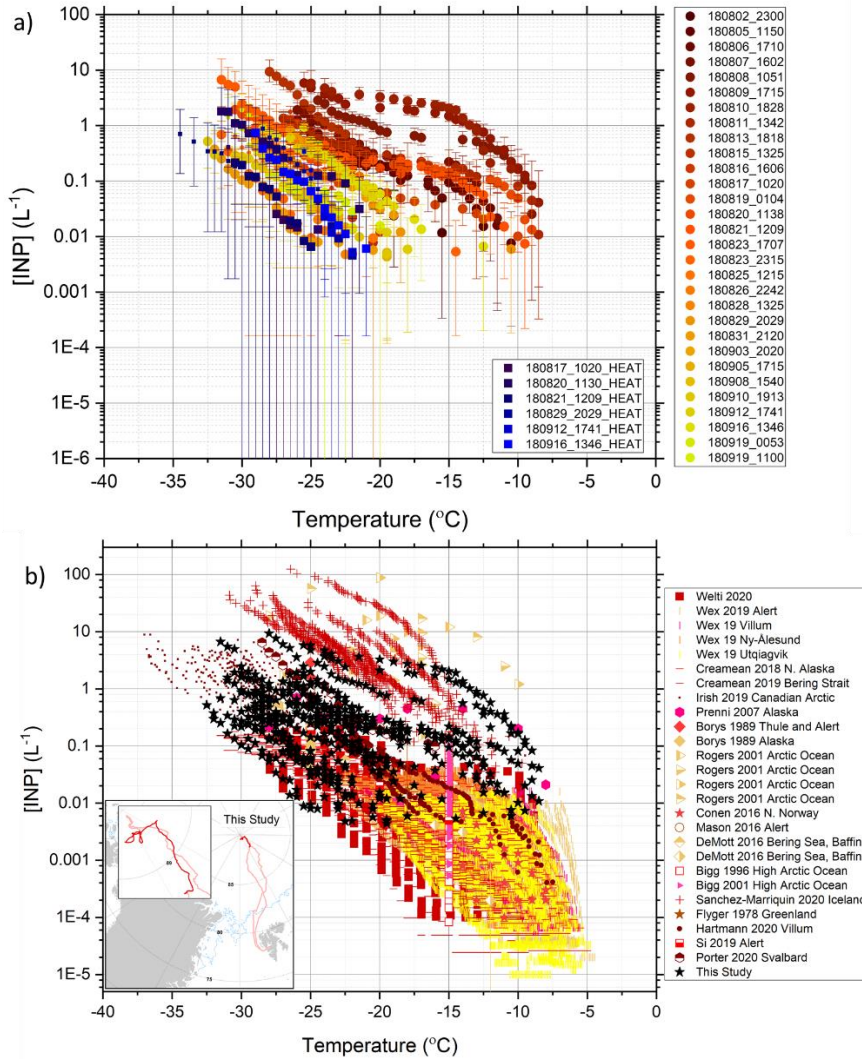
Figure 3.2 - INP concentrations throughout the campaign. a) The
number of INPs per litre of air sampled was calculated using data from
off-line droplet freezing experiments, conducted within hours of the
samples being taken. The spectra shown in blues represent samples
that were heated to 90 °C for 30 min. The INP data from this study has
had the backgrounds subtracted as described in the methods.
Sampling times varied from 6 h to 3 days and were taken using a
heated whole air inlet on the 4th deck (20-25 m above sea-level) of the
Oden Icebreaker. Temperature uncertainties (not shown) for the droplet
freezing experiments were estimated to be ±0.4 °C. The dates
(DD/MM/YY) for the respective periods are: MIZ 02/08/18-03/08/18,
Clean-air station 10/08/18-11/08/18, Ice-breaking 03/08/18-16/08/18,
Ice floe 16/08/18-15/09/18, Ice-breaking 15/09/18-19/09/18, MIZ
19/09/18. b) The data from this study are presented alongside literature
data for ground, ship, and aircraft-based campaigns around the central
Arctic Ocean. The insert presents the ship track during the campaign,
with the dark red line denoting the drift whilst the ship was moored to
an ice floe.
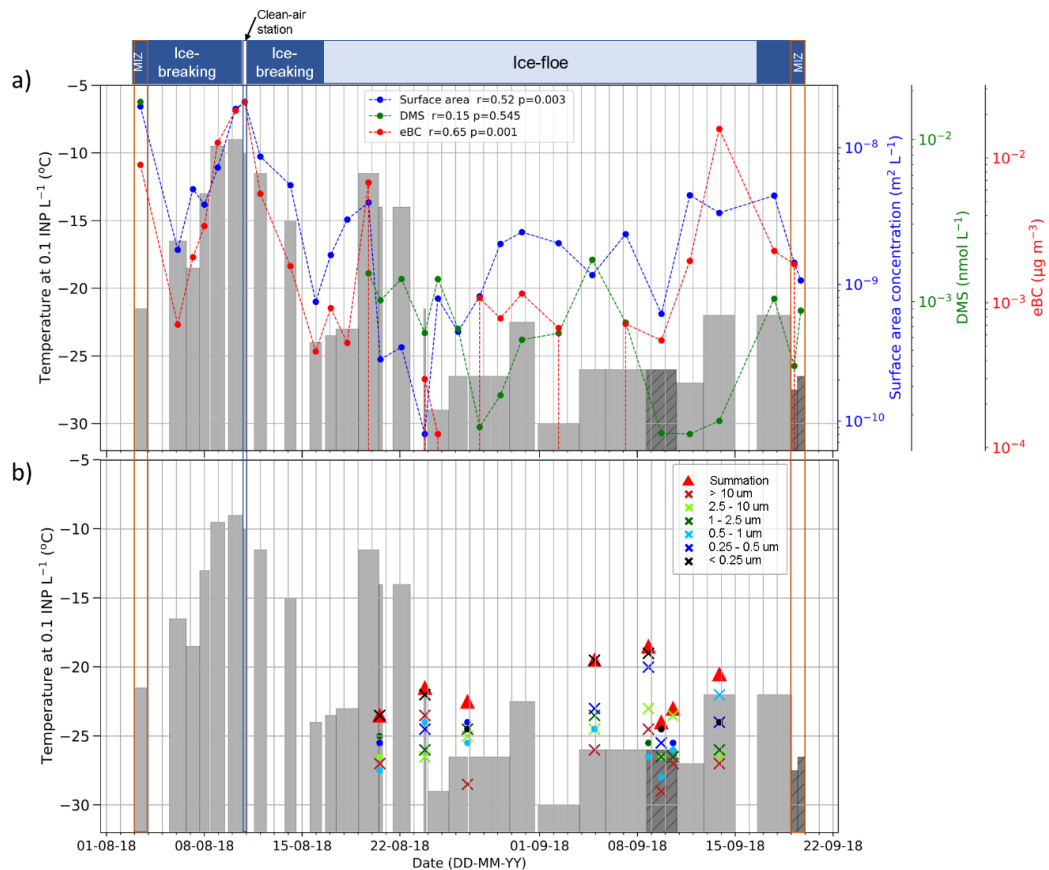
Figure 3.3 - Time series showing the temperature at which a concentration of 0.1 INP L-1 was measured throughout the campaign, a) alongside aerosol composition data and b) alongside airborne measurements. The tops of the grey bars represent the temperature of freezing for INPs at a concentration of 0.1 INP L-1, with the width of the bar representing the period over which air was sampled. The hatched grey bars are limiting values. a) The blue, green and red dots represent the average surface area of aerosol per litre, the dimethyl sulfide (DMS) concentration and the equivalent black carbon (eBC) concentrations measured in the aerosol, respectively. b) The crosses represent the temperature of freezing at 0.1 INP L-1 for different size cur-offs of aerosol, which are colour-coded with respect to the aerosol size range, and where the circle points represent limiting values for that size range. The red triangles represent a summation of these stages to give an estimate of the total INP population over all size ranges sampled during the flight. The dates for the respective periods are: MIZ 02/08/18-03/08/18, Clean-air station 10/08/18-11/08/18, Ice-breaking 03/08/18-16/08/18, Ice floe 16/08/18-15/09/18, Ice-breaking 15/09/18-19/09/18, MIZ 19/09/18. All INP data has been background subtracted as described in the methods.

The time series in Figure 3.3 shows the temperature at which a concentration of 0.1 INP L^{-1} was measured, ($T_{[INP]=0.1}$), and highlights the variability of INP concentrations at the North Pole in August and September of 2018. The highest ice-nucleating activity was observed earlier in the campaign, during a period in which the ship was breaking ice prior to being moored to an ice floe. It is reasonable to question whether the very high INP concentrations observed during the ice-breaking period resulted from the ice-breaking itself. During ice-breaking the ship was not always optimally pointing into the wind, and it involved frequent backward and forward motions. Hence, despite the precautions taken to eliminate sampling aerosol sourced from the ship (detailed in the methodology) it is difficult to completely exclude the possibility of contamination. In addition, breaking ice creates a degree of disruption at the sea surface which is conceivably a source of aerosol and INPs. There was also a period of very high ice-nucleating activity a few days after the ice-floe station had been established, indicating that the high INP concentrations measured during the ice-breaking period were not controlled by the act of breaking ice and the disruption of the sea surface. Fortuitously, there was also a pause in ice-breaking when a clean air station was established (12th August), which coincided with high INP and aerosol loading (these measurements are discussed in a subsequent section). At this "clean-air station" the ship was moored facing into the wind and we were confident that sampling of ship pollution and ice-breaking aerosol was eliminated, increasing confidence that these high values were indeed representative of the central Arctic Ocean.

3.2. Ice-nucleating particle concentration above the surface mixed layer

Eight flights with a balloon-borne size-resolved aerosol sampler that sampled particles up to 10 µm, the SHARK (Porter et al., 2020a), were conducted while the Oden was at the ice station (see SI for flight details). In these flights we used the live link to the on-board temperature and humidity measurements to ensure that we sampled above the surface mixed layer and thus in air decoupled from the surface but within the boundary layer. Hence, the flights occurred at 390 – 600 m throughout the campaign and we sampled for 3-6 hours. In addition, we only sampled when the RH was less than 80% to avoid sampling biases associated with hygroscopically swollen aerosol, which meant we only sampled in cloud free air.

Given the surface mixed layer is often decoupled from the rest of the boundary layer, these measurements in principle allow us to compare INP concentrations within and above the surface mixed layer. The total values of $T_{[INP]=0.1}$ are shown in Figure 3.3 (red triangles), whereas the individual INP spectra are shown in Figure B4. It should be borne in mind that for practical reasons the sampling durations on the ship and on the SHARK were not the same, however it is still possible to draw conclusions from this comparison. There is evidence that there are substantial differences between the INP concentrations in the surface mixed layer compared to above it. For example, on the 5th and 8th September the $T_{[INP]=0.1}$ was around -17 to -18°C above the surface mixed layer, whereas it was below -26°C within it. While, on the 20th August $T_{[INP]=0.1}$ was around -23°C above the surface mixed layer, but -14°C within it. In contrast, on other days, such as the 23rd August and the 10th and 15th Sept the INP concentrations within and above the surface mixed layer were similar. Overall, out of the eight SHARK samples there was one SHARK sample that had much lower ice nucleating activity than that in the surface mixed layer, three samples with higher activity, three with similar activity and one that was ambiguous (due to being close to the baseline). This indicates that the air at the surface is sometimes coupled to the surface, allowing transport of aerosol throughout the boundary layer, but at other times the measurements at the surface are not representative of those above the surface mixed layer.

The size resolved INP activity is also shown in Figure 3.3. Contrary to what might be expected, the smallest size ranges of < 0.25 µm and 0.25 – 0.5 µm particle diameter sometimes had the highest INP activity of our sampled size ranges. In most cases the coarse mode (2.5 – 10 µm) was in the baseline. The dominance of particles < 0.25 µm was particularly pronounced on the 23rd August and the 8th and 9th September. In contrast, the coarse mode dominated on the 10th September.

In many environments around the world, the coarse mode dominates the INP population, but the coarse mode has a relatively short lifetime in the Arctic boundary layer, being removed effectively by wet scavenging processes. Hence, it is perhaps not so surprising that the fine mode aerosol (<0.25 µm) appears to be so important in this region. However, INP are typically thought of as being the larger particles in a size distribution (Mason et al., 2016; Porter et al., 2020a), but there are INP that fall into this size range that are also very active. For example, film droplet aerosol resulting

from wave breaking are produced in a range of sizes centred around 100 nm and are often rich in organic material (O'Dowd et al., 2004), that is known to include small ice nucleating entities (Schnell and Vali, 1975; Wilson et al., 2015). Alternatively, ice-nucleating macromolecules from terrestrial biological sources internally mixed with other aerosol particles might fall into this size range (O'Sullivan et al., 2015; Pummer et al., 2015) and it has been proposed that fungal material, some of which is known to act as an INP (O'Sullivan et al., 2015), can fragment to form nanoparticles (Lawler et al., 2020).

3.3. Correlation between INP concentrations and dimethyl sulphide, equivalent black carbon and aerosol surface area

To investigate possible sources of INPs we detected in the central Arctic, we have correlated the ice-nucleating activity of the aerosol with: i) dimethyl sulfide (DMS), a product of marine biological activity, particularly in the marginal ice zone (MIZ); ii) equivalent black carbon (eBC), based on aerosol absorption at 637 nm; and iii) aerosol surface area, derived from size distribution measurements. We present the time series for aerosol particle surface area, DMS and eBC concentration, as well as the Pearson's r coefficient between ice-nucleation activity and each quantity in Figure 3.3a.

DMS is found in the marine atmosphere, originating from the metabolite of some marine algae (Leck and Persson, 1996; Lohmann and Leck, 2005). Hence, the presence of DMS indicates that an air mass has origins in a location rich in biological activity, which may also be expected to correlate with marine biological INP sources. DMS is thought to be relatively short-lived in the atmosphere, with a lifetime on the order of 1-3 days (Kerminen and Leck, 2001; Khan et al., 2016). Therefore, it is a useful indicator for the interaction of air masses with the MIZ at the outer edge of the pack ice region, and possibly the open leads within the pack ice if they were producing DMS at that time.

The concentration of DMS during the cruise was highest in the outbound 24 hour MIZ station, where the ship was close to open water, but was variable whilst in the pack ice (Figure 3.3), and remained relatively low in the inbound MIZ station (19th September) after the freeze-up began. The data in Figure 3.3 clearly shows that there is no obvious correlation with DMS and INP

activity ($r = 0.15$) suggesting that MIZ marine biogenic sources exerted little influence on the measured INP concentrations.

eBC is a quantity derived from aerosol absorption and is presented as the equivalent BC mass concentration which is needed to produce the observed absorption. It is worth bearing in mind that other aerosol types such as dust, brown carbon or other organic aerosol might also produce absorption, thus contaminating the small signal we observed. However, absorption by BC is much stronger than other materials at 637 nm, hence the signal is most likely dominated by BC. BC is produced through a range of combustion processes, including biomass burning, wildfires and fossil fuel combustion, which are all remote from the central Arctic (Bond et al., 2013). Other potential contributors to the absorption signal, such as dust or brown carbon are also remote from the central Arctic. Rigorous procedures were in place to ensure that BC (and other aerosol) from the ship stack did not affect measurements (see methods for details). Hence eBC is used here as an indicator of long-range transport. The literature indicates that BC is a relatively ineffective ice nucleator under mixed-phase cloud conditions (Chen et al., 2017; Vergara-Temprado et al., 2018; Adams et al., 2020; Kanji et al., 2020; Schill et al., 2020), hence we would not necessarily interpret a positive correlation as an indication of ice nucleation by BC. However, combustion processes are thought to be a source of ice-nucleating aerosol, even if BC itself is not an effective INP (Umo et al., 2015; Jahn et al., 2020; Barry et al., 2021). Hence, a correlation between BC and INP concentrations would indicate that aerosol particles transported along with BC from outside the central Arctic Ocean nucleate ice. Wildfires around the Arctic are a potential source of BC (Ding et al., 2013), and we note that during the cruise there were lasting Siberian wildfires, as can be seen using the NASA Worldview satellite imagery tool. There is also industry, shipping and mining as well as gas and oil extraction along the Arctic coast of Russia which may be sources of BC, e.g. through flaring (Stohl et al., 2013).

The overall correlation between eBC and INP concentration ($r = 0.65$) is much stronger than for DMS. In fact, the eBC concentration appears to track the INP concentration in Figure 3.3 until the 27th August, after which point the INP concentrations stay relatively low whilst the eBC remains highly variable. However, the decoupling of eBC and INPs later in the campaign indicates that distant sources of BC are not always connected to distant sources of highly active INP.

The surface area concentration of the bulk aerosol follows a similar trend to the eBC concentrations, but with a slightly weaker correlation strength to the INP activity ($r = 0.52$). As for eBC, the aerosol surface area concentration tracks the INP concentration up to the 27th August, but later on the INP concentration remains generally low while surface area is highly variable. This indicates that the variability in INP concentrations at the North Pole is not simply driven by aerosol surface area, rather that some specific component(s) of the aerosol population are ice-active and these particles must be associated with specific sources at latitudes further south than the MIZ. Therefore, using the aerosol particle size as an indicator for INP concentrations is unlikely to be suitable for the central Arctic ocean.

3.4. Trajectory analysis of aerosol collected in the central Arctic

Backward trajectories over 7 days are presented in Figure 3.4a, and show a clear relationship between the origin of the aerosol and the measured INP concentrations. The origin of the air masses with the most active INPs is around the Russian Arctic coast including the Barents, Kara and Laptev Seas. Out of the 30 filter runs, those filters with the highest INP activity (the top 20 % of filters) sampled air masses originating over the Barents and Kara Seas. The next seven highest (23 %) filters, in terms of INP activity, sampled air originating from over the Laptev and East Siberian Seas. The next six filters with lower INP activity (20 % of filters) sampled air that originated off the eastern coast of Greenland from over both the pack ice and open ocean. The 11 filters with the lowest INP activity (bottom 37 % of filters) all sampled air which mostly originated from the pack ice adjacent to North America (also see Figure B2).

The highest ice -nucleation activities from sampled aerosol originating along the Russian coast were also correlated with high wind speeds (Figure B2). This, together with the heat tests and size information presented above, point to a wind-driven marine biological source of INPs associated with organic rich film droplet sea spray aerosol. There are trajectories with high wind speeds over the North American continent, the pack ice and the coast of Greenland, but the ice-nucleating activity for these was not greatly enhanced. Hence, our results are consistent with a strong source of highly active INPs in the coastal marine waters of northern Russia which are aerosolised during windy conditions. These results are also consistent with

the eBC analysis, since those results indicated that the most active INPs were derived from sources distant to the central Arctic.
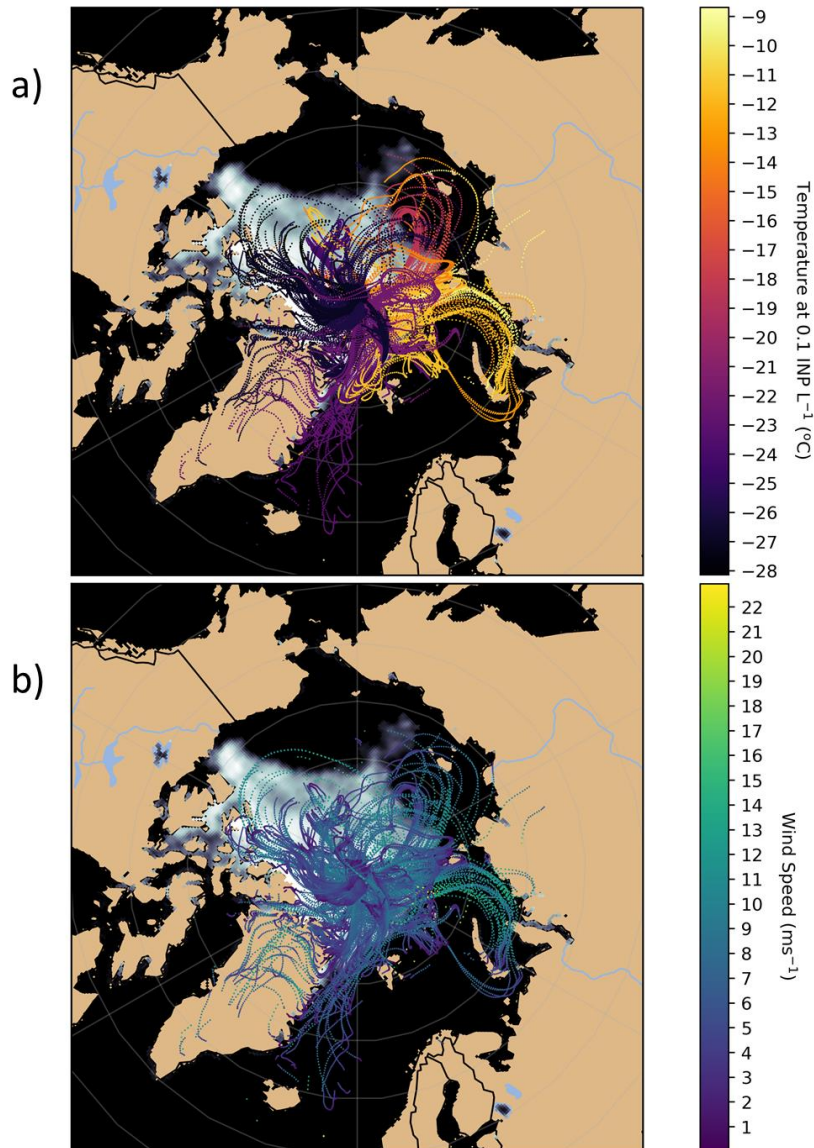
Figure 3.4 - Backward trajectories over 7 days, starting at the ship location, for the INP samples taken throughout the campaign. Trajectories were launched every hour during the sampling period, and each point represents an hour in time along the back trajectory. The starting height for the trajectories was 32 m above sea level. Any points along the trajectories which were above the model boundary layer were removed, and any points preceding precipitation events (>0.1 mm h-1) were removed. a) The colour of the trajectories represents the temperature at which 0.1 INP L-1 was measured for that sampling period. b) The colour of the trajectories represents the wind speed for each point along the trajectory.

Marine waters elsewhere in the world are thought to produce relatively low concentrations of INPs (Vergara-Temprado et al., 2017, McCluskey et al., 2018; Welti et al., 2020); however, our results suggest that the shallow seas off the Russian coast might be strong sources of highly active INPs. The marine waters off the coast of N. Russia are known to be biologically productive, which might produce marine INPs. Composition analysis also indicates that these samples were rich in Na, Cl and sulfate and were therefore likely of marine origin (See Table). This region is also increasingly influenced by riverine input from Russia that is rich in organic material and silt (Ahmed et al., 2020), and much of the dissolved organic matter in the Arctic Ocean is derived from river input (Juhls et al., 2019). Recent research has also shown that melting permafrost which could enter river outputs harbour copious quantities of warm temperature INPs (Jessie M. Creamean et al., 2020). Hence, it is possible that the highest INP concentrations we detected at the North Pole were derived from marine waters rich in terrestrially derived biological INPs, although a measurement campaign to determine the relationship between river discharge and aerosolised INP in the high Arctic would be necessary to confirm this. The INP activity of sources along the Russian coast may have important implications for the future of INP concentrations, since permafrost is expected to increasingly melt in a warmer world. The removal of ice from the Arctic could also expose sources of ice-nucleating aerosol around the Arctic Ocean, where they can be aerosolised by the action of wind (Schmale et al., 2021).

It is striking that the trajectories with the lowest INP concentrations spent most of the preceding seven days over the pack ice and to some extent over the MIZ. These results indicate that during this campaign open leads, sea ice and the MIZ were weak sources of INP.
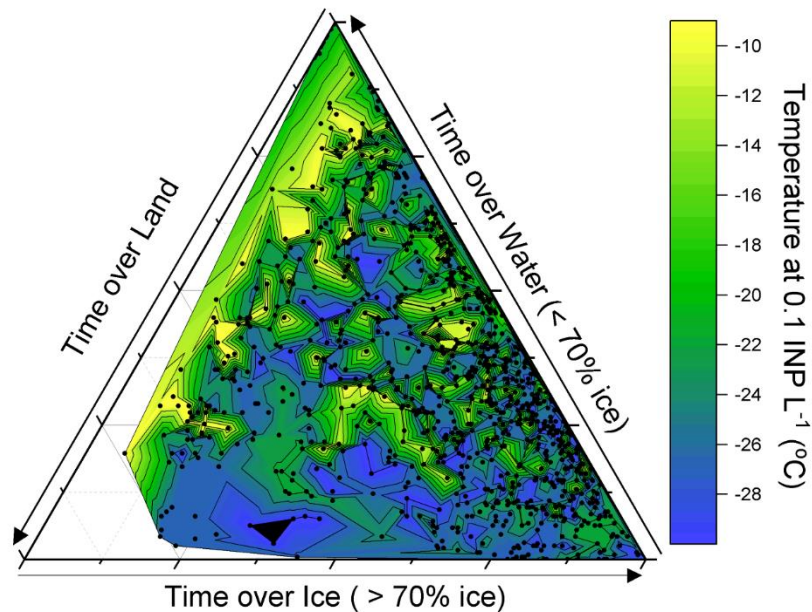
Figure 3.5 - Using back trajectory analysis, the time that air masses spent over water, ice and land is shown. The colour represents the temperature at which an INP concentration of 0.1 L-1 was reached.

Some of the back trajectories that had the highest INP concentrations passed over islands in the Barents and Kara seas, including Svalbard, Franz Josef Land, Novaya Zemlya and Severnaya Zemlya. Many of these locations have been identified as poorly defined dust sources (Bullard et al., 2016) and dust from Svalbard has been shown to contain biological ice-nucleating materials (Tobo et al., 2019). However, in a further analysis of the back trajectory data (Figure 3.5) we find that there was little to no correlation with time spent over land, whereas the ice-nucleating activity increased with time the air parcels spent over open ocean. Having said this, we cannot rule out relatively small island point sources being important sources of INP.

Overall, the evidence indicates that there is a strong source of biogenic INPs the Barents, Kara and Laptev seas off the Russian coast that can be sporadically transported to the central Arctic. There was high wind along the trajectories off the Russian coast which would be consistent with both the production of INPs in sea spray and dust from the various islands in this region.

3.5. Implications for ice production in boundary layer central Arctic mixed-phase clouds

In this section, we assess whether the measured INP concentrations are high enough to initiate a transition from liquid-dominated clouds to ice-dominated clouds. Model simulations indicate that 1 ice crystal L^{-1} or more is required to remove the bulk of liquid water from an Arctic cloud, whereas lower concentrations still reduce the liquid water path (Vergara-Temprado et al., 2018; Stevens et al., 2018).Hence, we determine the concentration of INP active within the surface and cloud mixed layers.

We refer to the INP concentration in the atmosphere that is active at the ambient temperature as $[INP]_{ambient}$. This quantity combines the atmospheric temperature with the INP spectra to indicate the effects on ice crystal formation. This is, of course, a crude analysis and a full cloud model would be required to represent ice crystal formation and sedimentation as well as INP recycling and latent heat release, but it does give an indication of what the measured INP spectra might mean for ice production in clouds. For our analysis, we must also assume that the INP measurements at ship altitude are representative of INP concentrations at the top of the boundary layer, which is not always consistent with our balloon-based measurements. Nevertheless, this analysis is a useful way of estimating the effect that the measured INP concentrations might have on clouds in the region. The minimum temperature within the main boundary layer was determined from radiosonde profiles, made every 6 hours throughout the entire cruise (Prytherch et al., 2019; Vüllers et al., 2021). The INP concentration at this temperature was determined using the INP spectra in Figure 3.2. The calculated $[INP]_{ambient}$ for the duration of the cruise are shown in Figure 3.6, where the minimum temperature of the surface and cloud mixed layers are indicated for each filter period.
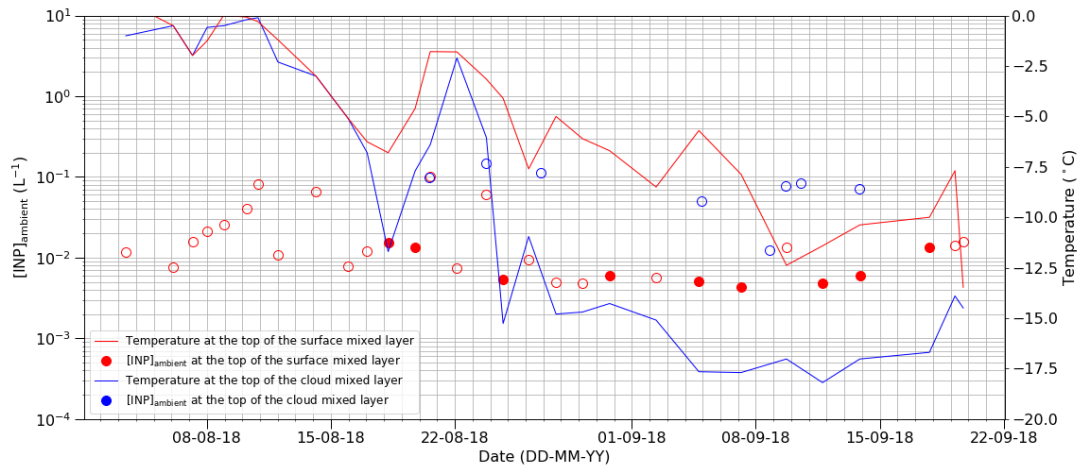
Figure 3.6 – Time series showing [INP]ambient for both the measurements taken at ship height (within the surface mixed layer) and using the SHARK (within the cloud mixed layer). The temperature of the mixed layers is shown alongside these measurements. When an INP concentration could not be determined at the mixed layer temperature, the highest measured [INP] value is shown to denote the limit of detection and is labelled as a limiting value. Limiting values are shown in open circles.

Interestingly, despite the large variability in INP concentrations within the surface mixed layer throughout the cruise, [INP]ambient is less variable, and is usually at or below ~10^{-2} L^{-1}. The periods of high INP concentration during the beginning of the campaign coincide with periods of higher ambient inversion temperatures, whereas later in the campaign the opposite is the case, which results in a relatively invariant [INP]ambient. Whether this is a coincidence, or if INP concentrations are correlated with ambient temperature, is unclear. For instance, it is possible that the efficiency with which clouds scavenge INPs at ambient temperature partially regulates the [INP]ambient, as a colder cloud may more efficiently remove INPs from the atmosphere compared to a warmer cloud. If the periods of high INP concentration were to coincide with lower temperatures in periods outside our campaign period, then we would anticipate a major impact on [INP]ambient and ice production in clouds. The [INP]ambient within the cloud mixed layer was also relatively consistent but appeared to be slightly larger than for the surface mixed layer, at ~10^{-1} L^{-1}. However, all of the values in the cloud mixed layer are limiting values and so it is likely that the true values lie below the ones shown.

The relatively low [INP]$_{ambient}$ concentrations indicate that a mixed-phase cloud would probably not fully glaciate due to primary ice production on INPs. Nevertheless, we anticipate some ice production in clouds, which would reduce the liquid water path to some extent. The phase of clouds during this campaign are discussed in Vüllers et al. (Vüllers et al., 2021). Overall, the fraction of single layer clouds (where seeding from above is unlikely) that were mixed-phase versus ice-dominated were relatively consistent throughout the campaign, despite the strong decrease in temperature; this is consistent with our constant [INP]$_{ambient}$ estimate.

3.6. Conclusions

Arctic mixed-phase and supercooled clouds play a crucial role in Arctic climate, but the processes that dictate their characteristics are poorly understood. Here, we show that INP concentrations at 88 - 90°N are extremely variable, and throughout the AO18 campaign between the 1st of August 2018 and the 18th of September 2018 the temperature at which 0.1 INP L^{-1} was reached varied between -9°C and -30 °C. The highest 20 % of observations, in terms of INP activity, related to air masses originating in the ice-free ocean environment off the Russian coast, while the lowest 37 % of observations related to air masses which originated over the pack ice north of Canada for most of the 7-day back trajectory. Trajectories of air with intermediate INP activity also originated over the ice-free ocean. These results indicate a strong dependence of the measured INP concentration on the origin of the air with pack ice, open leads and the MIZ apparently being weak sources of INP, whereas ice-free oceans were a significant source.

The heat sensitivity of the most active INPs was consistent with their being of proteinaceous, biogenic origin. This together with the trajectory analysis indicates that there are strong biogenic sources of INP in region off the Russian coast. The sources may be related to wind driven sea spray production and dust emissions from the islands in this region, but more work is needed to understand the INP sources in this part of the Arctic.

Tethered balloon flights showed that on four of the eight flights the INP concentrations were substantially different above the surface mixed layer compared to those measured at ship level within it. This is consistent with our understanding of Arctic boundary layer meteorology, where the surface

mixed layer is often decoupled from the cloud mixed layer (Brooks et al., 2017).

Calculating the concentration of particles which can activate at the ambient atmospheric temperature ($[INP]_{ambient}$) showed that, despite large variations in temperature and INP activity, the $[INP]_{ambient}$ within the surface mixed layer was roughly constant at around 10^{-2} L^{-1}, which is consistent with the persistence of Arctic mixed-phase clouds. The cloud mixed layer had a slightly larger calculated $[INP]_{ambient}$ at 10^{-1} L^{-1}, but all of the values were limiting.

Overall, it is striking that INP concentrations at the summertime North Pole vary from some of the lowest measured anywhere in the world, to as high as terrestrial locations rich in biological INPs. Since these INPs are transported from the seas off the Russian coast, they may be sensitive to changes in climate. In particular, reduced sea and land ice extent may open up more sources for more of the year around the Arctic, which may increase the future strength (and may already have done so) of the sources of INPs that are important for mixed-phase clouds in the central Arctic. More work needs to be undertaken to understand how changes in INP sources around the Arctic may influence Arctic clouds and future Arctic climate.

Methods

To determine the INP concentration spectra relevant for mixed-phase clouds in the central Arctic, 48 days of sampling were conducted aboard the Swedish icebreaker *Oden* during Arctic summertime and into the early freeze-up period. The dates for the respective periods were: MIZ 02/08/18-03/08/18, Clean-air station 10/08/18-11/08/18, Ice-breaking 03/08/18-16/08/18, Ice floe 16/08/18-15/09/18, Ice-breaking 15/09/18-19/09/18, MIZ 19/09/18. Filter samples were collected and analysed during the journey towards the North Pole from Svalbard whilst ice breaking, and whilst moored to an ice floe (the ship track is shown in Figure 3.2b, and the dates spent ice breaking and moored are shown in Figure 3.3).

Filter sampling

The filters (0.4 μm pore size, polycarbonate, Nuclepore Track-Etched Membrane Filters, Whatman) were collected from a heated whole-air inlet, with our filter sampling at 9 L min^{-1}), mounted on the 4th deck of the ship, and were analysed as soon as possible, usually within 1 - 12 h of being removed from the inlet. The filter samples were not frozen before off-line INP analysis, due to concerns this may affect the INP activity, but were stored at +4 °C for the minimum time possible (1-12 h) before analysis, as longer storage at any temperature is also expected to affect the activity of the samples (Beall et al., 2020). The aerosol particles on the filters were washed into ultra-pure water (Millipore Alpha-Q, with a resistivity of 18 MΩ cm at 25 °C) to suspend the collected aerosol particles. These particle suspensions were then pipetted to form an array of 1 μL droplets on a cold stage, the Microlitre Nucleation by Immersed Particle Instrument, μL-NIPI (Whale et al., 2015). The cold stage cooled at a controlled rate of 1 °C min^{-1} until all droplets had frozen, and the freezing events were recorded in order to determine the concentration of INPs with respect to the volume of air that had been sampled through the inlet. Heat sensitivity of the collected INP samples was determined by heat treatment, where subsamples of the particle suspensions were heated to 100 °C for 30 min in 50 mL conical centrifuge tubes using a water bath, before being analysed.

Filter samples from a balloon-borne sampler, the selective-height aerosol research kit (SHARK) (Porter et al., 2020a), were analysed in the same manner as above. The SHARK was deployed above the lowest temperature inversion, with all inlets covered until sampling was started via a radio signal

from the ground. Two cascade impactors (100 L min^{-1}, MSP Model 128, TSI, USA; 9 L min^{-1} Sioutas, SKC Ltd., UK) sampled aerosol whilst a radiosonde (S1H2-R, Windsond, Sweden) measured the temperature, pressure and relative humidity. The radiosonde was constantly operating to provide information to the user on the ground about the SHARK altitude and boundary-layer temperature and humidity structure as the SHARK was ascending. Sampling was paused if the relative humidity increased above 80 %, and was stopped completely before the SHARK was brought back down.

Tracer measurements

To evaluate the concentration of dimethyl sulfide (DMS), black carbon equivalent (eBC) and aerosol size throughout the campaign, filter samples of DMS were collected and analysed onboard, while eBC measurements were obtained from a multi-angle absorption photometer (MAAP, Model 5012, Thermo Fisher Scientific Inc.). Particle size distribution measurements were made continuously using an aerosol spectrometer (WELAS 2300HP, Palas GmbH) for particles of size 0.15 - 9.65 µm, and a differential mobility particle sizer (DMPS) with a custom-built medium Vienna-type differential mobility analyzer (DMA) with a mixing condensation particle counter (MCPC, Model 1720, Brechtel Manufacturing Inc.) for particles of size 10–921 nm. Transmission Electron Microscopy (TEM) analysis was also conducted on a grid collected during a period of the highest INP activity on the ice floe (19th August 21:02 – 21st August 22:08).

Ship stack pollution

Combustion products in the ship's exhaust may influence INP populations (Thomson et al., 2018). In order to ensure that the INP concentrations measured were not affected by the ship stack emissions, rigorous sampling procedures were put in place. The aerosol sampling inlets faced the ship bow and the ship was manoeuvred to face into the wind whenever the wind direction changed, which minimised the probability of sampling ship stack emissions. In addition, an auto-stop for the inlet pumps was operated if aerosol concentrations increased suddenly (which would be indicative of sampling the ship stack plume), halting the sampling until aerosol size distributions returned to normal. As a precaution, the direction and speed of the wind was monitored closely, and sampling was stopped when there was a chance that the wind might introduce ship stack to the sampled aerosol. Finally, sampling was stopped if any activity that could produce aerosol was

planned, including the movement of the ship, ice coring, and helicopter flights. Smoking was also only allowed in certain areas of the ship, to ensure there was no influence on aerosol sampling.

Backward trajectories

In order to define the potential origin of measured INPs, backward trajectories of the air reaching the sampling location was conducted. The 10-day (only 7 days of which are used here) back trajectories were calculated using the Lagrangian analysis tool LAGRANTO (Sprenger and Wernli, 2015) with wind fields from 3-hourly operational ECMWF analyses, interpolated to a regular grid with 0.5° horizontal resolution on the 137 model levels. The trajectory data contains the hourly positions (longitude, latitude, pressure) along the trajectory. To focus on the segments of the trajectories that can potentially be affected by surface aerosol emissions, the trajectories are only considered as long as they are within the model boundary layer. Additionally, removal of aerosol by precipitation, which may remove the signature of upwind aerosol sources, has been considered by removing all the trajectory points before the precipitation event (using a threshold of 0.1 mm h^{-1}). The overall relationship with origin is unchanged by the addition of this filter, which indicates that the results were insensitive to precipitation events.

Background subtraction

The INP concentration data is shown with the contribution from the background accounted for. The background influence on the INP concentration was determined by collating the differential nucleus concentrations for water and handling blanks, and removing this from the sample differential nucleus concentrations as described in a discussion by Vali (Vali, 2019).

References

Adams, M.P., Tarn, M.D., Sanchez-Marroquin, A., Porter, G.C.E., O'Sullivan, D., Harrison, A.D., Cui, Z., Vergara-Temprado, J., Carotenuto, F., Holden, M.A., Daily, M.I., Whale, T.F., Sikora, S.N.F., Burke, I.T., Shim, J.U., McQuaid, J.B. and Murray, B.J. 2020. A Major Combustion Aerosol Event Had a Negligible Impact on the Atmospheric Ice-Nucleating Particle Population. *Journal of Geophysical Research: Atmospheres*. **125**(22).

Ahmed, R., Prowse, T., Dibike, Y., Bonsal, B. and O'Neil, H. 2020. Recent Trends in Freshwater Influx to the Arctic Ocean from Four Major Arctic-Draining Rivers. *Water*. **12**(4), p.1189.

Barry, K.R., Hill, T.C.J., Levin, E.J.T., Twohy, C.H., Moore, K.A., Weller, Z.D., Toohey, D.W., Reeves, M., Campos, T., Geiss, R., Schill, G.P., Fischer, E. V., Kreidenweis, S.M. and DeMott, P.J. 2021. Observations of Ice Nucleating Particles in the Free Troposphere From Western US Wildfires. *Journal of Geophysical Research: Atmospheres*. **126**(3), e2020JD033752.

Beall, C.M., Lucero, D., Hill, T.C., Demott, P.J., Dale Stokes, M. and Prather, K.A. 2020. Best practices for precipitation sample storage for offline studies of ice nucleation in marine and coastal environments. *Atmospheric Measurement Techniques*. **13**(12), pp.6473–6486.

Bigg, E.K. 1996. Ice forming nuclei in the high Arctic. *Tellus, Series B: Chemical and Physical Meteorology*. **48**(2), pp.223–233.

Bigg, E.K. and Leck, C. 2001. Cloud-active particles over the central Arctic Ocean. *Journal of Geophysical Research Atmospheres*. **106**(D23), pp.32155–32166.

Bond, T.C., Doherty, S.J., Fahey, D.W., Forster, P.M., Berntsen, T., Deangelo, B.J., Flanner, M.G., Ghan, S., Kärcher, B., Koch, D., Kinne, S., Kondo, Y., Quinn, P.K., Sarofim, M.C., Schultz, M.G., Schulz, M., Venkataraman, C., Zhang, H., Zhang, S., Bellouin, N., Guttikunda, S.K., Hopke, P.K., Jacobson, M.Z., Kaiser, J.W., Klimont, Z., Lohmann, U., Schwarz, J.P., Shindell, D., Storelvmo, T., Warren, S.G. and Zender, C.S. 2013. Bounding the role of black carbon in the climate system: A scientific assessment. *Journal of Geophysical Research Atmospheres*. **118**(11), pp.5380–5552.

Boucher, O., Randall, D., Artaxo, P., Bretherton, C., Feingold, G., Forster, P., Kerminen, V.M., Kondo, Y., Liao, H. and Lohmann, U. 2013. Clouds and aerosols. Climate change 2013: The physical science basis. Contribution of working group I to the fifth assessment report of the intergovernmental panel on climate change. *Cambridge University Press, Cambridge, United Kingdom and New York, NY, USA.*, pp.571–657.

Brooks, I.M., Tjernström, M., Persson, P.O.G., Shupe, M.D., Atkinson, R.A., Canut, G., Birch, C.E., Mauritsen, T., Sedlar, J. and Brooks, B.J. 2017. The Turbulent Structure of the Arctic Summer Boundary Layer During

The Arctic Summer Cloud-Ocean Study. *Journal of Geophysical Research: Atmospheres*. **122**(18), pp.9685–9704.

Bullard, J.E., Baddock, M., Bradwell, T., Crusius, J., Darlington, E., Gaiero, D., Gassó, S., Gisladottir, G., Hodgkins, R., McCulloch, R., McKenna-Neuman, C., Mockford, T., Stewart, H. and Thorsteinsson, T. 2016. High-latitude dust in the Earth system. *Reviews of Geophysics*. **54**(2), pp.447–485.

Chen, J., Wu, Z., Augustin-Bauditz, S., Grawe, S., Hartmann, M., Pei, X., Liu, Z., Ji, D. and Wex, H. 2017. Ice nucleating particle concentrations unaffected by urban air pollution in Beijing, China 2. *Atmos. Chem. Phys. Discuss.*

Christner, B.C., Cai, R., Morris, C.E., McCarter, K.S., Foreman, C.M., Skidmore, M.L., Montross, S.N. and Sands, D.C. 2008. Geographic, seasonal, and precipitation chemistry influence on the abundance and activity of biological ice nucleators in rain and snow. *Proc. Natl. Acad. Sci. U.S.A.* **105**(48), pp.18854–18859.

Christner, B.C., Morris, C.E., Foreman, C.M., Cai, R. and Sands, D.C. 2008. Ubiquity of Biological Ice Nucleators in Snowfall. *Science*. **319**(5867), p.1214.

Cohen, J., Screen, J.A., Furtado, J.C., Barlow, M., Whittleston, D., Coumou, D., Francis, J., Dethloff, K., Entekhabi, D., Overland, J. and Jones, J. 2014. Recent Arctic amplification and extreme mid-latitude weather. *Nature Geoscience*. **7**(9), pp.627–637.

Creamean, Jessie M., Hill, T.C.J., Demott, P.J., Uetake, J., Kreidenweis, S. and Douglas, T.A. 2020. Thawing permafrost: An overlooked source of seeds for Arctic cloud formation. *Environmental Research Letters*. **15**(8), p.084022.

Creamean, Jessie M, Hill, T.C.J., DeMott, P.J., Uetake, J., Kreidenweis, S. and Douglas, T.A. 2020. Thawing permafrost: an overlooked source of seeds for Arctic cloud formation. *Environmental Research Letters*. **15**(8), p.084022.

DeMott, P.J., Hill, T.C.J., McCluskey, C.S., Prather, K.A., Collins, D.B., Sullivan, R.C., Ruppel, M.J., Mason, R.H., Irish, V.E., Lee, T., Hwang, C.Y., Rhee, T.S., Snider, J.R., McMeeking, G.R., Dhaniyala, S., Lewis, E.R., Wentzell, J.J.B., Abbatt, J., Lee, C., Sultana, C.M., Ault, A.P., Axson, J.L., Diaz Martinez, M., Venero, I., Santos-Figueroa, G., Stokes, M.D., Deane, G.B., Mayol-Bracero, O.L., Grassian, V.H., Bertram, T.H., Bertram, A.K., Moffett, B.F. and Franc, G.D. 2016. Sea spray aerosol as a unique source of ice nucleating particles. *Proceedings of the National Academy of Sciences*. **113**(21), pp.5797–5803.

Ding, X., Wang, X., Xie, Z., Zhang, Z. and Sun, L. 2013. Impacts of siberian biomass burning on organic aerosols over the north pacific ocean and the arctic: Primary and secondary organic tracers. *Environmental Science and Technology*. **47**(7), pp.3149–3157.

Hartmann, M., Adachi, K., Eppers, O., Haas, C., Herber, A., Holzinger, R., Hünerbein, A., Jäkel, E., Jentzsch, C., van Pinxteren, M., Wex, H., Willmes, S., Stratmann, F., Pinxteren, M., Wex, H., Willmes, S. and Stratmann, F. 2020. Wintertime Airborne Measurements of Ice Nucleating Particles in the High Arctic: A Hint to a Marine, Biogenic Source for Ice Nucleating Particles. *Geophysical Research Letters*. **47**(13).

Herbert, R.J., Murray, B.J., Dobbie, S.J. and Koop, T. 2015. Sensitivity of liquid clouds to homogenous freezing parameterizations. *Geophys. Res. Lett.* **42**(5), pp.1599–1605.

Hill, T.C.J., Demott, P.J., Tobo, Y., Fröhlich-Nowoisky, J., Moffett, B.F., Franc, G.D. and Kreidenweis, S.M. 2016. Sources of organic ice nucleating particles in soils. *Atmospheric Chemistry and Physics*. **16**(11), pp.7195–7211.

Hoose, C. and Möhler, O. 2012. Heterogeneous ice nucleation on atmospheric aerosols: a review of results from laboratory experiments. *Atmos. Chem. Phys. Atmospheric Chemistry and Physics*. **12**(20), pp.9817–9854.

Ickes, L., Porter, G.C.E., Wagner, R., Adams, M.P., Bierbauer, S., Bertram, A.K., Bilde, M., Christiansen, S., Ekman, A.M.L., Gorokhova, E., Höhler, K., Kiselev, A.A., Leck, C., Möhler, O., Murray, B.J., Schiebel, T., Ullrich, R. and Salter, M.E. 2020. The ice-nucleating activity of Arctic sea surface microlayer samples and marine algal cultures. *Atmospheric Chemistry and Physics*. **20**(18), pp.11089–11117.

Igel, A.L., Ekman, A.M.L., Leck, C., Tjernström, M., Savre, J. and Sedlar, J. 2017. The free troposphere as a potential source of arctic boundary layer aerosol particles. *Geophysical Research Letters*. **44**(13), pp.7053–7060.

Irish, V.E., Elizondo, P., Chen, J., Chou, C., Charette, J., Lizotte, M., Ladino, L.A., Wilson, T.W., Gosselin, M., Murray, B.J., Polishchuk, E., Abbatt, J.P.D.D., Miller, L.A., Bertram, A.K., Choul, C., Charette, J., Lizotte, M., Ladino, L.A., Wilson, T.W., Gosselin, M., Murray, B.J., Polishchuk, E., Abbatt, J.P.D.D., Miller, L.A. and Bertram, A.K. 2017. Ice-nucleating particles in Canadian Arctic sea-surface microlayer and bulk seawater. *Atmospheric Chemistry and Physics*. **17**(17), pp.10583–10595.

Jahn, L.G., Polen, M.J., Jahl, L.G., Brubaker, T.A., Somers, J. and Sullivan, R.C. 2020. Biomass combustion produces ice-active minerals in biomass-burning aerosol and bottom ash. *Proceedings of the National Academy of Sciences of the United States of America*. **117**(36), pp.21928–21937.

Juhls, B., Paul Overduin, P., Hölemann, J., Hieronymi, M., Matsuoka, A., Heim, B. and Fischer, J. 2019. Dissolved organic matter at the fluvial-marine transition in the Laptev Sea using in situ data and ocean colour remote sensing. *Biogeosciences*. **16**(13), pp.2693–2713.

Kanji, Z.A., Ladino, L.A., Wex, H., Boose, Y., Burkert-Kohn, M., Cziczo, D.J. and Krämer, M. 2017. Overview of Ice Nucleating Particles. *Meteorological Monographs*. **58**, 1.1-1.33.

Kanji, Z.A., Welti, A., Corbin, J.C. and Mensah, A.A. 2020. Black Carbon Particles Do Not Matter for Immersion Mode Ice Nucleation. *Geophysical Research Letters*. **47**(11).

Kay, J.E. and L'Ecuyer, T. 2013. Observational constraints on Arctic Ocean clouds and radiative fluxes during the early 21st century. *Journal of Geophysical Research Atmospheres*. **118**(13), pp.7219–7236.

Kerminen, V.-M. and Leck, C. 2001. Sulfur chemistry over the central Arctic Ocean during the summer: Gas-to-particle transformation. *Journal of Geophysical Research: Atmospheres*. **106**(D23), pp.32087–32099.

Khan, M.A.H., Gillespie, S.M.P., Razis, B., Xiao, P., Davies-Coleman, M.T., Percival, C.J., Derwent, R.G., Dyke, J.M., Ghosh, M. V., Lee, E.P.F. and Shallcross, D.E. 2016. A modelling study of the atmospheric chemistry of DMS using the global model, STOCHEM-CRI. *Atmospheric Environment*. **127**, pp.69–79.

Kupiszewski, P., Leck, C., Tjernström, M., Sjogren, S., Sedlar, J., Graus, M., Müller, M., Brooks, B., Swietlicki, E., Norris, S. and Hansel, A. 2013. Vertical profiling of aerosol particles and trace gases over the central Arctic Ocean during summer. *Atmospheric Chemistry and Physics*. **13**(24), pp.12405–12431.

Lawler, M.J., Draper, D.C. and Smith, J.N. 2020. Atmospheric fungal nanoparticle bursts. *Science Advances*. **6**(3), p.eaax9051.

Leck, C. and Persson, C. 1996. The central Arctic Ocean as a source of dimethyl sulfide Seasonal variability in relation to biological activity. *Tellus, Series B: Chemical and Physical Meteorology*. **48**(2), pp.156–177.

Lohmann, U. and Leck, C. 2005. Importance of submicron surface-active organic aerosols for pristine Arctic clouds. *Tellus B: Chemical and Physical Meteorology*. **57**(3), pp.261–268.

Mason, R.H., Si, M., Chou, C., Irish, V.E., Dickie, R., Elizondo, P., Wong, R., Brintnell, M., Elsasser, M., Lassar, W.M., Pierce, K.M., Leaitch, W.R., MacDonald, A.M., Platt, A., Toom-Sauntry, D., Sarda-Estève, R., Schiller, C.L., Suski, K.J., Hill, T.C.J., Abbatt, J.P.D., Huffman, J.A., DeMott, P.J. and Bertram, A.K. 2016. Size-resolved measurements of ice-nucleating particles at six locations in North America and one in Europe. *Atmospheric Chemistry and Physics*. **16**(3), pp.1637–1651.

Matsui, H., Kondo, Y., Moteki, N., Takegawa, N., Sahu, L.K., Zhao, Y., Fuelberg, H.E., Sessions, W.R., Diskin, G., Blake, D.R., Wisthaler, A. and Koike, M. 2011. Seasonal variation of the transport of black carbon aerosol from the Asian continent to the Arctic during the ARCTAS aircraft campaign. *Journal of Geophysical Research Atmospheres*. **116**(5), p.5202.

Mcbean, G., Alekseev, G., Chen, D., Førland, E., Fyfe, J., Groisman, P.Y.P., King, R., Melling, H., Vose, R. and Whitfield, P.P.H. 2005. Arctic climate: past and present. *Arctic Climate Impact Assessment. Cambridge, UK: Cambridge University Press.*, pp.21–60.

McCluskey, C.S., DeMott, P.J., Ma, P. -L. and Burrows, S.M. 2019. Numerical Representations of Marine Ice-Nucleating Particles in Remote Marine Environments Evaluated Against Observations. *Geophysical Research Letters.* **46**(13), pp.7838–7847.

McCluskey, C.S., Hill, T.C.J., Humphries, R.S., Rauker, A.M., Moreau, S., Strutton, P.G., Chambers, S.D., Williams, A.G., McRobert, I., Ward, J., Keywood, M.D., Harnwell, J., Ponsonby, W., Loh, Z.M., Krummel, P.B., Protat, A., Kreidenweis, S.M. and DeMott, P.J. 2018. Observations of Ice Nucleating Particles Over Southern Ocean Waters. *Geophysical Research Letters.* **45**(21), 11,989-11,997.

Morrison, A.E., Siems, S.T. and Manton, M.J. 2011. A Three-Year Climatology of Cloud-Top Phase over the Southern Ocean and North Pacific. *Journal of Climate.* **24**, pp.2405–2418.

Morrison, H., De Boer, G., Feingold, G., Harrington, J., Shupe, M.D. and Sulia, K. 2012. Resilience of persistent Arctic mixed-phase clouds. *Nature Geoscience.* **5**(1), pp.11–17.

Murray, B.J., Carslaw, K.S. and Field, P.R. 2021. Opinion: Cloud-phase climate feedback and the importance of ice-nucleating particles. *Atmospheric Chemistry and Physics.* **21**(2), pp.665–679.

Murray, B.J., O'sullivan, D., Atkinson, J.D. and Webb, M.E. 2012. Ice nucleation by particles immersed in supercooled cloud droplets. *Chemical Society Reviews.* **41**(19), pp.6519–6554.

O'Dowd, C.D., Facchini, M.C., Cavalli, F., Ceburnis, D., Mircea, M., Decesari, S., Fuzzi, S., Yoon, Y.J. and Putaud, J.-P. 2004. Biogenically driven organic contribution to marine aerosol. *Nature.* **431**(7009), pp.676–680.

O'Sullivan, D., Adams, M.P.P., Tarn, M.D.D., Harrison, A.D.D., Vergara-Temprado, J., Porter, G.C.E.C.E., Holden, M.A.A., Sanchez-Marroquin, A., Carotenuto, F., Whale, T.F.F., McQuaid, J.B.B., Walshaw, R., Hedges, D.H.P.H.P., Burke, I.T.T., Cui, Z. and Murray, B.J.J. 2018. Contributions of biogenic material to the atmospheric ice-nucleating particle population in North Western Europe. *Scientific Reports.* **8**(1), p.13821.

O'Sullivan, D., Murray, B.J., Ross, J.F., Whale, T.F., Price, H.C., Atkinson, J.D., Umo, N.S. and Webb, M.E. 2015. The relevance of nanoscale biological fragments for ice nucleation in clouds. *Scientific Reports.* **5**(1), p.8082.

Porter, G.C.E., Sikora, S.N.F., Adams, M.P., Proske, U., Harrison, A.D., Tarn, M.D., Brooks, I.M. and Murray, B.J. 2020. Resolving the size of ice-nucleating particles with a balloon deployable aerosol sampler: The SHARK. *Atmospheric Measurement Techniques.* **13**(6), pp.2905–2921.

Prytherch, J., Tjernström, M., Vuellers, J., Achtert, P., Brooks, I., Porter, G. and Adams, M. 2019. Radiosonde data from the Arctic Ocean 2018 expedition. [Accessed 29 January 2021]. Available from: https://bolin.su.se/data/ao2018-radiosonde-2.

Pummer, B.G., Budke, C., Augustin-Bauditz, S., Niedermeier, D., Felgitsch, L., Kampf, C.J., Huber, R.G., Liedl, K.R., Loerting, T., Moschen, T., Schauperl, M., Tollinger, M., Morris, C.E., Wex, H., Grothe, H., Pöschl, U., Koop, T. and Fröhlich-Nowoisky, J. 2015. Ice nucleation by water-soluble macromolecules. *Atmospheric Chemistry and Physics*. **15**(8), pp.4077–4091.

Sanchez-Marroquin, A., Arnalds, O., Baustian-Dorsi, K.J., Browse, J., Dagsson-Waldhauserova, P., Harrison, A.D., Maters, E.C., Pringle, K.J., Vergara-Temprado, J., Burke, I.T., McQuaid, J.B., Carslaw, K.S. and Murray, B.J. 2020. Iceland is an episodic source of atmospheric ice-nucleating particles relevant for mixed-phase clouds. *Science Advances*. **6**(26), pp.8137–8161.

Schill, G.P., DeMott, P.J., Emerson, E.W., Rauker, A.M.C., Kodros, J.K., Suski, K.J., Hill, T.C.J., Levin, E.J.T., Pierce, J.R., Farmer, D.K. and Kreidenweis, S.M. 2020. The contribution of black carbon to global ice nucleating particle concentrations relevant to mixed-phase clouds. *Proceedings of the National Academy of Sciences of the United States of America*. **117**(37), pp.22705–22711.

Schmale, J., Zieger, P. and Ekman, A.M.L.L. 2021. Aerosols in current and future Arctic climate. *Nature Climate Change*. **11**(2), pp.95–105.

Schneider, J., Höhler, K., Heikkilä, P., Keskinen, J., Bertozzi, B., Bogert, P., Schorr, T., Silas Umo, N., Vogel, F., Brasseur, Z., Wu, Y., Hakala, S., Duplissy, J., Moisseev, D., Kulmala, M., Adams, M.P., Murray, B.J., Korhonen, K., Hao, L., Thomson, E.S., Castarède, D., Leisner, T., Petäjä, T. and Möhler, O. 2021. The seasonal cycle of ice-nucleating particles linked to the abundance of biogenic aerosol in boreal forests. *Atmospheric Chemistry and Physics*. **21**(5), pp.3899–3918.

Schnell, R.C. and Vali, G. 1975. Freezing nuclei in marine waters. *Tellus*. **27**, pp.321–323.

Sprenger, M. and Wernli, H. 2015. The LAGRANTO Lagrangian analysis tool - Version 2.0. *Geoscientific Model Development*. **8**(8), pp.2569–2586.

Stevens, R.G., Loewe, K., Dearden, C., Dimitrelos, A., Possner, A., Eirund, G.K., Raatikainen, T., Hill, A.A., Shipway, B.J., Wilkinson, J., Romakkaniemi, S., Tonttila, J., Laaksonen, A., Korhonen, H., Connolly, P., Lohmann, U., Hoose, C., Ekman, A.M.L., Carslaw, K.S. and Field, P.R. 2018. A model intercomparison of CCN-limited tenuous clouds in the high Arctic. *Atmospheric Chemistry and Physics*. **18**(15), pp.11041–11071.

Stohl, A., Klimont, Z., Eckhardt, S., Kupiainen, K., Shevchenko, V.P., Kopeikin, V.M. and Novigatsky, A.N. 2013. Black carbon in the Arctic:

The underestimated role of gas flaring and residential combustion emissions. *Atmospheric Chemistry and Physics*. **13**(17), pp.8833–8855.

Tan, I. and Storelvmo, T. 2019. Evidence of Strong Contributions From Mixed-Phase Clouds to Arctic Climate Change. *Geophysical Research Letters*. **46**(5), pp.2894–2902.

Thomson, E.S., Weber, D., Bingemer, H.G., Tuomi, J., Ebert, M. and Pettersson, J.B.C. 2018. Intensification of ice nucleation observed in ocean ship emissions. *Scientific Reports*. **8**(1), pp.1–9.

Tjernström, M., Birch, C.E., Brooks, I.M., Shupe, M.D., Persson, P.O.G., Sedlar, J., Mauritsen, T., Leck, C., Paatero, J., Szczodrak, M. and Wheeler, C.R. 2012. Atmospheric Chemistry and Physics. *Atmos. Chem. Phys*. **12**, pp.6863–6889.

Tobo, Y., Adachi, K., DeMott, P.J., Hill, T.C.J., Hamilton, D.S., Mahowald, N.M., Nagatsuka, N., Ohata, S., Uetake, J., Kondo, Y. and Koike, M. 2019. Glacially sourced dust as a potentially significant source of ice nucleating particles. *Nature Geoscience*. **12**(4), pp.253–258.

Umo, N.S., Murray, B.J., Baeza-Romero, M.T., Jones, J.M., Lea-Langton, A.R., Malkin, T.L., O'Sullivan, D., Neve, L., Plane, J.M.C. and Williams, A. 2015. Ice nucleation by combustion ash particles at conditions relevant to mixed-phase clouds. *Atmospheric Chemistry and Physics*. **15**(9), pp.5195–5210.

Vali, G. 2019. Revisiting the differential freezing nucleus spectra derived from drop-freezing experiments: methods of calculation, applications, and confidence limits. *Atmos. Meas. Tech*. **12**, pp.1219–1231.

Vergara-Temprado, J., Miltenberger, A.K., Furtado, K., Grosvenor, D.P., Shipway, B.J., Hill, A.A., Wilkinson, J.M., Field, P.R., Murray, B.J. and Carslaw, K.S. 2018. Strong control of Southern Ocean cloud reflectivity by ice-nucleating particles. *Proc. Natl. Acad. Sci. U. S. A.* **115**(11), pp.2687–2692.

Vergara-Temprado, J., Murray, B.J., Wilson, T.W., O'Sullivan, D., Browse, J., Pringle, K.J., Ardon-Dryer, K., Bertram, A.K., Burrows, S.M., Ceburnis, D., Demott, P.J., Mason, R.H., O'Dowd, C.D., Rinaldi, M. and Carslaw, K.S. 2017. Contribution of feldspar and marine organic aerosols to global ice nucleating particle concentrations. *Atmospheric Chemistry and Physics*. **17**(5), pp.3637–3658.

Vüllers, J., Achtert, P., Brooks, I.M., Tjernström, M., Prytherch, J., Burzik, A. and Neely III, R. 2021. Meteorological and cloud conditions during the Arctic Ocean 2018 expedition. *Atmospheric Chemistry and Physics*. **21**(1), pp.289–314.

Welti, A., Keith Bigg, E., Demott, P.J., Gong, X., Hartmann, M., Harvey, M., Henning, S., Herenz, P., Hill, T.C.J., Hornblow, B., Leck, C., Löffler, M., Mccluskey, C.S., Rauker, A.M., Schmale, J., Tatzelt, C., Van Pinxteren, M. and Stratmann, F. 2020. Ship-based measurements of ice nuclei concentrations over the Arctic, Atlantic, Pacific and Southern oceans. *Atmos. Chem. Phys*. **20**, pp.15191–15206.

Wex, H., Huang, L., Zhang, W., Hung, H., Traversi, R., Becagli, S., Sheesley, R.J., Moffett, C.E., Barrett, T.E., Bossi, R., Skov, H., Hünerbein, A., Lubitz, J., Löffler, M., Linke, O., Hartmann, M., Herenz, P. and Stratmann, F. 2019. Annual variability of ice-nucleating particle concentrations at different Arctic locations. *Atmospheric Chemistry and Physics*. **19**(7), pp.5293–5311.

Whale, T.F., Murray, B.J., O'Sullivan, D., Wilson, T.W., Umo, N.S., Baustian, K.J., Atkinson, J.D., Workneh, D.A. and Morris, G.J. 2015. A technique for quantifying heterogeneous ice nucleation in microlitre supercooled water droplets. *Atmospheric Measurement Techniques*. **8**(6), pp.2437–2447.

Wilson, T.W., Ladino, L.A., Alpert, P.A., Breckels, M.N., Brooks, I.M., Browse, J., Burrows, S.M., Carslaw, K.S., Huffman, J.A., Judd, C., Kilthau, W.P., Mason, R.H., McFiggans, G., Miller, L.A., Nájera, J.J., Polishchuk, E., Rae, S., Schiller, C.L., Si, M., Temprado, J.V., Whale, T.F., Wong, J.P.S., Wurl, O., Yakobi-Hancock, J.D., Abbatt, J.P.D., Aller, J.Y., Bertram, A.K., Knopf, D.A. and Murray, B.J. 2015. A marine biogenic source of atmospheric ice-nucleating particles. *Nature*. **525**(7568), pp.234–238.

4. On-chip density-based sorting of supercooled droplets and frozen droplets in continuous flow

Grace C. E. Porter,[a,b] Sebastien N. F. Sikora,[a] Jung-uk Shim,[b] Benjamin J. Murray[a] and Mark D. Tarn[a,b]

[a] School of Earth and Environment, University of Leeds, Leeds LS2 9JT, UK
[b] School of Physics and Astronomy, University of Leeds, Leeds LS2 9JT, UK

Abstract. The freezing of supercooled water to ice and the materials which catalyse this process are of fundamental interest to a wide range of fields. At present, our ability to control, predict or monitor ice formation processes is poor. The isolation and characterisation of frozen droplets from supercooled liquid droplets would provide a means of improving our understanding and control of these processes. Here, we have developed a microfluidic platform for the continuous flow separation of frozen from unfrozen picolitre droplets based on differences in their density, thus allowing the sorting of ice crystals and supercooled water droplets into different outlet channels with 94 ± 2% efficiency. This will, in future, facilitate downstream or off-chip processing of the frozen and unfrozen populations, which could include the analysis and characterisation of ice-active materials or the selection of droplets with a particular ice-nucleating activity.

4.1. Introduction

The heterogeneous nucleation of ice is of fundamental importance to fields as diverse as cryobiology,(John Morris and Acton, 2013) atmospheric science,(Hoose and Möhler, 2012; Murray et al., 2012) the pharmaceutical industry,(Geidobler and Winter, 2013) and food science.(Kiani and Sun, 2011) However, our quantitative and mechanistic understanding and control over ice nucleation is poor. Many materials are completely inert when it comes to ice nucleation, and in the absence of the rare sites that catalyse ice nucleation, droplets of water can supercool. They remain in a supercooled liquid state down to ~−35 °C (depending on droplet volume), whereupon they can freeze homogeneously.(Pruppacher and Klett, 1997; Koop and Murray, 2016) This means that, in a population of droplets containing ice-nucleating material, some droplets will contain ice-active particles and freeze at warmer temperatures, while others might not and so remain in a supercooled state. This heterogeneity in ice nucleation makes freezing processes challenging to predict and control and has implications for a number of fields.

In cryopreservation, for instance, the survival of biological matter is strongly influenced by the freezing process. Some cryopreservation strategies avoid ice formation by cooling and vitrifying the samples, whereas others involve minimising the extent of supercooling by nucleating ice at as high a temperature as possible by inducing ice nucleation under controlled conditions.(John Morris and Acton, 2013; Elliott et al., 2017; Daily et al., 2020) If some aliquots freeze or vitrify in an optimal manner while others do not, this could result in a mixture of samples containing cells or tissues of varying viability. In principle, if the samples that have undergone controlled ice nucleation could be selected and only those aliquots expected to contain viable biological matter stored, the quality and reproducibility of the cryopreserved samples would be improved.

The formation of ice is also important for the Earth's atmosphere and climate. The properties and lifetime of clouds is strongly influenced by the formation of ice, which can form homogeneously or can be triggered heterogeneously by ice-nucleating particles.(Kanji et al., 2017; Vergara-Temprado et al., 2018) In atmospheric ice nucleation research, an aerosol sample from the lab or field may be analysed to determine the temperature at which nucleation occurs and the concentration of ice-nucleating particles in the sample.(Hoose and Möhler, 2012; Murray et al., 2012) However, the identification of these rare particles in a bulk sample of aerosol particles can be difficult. The separation of ice-nucleating materials from atmospheric samples would greatly facilitate their identification and characterisation, allowing a greater understanding of their sources and global transport.

In these areas and more, an ability to separate frozen from supercooled droplets would be advantageous. A desirable mechanism for achieving such a separation would be to first trigger the nucleation of ice in supercooled water droplets at a defined sub-zero temperature. Only those droplets containing material with the ability to nucleate ice at that temperature would induce ice nucleation, leaving the remaining droplets unfrozen. Since ice and water have different densities ($\rho_{water} > \rho_{ice}$), they are susceptible to separation based on their relative buoyancy in an immiscible medium (Figure 4.1a), and this principle may be used to separate frozen ice crystals from unfrozen water droplets.
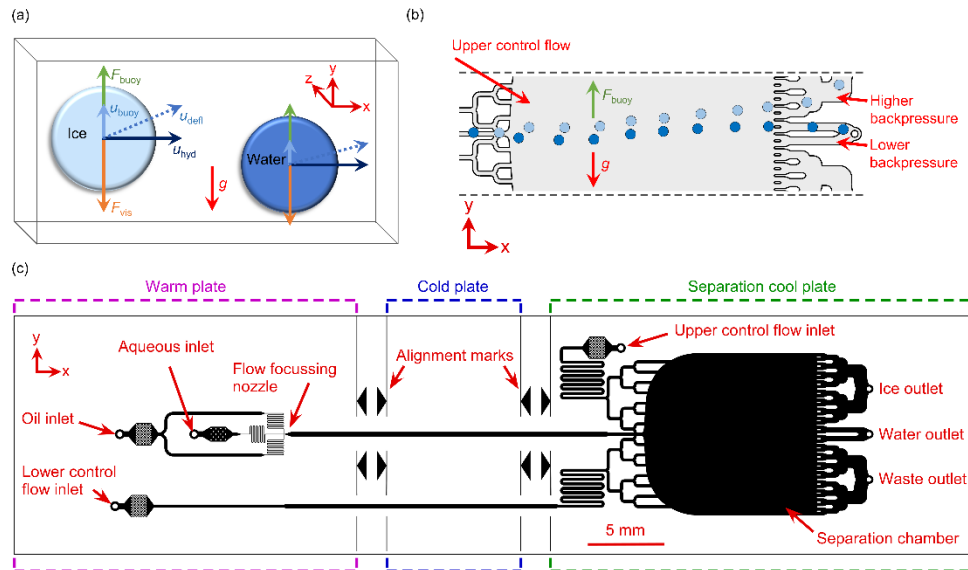
Figure 4.1 Principle of the on-chip sorting of ice crystals and water droplets in continuous flow, based on their differences in buoyancy. (a) A schematic showing the buoyancy forces (F_{buoy}) that give rise to different velocities in the y-direction (u_{buoy}), opposite to the direction of gravity (g), for the water droplets and ice crystals due to their different densities in an oil medium. When the droplets and crystals reach their terminal velocity, F_{buoy} is balanced by the opposing viscous forces (F_{vis}). The droplets and crystals are driven in the x-direction with a hydrodynamic velocity (u_{hyd}) and experience a deflection velocity (u_{defl}) to differing extents depending on their respective u_{buoy} values. (b) Water droplets and ice crystals experiencing different F_{buoy} forces in a tall microfluidic chamber are sorted into different outlet channels. (c) The design of the microfluidic chip. Water-in-oil droplets were generated in a flow focussing nozzle on a warm plate, before passing over a cold plate at a set temperature that froze part of a population of droplets. The frozen and unfrozen droplets then entered a vertically oriented separation chamber for their density-based sorting.

Fahy et al.(Fahy et al., 1990) found that ice crystals that formed in a solution of 50 % w/w propylene glycol in water floated to the top of their container upon cooling to sub-zero temperatures, and later suggested that this effect could be leveraged to separate frozen from unfrozen droplets via centrifugation or drop-sorting techniques.(Fahy, 1995) Recently, Kamijo and Derda(Kamijo and Derda, 2019) developed a "freeze-float" droplet selection system for the sorting of ice-nucleating material populations. 1 μL droplets were suspended in low viscosity silicone oil on a cushion layer of fluorinated oil ($\rho_{\text{fluorinated oil}} > \rho_{\text{water}} > \rho_{\text{silicone oil}} > \rho_{\text{ice}}$) within a cuvette, and then cooled to sub-zero temperatures. As droplets froze, they floated to the top of the

silicone oil layer, allowing their collection for analysis of their contents. However, the selection procedure was somewhat slow and only tens of droplets could be processed per experiment.

Microfluidic technology offers a number of elegant options for performing particle and droplet separations in continuous flow,(Pamme, 2007; Lenshof and Laurell, 2010; Wyatt Shields IV et al., 2015; Xi et al., 2017) which can enable the high-throughput sorting of different species with high efficiency and in large numbers. In a typical continuous flow sorting platform, a mixed particle population will enter a channel or chamber and experience a lateral force, causing the populations to migrate laterally across the channel/chamber to differing extents for collection from different outlet channels.

Several examples exist of the continuous density-based sorting of particles and cells in microfluidic devices in the vertical direction due to gravity,(Huh et al., 2007; Sugiyama et al., 2014) including the use of split flow thin-cell fractionation (SPLITT),(Springston et al., 1987) 3D-printed devices,(Norouzi et al., 2017) diamagnetic levitation,(Winkleman et al., 2007) and in numerical simulations.(Song et al., 2014) Density-based separations have also been performed in a horizontal orientation via the use of acoustic forces,(Lenshof et al., 2012; Nam et al., 2012; Jo and Guldiken, 2012; Xie et al., 2020) centrifugal platforms,(Haeberle et al., 2006; Strohmeier et al., 2015; Ukita et al., 2017) sedimentation pinched-flow fractionation in a centrifugal device,(Morijiri et al., 2011) and could potentially also be achieved in inertial microfluidics devices.(Sajeesh and Sen, 2014) However, none of these examples, nor any other continuous separation methods to our knowledge, have been applied to the sorting of ice crystals from supercooled water droplets.

Here, we demonstrate a microfluidic device for the density-based sorting of ice crystals from unfrozen water droplets (Figure 4.1b). The proof-of-concept device utilises our recently developed microfluidic apparatus for the generation and freezing of water-in-oil droplets for the analysis of ice-nucleating particles (INPs), the Lab-on-a-Chip Nucleation by Immersed Particle Instrument (LOC-NIPI).(Tarn et al., 2020) In the new device described here, the generated ice crystals and supercooled water droplets enter a downstream separation chamber with multiple outlet channels to allow sorting in a "free-flow" format, similar to designs used in free-flow magnetophoresis,(Pamme and Manz, 2004) electrophoresis,(Raymond et

al., 1994; Johnson and Bowser, 2018) isotachophoresis,(Park et al., 2015) acoustophoresis,(Lenshof et al., 2012) and diamagnetophoresis.(Peyman et al., 2009; Zhao et al., 2016) Since the sorting mechanism leverages the intrinsic differences in density between the ice and water, the separation acts in a passive manner without the need for actively applied external forces and associated apparatus.

The new platform was tested by generating droplets containing Snomax® Snow Inducer, comprised of highly ice-active material from the *Pseudomonas syringae* plant pathogen,(Hirano and Upper, 2000; Wex et al., 2015) at a concentration that resulted in around half of the droplet population freezing, before observing the subsequent behaviour of the ice crystals and supercooled water droplets as they flowed through the separation chamber. This concept is particularly timely given the recent surge in microfluidic platforms being developed for the droplet-based study of ice nucleation (Stan et al., 2009; Edd et al., 2009; Sgro and Chiu, 2010; Stan, Tang, et al., 2011; Riechers et al., 2013; Atig et al., 2018), including for applications such as cryobiology (Sgro et al., 2007; Weng et al., 2016; Weng et al., 2018; Eickhoff et al., 2019; Bissoyi et al., 2019) and atmospheric science (Peckhaus et al., 2016; Abdelmonem et al., 2017; Reicher et al., 2018; Häusler et al., 2018; Tarn et al., 2018; Zipori et al., 2018; Reicher et al., 2019; Brubaker et al., 2020; Tarn et al., 2020; Knopf et al., 2020).

4.1.1. Theory

The migration of an object, such as a droplet, due to its buoyancy in an immiscible medium depends on the buoyancy force, $\boldsymbol{F}_{\textbf{buoy}}$, exerted upon it:

$$\boldsymbol{F}_{\textbf{buoy}} = \left(\rho_{\mathrm{p}} - \rho_{\mathrm{m}}\right) V_{\mathrm{p}}\, g = \Delta\rho\, V_{\mathrm{p}}\, g \qquad\qquad (4)$$

where ρ_{p} is the density of the droplet (kg m^{-3}), ρ_{m} is the density of the medium (kg m^{-3}), V_{p} is the droplet volume (m^3), and g is the acceleration due to gravity (9.81 m s^{-2}). When the density of a droplet is greater than that of the liquid medium, $\Delta\rho$ is positive and the droplet will sediment, i.e. sink. However, if the medium is denser than the droplet then $\Delta\rho$ is negative and the droplet will cream, i.e. float (Figure 4.1a).

As a droplet moves through a medium, it also experiences a viscous drag force, $\boldsymbol{F}_{\textbf{vis}}$, that opposes its movement. In flow conditions with low Reynolds

numbers (Re << 1) and low particle Reynolds numbers (Re$_p$ < 0.2), this frictional force can be calculated using Stokes' law:

$$\boldsymbol{F}_{\textbf{vis}} = 6\,\pi\,\eta\,r\,\boldsymbol{u}_{\textbf{buoy}}\,C_{\text{W}} \tag{5}$$

where η is the viscosity of the medium (kg m^{-1} s^{-1}), r is the droplet radius (m), $\boldsymbol{u}_{\textbf{buoy}}$ is the velocity of the droplet in the y-direction due to sedimentation or creaming (m s^{-1}), and C_{W} is the viscous drag coefficient (dimensionless) on the droplet due to the walls of the microchannel. An analysis of the Reynolds number and particle Reynolds numbers in our microfluidic system is provided in Section 1 of the ESI, which yielded Re = 0.4 for the flow in the device and Re$_p$ < 0.18 for the water droplets and ice crystals, indicating that Equation 2 is applicable here. The equation for the calculation of C_{W} is provided in Section 2 of the ESI.(Happel and Brenner, 1973; Iiguni et al., 2004; Tarn et al., 2009)

When the droplet reaches its terminal velocity as it moves through a medium, the viscous forces are equal but opposite to the buoyancy forces, i.e. $\boldsymbol{F}_{\textbf{vis}} = \boldsymbol{F}_{\textbf{buoy}}$. Using this assumption, Equations 1 and 2 can be rearranged to allow the sedimentation/creaming velocity, $\boldsymbol{u}_{\textbf{buoy}}$, of a droplet or particle to be determined:(Huh et al., 2007)

$$\boldsymbol{u}_{\textbf{buoy}} = \frac{2\,\Delta\rho\,g\,r^2}{9\,\eta\,C_{\text{W}}} \tag{6}$$

Equation 3 holds true when the Archimedes number, Ar, is less than 32.9, where Ar is defined in a similar manner to the Reynolds number but for particle movement in the vertical direction.(Kalman et al., 2019) The Archimedes numbers were calculated in our system to be Ar ≤ 4.6, as described in detail in Section 1 of the ESI, thus demonstrating the applicability of using Equation 3 to describe the vertical motion of the water droplets and ice crystals here.

The droplet will also have a velocity in the x-direction due to the applied hydrodynamic flow, $\boldsymbol{u}_{\textbf{hyd}}$ (m s^{-1}). Therefore, the droplet has velocities in both the y-direction ($\boldsymbol{u}_{\textbf{buoy}}$) and the x-direction ($\boldsymbol{u}_{\textbf{hyd}}$), and the resultant deflection velocity ($\boldsymbol{u}_{\textbf{defl}}$) is the sum of the two:

$$u_{\text{defl}} = u_{\text{buoy}} + u_{\text{hyd}} \tag{7}$$

If u_{hyd} is held constant by maintaining a constant flow rate in the microfluidic chip, then the extent of droplet deflection depends only on the y-direction velocity due to the gravitational force on the droplet, u_{buoy}. Thus, objects with differing densities, such as ice crystals and supercooled water droplets (Figure 4.1a), will experience different u_{buoy} velocities that result in their deflection (u_{defl}) to differing extents, thereby allowing their separation in continuous flow (Figure 4.1b).

Theoretical values for F_{buoy} and u_{buoy} were calculated for supercooled water droplets and ice crystals using Equations 1-3 for a temperature range of 0 to −35 °C, in a medium of Novec™ 7500 Engineered Fluid, a fluorinated oil. Viscosity (η) and density (ρ_m) values for Novec™ 7500 were obtained using equations from the manufacturer's product information, as shown in the ESI (Equations S5-S8). The density (ρ_p) of supercooled water and ice were calculated from Equations S10 (from Hare and Sorenson(Hare and Sorensen, 1987)) and S11 (from Pruppacher and Klett(Pruppacher and Klett, 1997)) in the ESI, respectively. The viscous drag coefficient (C_w) was calculated as described in Equation S4 in the ESI for a microchannel, with a z-direction width of 140 μm.

The change in theoretical F_{buoy} with temperature for a water droplet (115 μm nominal diameter, 796 pL) and an ice crystal (117.2-118.4 μm diameter depending on temperature, 842-869 pL) is shown in Fig. C3a in the ESI, and demonstrates the greater buoyancy forces on the ice crystals across the full temperature range of 0 to −35 °C, below which homogeneous freezing is expected to start occurring for water droplets of this size. The difference in F_{buoy} between the ice crystals and water droplets, ΔF_{buoy}, is shown theoretically in Fig. C3b in the ESI, and provides the means by which the two can be separated in continuous flow. This effect is further reflected in the theoretical u_{buoy} values, as shown in Fig. C4a in the ESI, which indicates the increased velocity of ice crystals in the y-direction of the separation chamber compared to the water droplets. The difference in u_{buoy} between the water droplets and ice crystals, Δu_{buoy}, determines the extent of the separation of the two components in flow, and this difference is shown theoretically in Fig. C4b in the ESI. The F_{buoy} and u_{buoy} values for water and ice are negative,

indicating that they would each cream rather than sediment with respect to gravity, but are shown in ESI Figs. C3-C4 as positive values for simplicity.

It must also be noted that whilst the cold stages could reach temperatures below −40 °C, the temperature of the separation chamber was controlled separately to the main channel where freezing occurred. The separation chamber was held at temperature slightly below 0 °C, which would prevent any ice crystals formed in the main channel from melting, but would also not trigger ice nucleation in the unfrozen supercooled water droplets. This also meant that separations would occur in the temperature regime at which the differences in u_{buoy} were maximised (e.g. between 0 to −5 °C).

4.2. Experimental

4.2.1. Chemicals

3M™ Novec™ 7500 Engineered Fluid, a fluorinated heat transfer oil, was purchased from Fluorochem Ltd. (Hadfield, UK). Pico-Surf™ 1 fluorinated surfactant (5 % w/w in Novec™ 7500) was purchased from Sphere Fluidics Ltd. (Cambridge, UK), and further diluted to 0.2 % w/w in Novec™ 7500. Snomax® Snow Inducer (Snomax International, Englewood, CO, USA) was purchased from SMI Snow Makers AG (Thun, Switzerland) and prepared in purified water to a concentration of 0.01 % w/w. The purified water (18.2 MΩ cm at 25 °C, 0.22 μm filtered) was obtained via a Sartorius arium® pro water purification system. Poly(dimethylsiloxane) (PDMS, Dow Corning® Sylgard® 184 Kit) was purchased from Ellsworth Adhesives (East Kilbride, UK). MicroChem SU-8 2075 photoresist was purchased from A-Gas Electronic Materials Ltd. (Rugby, UK).

4.2.2. Microfluidic chip design

The microfluidic chip design was adapted from the continuous droplet freezing design of Tarn et al.,(Tarn et al., 2020) with the downstream addition of a wide separation chamber and corresponding inlet and outlet channels (Figure 4.1c). Briefly, the design featured a flow focussing nozzle (40 μm wide) for droplet generation, with pillar-based particle filters and fluidic resistors located between the inlets and the nozzle. The nozzle

expanded into a long, central main channel (300 μm wide) for the freezing of droplets as they flowed down the channel. The main channel then fed into a 10.9 mm wide by 11.6 mm long separation chamber, which was also fed by an "upper control flow" inlet channel (200 μm) at the top of the chamber and a "lower control flow" inlet channel (200 μm) at the bottom via branching inlet channels.

Branched outlet channels (218 μm wide each) were situated at the end of the separation chamber and consisted of an ice crystal outlet from the upper part of the chamber, a water droplet outlet from the middle of the chamber, and a waste outlet from the lower part of the chamber. The water droplet outlet was designed to have lower backpressure than the ice crystal outlet in order to capture any water droplets that were tending slightly towards the ice crystal outlet. Alignment marks were added to the design to enable alignment of the chip over a series of temperature-controlled plates on a cold stage platform.
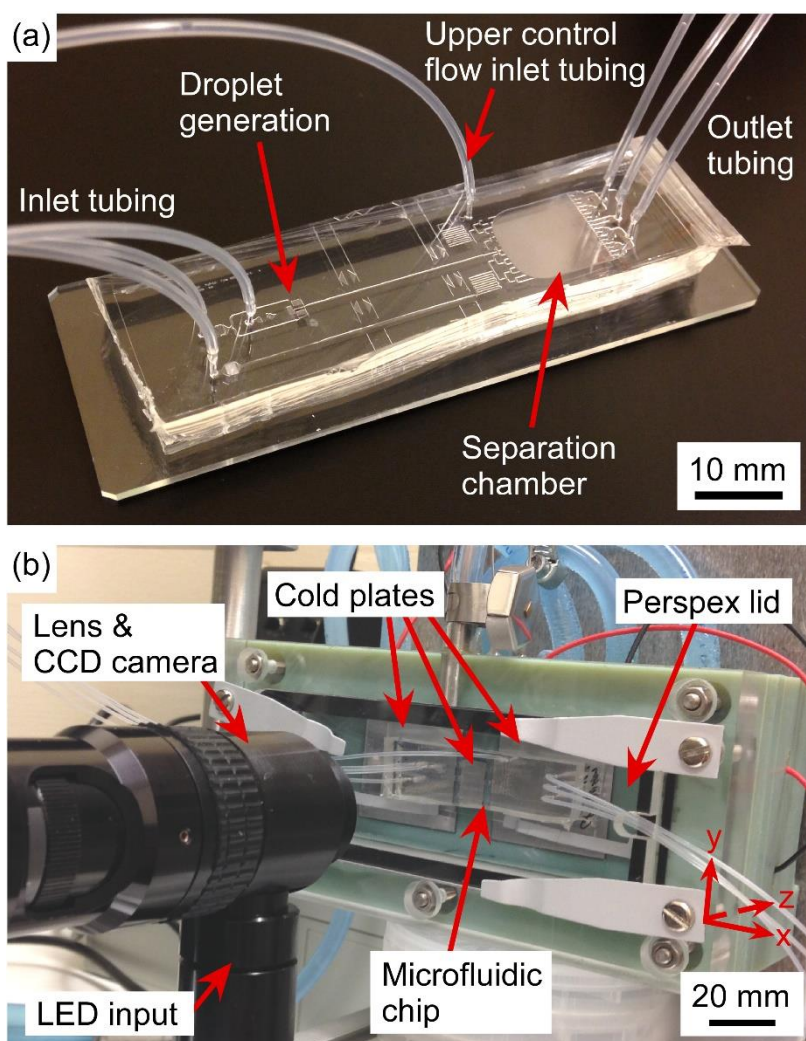
Figure 4.2 Setup of the microfluidic sorting apparatus. (a) The microfluidic chip fabricated in poly(dimethylsiloxane) (PDMS) and with tubing connected. (b) Photograph of the microfluidic device situated in the cold stage platform. Alignment marks on the chip allowed its accurate placement over three temperature-controlled plates that aligned with the droplet generation nozzle, the main channel for droplet freezing, and the separation chamber. The cold stage platform was placed on its side so that the separation chamber was oriented vertically.

4.2.3. Fabrication of the microfluidic device

The microfluidic device was fabricated in PDMS, as described by Tarn et al. (Tarn et al., 2020), using standard soft lithography techniques (Effenhauser et al., 1997; Duffy et al., 1998; McDonald et al., 2000). A detailed description of the process is provided in Section 8 of the ESI. Briefly, the microfluidic chip design was patterned via a mask aligner onto SU-8 2075 photoresist that had been spin-coated onto a silicon wafer. Following photodevelopment, PDMS was poured onto the mould, degassed, and cured. The PDMS was

then peeled off the mould, access holes (1 mm Ø) were punched into it, and it was finally bonded to a glass microscope slide via plasma treatment to yield the final device with a channel depth of 140 µm (Figure 4.2a).

4.2.4. Experimental setup

A detailed description of the experimental setup (Figure 4.2b) is provided in Section 8 of the ESI, and largely employed the apparatus and setup of the LOC-NIPI described by Tarn et al.(Tarn et al., 2020) Polyethylene tubing (0.38 mm i.d. × 1.09 mm o.d.) was inserted into the access holes of the PDMS chip and the inlet tubing was connected to syringes located in syringe pumps (PHD Ultra, Harvard Apparatus, Biochrom Ltd., UK). The chip was placed into the chamber of a custom-built cold stage that had been turned on its side, such that the separation chamber of the chip was oriented vertically so that its width (10.9 mm) was now its height and its height (140 µm) was now its width, and clips were used to hold the chip in place. A similar sideways orientation had been employed by Stan et al.(Stan, Guglielmini, et al., 2011; Stan et al., 2013) in their studies of the buoyancy and lift forces of water droplets and ice crystals.

The cold stage platform comprised three temperature-controlled aluminium plates that were set into a 3D printed body. The plate temperatures were controlled using Peltier elements via a proportional-integral-derivative (PID) loop, and the Peltier elements were themselves cooled using liquid heat exchangers connected to a refrigerated recirculating chiller. The alignment marks of the microfluidic chip were used to ensure that each major section of the chip (i.e. the flow focussing junction, main channel where freezing occurred, and separation chamber) was situated across one of the plates (see Figure 4.1c). The previous version of the platform required the microfluidic chips to be coated with a layer of chromium on the underside in order to provide a reflective surface on which to visualise droplets using reflected light microscopy.(Tarn et al., 2020) Here, however, the aluminium plates of the cold stage were polished to render them much more reflective, meaning that droplets could be observed in the chip without the need for a chromium layer.

A Perspex lid was placed onto the cold stage platform to form a chamber, and dry air was pumped into the chamber to purge it of moisture. Visualisation of the microchannels and separation chamber inside the

microfluidic device was achieved using a Navitar Zoom 6000® Lens System (Mengel Engineering, Denmark) with a Phantom Miro Lab 120 high-speed camera (Vision Research Ltd., Bedford, UK).

4.2.5. Experimental procedure

The channels of the microfluidic chip were first purged with Novec™ 7500 Engineered Fluid to wet the channel and tubing surfaces and to remove air bubbles. Water-in-oil droplets were generated at the flow focussing nozzle of the chip by pumping an aqueous suspension of 0.01 % w/w Snomax® into the aqueous inlet at 0.1 µL min⁻¹, while Novec™ 7500 Engineered Fluid was pumped into the oil inlet at 25 µL min⁻¹. Novec™ 7500 was pumped into the upper control flow channel at a flow rate of 113-115 µL min⁻¹ in order to control the flow rate in the x-direction that in turn would affect the deflection of water droplets and ice crystals in the chamber, as per Equation 4. However, the higher flow rate of the upper control flow compared to that of the droplet generation channel would also result in a downward flow in the y-direction near to the entrance of separation chamber, which would likely have an effect on u_{buoy} and therefore u_{defl} of the droplets and crystals. Novec™ 7500 was also pumped into the lower control flow channel only to purge the channel and fill the lower section of the separation chamber with fluid, but no flow from this inlet was necessary during experiments.

The microfluidic chip was aligned on the cold stage platform and the aluminium plate temperatures were set to a specific temperature for each stage of the chip. The plate beneath the flow focussing junction was set to +3 °C to ensure that water did not freeze in the aqueous inlet channel or the nozzle. The cold plate beneath the main channel was set to a temperature of −17 °C in order to freeze approximately half of the Snomax®-containing water droplets as they flowed over the plate. The plate beneath the separation chamber was set at −8 °C, which was determined to yield a temperature in the separation chamber of −4.8 ± 0.2 °C.

The measurement of the temperature inside the separation chamber was performed separately to the droplet experiments by inserting calibrated thermocouples into the central region of the chamber and then setting the flow rates and temperature setpoints to those used during droplet sorting (see Section 9 of the ESI for a more detailed description of the procedure). This allowed the fluid to flow over the tip of the thermocouples inside the

separation chamber in the region through which the droplets would traverse during the sorting experiments. Therefore, it was assumed that the temperatures measured by the thermocouples were equivalent to the temperature of the droplets in the separation chamber. These measurements were used to inform on the viscosity of the Novec™ 7500 oil and the densities of the Novec™ 7500 oil, supercooled water, and ice that were used in calculations of experimental F_{buoy} values and of the theoretically expected F_{buoy} and u_{buoy} values. However, we note that this temperature only applied to a specific region of the chamber, while the temperature throughout the chamber was likely varied and complex given the several sources of fast-flowing liquid entering from different points.

Images and videos of the water droplets and ice crystals were collected as they exited the separation chamber under specific flow rates and plate temperatures. ImageJ software (https://imagej.nih.gov/ij/) was used to measure the diameters and velocities of the objects in the x-direction and y-direction in the chamber to determine u_{hyd} and u_{buoy}, respectively. For each run, 25 water droplets and 25 ice crystals were chosen at random for analysis of their diameter and velocity. A scale was determined using a known distance inside the chamber (i.e. the width of an outlet channel). The velocities were determined by averaging the change in positions in the x- and y-directions over the separation chamber across multiple images, and using the framerate to determine the time taken for this change. Droplet diameter and velocity values are quoted as an average over all of the runs, along with the combined uncertainty of the standard deviation in these measurements and the measurement resolution of the video analysis (±4 µm).
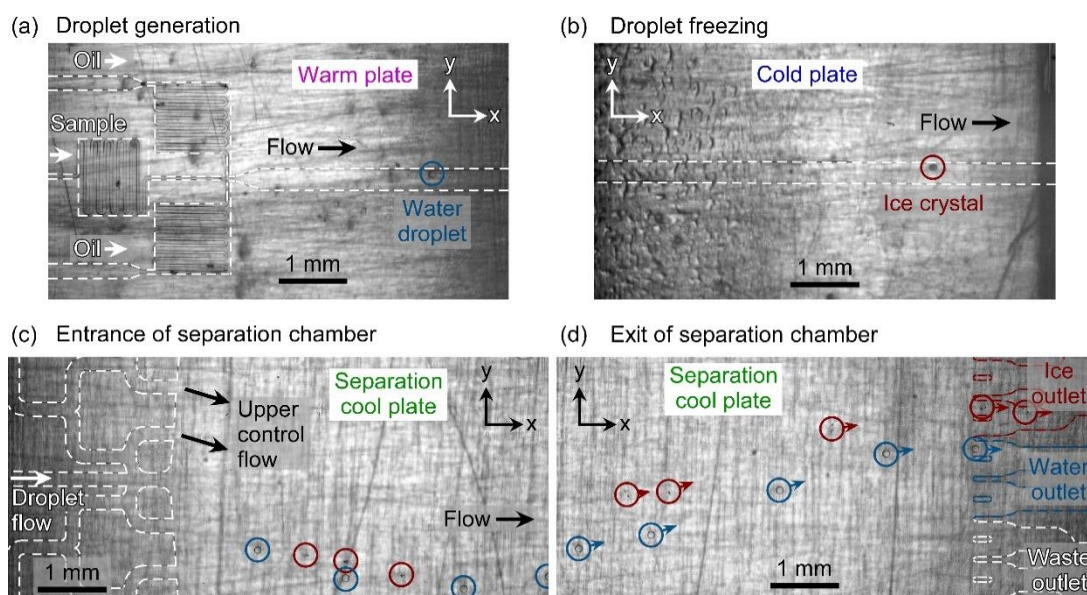
Figure 4.3 Photographs showing the lifetime of supercooled water droplets (circled in blue) and ice crystals (circled in red) as they (a) are generated at the flow focussing nozzle over a warm plate, (b) pass along the main channel above the cold plate and are potentially frozen (as demonstrated in this case), (c) enter the separation chamber at a temperature slightly below 0 °C and experience a brief downward motion due to the higher applied flow rate of the upper control flow, and (d) traverse the chamber and exit via different outlets depending on whether they are frozen or liquid.

4.3.   Results and Discussion

4.3.1. Droplet generation, freezing and flow in the separation channel

Aqueous droplets of Snomax® (0.01 % w/w) were generated in Novec™ 7500 fluorinated oil and flowed over the cold plate and into the separation chamber of the microfluidic device. Snomax® Snow Inducer is a non-viable, lyophilised form of *Pseudomonas syringae* bacteria (Hirano and Upper, 2000) that is well-known for its exceptional ice-nucleating ability (Wex et al., 2015; Polen et al., 2016), making it a very useful material for testing ice nucleation equipment and methodologies. The generated water-in-oil droplet diameters were 118 ± 6 µm (870 ± 139 pL), and were produced at a rate of 1.5 ± 0.4 droplets s^{-1}. This droplet production rate was appropriate for the current throughput of the current version of the LOC-NIPI platform,(Tarn et al., 2020) which is limited by the freezing step. Increasing the throughput significantly would require

the redesign of the freezing channel to maximise the time droplets spend over the cold plate.

The generated droplets (Figure 4.3a) passed along the main channel and over the central cold plate (Figure 4.3b), with around half of the droplet population freezing as they travelled over the plate. In the lighting conditions employed, water droplets were visualised as being clear and colourless with a black outline, whilst ice crystals appeared as nearly transparent circles with small, black imperfections. Upon freezing, the ice crystals retained their spherical shape, although the formation of small spicules (a single, needle-shaped protrusion that can form as part of the droplet freezing process)(Wildeman et al., 2017) was occasionally observed. These spicules would affect the drag of the ice crystals to some extent, and occasionally resulted in an ice crystal becoming temporarily stuck in the chamber, but this was only observed for a small number of crystals and have not been accounted for in our calculations.

After exiting the cold plate region, the supercooled water droplets and ice crystals continued along the main channel and into the separation chamber. Due to the flow from the upper control channel being greater than that of the main channel, and the lower part of the chamber experiencing no applied flow, the droplets/crystals momentarily travelled downwards in the y-direction immediately upon entering the chamber (Figure 4.3c). Within ~5 mm of entering the 11.6 mm long chamber (in the x-direction), however, the droplets and crystals began to rise in the Novec™ 7500 oil due to the effect of buoyancy, whereupon their deflection direction could be controlled by the applied flow rate of the upper control flow (Figure 4.3d)

4.3.2. Water droplet and ice crystal buoyancies

The water droplets that entered the chamber had a measured u_{hyd} velocity in the x-direction of 1,667 ± 82 µm s^{-1}, while the ice crystals had a measured u_{hyd} velocity of 1,817 ± 106 µm s^{-1}. This demonstrated an increase of 9 ± 2 % in u_{hyd} velocity of the ice crystals compared to the water droplets due to the difference in diameter, and possibly also due to the effect of the ice crystals entering the higher velocity flow stream of the upper control flow.

The migration of the droplets/crystals in the y-direction as they creamed in the separation chamber was measured to provide experimental u_{buoy} values, and these are provided in Table 1 for two identical microfluidic devices,

labelled Chip A and Chip B, with one experimental run performed in the former and three in the latter.
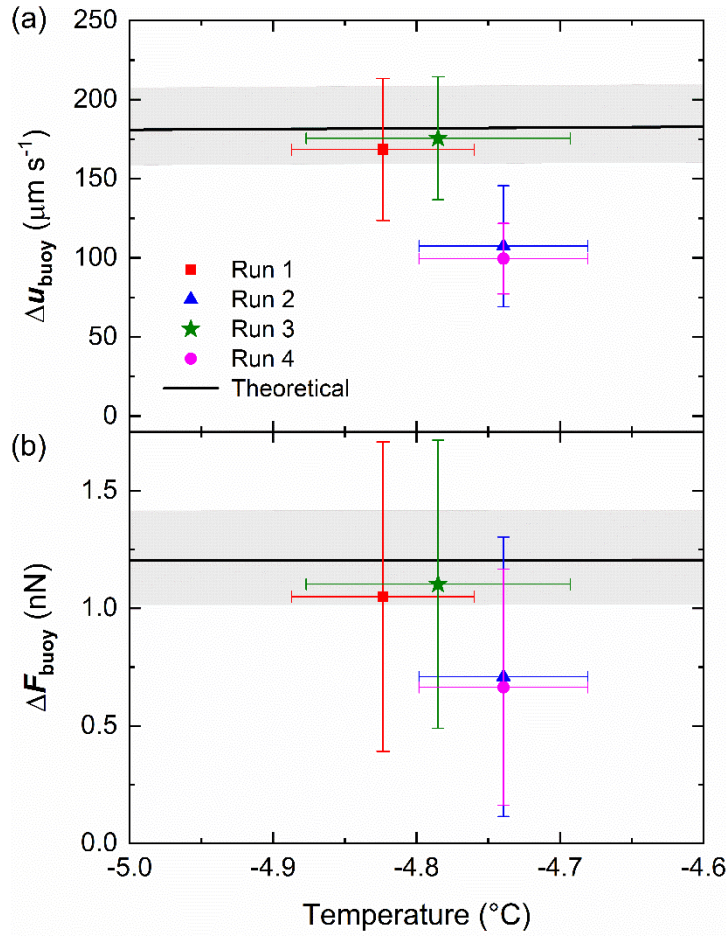
Figure 4.4 (a) The experimental and theoretically expected differences in ubuoy between ice crystals and water droplets in the microfluidic device. Theoretical values were calculated based on the measured diameters of the water droplets, with the average diameter shown by the black line and the standard deviation represented by the grey band (b) The corresponding experimental and theoretical values of the differences in Fbuoy between the water droplets and ice crystals. Further details of the experimental runs are provided in Table 1.

Table 1. Average experimental y-direction velocity (u_{buoy}) and gravitational force (F_{buoy}) values of liquid water droplets and ice crystals, together with the differences in u_{buoy} and F_{buoy} between the two, for Chips A and B. Uncertainties in Δu_{buoy} and ΔF_{buoy} were calculated in quadrature.

Experimental run	Chip	Droplets/ crystals	u_{buoy} (µm s⁻¹)	Δu_{buoy} (µm s⁻¹)	F_{buoy} (nN)	ΔF_{buoy} (nN)
1	A	Water droplets	491 ± 23	168 ± 45	2.7 ± 0.3	1.0 ± 0.7
		Ice crystals	659 ± 21		3.8 ± 0.3	
2	B	Water droplets	528 ± 19	107 ± 38	3.0 ± 0.3	0.7 ± 0.6
		Ice crystals	635 ± 20		3.7 ± 0.3	
3	B	Water droplets	460 ± 19	176 ± 39	2.6 ± 0.3	1.1 ± 0.6
		Ice crystals	636 ± 20		3.7 ± 0.3	
4	B	Water droplets	530 ± 11	100 ± 22	3.0 ± 0.3	0.7 ± 0.5
		Ice crystals	630 ± 12		3.7 ± 0.3	
Average		**Water droplets**	**502 ± 40**	**138 ± 55**	**2.8 ± 0.6**	**0.9 ± 0.8**
		Ice crystals	**640 ± 37**		**3.7 ± 0.6**	

The ice crystals experienced a greater u_{buoy} velocity in the y-direction as they creamed, an average increase of 28 ± 10 % compared to the water droplets, indicating the potential for their separation. The differences in experimental u_{buoy} between the ice crystals and water droplets, Δu_{buoy}, which directly determines the ability to separate the two, are illustrated in

Figure 4.4a. Theoretically expected Δu_{buoy} values were calculated from Equation 3, based on the average diameter of the water droplets, and are shown in Figure 4.4a as a black line (with the standard deviation shown as a grey band, based on the variation in droplet diameter).

The experimental Δu_{buoy} values from chips A and B matched the theory very well in two of the runs, and importantly for both chips, and were slightly lower than expected in two other runs despite an otherwise identical setup. The possible reasons for this will be discussed later. The experimental F_{buoy} values were also calculated from the measured u_{buoy} values using Equation 2 (assuming that $F_{buoy} = F_{vis}$), using viscosities and densities of supercooled water, ice crystals, and Novec™ 7500 determined as described in ESI Sections 3-6, and the temperature in the separation chamber discussed earlier. These experimental values are provided in Table 1. As expected given the u_{buoy} results, the F_{buoy} forces were greater on the ice crystals than the water droplets. The differences in F_{buoy} between the two are also provided in Table 1 and are plotted in Figure 4.4b alongside the theoretically expected ΔF_{buoy} values. Given that the ΔF_{buoy} were derived from the Δu_{buoy} values, the same trends are unsurprisingly observed in the former as the latter.

The lower than expected Δu_{buoy} and ΔF_{buoy} values that occurred in some experiments likely stemmed as a result of the placement on the cold stage platform. Since the chips were located over the cold plates without the presence of any oil between the two to assist in heat transfer, the temperature in the chamber may have been higher than expected if the contact between the chip and the separation cool plate was poor. This could have occurred since the chip and the cold plates were oriented vertically and so their contact was not assisted by gravity (the chip was held in place with clips connected to the cold stage platform). Furthermore, hydrodynamic lift forces(Stan, Guglielmini, et al., 2011; Stan et al., 2013) have not been accounted for in our analyses due to the large height of the chamber when oriented vertically. However, in the event that the setup was not perfectly oriented in the vertical direction and the chip was slightly tilted to differing extents in different experiments, this could introduce effects of lift forces and affect the viscous drag caused by the channel walls.

Some of these effects could be addressed in future iterations of the platform, e.g. by better controlling the orientation and clamping of the chip, and through the use of an oil between the chip and the platform to improve

thermal contact. Nevertheless, the results demonstrated that Δu_{buoy} and ΔF_{buoy} were positive and close to the theoretically expected values, indicating that the separation of frozen and unfrozen droplets was feasible using this technique.
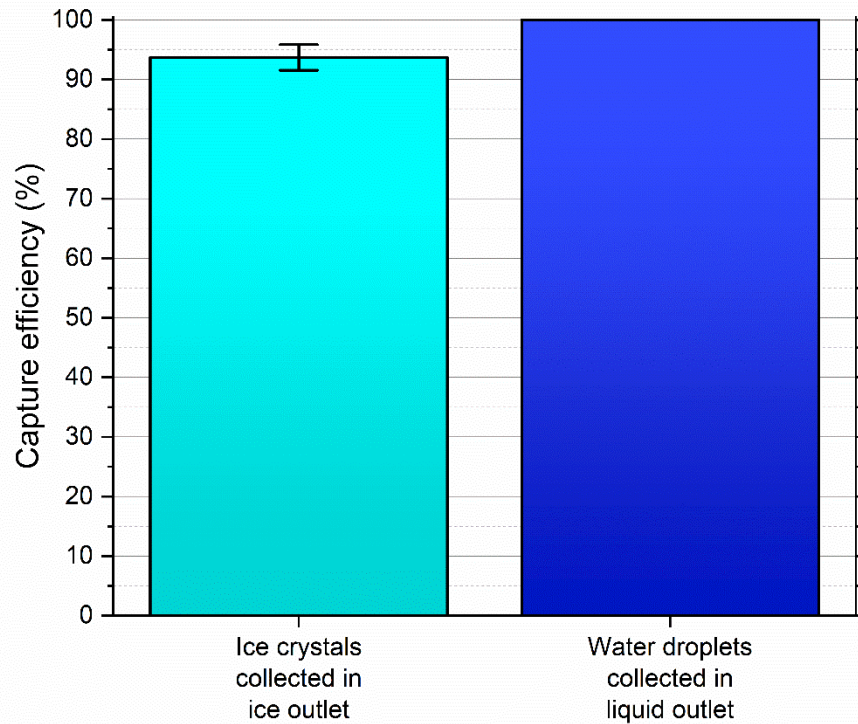
Figure 4.5 Plot showing the collection efficiencies of ice crystals and water droplets into their respective outlet channels in the microfluidic sorting chamber. The results were generated from three individual experiments, comprising 105 ± 16 water droplets/ice crystals in total per run.

4.3.3. Water droplet and ice crystal separations

The magnitude of Δu_{buoy} and ΔF_{buoy} between the water droplets and ice crystals is clear (see Figure 4.4), with the ice crystals migrating notably faster than water droplets in the y-direction in Novec™ 7500, and this difference was leveraged to enable their separation in the microfluidic chamber. As the objects travelled through the chamber and separated based on their u_{buoy} velocities, they each exited the chamber via one of the outlet channels (see Figure 4.3d and the ESI for video footage of droplet separation). The numbers of water droplets and ice crystals that exited via

the ice crystal outlet system and the water droplet outlet system were counted for a given droplet population, and this was used to determine the separation efficiencies. Results were obtained for three experimental runs (one in chip A and two in chip B), with 105 ± 16 water droplets/ice crystals counted in total per run, and are shown in Figure 4.5.

In all cases, only ice crystals were found to exit the separation chamber via the ice outlet (i.e. no water droplets entered this outlet), with a collection efficiency of 94 ± 2 % of the total ice crystal population. This meant that, while 100 % of water droplets exited via the water outlet, a small number of ice crystals (6 ± 2 % of the ice crystal population) also exited the chamber through the water outlet. Therefore, it was successfully demonstrated that ice crystals and water droplets could be separated into different outlets in continuous flow with high efficiency and reproducibility across multiple runs and in two different chips.

Continuous flow separations are affected by temperature, with changes in viscosity affecting not only the u_{buoy} component of the deflection velocity, u_{defl}, but also the u_{hyd} component (Tarn et al., 2009). It was found that the laboratory temperature could influence the migration of the droplets and crystals since the upper control flow rate into the chamber was so high that the Novec™ 7500 did not have time to fully equilibrate with the plate temperature, hence the temperature at which the fluid was held outside of the chip influenced its temperature inside the chip. This issue was largely eliminated in this particular instance by the use of air conditioning to control the laboratory temperature. In a future update of the chip design, this could be solved via the use of a longer serpentine inlet channel for the upper control flow inlet channel, which would allow a longer equilibration time over the separation cool plate prior to entering the separation chamber.

Several other changes to the chip design and operation could also be implemented to achieve 100 % separation efficiency with respect to both water droplets and ice crystals. Several of the features of the current chip design were somewhat superfluous, being a product of testing various mechanisms and flow regimes during the development of the technique. Therefore, future iterations of the design would be far more refined. The extent of the initial separation of the droplets and crystals could be enhanced relatively easily by employing a gradual or sudden expansion into the separation chamber, which would accentuate the difference in u_{buoy} velocities between the water droplets and ice crystals.(Huh et al., 2007;

Song et al., 2014) Such improvements would also enable the application of much higher droplet throughputs, since droplet/crystal sorting could potentially still be achieved at much higher flow rates and droplet generation rates. This would help to enable high-throughput downstream processing or analysis, or would allow the rapid collection of enough sample volume for off-chip operations.

Another possible means of enhancing the separation could be to adapt the methodology of Kamijo and Derda(Kamijo and Derda, 2019) to a microfluidic device. In this scenario, the upper control flow would comprise a low viscosity silicone oil (5 cSt at 25 °C), having a density between that of supercooled water and ice, rather than the Novec™ 7500 Engineered Fluid ($\rho_{\text{fluorinated oil}} > \rho_{\text{water}} > \rho_{\text{silicone oil}} > \rho_{\text{ice}}$). As the droplets and crystals rose to the top of the Novec™ 7500 phase, the former would be unable to cross the interface into the silicone oil whilst the latter could cross and continue migrating in the y-direction. However, this strategy may be less simple than it sounds due to the very low theoretical u_{buoy} velocities the ice crystals would experience in such a medium. Hence, a system comprised fully of Novec™ 7500 may still be the preferable option, particularly given the improvements proposed above. Section 10 of the ESI provides a more detailed analysis and discussion of the silicone oil strategy as well as its potential benefits and difficulties.

4.3.4. Outlook for the application of water droplet-ice crystal sorting

The density-based sorting of supercooled water droplets and ice crystals in continuous flow has been achieved for the first time in a microfluidic device, and quite possibly in any platform, with high separation efficiency. This technique could aid in a number of applications as outlined in the introduction. In particular, we can see immediate potential for use in two fields, namely low temperature biology(Daily et al., 2020) and atmospheric ice nucleation.(Hoose and Möhler, 2012; Murray et al., 2012) In the former case, it could be envisaged that water droplets containing cells could be exposed to "ideal" freezing conditions (e.g. with ice nucleation triggered at high temperatures to minimise supercooling)(John Morris and Acton, 2013) to ensure a high level of viability amongst the droplet population that froze in those specific conditions. Thereafter, those frozen specimens could be sorted and collected to ensure only cells with a high likelihood of viability were stored at low temperatures for future use. This might be a useful

method for reducing aliquot-to-aliquot variability in viability related to freezing temperature.(John Morris and Acton, 2013; Daily et al., 2020) While this approach is unlikely to be cost-effective for cells in plentiful supply, it might be useful for high-value cells such as human stem cells, which have potential for use in cancer treatments.(Chu et al., 2020)

A particularly useful application could be in the selection and concentration of biological ice-nucleating materials that exhibit exceptional ice-nucleating abilities at warmer temperatures, such as certain strains of bacteria, which would enable the subsequent culturing of a highly active form of ice nucleators. A similar approach might also be useful for identifying ice-nucleating materials or organisms in the environment, such as pathogenic ice-nucleating strains of bacteria that can cause frost damage to plants.(Lindow et al., 1982) At present, this is achieved through laborious processes,(Hill et al., 2014; Šantl-Temkiv et al., 2015) for example involving repeatedly dividing a sample and selecting the aliquot that has the highest freezing temperature and therefore the most active ice-nucleating entity.(Hill et al., 2016) Also, plating out environmental samples on a growth medium and then testing the resulting colonies for their ice-nucleating activity is often performed, but this approach is only sensitive to organisms amenable to culture.(Šantl-Temkiv et al., 2015) In principle, the frozen-unfrozen droplet sorting technique presented here could be used to isolate ice-nucleating biological material, such as a bacteria cells, which might then be cultured or the DNA analysed directly for identification.

The sorting technique could prove very powerful in its application to atmospheric ice nucleation. Currently, it can be very difficult to ascertain the identity of atmospheric ice-nucleating particles (INPs) given their rarity. While it is possible to determine the ice-nucleating activity of a collected aerosol sample using a droplet freezing assay, in which the sample is suspended in droplets of water that are subsequently frozen, it is much harder to determine which component of that sample actually triggered the nucleation event. By sorting frozen and unfrozen droplets whose ice nucleation was triggered at different temperatures, it should be possible to test the two collected outputs to determine which components were present in the frozen population that were not (or were present to a lesser extent) in the unfrozen population. In order to achieve separation of ice-active material from non-ice-active materials it would be necessary to use suspensions which were sufficiently dilute that they have around one insoluble aerosol

particle per droplet. Appropriate analyses on the collected droplet populations for INP identification could include scanning electron microscopy with energy dispersive X-ray spectroscopy (SEM-EDS),(McCluskey et al., 2014; Wang et al., 2016; Kiselev et al., 2017; Ault and Axson, 2017; Reicher et al., 2019; Sanchez-Marroquin et al., 2019) DNA analysis,(Garcia et al., 2012; Huffman et al., 2013; Hill et al., 2014; Šantl-Temkiv et al., 2019) Raman spectroscopy,(Iwata and Matsuki, 2018) and a variety of other microscopic and spectroscopic techniques used in aerosol particle analysis.(Ariya et al., 2009; Kolb and Worsnop, 2012; Ault and Axson, 2017; Laskin et al., 2018) The identification and characterisation of the INPs present in the frozen droplet populations would then help to inform on their sources and global transport. It can also be foreseen that such analytical techniques could be translated onto an integrated microfluidic platform that combines the droplet freezing and separation steps with upstream aerosol collection(Noblitt et al., 2009; Jing et al., 2013; Mirzaee et al., 2016; Damit, 2017; Metcalf et al., 2018) and downstream analytical processing, potentially yielding a micro total analysis system (μTAS) (Reyes et al., 2002; Patabadige et al., 2016) for atmospheric INPs. Indeed, there are any number of on-chip microanalytical techniques that could be applied to the chemical or biological analysis of the separated populations. (Yew et al., 2019; Song et al., 2019)

In addition to sorting droplets for collection, the separation of water droplets and ice crystals into different channels also provides an alternative avenue for determining the fraction frozen of a droplet population at a given temperature, $f_{ice}(T)$. Fraction frozen data allows information to be gleaned from both homogeneous ice nucleation (i.e. pure water without the presence of INPs) and heterogeneous ice nucleation experiments. For example, several properties of an ice- nucleating material can be calculated from $f_{ice}(T)$, including the ice nuclei concentration in the sample and the ice-active site density, which quantifies a material's effectiveness at nucleating ice. The current strategy of calculating $f_{ice}(T)$ in the LOC-NIPI platform involves the counting of droplets in the main channel using a high-speed camera, and determining the number that freeze based on a colour change during a nucleation event.(Tarn et al., 2020) While it is possible to automate this detection step it is also somewhat challenging, with the image requiring a clear background and the video file sizes being relatively large. However, sorting the droplets and crystals into separate channels could facilitate a far

simpler analysis by incorporating single-point detection systems over the two outlet channels, allowing the simple counting of the number of objects that pass through each. This would require 100% separation efficiency to ensure accurate results but should be achievable given the improvements to the platform detailed earlier, and would eliminate the need for an expensive high- speed camera and image analysis.

4.4.   Conclusions

We have developed a microfluidic platform, based on our LOC-NIPI ice nucleation analysis system, for the continuous sorting of ice crystals from supercooled water droplets. The ice crystals and water droplets were sorted based on the differences in their buoyancy as they traversed a separation chamber and exited via different outlet channels, with 94 ± 2 % separation efficiency achieved. Collection of the sorted populations will, in future, enable the concentration and isolation of the populations, and will allow further analysis to characterise their respective contents.

This represents a powerful new technique in ice nucleation that can be used to separate droplets with specific ice-nucleating activity for a range of applications. Its use in cryobiology could allow high levels of viability to be maintained in cryopreserved biological samples by ensuring only the droplets that froze under specific conditions were collected. The ability to isolate and culture highly ice-active biomaterials, such as bacteria, could additionally enable the production of new standards of highly active ice-nucleating agents. In atmospheric science, the technique could facilitate the identification and characterisation of ambient INPs via their separation from a bulk aerosol sample. This could help to revolutionise our understanding of the types, origins, and transport of different types of INPs around the globe.(Huh et al., 2007; Song et al., 2014) In addition to improvements in the separation efficiency of the platform, we can also envisage incorporation of upstream aerosol collection and downstream microanalytical techniques to yield an integrated analysis platform for ice nucleation applications.

References

The data sets for this paper and videos of the experimental runs are available in the University of Leeds Data Repository (https://doi.org/10.5518/848; Porter et al. 2020b).(Porter et al., 2020b)

Abdelmonem, A., Backus, E.H.G., Hoffmann, N., Sánchez, M.A., Cyran, J.D., Kiselev, A. and Bonn, M. 2017. Surface-charge-induced orientation of interfacial water suppresses heterogeneous ice nucleation on α-alumina (0001). *Atmospheric Chemistry and Physics*. **17**(12), pp.7827–7837.

Ariya, P.A., Sun, J., Eltouny, N.A., Hudson, E.D., Hayes, C.T. and Kos, G. 2009. Physical and chemical characterization of bioaerosols – Implications for nucleation processes. *Int. Rev. Phys. Chem.* **28**, pp.1–32.

Atig, D., Touil, A., Ildefonso, M., Marlin, L., Bouriat, P. and Broseta, D. 2018. A droplet-based millifluidic method for studying ice and gas hydrate nucleation. *Chemical Engineering Science*. **192**, pp.1189–1197.

Ault, A.P. and Axson, J.L. 2017. Atmospheric Aerosol Chemistry: Spectroscopic and Microscopic Advances. *Analytical Chemistry*. **89**(1), pp.430–452.

Bissoyi, A., Reicher, N., Chasnitsky, M., Arad, S., Koop, T., Rudich, Y. and Braslavsky, I. 2019. Ice nucleation properties of ice-binding proteins from snow fleas. *Biomolecules*. **9**(10), p.532.

Brubaker, T., Polen, M., Cheng, P., Ekambaram, V., Somers, J., Anna, S.L. and Sullivan, R.C. 2020. Development and characterization of a "store and create" microfluidic device to determine the heterogeneous freezing properties of ice nucleating particles. *Aerosol Science and Technology*. **54**(1), pp.79–93.

Chu, D.-T., Nguyen, T.T., Tien, N.L.B., Tran, D.-K., Jeong, J.-H., Anh, P.G., Thanh, V. Van, Truong, D.T. and Dinh, T.C. 2020. Recent Progress of Stem Cell Therapy in Cancer Treatment: Molecular Mechanisms and Potential Applications. *Cells*. **9**(3), p.563.

Daily, M.I., Whale, T.F., Partanen, R., Harrison, A.D., Kilbride, P., Lamb, S., Morris, G.J., Picton, H.M. and Murray, B.J. 2020. Cryopreservation of primary cultures of mammalian somatic cells in 96-well plates benefits from control of ice nucleation. *Cryobiology*. **93**, pp.62–69.

Damit, B. 2017. Droplet-based microfluidics detector for bioaerosol

detection. *Aerosol Science and Technology*. **51**(4), pp.488–500.

Duffy, D.C., McDonald, J.C., Schueller, O.J.A. and Whitesides, G.M. 1998. Rapid prototyping of microfluidic systems in poly(dimethylsiloxane). *Analytical Chemistry*. **70**(23), pp.4974–4984.

Edd, J.F., Humphry, K.J., Irimia, D., Weitz, D.A. and Toner, M. 2009. Nucleation and solidification in static arrays of monodisperse drops. *Lab on a Chip*. **9**(13), pp.1859–1865.

Effenhauser, C.S., Bruin, G.J.M., Paulus, A. and Ehrat, M. 1997. Integrated Capillary Electrophoresis on Flexible Silicone Microdevices: Analysis of DNA Restriction Fragments and Detection of Single DNA Molecules on Microchips. *Analytical Chemistry*. **69**(17), pp.3451–3457.

Eickhoff, L., Dreischmeier, K., Zipori, A., Sirotinskaya, V., Adar, C., Reicher, N., Braslavsky, I., Rudich, Y. and Koop, T. 2019. Contrasting Behavior of Antifreeze Proteins: Ice Growth Inhibitors and Ice Nucleation Promoters. *Journal of Physical Chemistry Letters*. **10**(5), pp.966–972.

Elliott, G.D., Wang, S. and Fuller, B.J. 2017. Cryoprotectants: A review of the actions and applications of cryoprotective solutes that modulate cell recovery from ultra-low temperatures. *Cryobiology*. **76**, pp.74–91.

Fahy, G.M. 1995. The Role of Nucleation in Cryopreservation *In*: R. E. Lee Jr., G. J. Warren and L. V Gusta, eds. *Biological Ice Nucleation and Its Applications*. St. Paul, MN: APS Press, p.331.

Fahy, G.M., Saur, J. and Williams, R.J. 1990. Physical problems with the vitrification of large biological systems. *Cryobiology*. **27**, pp.492–510.

Garcia, E., Hill, T.C.J., Prenni, A.J., DeMott, P.J., Franc, G.D. and Kreidenweis, S.M. 2012. Biogenic ice nuclei in boundary layer air over two U.S. high plains agricultural regions. *Journal of Geophysical Research Atmospheres*. **117**(17), p.D18.

Geidobler, R. and Winter, G. 2013. Controlled ice nucleation in the field of freeze-drying: Fundamentals and technology review. *European Journal of Pharmaceutics and Biopharmaceutics*. **85**(2), pp.214–222.

Haeberle, S., Brenner, T., Zengerle, R. and Ducrée, J. 2006. Centrifugal extraction of plasma from whole blood on a rotating disk. *Lab Chip*. **6**, pp.776–781.

Happel, J. and Brenner, H. 1973. *Low Reynolds number hydrodynamics*. 2nd Rev. Leyden: Noordhoff International Publishing.

Hare, D.E. and Sorensen, C.M. 1987. The density of supercooled water. II. Bulk samples cooled to the homogeneous nucleation limit. *J. Chem.*

Phys. **87**, pp.4840–4845.

Häusler, T., Witek, L., Felgitsch, L., Hitzenberger, R. and Grothe, H. 2018. Freezing on a Chip-A new approach to determine heterogeneous ice nucleation of micrometer-sized water droplets. *Atmosphere.* **9**(4), p.140.

Hill, T.C.J., Demott, P.J., Tobo, Y., Fröhlich-Nowoisky, J., Moffett, B.F., Franc, G.D. and Kreidenweis, S.M. 2016. Sources of organic ice nucleating particles in soils. *Atmospheric Chemistry and Physics.* **16**(11), pp.7195–7211.

Hill, T.C.J., Moffett, B.F., DeMott, P.J., Georgakopoulos, D.G., Stump, W.L. and Franc, G.D. 2014. Measurement of Ice Nucleation-Active Bacteria on Plants and in Precipitation by Quantitative PCR. *Appl. Environ. Microbiol.* **80**, pp.1256–1267.

Hirano, S.S. and Upper, C.D. 2000. Bacteria in the Leaf Ecosystem with Emphasis onPseudomonas syringae—a Pathogen, Ice Nucleus, and Epiphyte. *Microbiology and Molecular Biology Reviews.* **64**(3), pp.624–653.

Hoose, C. and Möhler, O. 2012. Heterogeneous ice nucleation on atmospheric aerosols: a review of results from laboratory experiments. *Atmos. Chem. Phys. Atmospheric Chemistry and Physics.* **12**(20), pp.9817–9854.

Huffman, J.A., Prenni, A.J., Demott, P.J., Pöhlker, C., Mason, R.H., Robinson, N.H., Fröhlich-Nowoisky, J., Tobo, Y., Després, V.R., Garcia, E., Gochis, D.J., Harris, E., Müller-Germann, I., Ruzene, C., Schmer, B., Sinha, B., Day, D.A., Andreae, M.O., Jimenez, J.L., Gallagher, M., Kreidenweis, S.M., Bertram, A.K. and Pöschl, U. 2013. High concentrations of biological aerosol particles and ice nuclei during and after rain. *Atmospheric Chemistry and Physics.* **13**(13), pp.6151–6164.

Huh, D., Bahng, J.H., Ling, Y., Wei, H.H., Kripfgans, O.D., Fowlkes, J.B., Grotberg, J.B. and Takayama, S. 2007. Gravity-driven microfluidic particle sorting device with hydrodynamic separation amplification. *Analytical Chemistry.* **79**(4), pp.1369–1376.

Iiguni, Y., Suwa, M. and Watarai, H. 2004. High-magnetic-field electromagnetophoresis of micro-particles in a capillary flow system. *J. Chromatogr. A.* **1032**(1–2), pp.165–171.

Iwata, A. and Matsuki, A. 2018. Characterization of individual ice residual particles by the single droplet freezing method: a case study in the Asian dust outflow region. *Atmos. Chem. Phys.* **18**, pp.1785–1804.

Jing, W., Zhao, W., Liu, S., Li, L., Tsai, C.T., Fan, X., Wu, W., Li, J., Yang, X. and Sui, G. 2013. Microfluidic device for efficient airborne bacteria

capture and enrichment. *Analytical Chemistry*. **85**(10), pp.5255–5262.

Jo, M.C. and Guldiken, R. 2012. Active density-based separation using standing surface acoustic waves. *Sensors and Actuators, A: Physical*. **187**, pp.22–28.

John Morris, G. and Acton, E. 2013. Controlled ice nucleation in cryopreservation - A review. *Cryobiology*. **66**(2), pp.85–92.

Johnson, A.C. and Bowser, M.T. 2018. Micro free flow electrophoresis. *Lab Chip*. **18**, pp.27–40.

Kalman, H., Portnikov, D., Gabrieli, O.G. and Tripathi, N.M. 2019. What do pneumatic conveying and hydraulic conveying have in common? *Powder Technology*. **354**, pp.485–495.

Kamijo, Y. and Derda, R. 2019. Freeze-Float Selection of Ice Nucleators. *Langmuir*. **35**(2), pp.359–364.

Kanji, Z.A., Ladino, L.A., Wex, H., Boose, Y., Burkert-Kohn, M., Cziczo, D.J. and Krämer, M. 2017. Overview of Ice Nucleating Particles. *Meteorological Monographs*. **58**, 1.1-1.33.

Kiani, H. and Sun, D.W. 2011. Water crystallization and its importance to freezing of foods: A review. *Trends in Food Science and Technology*. **22**(8), pp.407–426.

Kiselev, A., Bachmann, F., Pedevilla, P., Cox, S.J., Michaelides, A., Gerthsen, D. and Leisner, T. 2017. Active sites in heterogeneous ice nucleation-the example of K-rich feldspars. *Science*. **355**(6323), pp.367–371.

Knopf, D.A., Alpert, P.A., Zipori, A., Reicher, N. and Rudich, Y. 2020. Stochastic nucleation processes and substrate abundance explain time-dependent freezing in supercooled droplets. *npj Climate and Atmospheric Science*. **3**(1), pp.1–9.

Kolb, C.E. and Worsnop, D.R. 2012. Chemistry and Composition of Atmospheric Aerosol Particles. *Annu. Rev. Phys. Chem.* **63**, pp.471–491.

Koop, T. and Murray, B.J. 2016. A physically constrained classical description of the homogeneous nucleation of ice in water. *The Journal of Chemical Physics*. **145**(21), p.211915.

Laskin, J., Laskin, A. and Nizkorodov, S.A. 2018. Mass Spectrometry Analysis in Atmospheric Chemistry. *Analytical Chemistry*. **90**(1), pp.166–189.

Lenshof, A. and Laurell, T. 2010. Continuous separation of cells and particles in microfluidic systems. *Chem. Soc. Rev.* **39**, pp.1203–1217.

Lenshof, A., Magnusson, C. and Laurell, T. 2012. Acoustofluidics 8: Applications of acoustophoresis in continuous flow microsystems. *Lab Chip.* **12**, pp.1210–1223.

Lindow, S.E., Arny, D.C. and Upper, C.D. 1982. Bacterial Ice Nucleation: A Factor in Frost Injury to Plants. *Plant Physiol.* **70**, pp.1084–1089.

McCluskey, C.S., DeMott, P.J., Prenni, A.J., Levin, E.J.T., McMeeking, G.R., Sullivan, A.P., Hill, T.C.J., Nakao, S., Carrico, C.M. and Kreidenweis, S.M. 2014. Characteristics of atmospheric ice nucleating particles associated with biomass burning in the US: Prescribed burns and wildfires. *J. Geophys. Res. Atmos.* **119**, pp.10458–10470.

McDonald, J.C., Duffy, D.C., Anderson, J.R., Chiu, D.T., Wu, H., Schueller, O.J.A. and Whitesides, G.M. 2000. Fabrication of microfluidic systems in poly(dimethylsiloxane). *Electrophoresis.* **21**(1), pp.27–40.

Metcalf, A.R., Narayan, S. and Dutcher, C.S. 2018. A review of microfluidic concepts and applications for atmospheric aerosol science. *Aerosol Science and Technology.* **52**(3), pp.310–329.

Mirzaee, I., Song, M., Charmchi, M. and Sun, H. 2016. A microfluidics-based on-chip impinger for airborne particle collection. *Lab on a Chip.* **16**(12), pp.2254–2264.

Morijiri, T., Sunahiro, S., Senaha, M., Yamada, M. and Seki, M. 2011. Sedimentation pinched-flow fractionation for size- and density-based particle sorting in microchannels. *Microfluidics and Nanofluidics.* **11**(1), pp.105–110.

Murray, B.J., O'sullivan, D., Atkinson, J.D. and Webb, M.E. 2012. Ice nucleation by particles immersed in supercooled cloud droplets. *Chemical Society Reviews.* **41**(19), pp.6519–6554.

Nam, J., Lim, H., Kim, C., Yoon Kang, J. and Shin, S. 2012. Density-dependent separation of encapsulated cells in a microfluidic channel by using a standing surface acoustic wave. *Biomicrofluidics.* **6**(2), p.024120.

Noblitt, S.D., Lewis, G.S., Liu, Y., Hering, S. V., Collett, J.L. and Henry, C.S. 2009. Interfacing microchip electrophoresis to a growth tube particle collector for semicontinuous monitoring of aerosol composition. *Analytical Chemistry.* **81**(24), pp.10029–10037.

Norouzi, N., Bhakta, H.C. and Grover, W.H. 2017. Sorting cells by their density. *Plos One.* **12**, p.e0180520.

Pamme, N. 2007. Continuous flow separations in microfluidic devices. *Lab Chip.* **7**, pp.1644–1659.

Pamme, N. and Manz, A. 2004. On-chip free-flow magnetophoresis: Continuous flow separation of magnetic particles and agglomerates. *Anal. Chem.* **76**, pp.7250–7256.

Park, J.K., Campos, C.D.M., Neužil, P., Abelmann, L., Guijt, R.M. and Manz, A. 2015. Direct coupling of a free-flow isotachophoresis (FFITP) device with electrospray ionization mass spectrometry (ESI-MS). *Lab Chip.* **15**, pp.3495–3502.

Patabadige, D.E.W., Jia, S., Sibbitts, J., Sadeghi, J., Sellens, K. and Culbertson, C.T. 2016. Micro Total Analysis Systems: Fundamental Advances and Applications. *Analytical Chemistry.* **88**(1), pp.320–338.

Peckhaus, A., Kiselev, A., Hiron, T., Ebert, M. and Leisner, T. 2016. A comparative study of K-rich and Na/Ca-rich feldspar ice-nucleating particles in a nanoliter droplet freezing assay. *Atmospheric Chemistry and Physics.* **16**(18), pp.11477–11496.

Peyman, S.A., Kwan, E.Y., Margarson, O., Iles, A. and Pamme, N. 2009. Diamagnetic repulsion - A versatile tool for label-free particle handling in microfluidic devices. *J. Chromatogr. A.* **1216**(52), pp.9055–9062.

Polen, M., Lawlis, E. and Sullivan, R.C. 2016. The unstable ice nucleation properties of Snomax® bacterial particles. *Journal of Geophysical Research.* **121**(19), pp.11666–11678.

Porter, G.C.E., Sikora, S.N.F., Shim, J., Murray, B.J. and Tarn, M.D. 2020. *Data for 'On-chip density-based sorting of ice crystals and supercooled water droplets in continuous flow' University of Leeds. [Dataset]. https://doi.org/10.5518/848.*

Pruppacher, H.R. and Klett, J.D. 1997. *Microphysics of Clouds and Precipitation* 2nd ed. Kluwer Academic Publishers.

Raymond, D.E., Manz, A. and Widmer, H.M. 1994. Continuous Sample Pretreatment Using a Free-Flow Electrophoresis Device Integrated onto a Silicon Chip. *Anal. Chem.* **66**, pp.2858–2865.

Reicher, N., Budke, C., Eickhoff, L., Raveh-Rubin, S., Kaplan-Ashiri, I., Koop, T. and Rudich, Y. 2019. Size-dependent ice nucleation by airborne particles during dust events in the eastern Mediterranean. *Atmos. Chem. Phys.* **19**, pp.11143–11158.

Reicher, N., Segev, L. and Rudich, Y. 2018. The Weizmann Supercooled Droplets Observation on a Microarray (WISDOM) and application for ambient dust. *Atmospheric Measurement Techniques.* **11**(1), pp.233–

248.

Reyes, D.R., Iossifidis, D., Auroux, P.A. and Manz, A. 2002. Micro total analysis systems. 1. Introduction, theory, and technology. *Analytical Chemistry*. **74**(12), pp.2623–2636.

Riechers, B., Wittbracht, F., Hütten, A. and Koop, T. 2013. The homogeneous ice nucleation rate of water droplets produced in a microfluidic device and the role of temperature uncertainty. *Physical Chemistry Chemical Physics*. **15**(16), pp.5873–5887.

Sajeesh, P. and Sen, A.K. 2014. Particle separation and sorting in microfluidic devices: A review. *Microfluid. Nanofluid.* **17**(1), pp.1–52.

Sanchez-Marroquin, A., Hedges, D.H.P., Hiscock, M., Parker, S.T., Rosenberg, P.D., Trembath, J., Walshaw, R., Burke, I.T., McQuaid, J.B. and Murray, B.J. 2019. Characterisation of the filter inlet system on the FAAM BAe-146 research aircraft and its use for size-resolved aerosol composition measurements. *Atmospheric Measurement Techniques*. **12**(11), pp.5741–5763.

Šantl-Temkiv, T., Lange, R., Beddows, D., Rauter, U., Pilgaard, S., Dall'osto, M., Gunde-Cimerman, N., Massling, A. and Wex, H. 2019. Biogenic Sources of Ice Nucleating Particles at the High Arctic Site Villum Research Station. *Environmental Science and Technology*. **53**(18), pp.10580–10590.

Šantl-Temkiv, T., Sahyoun, M., Finster, K., Hartmann, S., Augustin-Bauditz, S., Stratmann, F., Wex, H., Clauss, T., Nielsen, N.W., Sørensen, J.H., Korsholm, U.S., Wick, L.Y. and Karlson, U.G. 2015. Characterization of airborne ice-nucleation-active bacteria and bacterial fragments. *Atmos. Environ.* **109**, pp.105–117.

Sgro, A.E., Allen, P.B. and Chiu, D.T. 2007. Thermoelectric manipulation of aqueous droplets in microfluidic devices. *Analytical Chemistry*. **79**(13), pp.4845–4851.

Sgro, A.E. and Chiu, D.T. 2010. Droplet freezing, docking, and the exchange of immiscible phase and surfactant around frozen droplets. *Lab on a Chip*. **10**(14), pp.1873–1877.

Song, J., Song, M., Kang, T., Kim, D. and Lee, L.P. 2014. Label-free density difference amplification-based cell sorting. *Biomicrofluidics*. **8**(6), p.64108.

Song, Y., Lin, B., Tian, T., Xu, X., Wang, W., Ruan, Q., Guo, J., Zhu, Z. and Yang, C. 2019. Recent Progress in Microfluidics-Based Biosensing. *Analytical Chemistry*. **91**(1), pp.388–404.

Springston, S.R., Myers, M.N. and Giddings, J.C. 1987. Continuous Particle Fractionation Based on Gravitational Sedimentation in Split-Flow Thin Cells. *Analytical Chemistry*. **59**(2), pp.344–350.

Stan, C.A., Ellerbee, A.K., Guglielmini, L., Stone, H.A. and Whitesides, G.M. 2013. The magnitude of lift forces acting on drops and bubbles in liquids flowing inside microchannels. *Lab on a Chip*. **13**(3), pp.365–376.

Stan, C.A., Guglielmini, L., Ellerbee, A.K., Caviezel, D., Stone, H.A. and Whitesides, G.M. 2011. Sheathless hydrodynamic positioning of buoyant drops and bubbles inside microchannels. *Physical Review E*. **84**(3), p.036302.

Stan, C.A., Schneider, G.F., Shevkoplyas, S.S., Hashimoto, M., Ibanescu, M., Wiley, B.J. and Whitesides, G.M. 2009. A microfluidic apparatus for the study of ice nucleation in supercooled water drops. *Lab on a Chip*. **9**(16), pp.2293–2305.

Stan, C.A., Tang, S.K.Y., Bishop, K.J.M. and Whitesides, G.M. 2011. Externally applied electric fields up to 1.6 × 105 V/m do not affect the homogeneous nucleation of ice in supercooled water. *Journal of Physical Chemistry B*. **115**(5), pp.1089–1097.

Strohmeier, O., Keller, M., Schwemmer, F., Zehnle, S., Mark, D., Von Stetten, F., Zengerle, R. and Paust, N. 2015. Centrifugal microfluidic platforms: advanced unit operations and applications. *Chemical Society Reviews*. **44**(17), pp.6187–6229.

Sugiyama, D., Teshima, Y., Yamanaka, K., Briones-Nagata, M.P., Maeki, M., Yamashita, K., Takahashi, M. and Miyazaki, M. 2014. Simple density-based particle separation in a microfluidic chip. *Anal. Methods*. **6**, pp.308–311.

Tarn, M., Sikora, S., Porter, G., Wyld, B., Alayof, M., Reicher, N., Harrison, A., Rudich, Y., Shim, J. and Murray, B. 2020. On-chip analysis of atmospheric ice-nucleating particles in continuous flow. *Lab on a Chip*. **20**(16), pp.2889–2910.

Tarn, M.D., Peyman, S.A., Robert, D., Iles, A., Wilhelm, C. and Pamme, N. 2009. The importance of particle type selection and temperature control for on-chip free-flow magnetophoresis. *Journal of Magnetism and Magnetic Materials*. **321**(24), pp.4115–4122.

Tarn, M.D., Sikora, S.N.F., Porter, G.C.E., O'Sullivan, D., Adams, M., Whale, T.F., Harrison, A.D., Vergara-Temprado, J., Wilson, T.W., Shim, J. uk and Murray, B.J. 2018. The study of atmospheric ice-nucleating particles via microfluidically generated droplets. *Microfluid. Nanofluid.* **22**(5), p.52.

Ukita, Y., Oguro, T. and Takamura, Y. 2017. Density-gradient-assisted centrifugal microfluidics: an approach to continuous-mode particle separation. *Biomed. Microdevices*. **19**, p.24.

Vergara-Temprado, J., Miltenberger, A.K., Furtado, K., Grosvenor, D.P., Shipway, B.J., Hill, A.A., Wilkinson, J.M., Field, P.R., Murray, B.J. and Carslaw, K.S. 2018. Strong control of Southern Ocean cloud reflectivity by ice-nucleating particles. *Proc. Natl. Acad. Sci. U. S. A.* **115**(11), pp.2687–2692.

Wang, B., Knopf, D.A., China, S., Arey, B.W., Harder, T.H., Gilles, M.K. and Laskin, A. 2016. Direct observation of ice nucleation events on individual atmospheric particles. *Physical Chemistry Chemical Physics*. **18**, pp.29721–29731.

Weng, L., Swei, A. and Toner, M. 2018. Role of synthetic antifreeze agents in catalyzing ice nucleation. *Cryobiology*. **84**, pp.91–94.

Weng, L., Tessier, S.N., Smith, K., Edd, J.F., Stott, S.L. and Toner, M. 2016. Bacterial Ice Nucleation in Monodisperse D2O and H2O-in-Oil Emulsions. *Langmuir*. **32**(36), pp.9229–9236.

Wex, H., Augustin-Bauditz, S., Boose, Y., Budke, C., Curtius, J., Diehl, K., Dreyer, A., Frank, F., Hartmann, S., Hiranuma, N., Jantsch, E., Kanji, Z.A., Kiselev, A., Koop, T., Möhler, O., Niedermeier, D., Nillius, B., Rösch, M., Rose, D., Schmidt, C., Steinke, I. and Stratmann, F. 2015. Intercomparing different devices for the investigation of ice nucleating particles using Snomax® as test substance. *Atmospheric Chemistry and Physics*. **15**(3), pp.1463–1485.

Wildeman, S., Sterl, S., Sun, C. and Lohse, D. 2017. Fast Dynamics of Water Droplets Freezing from the Outside in. *Physical Review Letters*. **118**(8), p.084101.

Winkleman, A., Perez-Castillejos, R., Gudiksen, K.L., Phillips, S.T., Prentiss, M. and Whitesides, G.M. 2007. Density-Based Diamagnetic Separation: Devices for Detecting Binding Events and for Collecting Unlabeled Diamagnetic Particles in Paramagnetic Solutions. *Anal. Chem.* **79**, pp.6542–6550.

Wyatt Shields IV, C., Reyes, C.D. and Lopez, G.P. 2015. Microfluidic cell sorting: a review of the advances in the separation of cells from debulking to rare cell isolation. *Lab Chip*. **15**, pp.1230–1249.

Xi, H.-D., Zheng, H., Guo, W., Gañán-Calvo, A.M., Ai, Y., Tsao, C.-W., Zhou, J., Li, W., Huang, Y., Nguyen, N.-T. and Tan, S.H. 2017. Active droplet sorting in microfluidics: a review. *Lab Chip*. **17**, pp.751–771.

Xie, Y., Mao, Z., Bachman, H., Li, P., Zhang, P., Ren, L., Wu, M. and Huang,

T.J. 2020. Acoustic Cell Separation Based on Density and Mechanical Properties. *Journal of Biomechanical Engineering.* **142**(3), p.031005.

Yew, M., Ren, Y., Koh, K.S., Sun, C. and Snape, C. 2019. A Review of State-of-the-Art Microfluidic Technologies for Environmental Applications: Detection and Remediation. *Glob. Chall.* **3**(1), p.1800060.

Zhao, W., Cheng, R., Miller, J.R. and Mao, L. 2016. Label-Free Microfluidic Manipulation of Particles and Cells in Magnetic Liquids. *Adv. Funct. Mater.* **26**, pp.3916–3932.

Zipori, A., Reicher, N., Erel, Y., Rosenfeld, D., Sandler, A., Knopf, D.A. and Rudich, Y. 2018. The Role of Secondary Ice Processes in Midlatitude Continental Clouds. *Journal of Geophysical Research: Atmospheres.* **123**(22), pp.12762–12777.

5. Overview and conclusions

The central Arctic is a unique environment, and due to the difficulty in obtaining measurements of INP in such a remote and low-aerosol location, information about the sources, concentrations and effects of INP on mixed-phase clouds over the central Arctic ocean is lacking (Schmale et al., 2021). In part due to this lack of understanding, Arctic mixed-phase clouds are not well represented in large-scale models (Morrison et al., 2012; Pithan et al., 2016; Schmale et al., 2021) and this has consequences for the prediction of the surface energy budget in the Arctic (Xie et al., 2013). This thesis aimed to address this challenge through the use of current and novel instrumentation to elucidate potential sources, characteristics and effects of the INP population over the central Arctic ocean. Firstly, with the development of a high-volume balloon-borne sampler that allows the collection of aerosol in different atmospheric layers, in order to determine the difference in INP populations between decoupled layers. This was followed by an intensive measurement campaign over the central Arctic ocean within the MOCCHA campaign, aboard the icebreaker Oden that culminated in a unique dataset which revealed valuable characteristics about high Arctic INP during the campaign. Finally, towards the isolation and identification of INP, a novel instrument was designed which would allow the non-disruptive separation of INP in a mixed sample. This chapter provides conclusions for each project objective and for the project as a whole.

5.1.   Project objective 1)   The building of a high-flow rate, size-selective aerosol sampling system which could be remotely operated, and deployed above the surface mixed boundary layer

It came to my attention early in the project that field campaigns that involved ground-based measurements were extremely useful because they allowed long-term monitoring of INP populations at interesting locations, and were accessible to many research groups. However, the relationship between ground-based INP concentrations and those which could affect low-level mixed-phase clouds is not well defined. For places such as the high Arctic where ground/ship-based measurements are already difficult to attain, aircraft measurements are even rarer. Factors such as the distance of the

central Arctic ocean from land, have resulted in there being no arial INP measurements made thus far near the North Pole (88-90°N). However, the regular appearance of stratified, separated mixed layers in the Arctic (Brooks et al., 2017), make the difference between ground and arial INP concentrations all the more important to understand.

Knowing that I was planning to lead a research project on the MOCCHA campaign to the central Arctic, a sampler which was capable of determining INP populations above the surface mixed layer was of great interest to me. No commercially available options would have suited the purpose. We expected low INP concentrations based on previous campaigns, and so estimated that we needed to sample 10s-100s of litres of air per minute over a period of hours to observe an INP signal. Drones were an obvious choice, but their battery lives of the order of 30 minutes, and low payload capacities meant we quickly discounted them as an option until battery technology improved. Weather balloons are often used to launch radiosondes, and access to helium is available through gas cylinders. Tethered balloons provide an option for larger payloads than drones and can be kept airborne for periods of many hours. Therefore, a tethered balloon-borne system was designed, and called the selective height aerosol research kit, or SHARK.

In order to attain the desired flow rates, cascade impactors were chosen. The pressure required to pull air over a set of cascading stages is much lower than to pull air through a filter. Therefore, the pump could be smaller, lighter, and operate for longer than using filter based collection of aerosol. This was ideal for an arial collection device. Additionally, the cascade impactors provided sample collection onto substrates which were made from the filters we used in our ground-based measurements using the µL-NIPI technique (Whale et al., 2015), and so could be directly compared. The cascade impactors also give information about INP concentrations in different size ranges, since aerosol of different diameter will be preferentially collected on different plates. Two cascade impactors were used to cover a larger size range. The smaller impactor for <0.25 (via an after-filter) to >2.5 µm in diameter, and the larger impactor for 1 to >10 µm.

Finally, the size of the payload allowed by tethered balloons allowed an optical particle counter to be mounted alongside the aerosol sampling instrumentation in order to be able to determine the INP concentrations with respect to aerosol size. All of these instruments were remotely operated from the ground, meaning sampling could be turned on and off when the

temperature or humidity around the instrument (which was being monitored via instrumentation within the SHARK housing) was not ideal for sampling, or during ascent and descent.

The instrument was tested in four locations, and the results of this are detailed in Chapter 1. Although the chapter was focused on the building and design of the SHARK, the results from these campaigns paint an interesting picture of the way INP concentrations vary with aerosol size in different environments. It was shown that larger aerosol size does not always correlate with more active INP populations.

In future, the SHARK should be used on field campaigns where ground/ship-based measurements of INP are being taken, and a distinct atmospheric structure may affect the ability of ground-based INP to access mixed-phase clouds. For instance, in a boreal forest location, where INP relating to plant matter around the forest may/may not enter the cloud mixed layer.

5.2. Project objective 2) To gather ice-nucleating particle concentration data in the high Arctic, specifically the central Arctic ocean, towards elucidating the characteristics and effects of the ice-nucleating particles present

The second, and arguably largest objective in this project was to conduct a field campaign to the central Arctic ocean, and determine potential sources of INP which could enter the mixed-phased clouds there. The radiative budget of the Arctic is partly modulated by persistent mixed-phased clouds, and so is of current interest due to the rapid changes the Arctic is experiencing owing to global warming (Serreze and Barry, 2011). Constraining the INP concentrations of the Arctic, and understanding how INP concentrations may change with the Arctic over time, is imperative to be able to understand the predict the effects on mixed-phase clouds there. To this end, a successful INP field campaign was completed during the Arctic summer of 2018 during the MOCCHA expedition. The results are presented and described throughout Chapter 2.

The first and most fundamental dataset we wished to capture was the INP concentrations measured on-ship throughout the entire duration of the two-month campaign, including the travel through open water, over the MIZ, during ice-breaking, and adrift with an ice-floe. We were hopeful that we

would be able to capture the effects of the autumnal freeze-up on INP concentrations, and were lucky enough to have achieved this. The picture of INP in the central Arctic ocean was very different to what we had expected. The variability was extreme, with INP activation temperatures ranging from -9 to -30 °C for a concentration of 0.1 INP L^{-1}, and concentrations varying from 6×10^{-3} INP L^{-1} to 2 INP L^{-1} at -15 °C. We measured concentrations as low as would be expected in the Southern Ocean, to as high as those we had seen in UK farmland. This is higher than we would expect for such a pristine environment, where the aerosol concentrations were orders of magnitude lower than those in terrestrial environments like the rural UK. Some of the concentrations measured were similar to INP measurements made around the periphery of the Arctic ocean, at ground-based stations in the summer. Additionally, the samples which were tested for the presence of biogenic material through a heat-test, consistently demonstrated that the warmer temperature INP above around -15 to -20 °C was removed by heating and so likely related to ice-nucleating proteins of biogenic origin.

The SHARK was deployed above the surface mixed layer. This culminated in eight total flights where the INP concentration was determined in the "cloud mixed layer", which was just above and decoupled from the surface mixed layer. We assumed that the temperature inversion signalled the decoupling of the aerosol in both of these layers and so the measurements in the cloud mixed layer were compared to those taken on ship within the surface mixed layer. There was often a significant difference between the measurements within and above the surface mixed layer. Out of the eight SHARK samples, a single SHARK sample had much lower ice nucleating activity than that within the surface mixed layer, three samples had higher activity, three had similar activity and one that was close to the baseline. The INP concentration within the surface mixed layer, measured on-ship, was intermittently decoupled to the concentrations in the cloud mixed layer.

Additionally, the size of INP above in the cloud mixed layer was captured, and interestingly, it was often the smallest aerosol, <0.25 μm which gave the highest measured INP concentrations. The larger, coarse mode aerosol, at 2.5 – 10 μm, was often in the baseline, excluding one flight when this size range dominated. These smaller size ranges dominating INP concentrations could be expected for long-range transported aerosol.

There was no correlation between the INP concentrations and DMS, a product of marine biogenic processes which was thought to be transported

to the ship location (88-90°N) from the MIZ. There was however, a positive correlation between transported eBC and INP ($r = 0.65$), indicating the more INP laden aerosol originated from further afield than the central Arctic ocean.

The analysis of air parcel 7-day back trajectories concluded that air that was rich in highly active INP originated from the costal seas of Russia, whereas air parcels containing the least active INP were more local, and spent the majority of the trajectory over the pack ice.

Thanks to consistent radiosonde launches, which we helped with when we could, we were able to calculate the INP concentration which would occur at ambient atmospheric temperature, $[INP]_{ambient}$. Despite the large variability in INP concentrations within the surface mixed layer, $[INP]_{ambient}$ was far less variable, and was usually at or below $\sim 10^{-2}$ L^{-1}. Within the cloud mixed layer, $[INP]_{ambient}$ was on average slightly higher, between 10^{-1}-10^{-2} L^{-1}, however these were all limiting values, and so the actual values are likely to be below this.

Overall, this part of the project culminated in a deeper understanding of Arctic INP close to the North Pole, and a characterisation of INP during the summer-autumn of 2018. This included determining that a likely potential source of highly active INP to the central Arctic ocean was the costal seas of Russia, whereas locally produced aerosol was less active. The biogenic nature of the INP and the correlation with costal locations away from the central Arctic ocean suggest that these sources may be susceptible to change with global warming. Finally, we concluded that the $[INP]_{ambient}$ determined from the expedition data was consistent with the observed persistence of Arctic mixed-phase clouds, and that INP concentrations measured within the surface mixed layer were intermittently decoupled from the cloud mixed layer. These conclusions should be used to encourage future measurement campaigns in the Arctic, specifically using samplers that can probe the cloud mixed layer, to gain a better insight into the temporal and spatial variability in INP close to the North Pole.

5.3.   Project objective 3)   To design and create a method by which droplets containing low concentrations of sampled atmospheric aerosol could be separated, depending on the presence of an INP

The final part of the project was to determine a method for the non-invasive separation of INP active at a specific temperature. Such a method would facilitate comparisons between the sample populations which were and were not active at specific temperatures in a variety of instruments, or the probing of single INPs which were seen to freeze at the desired temperature. This type of separation would not only be useful for fundamental atmospheric ice nucleation research and field sample analysis, but for disciplines such as food science, medical science and cryobiology, and in the production of artificial snow.

Very near the beginning of this body of work, I decided to try and use microfluidics to separate droplets from ice crystals in flow. This was owing to the unique LOC-NIPI platform being developed at the time, designed for the high throughput freezing of droplets in-flow, which would allow the integration of such a sorting device. After returning from the Arctic, I was able to spend time with the newly finished LOC-NIPI (Tarn et al., 2021) and test various configurations that would allow the autonomous sorting of droplets in flow.

Initially, a weir design was trialled, attempting to use the difference in size and compressibility between the droplets and ice crystals to separate the populations. However, the tolerances needed to achieve this were beyond what was practical for a disposable device. Secondly, a density based-approach based on the one shown by Kamijo and Derda, (2019) was trialled. This involved a separation chamber filled with different oil layers, where the upper oil layer had a density between that of water and ice, allowing only ice to pass into the upper oil layer of the chamber. The timescales for this were too long however, and so this was also not used. Finally, a variation of the density based chamber was produced. The chamber was filled with an oil which was less dense than both water and ice. The chamber was made to be long and tall enough to allow the passive, density-based sorting of the liquid droplets and ice crystals, and their subsequent collection via different outlets. The description of this technique is given in Chapter 3.

The density-based sorting technique proved to be 94 ± 2% effective at separating the ice and liquid droplets into different outlet channels. This was the first time that ice and water droplets had been successfully separated in-flow on a microfluidic device. The nature of microfluidic devices means that this technique can be integrated into devices which contain other on-chip analysis, or used alone for the quick separation of populations which exhibit different ice-nucleating activity.

Looking forward, this sorting technique could also be made more efficient. The chip design could be refined to include pinched-flow fractionation, and longer channels could be used to reduce temperature fluctuations. Then, ideally this technique would be used to identify the specific particles responsible for ice-nucleation within a sample, and therefore aid in the determination of the characteristics which make a good ice-nucleator, or the identification of which parts of an atmospheric sample are responsible for the ice-nucleating activity. This is especially useful for samples from low-aerosol environments such as the central Arctic ocean. This is because the entire sample can be used with little contamination, meaning relatively, there is a very low detection limit. Additionally, in low-aerosol environments it is harder to relate INP concentrations to changes in bulk aerosol, so being able to separate out the INPs would allow more in-depth analysis.

5.4.   Concluding remarks

This thesis describes progress towards the characterisation of INP in remote and low-aerosol environments such as the central Arctic ocean. Instrumentation which will allow better access to relevant and important INP measurements and analysis, has been designed, developed and tested. The SHARK allows the determination of INP concentrations within the cloud mixed layer without the need for aircraft, and the passive sorting of INP from a bulk sample allows the analysis of INP in a way which has thus far not been available to the community. Fieldwork has been conducted which has elucidated properties and effects of INP in a location unlike anywhere on earth, which is changing faster than anywhere else.

The INP population close to the North Pole (88-90°N), was extremely variable, and influenced by sources outside of the central Arctic ocean. Air packets which transported highly active, biogenic INPs to the surface mixed layer close to the North Pole originated in the costal seas of Russia. The

pack ice and MIZ were weak sources of INP. Additionally, the cloud mixed layer was often decoupled from the surface mixed layer in terms of INP population, highlighting the need for more arial measurements. The INP concentration calculated at ambient temperature stayed relatively constant throughout the campaign, and the values indicated the persistence of Arctic mixed-phase clouds, which has been observed.

Future work would ideally see the instrumentation developed here used on further field campaigns to the central Arctic, building on the dataset shown here. Specifically, obtaining more measurements both in the cloud-mixed layer and the surface-mixed layer, and using the microfluidic sorting device to determine the chemical differences between aerosol particles that acted as INPs and those which did not. The development of an on-line microfluidic device for this purpose may allow the airborne, on-line collection and analysis of INP above the surface mixed-layer, which would drastically alter the speed at which valuable characteristics of Arctic INPs could be obtained.

References

Brooks, I.M., Tjernström, M., Persson, P.O.G., Shupe, M.D., Atkinson, R.A., Canut, G., Birch, C.E., Mauritsen, T., Sedlar, J. and Brooks, B.J. 2017. The Turbulent Structure of the Arctic Summer Boundary Layer During The Arctic Summer Cloud-Ocean Study. *Journal of Geophysical Research: Atmospheres*. **122**(18), pp.9685–9704.

Kamijo, Y. and Derda, R. 2019. Freeze-Float Selection of Ice Nucleators. *Langmuir*. **35**(2), pp.359–364.

Morrison, H., De Boer, G., Feingold, G., Harrington, J., Shupe, M.D. and Sulia, K. 2012. Resilience of persistent Arctic mixed-phase clouds. *Nature Geoscience*. **5**(1), pp.11–17.

Pithan, F., Ackerman, A., Angevine, W.M., Hartung, K., Ickes, L., Kelley, M., Medeiros, B., Sandu, I., Steeneveld, G.J., Sterk, H.A.M., Svensson, G., Vaillancourt, P.A. and Zadra, A. 2016. Select strengths and biases of models in representing the Arctic winter boundary layer over sea ice: the Larcform 1 single column model intercomparison. *Journal of Advances in Modeling Earth Systems*. **8**(3), pp.1345–1357.

Schmale, J., Zieger, P. and Ekman, A.M.L.L. 2021. Aerosols in current and future Arctic climate. *Nature Climate Change*. **11**(2), pp.95–105.

Serreze, M.C. and Barry, R.G. 2011. Processes and impacts of Arctic amplification: A research synthesis. *Global and Planetary Change*. **77**(1–2), pp.85–96.

Tarn, M.D., Sikora, S.N.F., Porter, G.C.E., Shim, J.U. and Murray, B.J. 2021. Homogeneous freezing of water using microfluidics. *Micromachines.* **12**(2), pp.1–23.

Whale, T.F., Murray, B.J., O'Sullivan, D., Wilson, T.W., Umo, N.S., Baustian, K.J., Atkinson, J.D., Workneh, D.A. and Morris, G.J. 2015. A technique for quantifying heterogeneous ice nucleation in microlitre supercooled water droplets. *Atmospheric Measurement Techniques.* **8**(6), pp.2437–2447.

Xie, S., Liu, X., Zhao, C. and Zhang, Y. 2013. Sensitivity of CAM5-simulated arctic clouds and radiation to ice nucleation parameterization. *Journal of Climate.* **26**(16), pp.5981–5999.

Appendix A
Supplementary information for:
Resolving the size of ice-nucleating particles with a balloon deployable aerosol sampler: the SHARK

A.1 Sampling information

Table A1. Details of SHARK sampling dates, times, locations components.

Site	Date (dd/mm/yy)	Sampling period	Impactors	Volume sampled by Impactor 1 at 9 L min⁻¹ (L)	Volume sampled by Impactor 2 at 100 L min⁻¹ (L)	Impactor 1 after-filter?	Windsond?	OPC?
Cardington (UK)	15/05/2018	14:15-16:15 (2 h)	Impactor 1 and 2 installed, only Impactor 2 sampling	-	12,000	No	No	Installed but not sampling
Hyytiälä (Finland)	11/03/2018	10:45-16:00 (5 h 15)	Impactor 1 only	2,835	-	No	No	No
Leeds (UK)	07/06/2018	12:21-15:21 (3 h)	Both impactors	1,620	18,000	Yes	Yes	Yes
Longyearbyen (Svalbard)	23/09/18-24/09/18	20:00-04:30 (8 h 30)	Both impactors	4,590	51,000	Yes	Yes	Yes
High Arctic	20/08/2018	10:40-15:30 (4 h 50)	-	-	-	-	Yes	Yes

A.2 Fraction frozen curves for collected samples
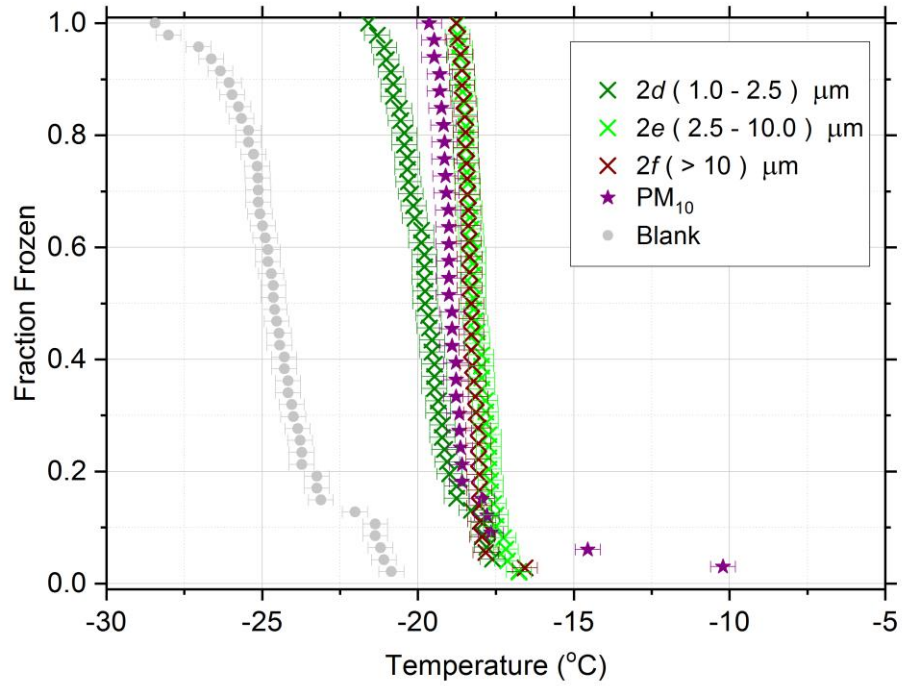
Figure A0.1. Fraction frozen curves for samples collected in Cardington (UK).
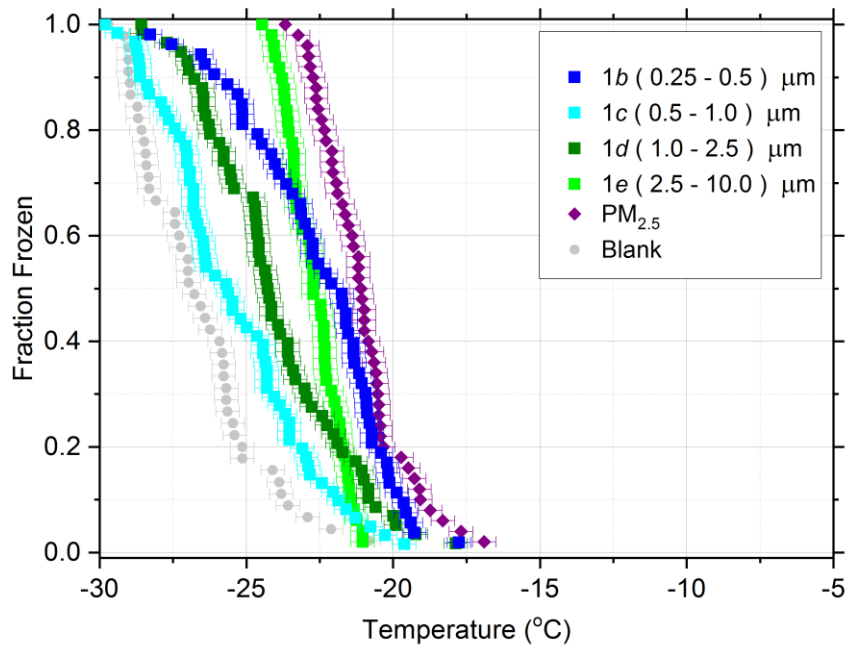
Figure A0.2. Fraction frozen curves for samples collected in Hyytiälä (Finland).
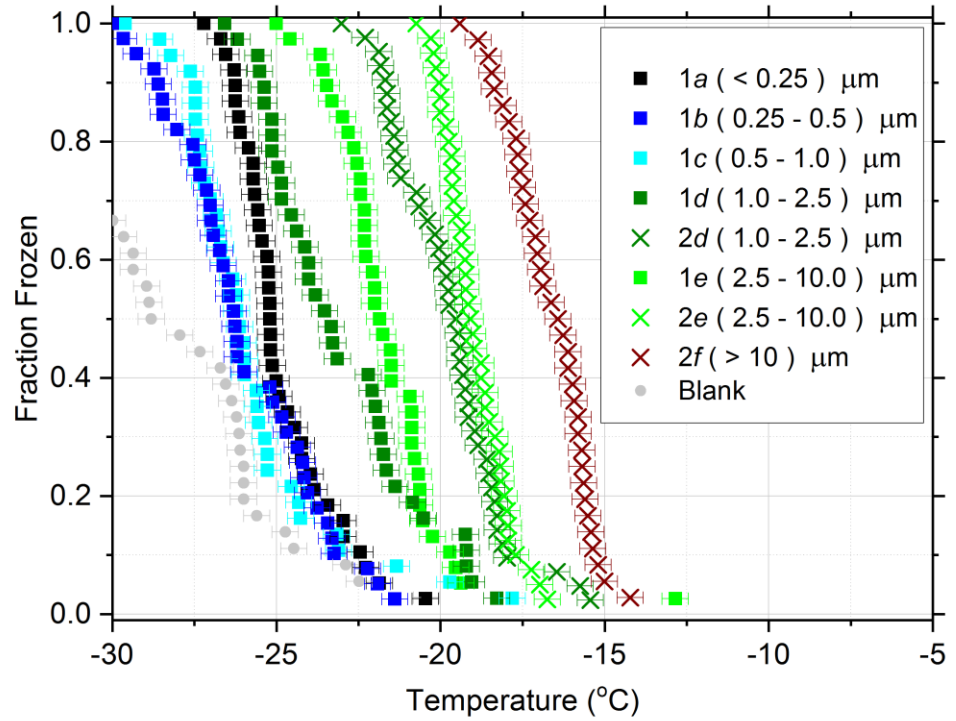
Figure A0.3. Fraction frozen curves for samples collected in Leeds (UK).
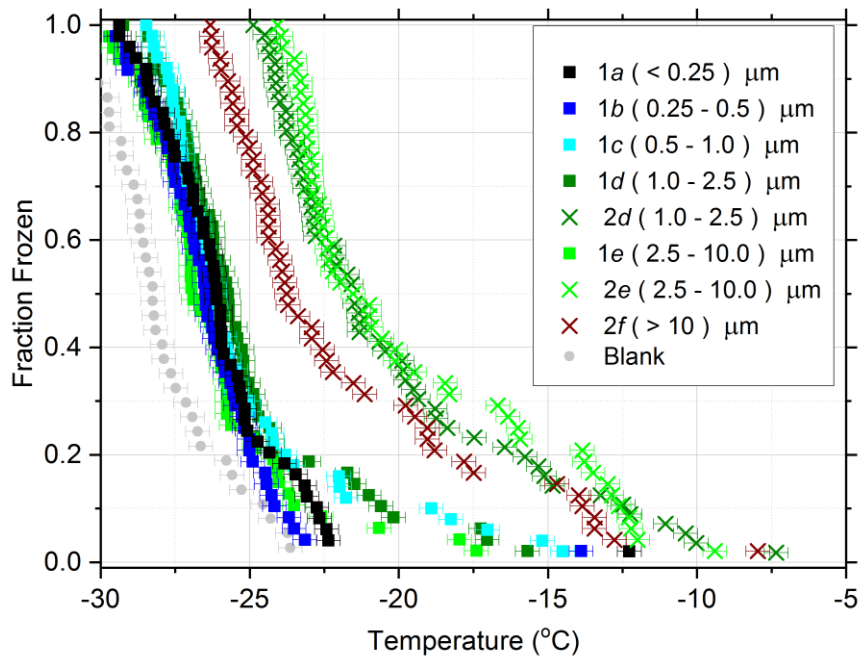
Figure A0.4. Fraction frozen curves for samples collected in Longyearbyen (Svalbard).

A.3   Aerosol data from sampling in Leeds (UK)
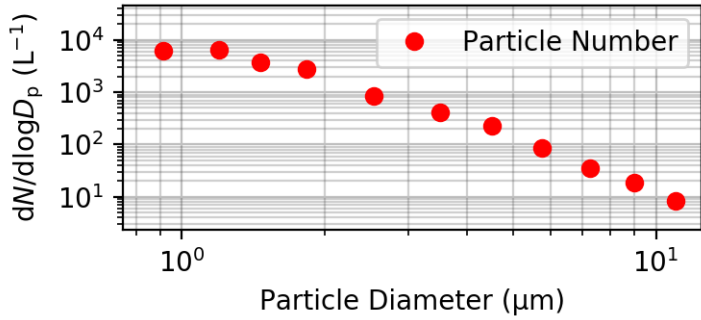
Figure A0.5. Particle number size distribution data for samples collected in Leeds (UK).
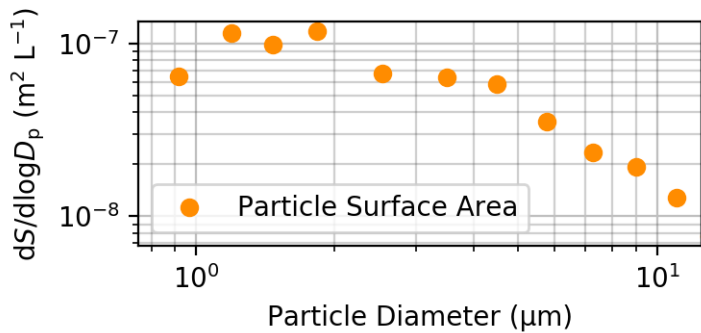
Figure A0.6. Particle surface area size distribution data for samples collected in Leeds (UK).
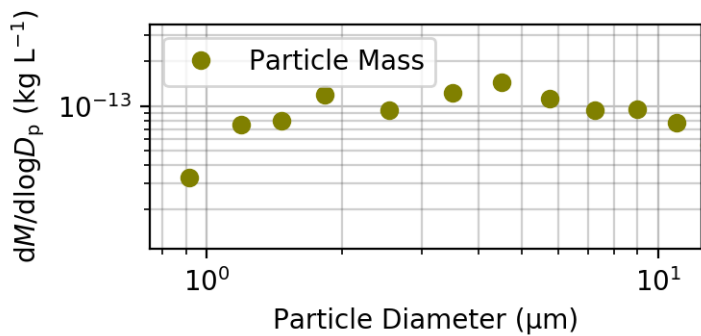
Figure A0.7. Particle mass size distribution data for samples collected in Leeds (UK).

A.4 Aerosol data from sampling in Longyearbyen (Svalbard)
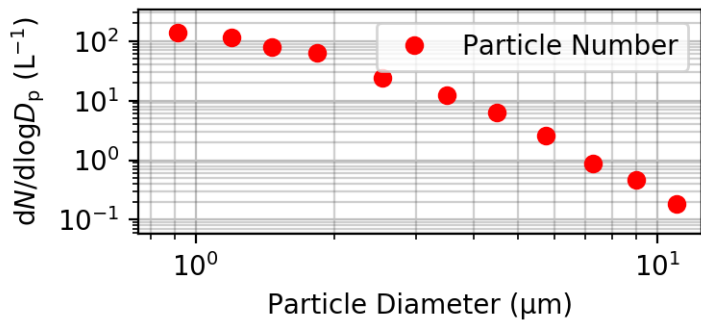
Figure A0.8. Particle number size distribution data for samples collected in Longyearbyen (Svalbard).
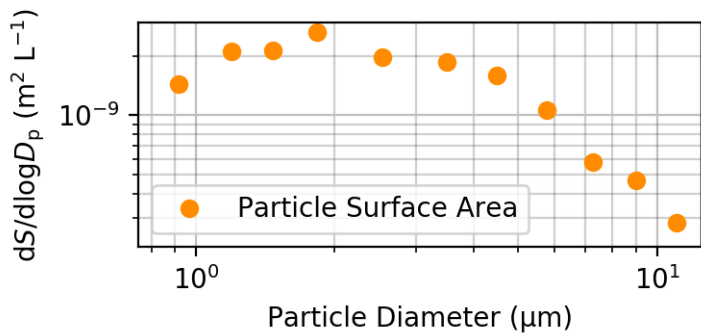
Figure A0.9. Particle surface area size distribution data for samples collected in Longyearbyen (Svalbard).
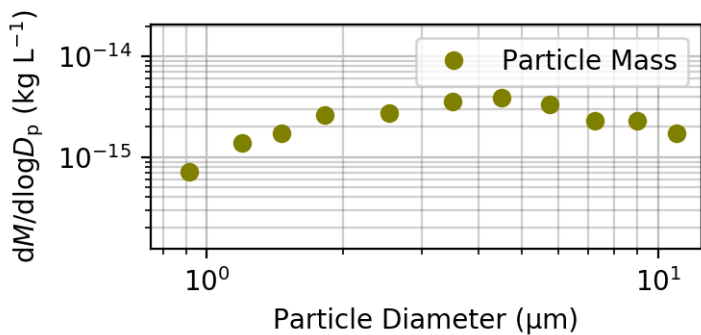
Figure A0.10. Particle mass size distribution data for samples collected in Longyearbyen (Svalbard).

Appendix B
Supplementary information for:
Origin and variability of ice-nucleating particles close to the summertime North Pole

Table B1. Concentration of major ions derived using ion chromatography for several of the filter samples.

| Sample Name	Sampling time	Concentration (µeq/L)										T at [INP]=0.1 L-1
	(mins)	Fluoride	MSA	Chloride	Nitrate	Sulphate	Sodium	Ammonium	Potassium	Magnesium	Calcium	
180811	1264	0.0E+00	7.4E-04	1.0E-02	4.2E-04	1.6E-03	8.6E-03	1.4E-03	5.2E-04	1.7E-03	1.6E-03	-11.5
180816	1093	5.3E-04	5.3E-04	7.8E-04	7.2E-04	5.9E-04	9.3E-04	1.8E-03	4.1E-04	1.1E-04	1.3E-03	-23.5
180819	2065	1.9E-03	6.1E-05	2.8E-03	4.2E-04	9.6E-04	2.8E-03	2.2E-03	1.8E-03	9.3E-05	8.9E-04	-11.5
180831	4260	6.1E-04	4.0E-05	2.0E-03	1.9E-04	5.7E-04	1.7E-03	5.3E-04	4.2E-04	2.6E-04	3.5E-04	-30
180912	3274	3.7E-04	4.3E-06	6.7E-03	3.7E-04	1.1E-03	5.8E-03	9.4E-04	6.2E-04	1.1E-03	6.9E-04	-22

Table B2. Details of sampling dates, times and volumes for the SHARK samples in the cloud mixed layer.

Date	Sampling period	Volume sampled by Impactor 1 at 9 L min⁻¹ (L)	Volume sampled by Impactor 2 at 100 L min⁻¹ (L)	Total volume sampled (L)
180820	1040-1530	2610	29000	31610
180823	1720-2020	1620	18000	19620
180826	1730-2220	2610	29000	31610
180904-180905	2000-0015	2295	25500	27795
180908	1705-2005	1620	18000	19620
180909	1315-1955	3600	40000	43600
180910	1015-1535	2880	32000	34880
180913	1745-2335	3150	35000	38150
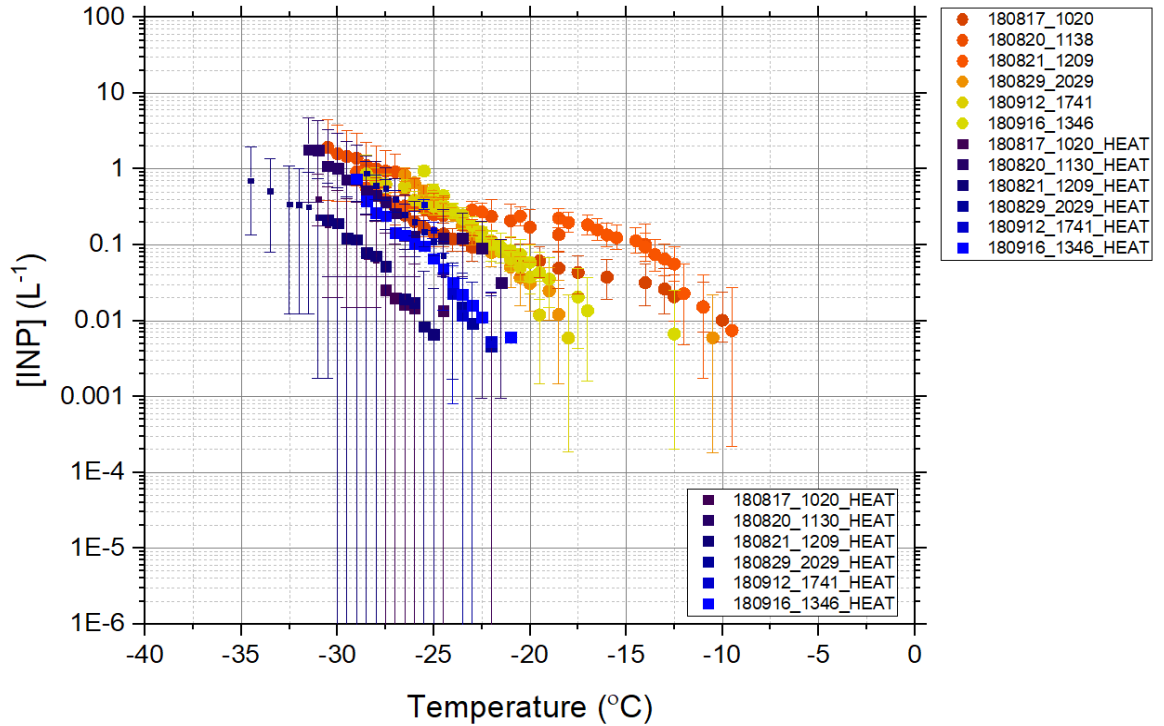
Figure B0.1 - INP concentration results for heat-tested samples throughout the AO18 campaign. The number of INPs per litre of air sampled was calculated using data from droplet freezing experiments, conducted within hours of the samples being taken. The spectra shown in blues are samples that were heated to 90 °C for 30 min. The data has had the backgrounds subtracted and the limiting values are shown as smaller points. Samples were taken using a heated whole air inlet on the second deck of the Oden Icebreaker. Temperature uncertainties (not shown) for the droplet freezing experiments were estimated to be ±0.4 °C. The dates for the respective periods are: Ice floe 16/08/18-15/09/18, Ice-breaking 15/09/18-19/09/18.
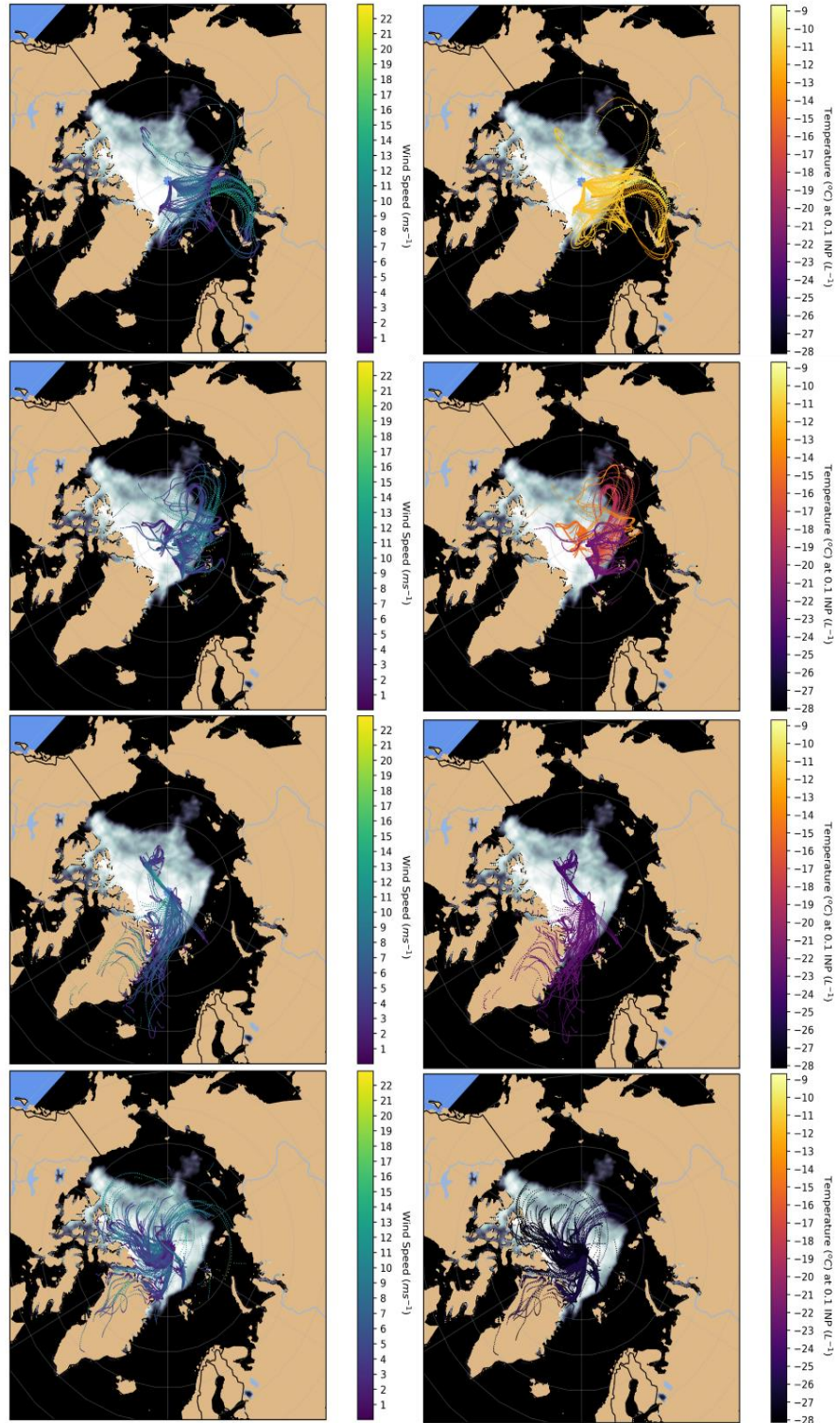
Figure B0.2 – Backward trajectories over 7 days with wind speed (left column) and temperature at 0.1 INP L-1 (right column) as the colour of the points.
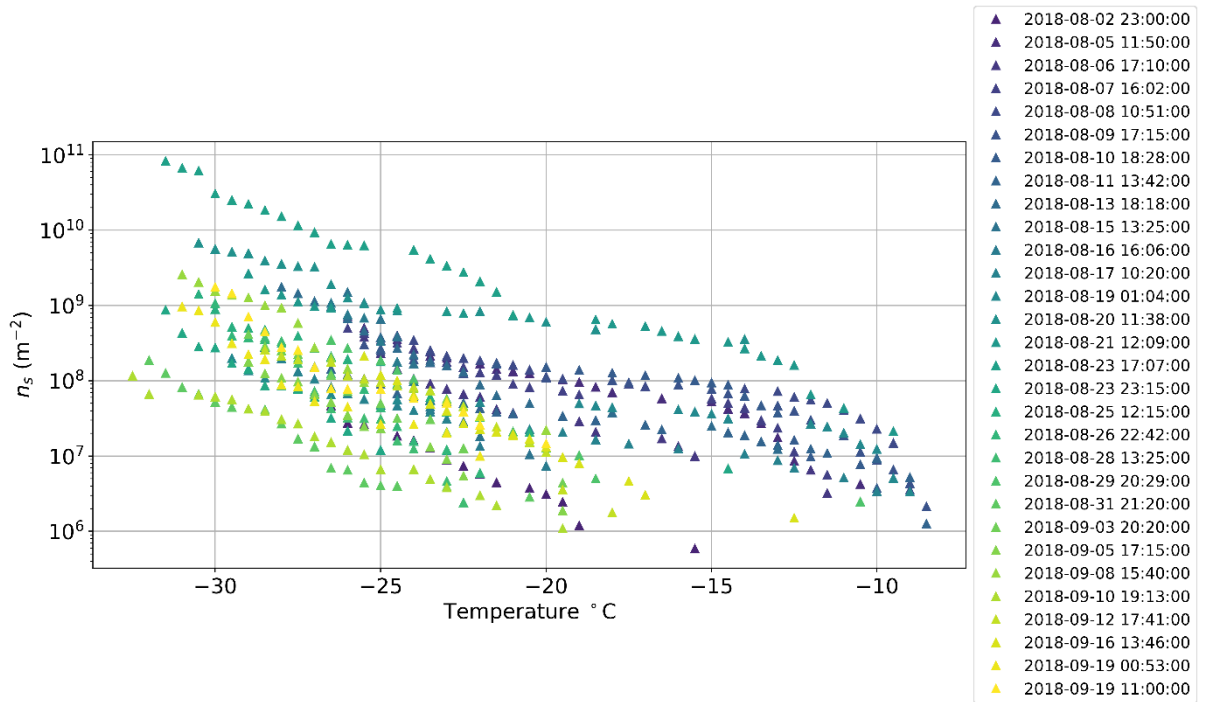
Figure B0.3 - The number of ice-active sites per unit surface area, ns, for each whole air filter run.
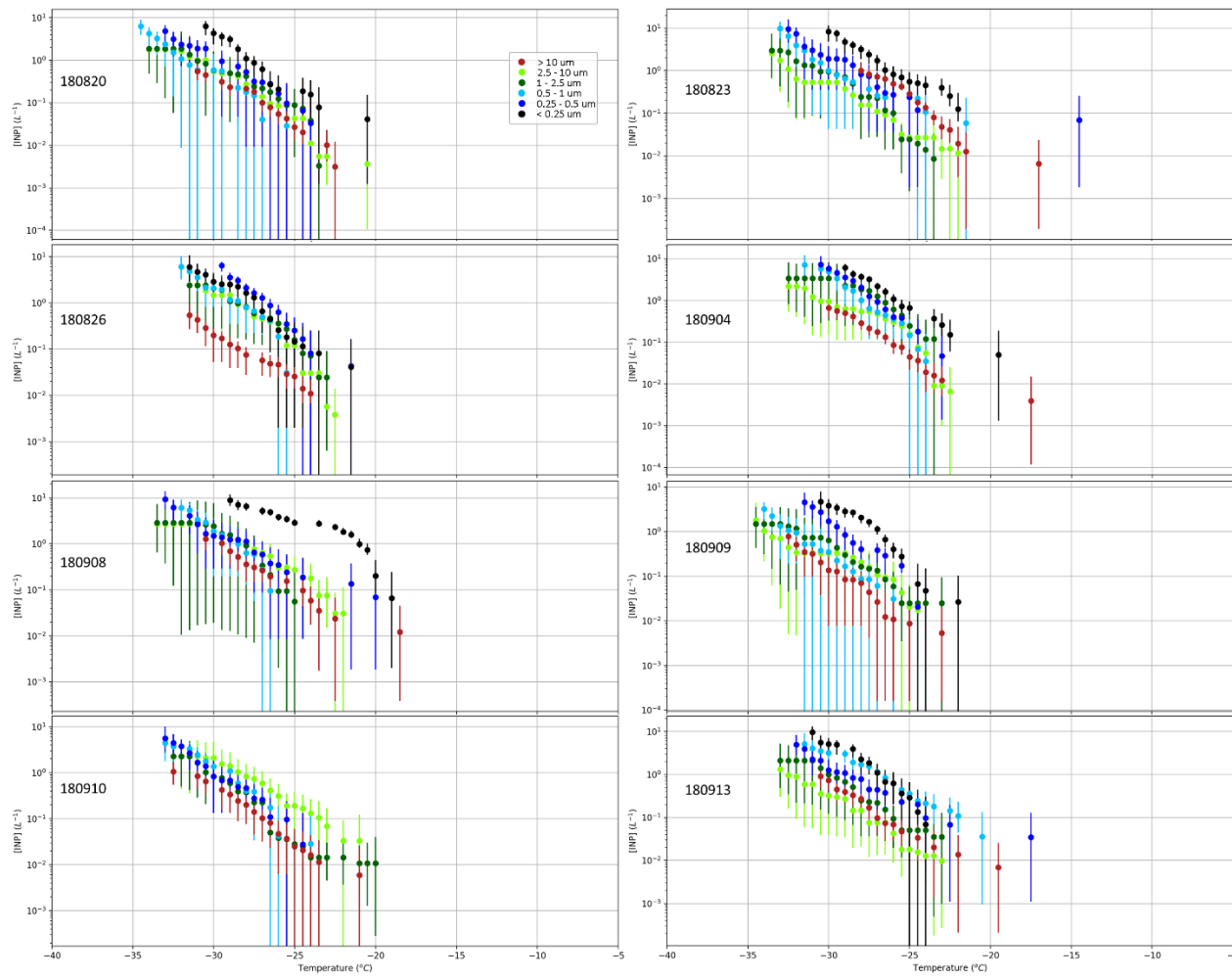
Figure B0.4 - The size-separated filter results for the SHARK flights in the cloud mixed layer on the dates shown.

Appendix C
Supplementary information for:
On-chip density-based sorting of supercooled droplets
and frozen droplets in continuous flow

C.1   Reynolds numbers and Archimedes number

The Reynolds number, Re (dimensionless), of a flowing system of fluid is the ratio of the inertial force to the viscous force, where flow in a microfluidic channel is typically considered to be laminar when $Re < 2,000$-$2,300$ (depending on the features of the system), turbulent when $Re > 3,000$-$4,000$, and transitional when $2,000 < Re < 3,000$-4000 [1-3]:

$$Re = \frac{\text{inertial force}}{\text{viscous force}} = \frac{\rho_m\, u_m\, D_H}{\eta} \qquad\qquad \text{(S1)}$$

where ρ_m is the density of the fluid (kg m^{-3}), u_m is the velocity of the fluid (m s^{-1}), D_H is the hydraulic diameter of the channel (m), and η is the viscosity of the fluid (kg m^{-1} s^{-1}). In the case of a very wide or tall but flat channel having a width of a and a height of b where $a << b$, as in the case of the microfluidic device used here, then $D_H = 2a$ [4].

The Stokes' law approximation that describes the viscous force on a particle moving through a fluid (see Equation 2 in the main paper) is only valid for fluid systems in the Stokes flow regime (also known as *creeping flow*), where the Reynolds number is so low ($Re << 1$) that the viscous forces dominate the inertial forces [1]. In order to assess whether the Stokes' law approximation held true for our microfluidic system, the Re in the separation chamber was calculated assuming a constant temperature (−4.8 °C, which determined the values of ρ_m and η as described in Section 3 of the ESI) and flow velocity across the top ¾ of the separation chamber (to account for the approximate location of the interface between the flowing liquid and the stationary liquid at the bottom of the channel). Therefore, with an estimated channel height of 8,175 µm (the full height of the separation chamber was 10,600 µm), the fluid velocity was determined to be 2.04 mm s^{-1} based on the applied flow rates in the chip. Using these assumptions, the flow in the separation chamber was determined to have an $Re = 0.4$. Therefore, while this was perhaps in the upper range of the Stokes flow regime, the assumptions should hold for the use of Stokes' law as per Equation 2 in the main paper.

Also particularly pertinent to the Stokes' law assumption is the particle Reynolds number, Re_p (dimensionless), which describes the flow of fluid around a particle [5,6]:

$$\text{Re}_\text{p} = \frac{\text{inertial force}}{\text{viscous force}} = \frac{\rho_\text{m}\, u_\text{p}\, D_\text{p}}{\eta} \tag{S2}$$

where D_p is the particle diameter (m), and u_p is the velocity of the particle (m s^{-1}), either in the x-direction as the velocity due to the hydrodynamic flow, $u_\textbf{hyd}$, or in the y-direction as the velocity due to the particle's buoyancy, $u_\textbf{buoy}$. Re_p was calculated for both $u_\textbf{buoy}$ and $u_\textbf{hyd}$ using the average velocity values and particle diameters for the experimental runs in each case, as shown in Table C1.

Table C1. The particle Reynolds numbers, $\text{Re}_\textbf{p}$ (dimensionless), determined for water droplets and ice crystals in the x-direction and y-direction in the microfluidic separation chamber, based on the experimentally determined particle velocities and diameters.

	$\text{Re}_\textbf{p}$	
	x-direction (u_hyd)	y-direction (u_buoy)
Water droplets	0.15	0.05
Ice crystals	0.17	0.06

Stokes' law holds true for $\text{Re}_\text{p} < 0.2\text{-}1$ [5,6], and as Re_p exceeds 1 the theory begins to deviate from experimental data [6]. In our system, the water droplets and ice crystals demonstrated $\text{Re}_\text{p} < 0.2$ in both the x- and y-directions, further indicating that the use of Stokes' law in Equation 2 is appropriate. Most importantly, the Re_p value in the y-direction due to $u_\textbf{buoy}$ was much smaller than 0.2, and this is the relevant quantity regarding the use of Equations 1 and 2 in the main paper to describe the sedimentation or creaming of a particle due to gravity.

Additionally, the settling regime of our system can be described by the Archimedes number, Ar (dimensionless). Ar is defined in a similar manner as Re_p, in that it describes a force encouraging particle movement against a force resisting that movement, but is more specifically for the vertical

movement of a particle in that it is the ratio between the sinking force (the particle's weight minus its buoyancy) and the viscous force [7,8]:

$$\text{Ar} = \left(\frac{\text{sinking force}}{\text{viscous force}}\right)^2 = \frac{\rho_m \left(\rho_p - \rho_m\right) g \left(D_p\right)^3}{\eta^2} \tag{S3}$$

where ρ_p is the density of the particle (kg m^{-3}) and g is the acceleration due to gravity (9.81 m s^{-2}). An $\text{Ar} < 32.9$ places the particle in fluid in the Stokes regime, the intermediate regime is $32.9 < \text{Ar} < 106{,}520$, and $\text{Ar} > 106{,}520$ is the Newton regime [7]. Equation 3 in the main paper, which describes the sedimentation/creaming velocity (u_{buoy}) of a particle in a fluid, can only be used in its presented form when the particle is in the Stokes regime. In our system, the Ar values of the water droplets and ice crystals were calculated to be 3.8 and 4.6, respectively, hence they were in the Stokes regime and so Equation 3 holds true for the calculation of u_{buoy}.

C.2 Viscous drag coefficient, C_W

The viscous drag coefficient, C_W (dimensionless), describes the effect of viscous drag experienced by particles due to the surfaces of a microchannel through which they flow, and can be calculated using Equation S4 [9-11]:

$$C_W = \left[1 - 1.004\left(\frac{r}{h_z}\right) + 0.418\left(\frac{r}{h_z}\right)^3 + 0.21\left(\frac{r}{h_z}\right)^4 - 0.169\left(\frac{r}{h_z}\right)^5\right]^{-1} \tag{S4}$$

where r is the particle radius (m), and h_z is half the distance of the shortest dimension of the microchannel (m). In this case, the shortest dimension of the microfluidic separation chamber was its width of 140 μm, hence h_z was 7 × 10^{-5} m. C_W was calculated for experimentally measured radii of the water droplets (average radius = 59.2 μm) and ice crystals (average radius = 60.9 μm), yielding a C_W value of 2.28 for the water droplets and ice crystals.

C.3 Properties of Novec™ 7500 Engineered Fluid

The absolute (dynamic) viscosity, η (kg m^{-1} s^{-1}; Pa s; Poise), of the 3M™ Novec™ 7500 Engineered Fluid (2-trifluoromethyl-3-ethoxydodecafluorohexane; $C_7F_{15}OC_2H_5$; CAS No. 297730-93-9) was calculated from the kinematic viscosity, v_k (m^2 s^{-1}), and the density, ρ_m (kg m^{-3}), of the fluid at temperature T (°C) using Equation S5:

$$\eta = v_k\,\rho_m \tag{S5}$$

The kinematic viscosity, v_k (m^2 s^{-1}), of the fluid temperature T (°C) inside the separation chamber of the microfluidic device was determined using Equations S6 and S7, which were adapted from the manufacturer's product information [12]:

$$v_k = [(Z - 0.7) - \exp(-0.7487 - 3.295(Z - 0.7) \\ + 0.6119(Z - 0.7)^2 - 0.3193(Z - 0.7)^3)] \times 10^{-6} \tag{S6}$$

where

$$Z = 10\verb|^|(10^{11.843 - 5.0874\,\log(T + 273.15)}) \tag{S7}$$

The density, ρ_m (kg m^{-3}), of the Novec™ 7500 Engineered Fluid at temperature T (°C) was calculated using Equation S8, obtained from the manufacturer's product information [12]:

$$\rho_m = -2.0845\,T + 1665.8 \tag{S8}$$

The changes in viscosity and density of Novec™ 7500 Engineered Fluid with decreasing temperature below 0 °C are shown in Fig. C1 and Fig. C2, respectively.

C.4   Viscosity of supercooled water

Although the calculation of the viscosity of supercooled water was not needed for any calculations related to the droplet sorting experiments, it was of general interest and is useful to compare to the viscosity of the Novec™ 7500 Engineered Fluid. The viscosity of water, η_w (kg m^{-1} s^{-1}), at temperature T (K) was calculated using the parameterisation of Dehaoui et al. [13], which both fit well with and extended the datasets of Hallett [14], Collings and Bajenov [15], and Osipov et al. [16], as shown in Equation S9.

$$\eta_w = \eta_0 \left(\left(\frac{T}{T_s} \right) - 1 \right)^{-\gamma} \tag{S9}$$

where $\eta_0 = 1.38 \times 10^{-4}$ kg m^{-1} s^{-1}, $T_s = 225.66$ K, and $\gamma = 1.6438$.

The viscosity of supercooled water at sub-zero temperatures (calculated using Equation S9) was compared to that of the Novec™ 7500 Engineered Fluid (calculated using Equations S5-S8), which highlighted the small response to changes in temperature of the Novec™ 7500 compared to supercooled water (Fig. C1).
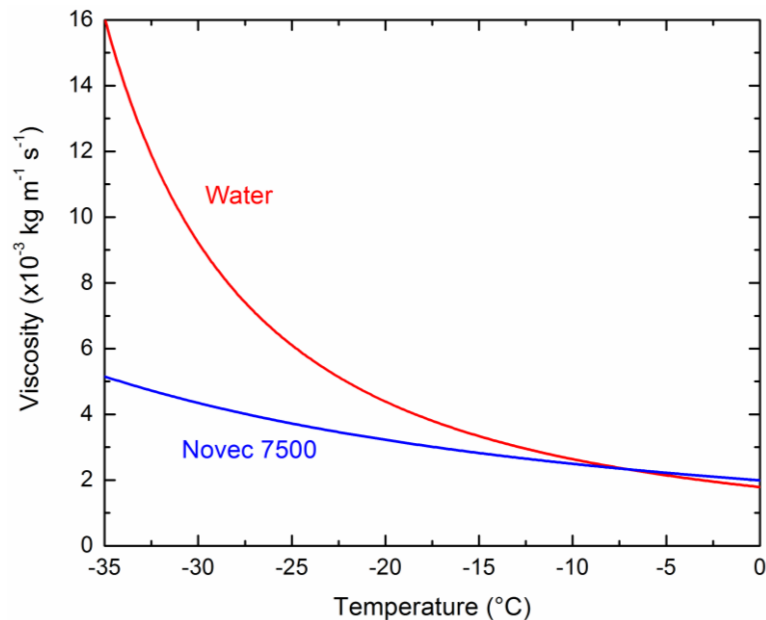
Figure C0.1 The change in viscosity at sub-zero temperatures for Novec™ 7500 Engineered Fluid and supercooled water.

C.5 Density of supercooled water

The density of water, ρ_w (g cm^{-3}), at temperature T (°C) below 0 °C was calculated using the parameterisation of Hare and Sorensen [17], whose values are used in the *CRC Handbook of Chemistry and Physics* [18], as shown in Equation S10. The ρ_w values were then converted to kg m^{-3} in later calculations and these values can be seen in Fig. C2.

$$\rho_\mathrm{w} = \sum_{n=0}^{6} a_n \, T^n \tag{S10}$$

where the a_n constants are as follows:

a_0 = 0.99986

a_1 = 6.690×10^{-5}

a_2 = -8.486×10^{-6}

a_3 = 1.518×10^{-7}

a_4 = -6.9484×10^{-9}

a_5 = -3.6449×10^{-10}

a_6 = -7.497×10^{-12}

C.6   Density of ice

The density of ice, ρ_i (g cm^{-3}), at temperature T (°C) was calculated using the parameterisation of Pruppacher and Klett [19], as shown in Equation S11, which is based on a fit of the data from La Placa and Post [20], Ginnings and Corruccini [21], and Lonsdale [22]. As such, it effectively also represents a fit of the ρ_i values in the *CRC Handbook of Chemistry and Physics* [18], which were taken from Eisenberg and Kauzmann [23] based on their computation of the X-ray diffraction data of La Placa and Post [20]. The ρ_i values calculated using Equation S11 were later converted to kg m^{-3} for subsequent calculations.

$$\rho_i = \sum_{n=0}^{2} a_n\, T^n \qquad \text{(S11)}$$

where the a_n constants are as follows:

a_0 = 0.9167

a_1 = -1.75×10^{-4}

a_2 = -5.00×10^{-7}

A comparison of the differences in density for Novec™ 7500 Engineered Fluid, water, and ice over a range of temperatures below 0 °C is shown in Fig. C2, based on calculations using Equations S8, S10, and S11, respectively.
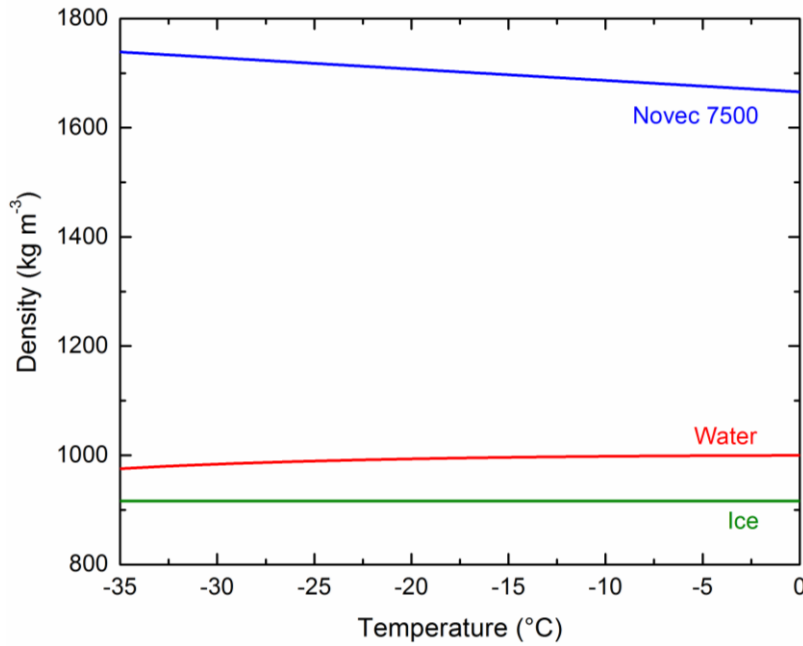
Figure C0.2 The densities of Novec™ 7500 Engineered Fluid, water, and ice at sub-zero temperatures.

C.7   Theoretical Fbuoy and ubuoy values

Theoretical values for the buoyancy force, F_{buoy}, and the velocity in the y-direction of the microfluidic separation chamber due to the buoyancy, u_{buoy}, were calculated for liquid water droplets and ice crystals using Equations 1-3 from the main paper. Viscosity and density values for the calculations were obtained using Equations S5-S8, S10, and S11 for Novec™ 7500 Engineered Fluid, water, and ice, and a nominal water droplet diameter of 115 µm (equivalent to 796 pL) was selected. The change in F_{buoy} with temperature for water droplets and ice crystals is shown in Fig. C3a, and demonstrates the greater buoyancy forces on the ice crystals across the full temperature range of 0 to −35 °C. The difference in F_{buoy} between the water droplets and ice crystals (ΔF_{buoy}) is shown in Fig. C3b. This effect is further reflected in the u_{buoy} values, shown in Fig. C4a, which used the viscous drag coefficient, C_w, calculated as described in Equation S4 for the microfluidic separation chamber. This shows an increase in the u_{buoy} velocity of ice crystals in the y-direction of the separation chamber compared to the water droplets, illustrated in Fig. C4b as the difference in velocities (Δu_{buoy}) between the ice crystals and water droplets. The differences in F_{buoy} and u_{buoy} between the water droplets and ice crystals provide the means by which the two species can be separated in continuous flow. The F_{buoy} and

u_{buoy} values for water and ice are actually negative, indicating that they would each cream rather than sediment with respect to gravity, but are shown in Figs. C3 and C4 as positive values for simplicity.
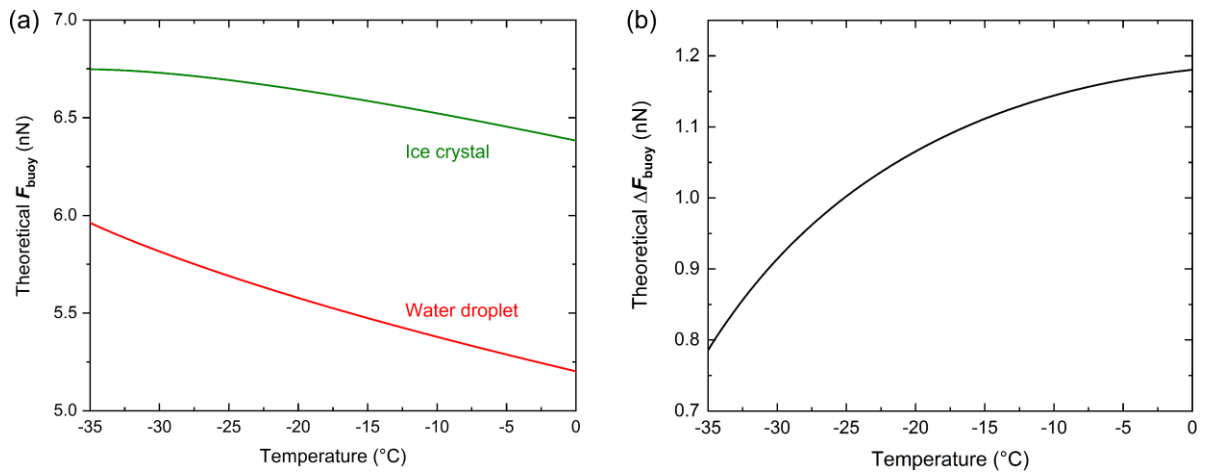
Figure C0.3 (a) The temperature-dependent change in theoretical buoyancy force in the y-direction, F_{buoy}, for a water droplet of 115 μm nominal diameter and an ice crystal (117.2-118.4 μm diameter depending on the temperature, based on the volume increase upon the freezing of a 115 μm water droplet) in Novec™ 7500 Engineered Fluid. (b) The difference in F_{buoy} between a water droplet and an ice crystal in Novec™ 7500 Engineered Fluid, based on the parameters in (a).

Figure C0.4 (a) The temperature-dependent change in the theoretical velocity in the y-direction, u_{buoy}, of a water droplet (115 μm nominal diameter) and an ice crystal (117.2-118.4 μm diameter depending on the temperature) in Novec™ 7500 Engineered Fluid. (b) The difference in u_{buoy} between a water droplet and an ice crystal in Novec™ 7500 Engineered Fluid, based on the parameters in (a).
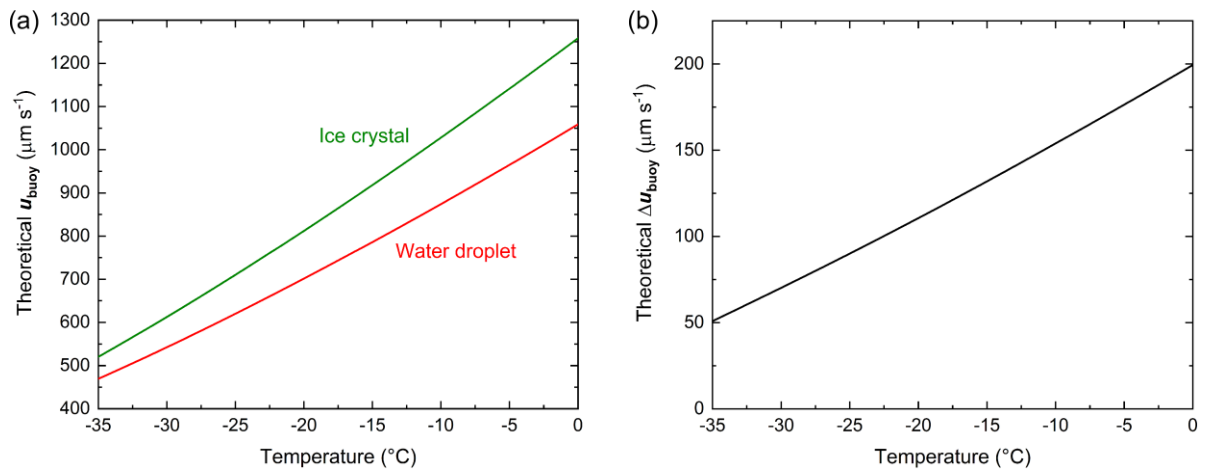
C.8   Fabrication and setup of the microfluidic device

C.8.1.   Fabrication of the microfluidic device

The fabrication of the microfluidic device was performed as described by Tarn et al. [24], using standard soft lithography procedures [24-26]. The chip design (see Fig. 1c in the main paper) was prepared using AutoCAD 2017 software (Autodesk, Inc., San Rafael, CA, USA), from which an emulsion-on-film photomask was printed by JD Photo Data (Hitchin, UK). A 140 μm thick layer of MicroChem SU-8 2075 negative photoresist (A-Gas Electronic Materials Ltd., Rugby, UK) was spin-coated onto a silicon wafer (3" diameter, PI-KEM Ltd., Tamworth, UK) and baked on. The wafer was then exposed to ultraviolet (UV) light (210 mJ cm^{-2}) through the film photomask using a mask aligner (Model 200, OAI). Following another baking step, the wafer was developed in photodeveloper solution (Microposit EC Solvent Developer, A-Gas Electronic Materials Ltd.), rinsed with isopropanol (Fisher Scientific, Loughborough, UK) and dried with nitrogen gas. The final SU-8 structure of the microfluidic design on the silicon wafer was then profiled using a surface profiler (Dektak XT, Bruker), with the final thickness of the SU-8 structures being 140 ± 5 μm in height.

Poly(dimethylsiloxane) (PDMS, Dow Corning® Sylgard® 184 Kit, Ellsworth Adhesives, East Kilbride, UK) was mixed in a 10:1 ratio of base elastomer to curing agent and poured onto the silicon wafer, before being degassed in a vacuum desiccator for 1-2 h and finally allowed to cure at 75 °C for 1 h. The PDMS was then peeled off the silicon wafer and the microfluidic chips cut out using a scalpel. Access holes (1 mm Ø) were punched into the PDMS devices, which were then bonded to glass microscope slides (76 x 26 x 1 mm^3, Academy Science Products, Kent, UK) following plasma treatment (Zepto Version B, Diener Electronic GmbH, Germany) and allowed to cure at 75 °C for 1 h (see Fig. 2a in the main paper).

C.8.2.   Setup and operation of the microfluidic device

Polyethylene tubing (Smiths Medical, 0.38 mm inner diameter (i.d.) × 1.09 mm outer diameter (o.d.), Harvard Apparatus, Biochrom Ltd., Cambridge, UK) was inserted into the inlet and outlet access holes of the PDMS microfluidic device (see Fig. 2a in the main paper). The inlet tubing had

syringe needles (26 G x 23 mm, Terumo Neolus®, VWR, Lutterworth, UK) inserted into their opposite ends to allow their connection to glass syringes (SGE, Sigma-Aldrich, UK), which were inserted into separate syringe pumps (PHD Ultra, Harvard Apparatus, Biochrom Ltd.). An aqueous sample of 0.01 % w/w Snomax® Snow Inducer (Snomax International, purchased from SMI Snow Makers AG, Thun, Switzerland), a non-viable lyophilised form of *Pseudomonas syringae* bacteria, in a 1 mL glass syringe was pumped into the aqueous inlet channel at a flow rate of 0.1 μL min^{-1} for droplet generation. A solution of 0.2 % w/w Pico-Surf™ 1 surfactant (prepared from a stock concentration of 5 % w/w, Sphere Fluidics Ltd., Cambridge, UK) in 3M™ Novec™ 7500 Engineered Fluid (Fluorochem Ltd., Hadfield, UK) in a 1 mL glass syringe was pumped into the droplet generation oil inlet at a flow rate of 25 μL min^{-1} for the production of droplets. Novec™ 7500 Engineered Fluid, without the addition of surfactant, was pumped into the upper control flow inlet of the separation chamber at a flow rate of 113-115 μL min^{-1}. A 1 mL syringe containing Novec™ 7500 Engineered Fluid was connected to the lower control flow inlet of the separation chamber and was used to assist in the flushing of the chamber with Novec™ 7500, but was thereafter not used although it remained in place on the syringe pump to prevent fluctuations in the flow regime from that inlet. The three outlet tubes connected to the outlet access holes of the separation chamber were fed into a waste vial containing a small amount of Novec™ 7500.

C.8.3. Setup of the cold stage platform

The microfluidic device, with the tubing connected, was turned sideways and inserted into a cold stage platform that had been also been turned sideways, such that the wide separation chamber was now oriented vertically (see Fig. 2b in the main paper). The construction and operation of the cold stage platform and its associated temperature control unit are described in detail by Tarn et al. [24]. Briefly, the cold stage platform comprised three Peltier elements housed within a 3D printed body. Aluminium liquid heat exchangers located beneath each Peltier element allowed the flow of coolant (polyethylene glycol in water) through the system via a refrigerated recirculating chiller (WK 500, Lauda, UK) that was set to +5 °C. Polished aluminium plates were set upon each Peltier element and featured access holed that allowed the insertion of thermocouples. The Peltier elements and thermocouples were connected to a custom-built, four-channel temperature

control unit based on an Arduino Nano microcontroller (purchased from RS Components, Northants, UK) and bidirectional motor drivers (IBT_2 BTS7960 43A High Power Motor Driver) controlled via a pulse width modulation (PWM) driver (PCA9685, Adafruit Industries, USA) that allowed the temperature of the aluminium plates to be controlled using a proportional-integral-derivative (PID) loop written in Python (Python Software Foundation, Delaware, USA). The electronics package in the temperature control unit featured improvements over the previous version used by Tarn et al. [24], with the wiring layout now integrated onto a printed circuit board (PCB; fabricated by Seeed Technology Co. Ltd., Shenzhen, People's Republic of China), as shown in Fig. C5, rather than the hand-wired breadboard previously used, and featuring a universal serial bus (USB) isolator to reduce signal noise and interference.

The three aluminium plates were located in serial such that the microfluidic chip lay across all three, allowing the first plate (37 mm × 33 mm) to control the temperature of the droplet generation region of the chip (at a setpoint of +3 °C), the middle plate (8 mm × 14 mm) to allow the freezing of water-in-oil droplets in the main channel (at a setpoint of −17 °C), and the final plate (37 mm × 33 mm) to control the temperature of the separation chamber (at a setpoint of −8 °C). Whilst the previous version of the cold stage platform had required the underside of the microfluidic chips to be coated with a layer of chromium to aid visualisation via reflected light microscopy [24], here the aluminium plates were polished to render them reflective enough that chromium-coating of the chips was no longer required.

The chip was held in place in the cold stage platform using clips, and a Perspex lid was placed on the stage to form a chamber around the chip, with the tubing fed through access holes to the syringe pumps and waste vials outside the chamber. The chamber was purged with compressed air that had been passed through a drying unit in order to remove moisture that would otherwise condense onto the chip upon cooling to sub-zero temperatures. A modular Navitar Zoom 6000® Lens System (Mengel Engineering, Denmark) with coaxial lighting provided by an OPT Machine Vision 3 W light-emitting diode (LED) light source (Mengel Engineering) ws used for visualisation of water droplets and ice crystals inside the microfluidic device. A Phantom Miro Lab 120 high-speed camera with PCC 2.7 software (Vision Research Ltd., Bedford, UK) connected to the Navitar Zoom 6000® Lens System was used to record videos and take images of

droplet/crystal separations at a frame rate of 25 fps. A photograph of the complete setup is shown in Fig. C6, while a close-up photograph of a microfluidic chip positioned over the three cold stage plates in the chamber of the platform can be seen in Fig. 2b in the main paper.
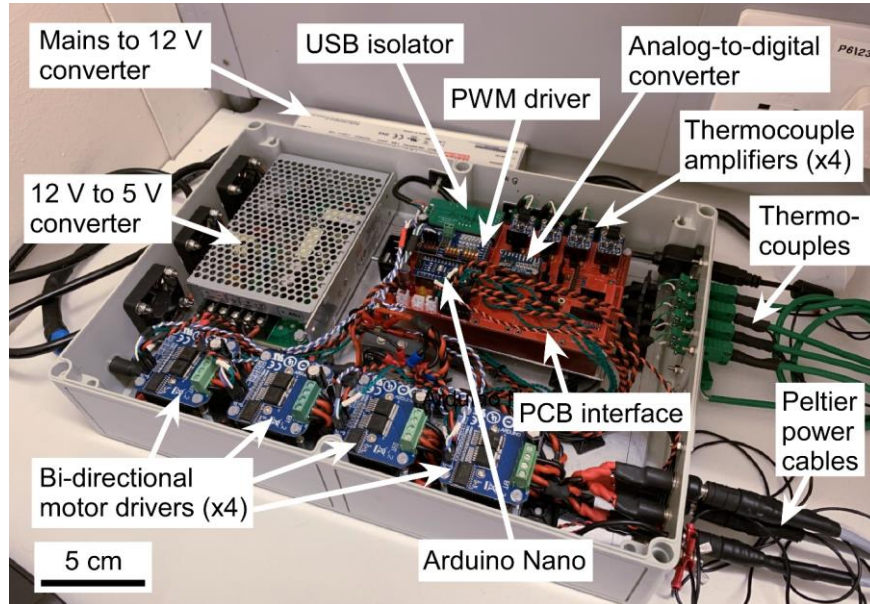

Figure C0.5 Photograph of the updated electronics package of the temperature control unit used to power the Peltier elements in the cold stage platform. The new package included a printed circuit board (PCB) that contained the wiring layout, compared to the hand-wired breadboard of the previous platform [24], and also featured a USB isolator to reduce electrical noise and interference.
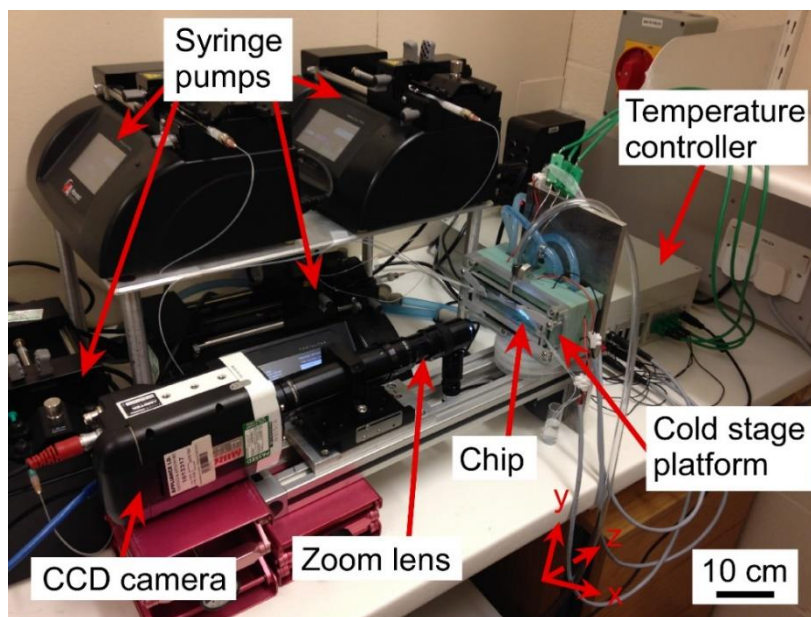
Figure C0.6 Photograph of the apparatus used to perform the continuous flow separation of liquid water droplets and ice crystals in a microfluidic device. The photograph highlights the cold stage platform in which the microfluidic chip was placed, the temperature control unit, syringe pumps, and the visualisation setup. The recirculating chiller used to pump coolant through the cold stage platform is out of shot, and was located beneath the bench.

C.9   On-chip temperature measurements

On-chip temperature measurements of the Novec™ 7500 Engineered Fluid as it flowed through the microfluidic separation chamber were performed in order to inform calculations of F_{buoy} and u_{buoy}, which incorporate the temperature-dependent fluid viscosity (η) and density (ρ). The procedure was performed in a similar fashion to that described by Tarn et al. [24]. Two access holes (1 mm Ø) were punched into the chamber of the PDMS chip, one in the centre of the separation chamber and one above it (approximately ¾ of the way up the chamber), prior to bonding the PDMS to a glass microscope slide. After bonding, the access holes allowed the insertion of two thermocouples (80 μm diameter, 5SRTC-TT-KI-40-1M series K-type, Omega Engineering Ltd., Manchester, UK) into the chamber, as shown in Fig. C7.

The thermocouples were connected to a data logger (TC-08, ±0.025 °C, Pico Technology, St. Neots, UK), and had been calibrated against a platinum resistance thermometer (PRT; Netushin NR-141-N L10, RS Components, UK) connected to a custom-built Arduino-based temperature logger. This PRT, in turn, had been calibrated against a high-precision PRT probe (Model 5608, ±0.0013 °C, Fluke Corporation, USA) and temperature logger (Model 1560, Fluke Corporation, USA) that had been calibrated by the National Physical Laboratory (NPL, Teddington, UK). Following calibration, the thermocouples were estimated to have an uncertainty of ±0.03 °C in their readings. Short sections of polyethylene tubing (0.38 mm i.d. × 1.09 mm o.d., Smiths Medical) were used as sleeves around the thermocouple wires and sealed with glue, allowing the thermocouples to be inserted easily into the access holes of the chip via the sleeves without any leakage.

Temperature measurements in the separation chamber were taken under the same operating conditions (i.e. flow rates and cold stage plate temperatures) as were used in droplet separation experiments, albeit with only Novec™ 7500 Engineered Fluid being pumped into the chip (i.e. no aqueous sample, hence no droplets were formed during temperature measurements). The logged temperatures were corrected according to their calibration factors at each operating parameter, and the two temperature readouts (for the middle and top of the separation chamber) were averaged to obtain a typical temperature value for the chamber.

The variation in temperature in the measured region of the chamber under the operating conditions was no greater than 0.05 ± 0.03 °C, and this variation was largely caused by the duty cycle of the refrigerated recirculating chiller that was used to pump coolant through the cold stage platform. The difference in temperature between the two thermocouples was 0.07 ± 0.07 °C at its greatest. At a separation cool plate set temperature of −8 °C, the temperature inside the measured region of the chamber was −4.8 ± 0.2 °C, and this was used to calculate experimental F_{buoy} values from the experimental u_{buoy}, in addition to being used to calculate theoretical F_{buoy} and u_{buoy} values for comparison. However, these calculations were made with the caveat that the temperature measurements taken at specific locations in the chamber were used to represent the chamber as a whole, while the temperatures at different parts of the chamber likely varied due to the multiple sources of fluids at different flow rates and temperatures entering the chamber.

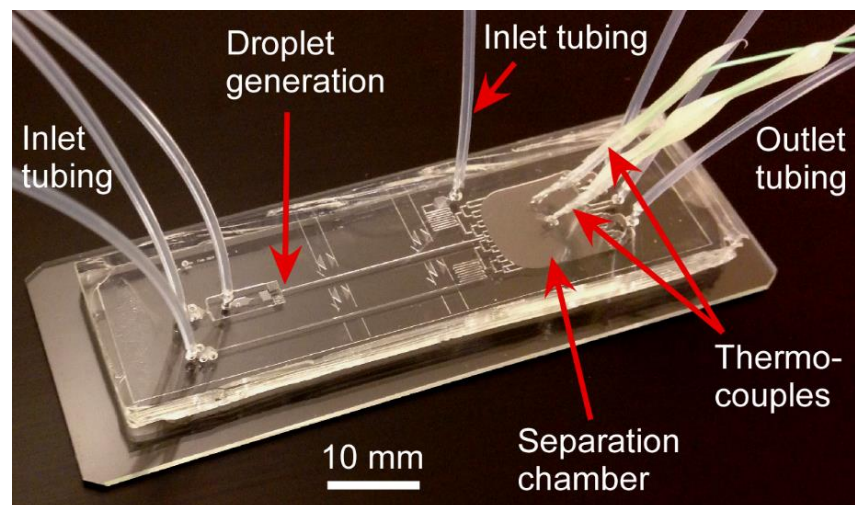**Figure C0.7 Setup of the microfluidic chip for on-chip temperature measurements of the Novec™ 7500 Engineered Fluid as it flowed through the separation chamber.** Two K-type thermocouples were inserted into the chamber, one at the midpoint and one slightly above it, and the two readings were averaged to indicate the temperature in the chamber where the water droplets and ice crystals would pass.

C.10   Properties of low viscosity silicone oil

The properties of low viscosity silicone oil (kinematic viscosity of 5 cSt at 25 °C) were explored theoretically as a potential means of improving the separation of water droplets and ice crystals in future iterations of the microfluidic sorting platform. Kamijo and Derda [28] used a low viscosity silicone oil, DM-FLUID-5cs (polydimethylsiloxane (PDMS); $(C_2H_6OSi)_n$) from Shin-Etsu Chemical Co., Ltd., containing 1 % v/v KF-6017 silicone-based emulsifier (Shin-Etsu Chemical Co., Ltd.) to assist in their static, cuvette-based method of separating water droplets and ice crystals (1 μL volume, ≈1.24 mm diameter) via buoyancy forces. Their system comprised a cushion fluid of Novec™ 7500 Engineered Fluid beneath a layer of DM- FLUID-5cs silicone fluid. Water droplets, having a density between the Novec™ 7500 and DM- FLUID-5cs, remained at the biphasic interface between the two fluids, but when droplets froze the resultant ice crystals had a density lower than both fluids, causing them to float to the top of the silicone oil and thus achieving separation.

This strategy could potentially be adapted to the continuous flow microfluidic sorting platform by pumping a low viscosity silicone oil, such as DM-FLUID-5cs, into the top of the separation chamber instead of Novec™ 7500, as illustrated in Fig. C8. Assuming the ice crystals could cross the interface from the Novec™ 7500 into the silicone oil (surface tension of DM-FLUID-5cs = 19.7 mN m^{-1} at 25 °C [29]), which may require the addition of a surfactant such as KF-6017 in the silicone oil phase, then the ice crystals could continue to migrate through the silicone oil in the y-direction whilst the water droplets would be unable to pass into the silicone oil and so remain at the same height throughout the chamber, thus potentially increasing the separation distances and efficiencies.
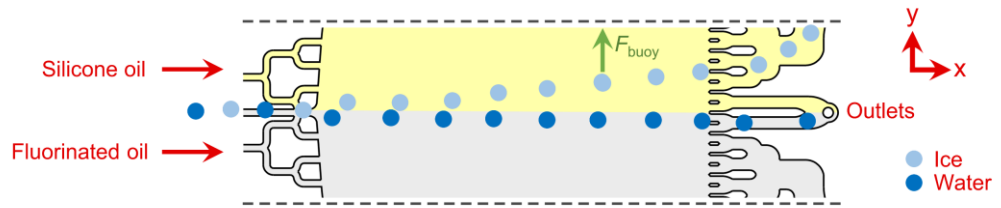
Figure C0.8 Schematic showing the principle of employing a low viscosity silicone oil as the upper control flow in the separation chamber of the microfluidic device. Here, water droplets would be unable to pass from the Novec™ 7500 Engineered Fluid into the silicone phase due to their being denser than the silicone oil, thereby providing a barrier to their migration in the y-direction. Ice crystals, on the hand, would have a lower density than the silicone oil and so would continue to travel in the y-direction, thus achieving separation.

In a similar manner to above, in which the theoretical F_{buoy} and u_{buoy} values of water droplets and ice crystals in Novec™ 7500 Engineered Fluid were calculated, here the theoretical values for water and ice in DM-FLUID-5cs, as a representative low viscosity silicone oil, were calculated based on data provided by the manufacturer [29]. The technical data sheet only provides a handful of data points for the kinematic viscosity and density of the silicone fluid below 0 °C, and not always at corresponding temperatures, but these data points were used to calculate the absolute viscosity for a limited number of temperatures using Equation S5. Fits were then applied to the available data points in order to approximate the absolute viscosity, η_s, and density, ρ_s, of DM-FLUID-5cs over a temperature range of 0 to −35 °C.

An Arrhenius-type equation was generated for the absolute viscosity, η_s, by first plotting the available data in terms of $\ln(\eta_s)$ vs $1/T$, with temperature in units of K, in order to obtain parameters for A (from the intercept) and B (from the slope). Thus, η_s (kg m⁻¹ s⁻¹) could be calculated for temperature T (K) as shown in Equation S12:

$$\eta_s = A \, e^{B/T} \tag{S12}$$

where $A = 7.935 \times 10^{-6}$ kg m⁻¹ s⁻¹, and $B = 1889.608$ K. A plot of DM-FLUID-5cs viscosities calculated using Equation S12 is shown in Fig. C9a alongside the viscosities of water and Novec™ 7500.

A linear fit was applied to the available density data, ρ_s (kg m^{-3}), for the DM-FLUID-5cs fluid for temperature T (°C), as shown in Equation S13:

$$\rho_s = -0.98237\,T + 939.8938 \tag{S13}$$

A plot of the DM-FLUID-5cs density calculated using Equation S13 is shown in Fig. C9b alongside the densities of water, ice, and Novec™ 7500, and clearly demonstrates how the density of a low viscosity silicone oil such as DM-FLUID-5cs sits between the densities of water and ice for the temperature range shown.
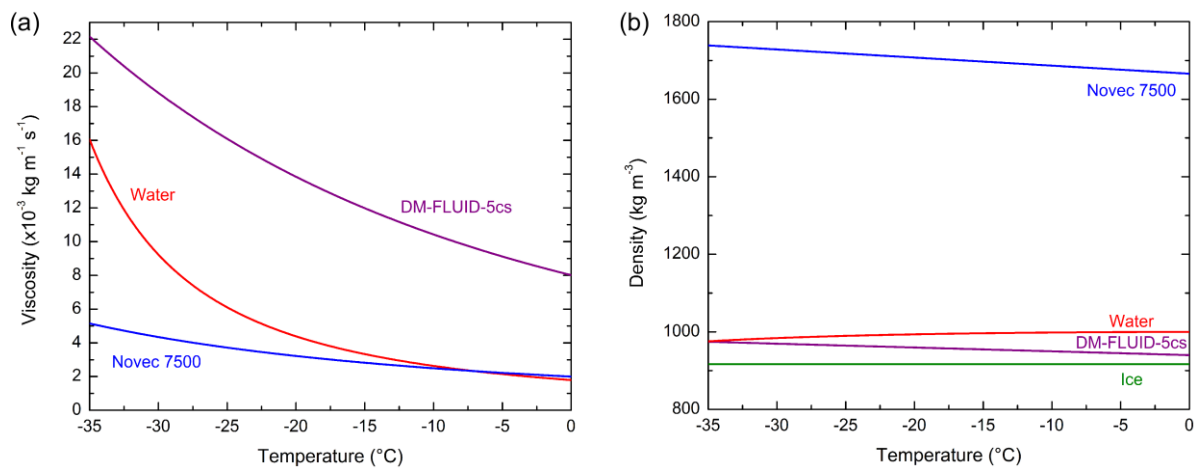

Figure C0.9 The properties of DM-FLUID-5cs, as a representative low viscosity silicone oil, calculated by fitting the data provided by the manufacturer [29]. (a) The viscosity, η_s, of DM-FLUID-5cs with temperature, and (b) the density, ρ_s, of DM-FLUID-5cs with temperature. The values of water, ice, and Novec™ 7500 Engineered Fluid are shown for comparison, using the data from Figs. C1 and C2.

The calculated η_s and ρ_s values were used to estimate the $\boldsymbol{F_{buoy}}$ and $\boldsymbol{u_{buoy}}$ values of ice crystals and water droplets in DM-FLUID-5cs using Equations 1-3 in the main paper, assuming an initial water droplet diameter of 115 μm that would yield ice crystals of 117.2-118.4 μm. depending on the temperature). The $\boldsymbol{F_{buoy}}$ results are shown in Fig. C10a, while the differences between the ice crystals and water droplets, $\Delta\boldsymbol{F_{buoy}}$, are shown in Fig. C10b, with the results for ice crystals and water droplets in Novec™ 7500 also shown for comparison. The results in Fig. C10 demonstrate that the $\boldsymbol{F_{buoy}}$ forces in DM-FLUID-5cs are orders of magnitude lower than in Novec™ 7500, and, importantly, even the $\Delta\boldsymbol{F_{buoy}}$ values between a water droplet and ice crystal are much smaller in DM-FLUID-5cs compared to Novec 7500™.

Notably, the F_{buoy} values for a water droplet in DM-FLUID-5cs are below 0 nN, thus reaffirming that water droplets would sediment in DM-FLUID-5cs.

Similar trends can be seen in the u_{buoy} values for water droplets and ice crystals, as shown in Fig. C11a, together with the Δu_{buoy} values between the two shown in Fig. C11b. The results show that the water droplets and ice crystals would move far more slowly in DM-FLUID-5cs compared to being in Novec™ 7500, and the Δu_{buoy} values in DM-FLUID-5cs would be far smaller than in Novec™ 7500, due to both the smaller ΔF_{buoy} and the high viscosity of DM-FLUID-5cs. The water droplets are shown as having a velocity below 0 μm s^{-1}, indicating that they would sediment in the y-direction rather than creaming when suspended in DM-FLUID-5cs, but in the context of the proposed experiment (see Fig. C8), the water droplets would not be able to enter the silicone phase in the first place based on their respective densities.

Therefore, even given the fact that in a continuous sorting system the water droplets should be unable to cross into the silicone phase, the velocity of the ice crystals in the y-direction in the silicone oil may be too low (up to 8 μm s^{-1}) to achieve a better separation than when only using Novec™ 7500, or to achieve a reasonable separation at all, at least without changes to the chip and the method. For example, the silicone oil flow rate could be greatly decreased in order to provide much longer residence times of the ice crystals in the separation chamber, thus allowing the crystals to migrate further in the y-direction, although this would impact on the throughput. A further issue could be that, given that the current microfluidic device is prepared from PDMS, there may also be issues with trying to use a PDMS fluid in the chip, though this could be alleviated by fabricating the device from other materials. Thus, although the use of silicone oil to enable a separation, as envisaged in Fig. C8, may be a viable strategy, further work would be required to ensure that ice crystals could migrate far enough in the y-direction to achieve a separation given the low u_{buoy} velocities. Given this, continuing to use Novec™ 7500 as the only oil in the system is likely still the better strategy for the platform going forward.
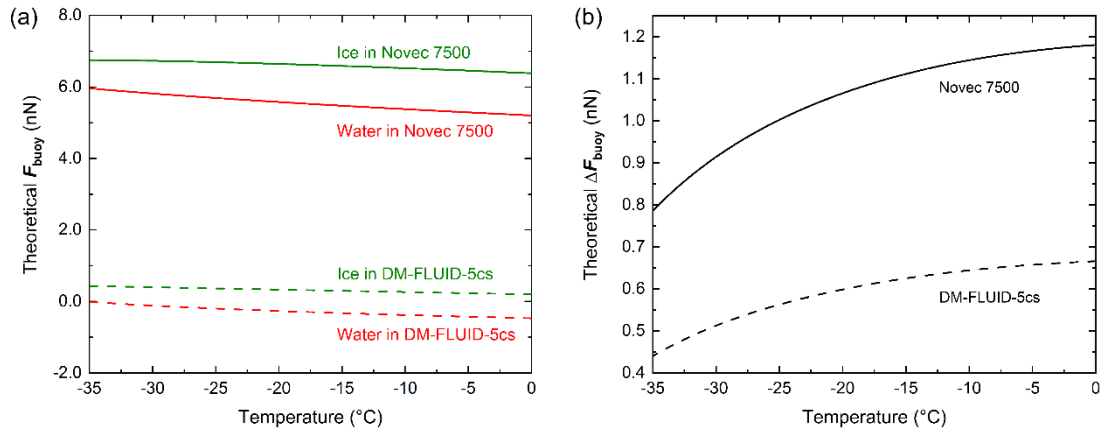
Figure C0.10 (a) The theoretical buoyancy forces, F_{buoy}, on a water droplet and an ice crystal in Novec™ 7500 Engineered Fluid fluorinated oil (solid lines) and DM-FLUID-5cs low viscosity silicone oil (dashed lines). The water droplet was assumed to have a diameter of 115 μm, while the ice crystal had a temperature-dependent diameter of 117.2-118.4 μm based on the freezing of a 115 μm diameter water droplet. The negative values for the water droplets in DM-FLUID-5cs indicate that the droplets would sediment in this silicone oil phase instead of creaming. The data for water and ice in Novec™ 7500 are the same as shown in Fig. C3. (b) The difference in theoretical F_{buoy} values between a water droplet and ice crystal in Novec™ 7500 Engineered Fluid fluorinated oil and DM-FLUID-5cs silicone oil.
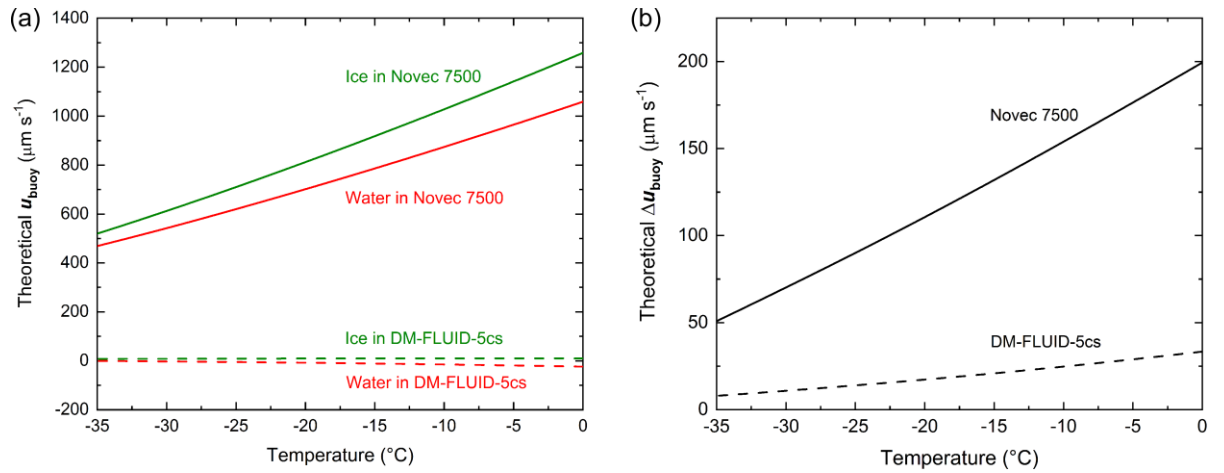
Figure C0.11 (a) The theoretical velocities in the y-direction, u_{buoy}, of a water droplet and an ice crystal in Novec™ 7500 Engineered Fluid fluorinated oil (solid lines) and DM-FLUID-5cs silicone oil (dashed lines), based on the same parameters described in Fig. C10 for a water droplet of 115 μm diameter. The data for water and ice in Novec™ 7500 are the same as shown in Fig. C4. (b) The difference in theoretical u_{buoy} values between a water droplet and ice crystal in Novec™ 7500 Engineered Fluid fluorinated oil and DM-FLUID-5cs silicone oil.

References

[1]   B. J. Kirby, Micro- and Nanoscale Fluid Mechanics: Transport in Microfluidic Devices, Cambridge University Press, Cambridge, 2010.

[2]   T. M. Squires and S. R. Quake, *Rev. Mod. Phys.*, 2005, **77**, 977-1026.

[3]   K. W. Oh, K. Lee, B. Ahn and E. P. Furlani, *Lab Chip*, 2012, **12**, 515-545.

[4]   F. M. White, *Fluid Mechanics, Seventh Edition*, McGraw-Hill, New York, 2011.

[5]   J. Zhang, S. Yan, D. Yuan, G. Alici, N. T. Nguyen, M. Ebrahimi Warkiani and W. Li, *Lab Chip*, 2016, 16, 10-34.

[6]   S. Dey, S. Z. Ali and E. Padhi, *Proc. R. Soc. A*, 2019, **475**, 20190277.

[7]   E. Rabinovich and H. Kalman, *Powder Technol.*, 2008, **183**, 304-313.

[8]   H. Kalman, D. Portnikov, O. G. Gabrieli, N. M. Tripathi, *Powder Technol.*, 2019, **354**, 485-495.

[9]   J. Happel and H. Brenner, *Low Reynolds Number Hydrodynamics*, Noordhoff International Publishing, Leyden, 2nd Revised Edition, 1973.

[10]   Y. Iiguni, M. Suwa and H. Watarai, *J. Chromatogr. A*, 2004, **1032**, 165-171.

[11]   M. D. Tarn, N. Hirota, A. Iles and N. Pamme, *Sci. Technol. Adv. Mater.*, 2009, **10**, 014611.

[12]   *3M™ Novec™ 7500 Engineered Fluid - Product Information* sheet, http://multimedia.3m.com/mws/media/65496O/3mtm-novectm-7500-engineered-fluid.pdf, 3M Company, accessed September 2019.

[13]   A. Dehaoui, B. Issenmann and F. Caupin, *Proc. Natl. Acad. Sci. U.S.A.*, 2015, **112**, 12020.

[14]   J. Hallett, *Proc. Phys. Soc.*, 1963, **82**, 1046-1050.

[15]   A. F. Collings and N. Bajenov, *Metrologia*, 1983, **19**, 61-66.

[16]   Y. A. Osipov, B. V. Zheleznyi and N. F. Bondarenko, *Russ. J. Phys. Chem.*, 1977, **51**, 748-749.

[17]   D. E. Hare and C. M. Sorensen, *J. Chem. Phys.*, 1987, **87**, 4840-4845.

[18]   *Properties of Ice and Supercooled Water*, in *CRC Handbook of Chemistry and Physics (CD-ROM Version 2010)*, 90th Edition, ed. D. R. Lide, CRC Press/Taylor and Francis, Boca Raton, FL, 2010, Chapter 6-12.

[19]   H. R. Pruppacher and J. D. Klett, *Microphysics of Clouds and Precipitation*, Kluwer Academic Publishers, Dordrecht, 1997.

[20]   S. J. La Placa and B. Post, *Acta Crystallogr.*, 1960, **13**, 503-505.

[21]   D. C. Ginnings and R. J. Corrucini, *J. Res. Natl. Bur. Stand.*, 1947, **38**, 583-591.

[22]   K. Y. Lonsdale and J. D. Bernal, *Proc. Royal Soc. A*, 1958, **247**, 424-434.

[23]   D. Eisenberg and W. Kauzmann, *The Structure and Properties of Water*, Oxford University Press, Oxford, 1969.

[24]   M. D. Tarn, S. N. F. Sikora, G. C. E. Porter, B. V. Wyld, N. Reicher, M. Alayof, A. D. Harrison, Y. Rudich, J.-u. Shim and B. J. Murray, *Lab Chip*, 2020, **20**, 2889-2910.

[25]   C. S. Effenhauser, G. J. M. Bruin, A. Paulus and M. Ehrat, *Anal. Chem.*, 1997, **69**, 3451-3457.

[26]   D. C. Duffy, J. C. McDonald, O. J. A. Schueller and G. M. Whitesides, *Anal. Chem.*, 1998, **70**, 4974-4984.

[27]   J. C. McDonald, D. C. Duffy, J. R. Anderson, D. T. Chiu, H. Wu, O. J. A. Schueller and G. M. Whitesides, *Electrophoresis*, 2000, **21**, 27-40.

[28]   Y. Kamijo and R. Derda, *Langmuir*, 2019, **35**, 359-364.

[29]   *Shin-Etsu Silicone Fluid DM-FLUID Technical Data Sheet*, https://www.shinetsusilicone-global.com/catalog/pdf/kf96_us.pdf, Shin-Etsu Chemical Co., Ltd., accessed August 2020.